Measurement of the High Q^2 Neutral Current DIS Cross Section at HERA

by

Matthias Moritz

Measurement of the High Q^2 Neutral Current DIS Cross Section at HERA

DISSERTATION

zur Erlangung des Doktorgrades
des Fachbereichs Physik
der Universität Hamburg

vorgelegt von

Matthias Moritz
aus Lüneburg

Hamburg
Dezember 2001

Gutachter der Dissertation: Prof. Dr. R. Klanner
Prof. Dr. J. Meyer

Gutachter der Disputation: Prof. Dr. B. Naroska
Prof. Dr. G. Heinzelmann

Datum der Disputation: 12.02.2002

Dekan des
Fachbereichs Physik und
Vorsitzender des
Promotionsausschusses: Prof. Dr. Fr.-W. Büßer

Abstract

This thesis presents the measurement of high Q^2 neutral current deep inelastic scattering (DIS) cross sections using e^+p data taken with the ZEUS detector at a centre of mass energy of $\sqrt{s} \approx 318\,\text{GeV}$. The analysed data was recorded in the run period 1999/2000 and corresponds to an integrated luminosity of $63\,\text{pb}^{-1}$. This high statistics data set allows the most precise look at the proton structure at length scales $\mathcal{O}(1/1000)$ of the proton radius to date. The single ($d\sigma/dQ^2$, $d\sigma/dy\,(Q^2 > 400\,\text{GeV}^2)$, $d\sigma/dx(Q^2 > 400\ \text{GeV}^2)$, $d\sigma/dx\,(Q^2 > 2500\,\text{GeV}^2)$ and $d\sigma/dx\,(Q^2 > 10000\,\text{GeV}^2)$) and double differential ($d^2\sigma/dxdQ^2$) cross section measurements were compared with Standard Model predictions obtained with CTEQ5D parton density functions (PDFs). They are able to describe the data towards the highest values of Q^2. Furthermore precise systematic studies were performed which increased the general knowledge of the ZEUS detector and led to an improved understanding of the systematic uncertainties. By also analysing the e^-p data set taken in the run period 1998/1999 the different contribution of the γ–Z^0–interference to e^-p and e^+p cross section is presented and hence the structure function xF_3 was extracted. This exciting measurement which gives direct access to the valence quarks, is up to now statistically limited. More precise measurements will be possible after the HERA upgrade when more luminosity will be available. To fully profit from the higher statistics the ZEUS experiment was improved by additional devices. The new microvertex detector is introduced together with a performance study of the silicon strip detectors used in a separate chapter.

Zusammenfassung

Diese Arbeit behandelt die Messung der Wirkungsquerschnitte des neutralen Stromes in tief unelastischer Streuung (DIS) bei hohem Q^2 in e^+p Daten, gesammelt mit dem ZEUS Detektor bei einer Schwerpunktsenergie von $\sqrt{s} \approx 318\,\text{GeV}$. Die analysierten Daten stammen aus der Runperiode 1999/2000 und entsprechen einer integrierten Luminosität von $63\,\text{pb}^{-1}$. Dieser Datensatz mit hoher Statistik ermöglicht die bisher genaueste Untersuchung der Protonstruktur bei einer Auflösung von bis zu $\mathcal{O}(1/1000)$ des Protonradius. Die einzel- ($d\sigma/dQ^2, d\sigma/dy\,(Q^2 > 400\,\text{GeV}^2)$, $d\sigma/dx\,(Q^2 > 400\ \text{GeV}^2)$, $d\sigma/dx\,(Q^2 > 2500\,\text{GeV}^2)$ und $d\sigma/dx\,(Q^2 > 10000\,\text{GeV}^2)$) und doppeltdifferenziellen ($d^2\sigma/dxdQ^2$) Wirkungsquerschnitte wurden verglichen mit den Standard Modell Vorhersagen, berechnet mit den CTEQ5D Partondichtefunktionen (PDFs), die in der Lage sind, die Daten bis zu höchsten Werten von Q^2 zu beschreiben. Weiterhin vergrößern präzise systematische Studien das generelle Verständnis des ZEUS Detektors und führen so zu einem besseren Verständnis der systematischen Unsicherheiten. Durch die zusätzliche Analyse des e^-p Datensets der Runperiode 1998/1999 wird der unterschiedliche Beitrag der γ–Z^0–Interferenz zu e^-p und e^+p Wirkungsquerschnitten bestimmt und daraus die Strukturfunktion xF_3 extrahiert. Diese interessante, zu den Valenzquarks sensitive Messung ist bis jetzt noch statistisch limitiert. Ein präziseres Ergebnis wird möglich nach dem HERA Upgrade, der gleichzeitig Anlaß war für eine Erweiterung des ZEUS Experimentes. In einem separaten Kapitel werden der neue Mikrovertex Detektor und Untersuchungen zu den Eigenschaften der benutzten Silizium-Streifendetektoren vorgestellt.

Contents

List of Figures

List of Tables

What is inside? - An Introduction

The question about the structure of matter is very fundamental. It has fascinated many generations of scientists in the past and will still be topical in the future. Rutherford's idea of scattering 'point-like' projectiles like α particles off a target, which was a gold foil in his case, started a series of scattering experiments in the last century. This led to a fundamental understanding of the building blocks of matter and their interactions. This knowledge is embedded in the Standard Model.

Deep inelastic lepton proton scattering (DIS) has played a key role in the investigation of the structure of the proton. The HERA collider has offered the possibility to probe the proton structure at small resolution scales, a previously unexplored kinematic domain.

This thesis presents a new measurement of high Q^2 neutral current single and double differential cross sections with e^+p data recorded in the years 1999/2000 with the ZEUS detector. In comparison to previous analyses the available centre of mass energy is increased to $\sqrt{s} \approx 318\,\mathrm{GeV}$ and the statistical precision was improved by analysing data corresponding to an integrated luminosity of $63\,\mathrm{pb}^{-1}$, which exceeds the one of previous double differential ZEUS measurements by a factor two. In combination with an analysis of the e^-p data set taken in 1998/1999 the nature of the weak interaction can be studied by the opposite contribution of the γ–Z^0-interference to e^-p and e^+p cross sections. The structure function xF_3, which is a measure of the valence quark distribution, can be extracted taking both data sets into account.

This thesis is organised as follows: The first chapter gives an overview of the theoretical concepts on which this thesis is based. The structure functions are introduced and their relation to the quark content of the proton and to the electroweak couplings are illustrated. The next chapter gives a description of the apparatus used to perform the presented analysis: the HERA collider and the ZEUS detector. In conjunction to the previously described ZEUS detector chapter three describes the new micro-vertex detector which will be of large impact for any future measurement with the ZEUS detector. The silicon strip detectors used are studied in detail to allow an optimised use of the final device.

The Monte Carlo simulations (MC) used for the measurement of the cross sections are discribed in the fourth chapter. After the description of the trigger preselection in chapter five the measurement of the event variables, which is a main part of the analysis, is discussed in chapter six. The positron energy measurement and the reconstruction of the underlying (true) longitudinal vertex distribution are presented in detail. The final event selection which should remove as much background as possible and the applied reconstruction method are explained in the following chapters. Chapter nine presents the unfolding procedure and the results of the cross section measurements. Furthermore, the systematic uncertainties are discussed as well as the extraction of the structure function xF_3 is presented. As an application of the presented analysis the results (obtained by the ZEUS collaboration) of a search for contact interactions by combining all ZEUS data is shown in addition.

Chapter 1

Deep Inelastic Scattering - Theoretical Overview

In this chapter the necessary basics for the understanding of the theoretical background of the presented measurements are given. After the explanation of the deep inelastic scattering process $e^{\pm}p \to e^{\pm}X$ and the definition of the kinematic variables the cross section is described in terms of the structure functions. A short introduction to the quark parton model and the electroweak theory is given in the following sections to give a simplified interpretation of the structure functions and to discuss the couplings involved. Then a brief description of the strong interaction and the underlying parton density distributions is given. The chapter ends with a paragraph about possibilities of detecting new interactions (beyond the Standard Model) in processes at high momentum transfers which can be parameterised in four fermion contact interactions.

1.1 Kinematic Variables

The probing of the proton with a highly energetic lepton such as an electron or a positron can occur via the charged current (CC) or via the neutral current (NC) process. In the CC process the interaction is mediated by a virtual, charged W-boson, which causes a change in the flavour of the incoming electron or positron to a neutrino or antineutrino respectively. In the NC process, which can be mediated either by a virtual photon or a Z^0-boson, the lepton retains its identity. Both processes are depicted in Figure 1.1.

The definition of the kinematic variables is identical for both processes. Since the present analysis studies only NC interactions, the description of the kinematic variables will concentrate on this process in the following. Describing the incoming lepton and proton by their four-momenta k and P respectively and the scattered lepton by its momentum k' the event kinematics can be described by the following Lorentz-invariant variables:

$$Q^2 = -q^2 = -(k-k')^2\,, \tag{1.1}$$

$$x = \frac{Q^2}{2P\cdot q}\,, \tag{1.2}$$

$$y = \frac{P\cdot q}{P\cdot k}\,. \tag{1.3}$$

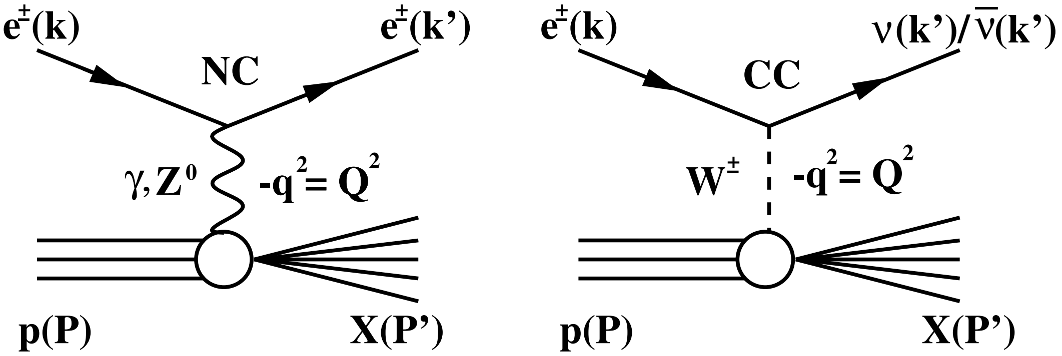

Figure 1.1: Schematic pictures of DIS events. The neutral current DIS process is shown on the left, whereas the charged current process can be seen on the right.

The variable Q^2, the negative squared difference of the incoming and scattered lepton four-momenta, denotes the virtuality of the exchanged boson, i.e $Q^2 = 0$ corresponds to a real photon. The wavelength of the virtual photon and therefore the resolvable distance scale is given by $\lambda \approx \hbar c/\sqrt{Q^2}$ resulting in a resolving power of $\sim 10^{-18}$ m (which corresponds to 1/1000 of the proton radius) at virtualities of $Q^2 \sim 10^4\,\mathrm{GeV}^2$. The Bjorken scaling variable x can be regarded in the Quark Parton Model (cf. section 1.3) as the proton momentum fraction carried by the struck quark. The variable y measures the fraction of the lepton energy transferred to the proton in the proton rest frame. All three variables are related to the squared centre of mass energy s:

$$s = (k + P)^2 = \frac{Q^2}{xy}\,, \tag{1.4}$$

neglecting the masses of the proton and the lepton. The fixed beam energies of 27.5 GeV and 920 GeV for leptons and protons respectively result in a fixed value of $\sqrt{s} = 318\,\mathrm{GeV}$ and therefore only two variables are independent. The value of x and y are restricted to the range between zero and one, limiting the value of Q^2 to s. At the electron proton collider HERA (cf. section 2.1) the accessible kinematic range was significantly increased compared to previous fixed target experiments (by two orders of magnitude towards large Q^2 and low x), as shown in Figure 1.2.

1.2 The DIS Cross Section

The inclusive $ep \to eX$ cross section can be factorised and therefore can be written as the product of a leptonic and a hadronic part:

$$d\sigma \sim L_{\mu\nu} \cdot W^{\mu\nu}\,. \tag{1.5}$$

The leptonic tensor $L_{\mu\nu}$ can be completely described by the electroweak theory, at values of $Q^2 \ll M_Z^2$ even completely by QED, since the exchange of a virtual Z^0-boson can be neglected in this kinematic region. The hadronic tensor $W^{\mu\nu}$ describes the structure of the proton, which cannot be calculated from first principles and has to be parameterised from measurements. It depends on the momentum of the probe, the momentum of the involved object of the proton (the participating quark) and the spin of both objects. The most general Lorentz-invariant ansatz (with restrictions of current conservation and time reversal invariance) results in eight structure

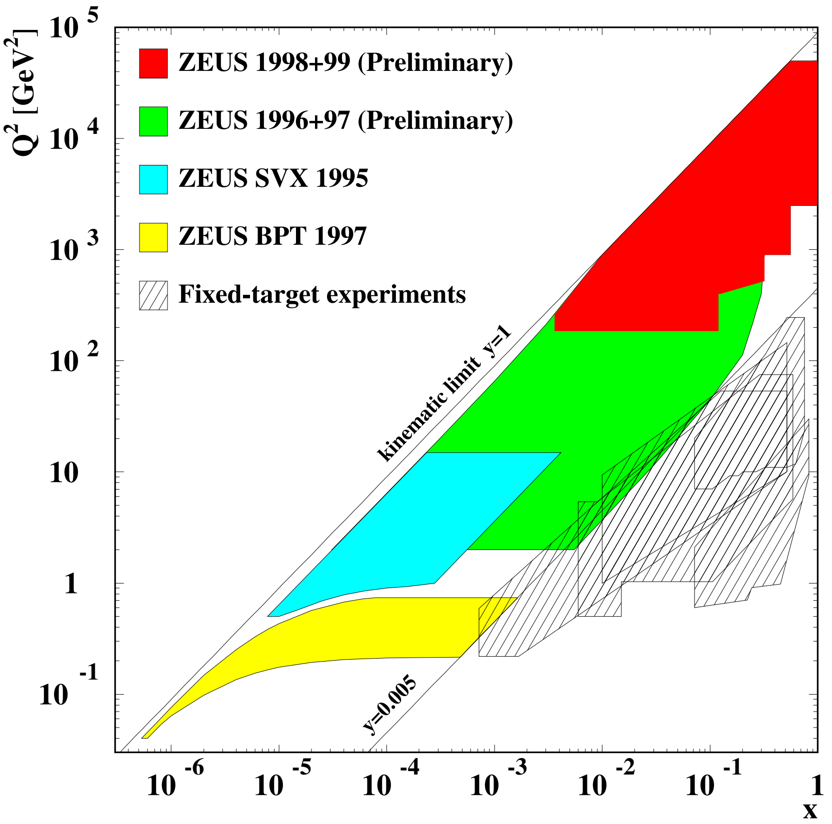

Figure 1.2: Kinematic (x, Q^2) region accessible at HERA compared to fixed target experiments. The studied kinematic region was enlarged by two orders of magnitude in both x and Q^2.

functions from which only three are spin independent and relevant in the case of unpolarised leptons. Using the previously described Lorentz-invariant variables the double differential $e^{\pm}p$ NC cross section at Born level (QED corrections to the cross section are discussed in section 4.1.1) can be expressed as a function of these three structure functions:

$$\frac{d^2\sigma_{NC}^{e^{\pm}p}}{dxdQ^2} = \frac{2\pi\alpha^2}{Q^4 x}\left[\frac{y^2}{2}2xF_1^{NC} - (1-y)F_2^{NC} \mp \left(y - \frac{y^2}{2}\right)xF_3^{NC}\right], \tag{1.6}$$

where α is the fine structure constant. The dependence on Q^{-4} (the squared photon propagator) reflects the dominating effect of photon exchange at low momentum transfers. All three structure functions depend on x, Q^2. The longitudinal structure function F_L^{NC} can be introduced as follows:

$$F_L^{NC} = F_2^{NC} - 2xF_1^{NC}, \tag{1.7}$$

which corresponds to the subtraction of the part originating from the absorption of purely transversely polarised probes (F_1^{NC}) from (F_2^{NC}) which includes both contributions of photon polarisation. Thus one obtains for the double differential cross section:

$$\frac{d^2\sigma_{NC}^{e^{\pm}p}}{dxdQ^2} = \frac{2\pi\alpha^2}{Q^4 x}[Y_{(+)}F_2^{NC} \mp Y_{(-)}xF_3^{NC} - y^2 F_L^{NC}], \tag{1.8}$$

where $Y_{(\pm)} = 1 \pm (1-y)^2$.

F_L^{NC} describes the absorption of a longitudinally polarised virtual photon. The ratio R between longitudinal and transverse cross section which is related to $F_L^{NC}/2xF_1^{NC}$ is proportional to Q^{-2}. Therefore, the F_L^{NC} contribution to the cross section is very small in case of large values of Q^2 and thus it is negligible in this analysis. In contrast to that, the effect of the parity violating part of the cross section included in xF_3^{NC} arising from the exchange of the Z^0 boson and its interference with the virtual photon exchange becomes measurable only for values of Q^2 similar or higher to M_Z^2. This part of the cross section is of particular interest in this analysis. An interpretation of the structure functions in terms of momentum distributions of partons inside the proton is given in the Quark-Parton-Model introduced in the next section.

The most characteristic feature of the double differential cross section is its strong dependence on Q^{-4}. This kinematic factor can be disadvantageous in the presentation of the results therefore the reduced cross section is introduced:

$$\tilde{\sigma}_{NC}^{e^\pm p} = \frac{Q^4 x}{2\pi\alpha^2}\frac{1}{Y_{(+)}}\frac{d^2\sigma_{NC}^{e^\pm p}}{dxdQ^2} = F_2^{NC} \mp \frac{Y_{(-)}}{Y_{(+)}}xF_3^{NC} - \frac{y^2}{Y_{(+)}}F_L^{NC} \,. \tag{1.9}$$

1.3 The Quark-Parton-Model

At the end of the sixties first high energy measurements of the inelastic *ep* cross section at SLAC[1] (USA) found the structure function F_2 to be independent of Q^2 for values of $x \sim 0.2$ [1]. This so called scaling behaviour had already been predicted by Bjorken [2]. Since the structure functions are related to the charge distribution inside the proton via a Fourier transformation a constant value of F_2 reflects the point-like structure of the probed object. An explanation of this observation is given in the Quark-Parton-Model (QPM) [3]. In the QPM the proton is a static object consisting of free (non-interacting), point-like partons (quarks). Thus lepton proton deep inelastic scattering can be regarded as the incoherent sum of elastic lepton quark scattering. In this model the Bjorken scaling variable x is the fraction of the proton momentum carried by the parton involved.

In addition to the observation of scaling, measurements were able to verify the Callan-Gross-relation [4]:

$$2xF_1(x) = F_2(x)\,, \tag{1.10}$$

which was predicted by assuming that the non-interacting partons have spin 1/2. The partons of the QPM can be identified with the predicted spin 1/2 constituents of hadrons called 'quarks' by Gell-Mann [5]. This equation excludes the absorption of a longitudinally polarised photon and therefore in this picture is $F_L = 0$.

Besides the three valence quarks (q_v) responsible for the quantum numbers, the proton consists of a sea of quark-antiquark pairs. With the quark (antiquark) density distribution $q(x)$ ($\bar{q}(x)$) the following flavour sum rules can be derived:

$$\int_0^1 dx\,(u(x) - \bar{u}(x)) = \int_0^1 dx\, u_v(x) = 2\,, \tag{1.11}$$

$$\int_0^1 dx\,(d(x) - \bar{d}(x)) = \int_0^1 dx\, d_v(x) = 1\,, \tag{1.12}$$

---

[1] Stanford Linear Accelerator

$$\int_0^1 dx\,(s(x) - \bar{s}(x)) = \int_0^1 dx\, s_v(x) = 0\,. \tag{1.13}$$

In the QPM the structure functions F_2 and xF_3 can be expressed in terms of the parton density functions $q = q(x, Q^2)$

$$F_2(x, Q^2) = \sum_i x(q + \bar{q})A_i \;\;;\;\; xF_3(x, Q^2) = \sum_i x(q - \bar{q})B_i\,, \tag{1.14}$$

where q is the probability to find a parton of type i in the fractional momentum range between x and $x + dx$ and in the resolution range between Q^2 and $Q^2 + dQ^{2\dagger}$. A_i and B_i include the coupling between the exchanged boson and the participating fermions. In case of smaller values of Q^2 where the Z^0 exchange can be neglected, A_i becomes e_i^2, the charge of the involved quark squared, whereas $B_i = 0$. For larger Q^2 values A_i and B_i are more complex functions, they are discussed in the next section in detail. In measurements of the lepton-nucleon cross section it was observed that only $\sim$ 50% of the proton momentum is carried by the charged partons which showed that the QPM can not give a complete description of the data [6]. Neutral particles, not coupling to the photon, had to be introduced to carry the other half of the proton momentum. These particles were identified as the gluons which mediate the strong force between the quarks. An overview of the corresponding theoretical framework called quantum-chromodynamics (QCD) is given after a more detailed discussion of the structure functions.

1.4 Electroweak Theory and the Structure Functions

The electromagnetic and the weak forces are unified in the Standard Model (SM) in the electroweak theory [7]. An unbroken electroweak theory involving the massless photon would require all fields to have zero mass whereas $W^\pm$ and Z^0 boson are massive. These masses can be included in the theory by spontaneous symmetry breaking with the consequence of introducing another massive particle into the theory. This uncharged and spin zero particle is the Higgs boson [8], which has not yet been observed in an experiment. Of great importance for this theory was the renormalisability which was proven in the early seventies [9].

In the electroweak theory there are two kinds of weak charges: the weak isospin and the weak hypercharge. Quarks and leptons are organised in left-handed doublets with weak isospin $t = 1/2$ and in right-handed singlets with weak isospin $t = 0$. In Table 1.1 the values of the weak charges are given for quarks and leptons. The charged $W^\pm$ bosons couple only to left-handed particles[2] which have a weak isospin different from zero, changing the third component t_3 from $-1/2$ to $+1/2$ or the other way around. The neutral mass eigenstates, the Z^0 boson and the photon (or their fields), are a mixture of the (in nature not observed) W^0 (neutral carrier of weak isospin) and the B^0 (neutral carrier of weak hypercharge). The mixing is illustrated in Figure 1.3, the Weinberg angle θ_W is a parameter of the theory which is related to the masses of the massive bosons:

$$\cos\theta_W = \frac{M_W}{M_Z}\,. \tag{1.15}$$

[†] Although previously scaling behaviour and therefore no Q^2-dependence was discussed, later measurements led to a modification of the simple QPM picture and a Q^2-dependence of the structure functions (cf. 1.5).

[2] This is the origin of the parity violation of the weak interaction.

	Particles			t	t_3	y_h	e_f/e
Leptons	$\binom{\nu_e}{e}_L$	$\binom{\nu_\mu}{\mu}_L$	$\binom{\nu_\tau}{\tau}_L$	1/2 1/2	+1/2 -1/2	-1 -1	0 -1
	e_R	μ_R	τ_R	0	0	-2	-1
Quarks	$\binom{u}{d}_L$	$\binom{c}{s}_L$	$\binom{t}{b}_L$	1/2 1/2	+1/2 -1/2	1/3 1/3	2/3 -1/3
	u_R	c_R	t_R	0	0	4/3	2/3
	d_R	s_R	b_R	0	0	-2/3	-1/3

Table 1.1: Weak isospin and weak hypercharge of leptons and quarks. Given are the values of the isospin t, of its third component t_3, of the weak hypercharge y_h and of the charge of the particle e_f with respect to the positron charge e. L and R denote the left- or right-handed particles respectively [10].

The electric charge e_f can be related to the weak charges in the following way:

$$e_f = e\left(t_3 + \frac{y_h}{2}\right) , \tag{1.16}$$

with the charge of the positron e. Moreover, the weak coupling constants are related to e:

$$g_W = \frac{e}{\sin\theta_W} , \quad g_Z = \frac{e}{\sin\theta_W \cos\theta_W} . \tag{1.17}$$

In addition the different couplings of the Z^0 boson to left- and right-handed fermions has to be taken into account. Usually they are defined in the form of an axial, a_f, and a vector, v_f coupling:

$$a_f = t_3^f \quad \text{and} \quad v_f = t_3^f - 2e_f \sin^2\theta_W , \tag{1.18}$$

where t_3^f is the third component of the isospin of the fermion (lepton l and quark q) with flavour f and e_f is its charge. Now the coupling terms in the structure function equation 1.14 can be derived completely [11]:

$$A_q = e_q^2 - 2e_q v_q v_l \chi_Z + (v_q^2 + a_q^2)(v_l^2 + a_l^2)\chi_Z^2 \;\text{ and }\; B_q = -2e_q a_q a_l \chi_Z + 4v_q a_q v_l a_l \chi_Z^2 , \tag{1.19}$$

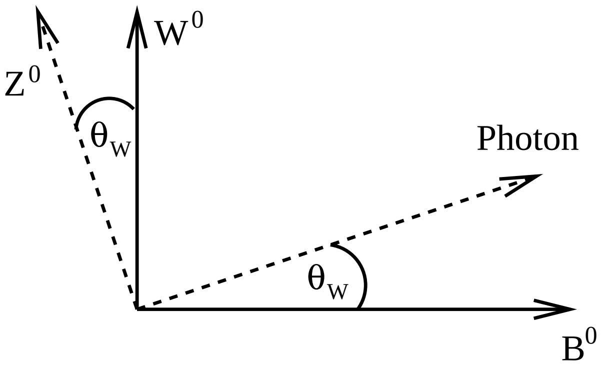

Figure 1.3: The neutral carriers of weak isospin W^0 and of weak hypercharge B^0 mix to the photon and Z^0 which are the particles observable in nature.

with

$$\chi_Z = \frac{1}{4\sin^2\theta_W\cos^2\theta_W}\cdot\left(\frac{Q^2}{M_Z^2+Q^2}\right) = \kappa_W\cdot\left(\frac{Q^2}{M_Z^2+Q^2}\right)\,, \tag{1.20}$$

which is proportional to the ratio between the Z^0 and the photon propagator. The terms proportional to χ_Z originate from the interference between photon and Z^0 boson whereas the pure Z^0 exchange is responsible for the χ_Z^2 terms. The structure functions can now be written separating the individual processes:

$$F_2 = F_2^\gamma - v_l\left[\frac{\kappa_W Q^2}{Q^2+M_Z^2}\right]F_2^{\gamma Z} + (v_l^2+a_l^2)\left[\frac{\kappa_W Q^2}{Q^2+M_Z^2}\right]^2 F_2^Z\,, \tag{1.21}$$

$$xF_3 = -a_l\left[\frac{\kappa_W Q^2}{Q^2+M_Z^2}\right]xF_3^{\gamma Z} + 2a_l v_l\left[\frac{\kappa_W Q^2}{Q^2+M_Z^2}\right]^2 xF_3^Z\,, \tag{1.22}$$

where the structure functions $F_2^{\gamma,\gamma Z,Z}$ ($xF_3^{\gamma Z,Z}$) include the parton density distributions and the corresponding process dependent coupling of the involved quark $e_q^2, 2e_q v_q, v_q^2 + a_q^2$ ($2e_q a_q, 2v_q a_q$). Since the vector coupling of the electron or positron $v_f = t_3^f - 2e_f\sin^2\theta_W$ is very small ($\approx$ -0.04 and 0.04 respectively) the contributions to the cross section of $F_2^{\gamma Z}$ and xF_3^Z are negligible. The DIS NC cross section can then be written in the following way[3]:

$$\frac{d^2\sigma_{NC}^{e^\pm p}}{dxdQ^2} \simeq \frac{2\pi\alpha^2}{x}\left(\frac{1}{Q^4}Y_{(+)}F_2^\gamma + \frac{1}{4}\kappa_W^2\left[\frac{1}{Q^2+M_Z^2}\right]^2 Y_{(+)}F_2^Z \mp \frac{\kappa_W}{2}\left[\frac{1}{Q^2(Q^2+M_Z^2)}\right]Y_{(-)}xF_3^{\gamma Z}\right)\,. \tag{1.23}$$

The different contributions to the cross section from photon exchange, Z^0 exchange and γZ^0 interference are now separated and can easily be identified by the propagator terms. The destructive interference in case of e^+p in comparison to e^-p scattering causes the NC DIS cross sections to differ at large values of Q^2 and therefore offers the possibility to measure the structure function xF_3 in this kinematic region by a comparison of e^+p and e^-p data (cf. chapter 9.15). HERA (cf. 2.1) is the first accelerator which offers the possibility to measure the structure function xF_3 in e^+p and e^-p scattering. Previous measurements were done in neutrino nucleon and muon nucleon scattering experiments (CCFR and BCDMS experiment) at much lower values of Q^2 [12, 13].

1.5 Quantum Chromodynamics

Quantum Chromodynamics (QCD) is a non-abelian gauge theory based on the SU(3) symmetry group which describes the strong force mediated by bosons called 'gluons'. Quarks and gluons carry an additional quantum number which is exchanged in their interaction. This quantum number is called 'colour' and it can have three different values, usually called red, blue and green. As a consequence of the non-abelian nature of the interaction gluons also carry colour and therefore interact with each other. In contrast to the quarks which carry only one colour the gluons carry colour and anti-colour (in eight possible combinations). In the same way as vacuum polarisation loops in QED lead to a redefinition of the charge (renormalisation) and

---

[3] The different sign in front of the last term in the cross section originates from the different sign of a_l for electrons and positrons. The value was already inserted into the equation not to hide the change of sign.

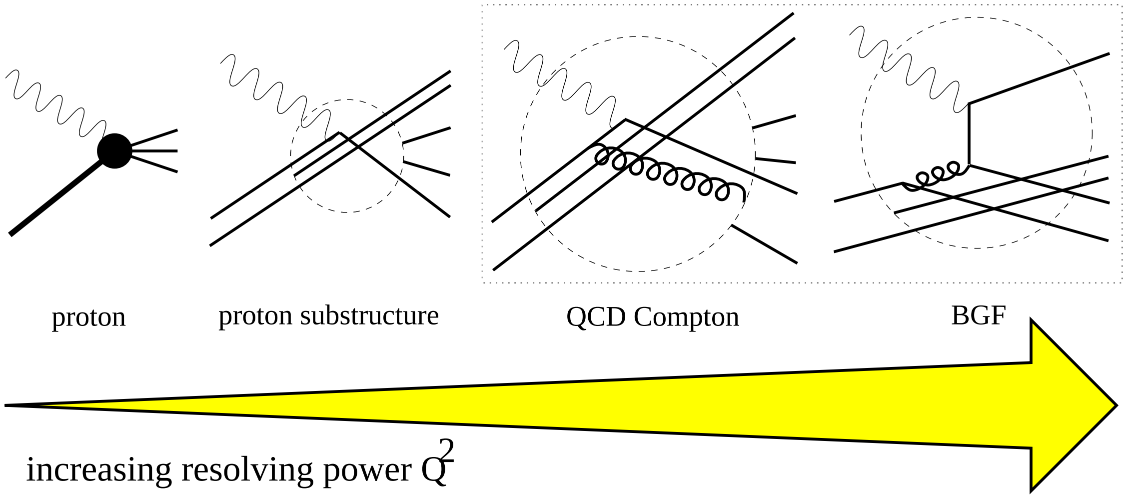

Figure 1.4: Schematic diagram of the scaling violations: With increasing Q^2 more structure in the proton due to the radiation of gluons and quark-antiquark splitting can be resolved. This happens via processes as QCD Compton or Boson-Gluon-Fusion (BGF) (figure from [16]).

therefore to a scale (Q^2) dependent behaviour of the coupling α, the coupling in QCD α_s also depends on a scale. In contrast to QED the coupling α_s decreases with smaller distances (larger values of Q^2) and it increases to larger distances (smaller values of Q^2). The behaviour at small distances is called 'asymptotic freedom' and is responsible for the observation of quasi free quarks in the proton for high Q^2 DIS events. The large distance behaviour is expected to be responsible for the fact that quarks can not be observed as single, free particles and is known as 'confinement'. In leading order perturbation theory the scale dependence of α_s is given by (e.g. [14]):

$$\alpha_s(Q^2) = \frac{12\pi}{(33 - 2n_f) \cdot \ln(Q^2/\Lambda^2)} , \quad (Q^2 > \Lambda^2) \ , \tag{1.24}$$

where n_f is the number of quark flavours. In the parameter Λ the scale μ introduced in the renormalisation is included. Λ can be thought of as the threshold between the region of quasi-free quarks and bound hadrons and therefore defines the point where the theory breaks down. In the case where $Q^2 \gg \Lambda^2$ the coupling is small and perturbative methods can be used for calculations. For $Q^2 \approx \Lambda^2$ the coupling becomes large and the quarks form hadrons. Λ has to be measured and can not be determined from first principles. Its size is comparable with a typical hadron mass (0.1-0.5 GeV [15]).

QCD modifies the simple Quark Parton Model. The static model has to be replaced by a dynamic one in which, due to gluon radiation and quark-antiquark splitting, more and more partons with low momentum (at low x) can be resolved with increasing Q^2 as sketched in Figure 1.4 and less partons are found with high momentum (at large x). Therefore the formerly observed scaling behaviour of the structure function F_2 was found to be valid only for a particular region of x (~ 0.2) whereas scaling violations are observed in case of higher and lower x values. The probability of finding a quark with very high momentum fraction gets smaller with increased resolution and therefore also F_2 becomes smaller. In contrast the probability of finding a quark with low momentum fraction increases with Q^2 and therefore the structure function F_2 rises with Q^2 for low values of x. At HERA measurements from ZEUS [17] and H1 [18] have impressively shown the scaling violating behaviour as can be seen in Figure 1.5.

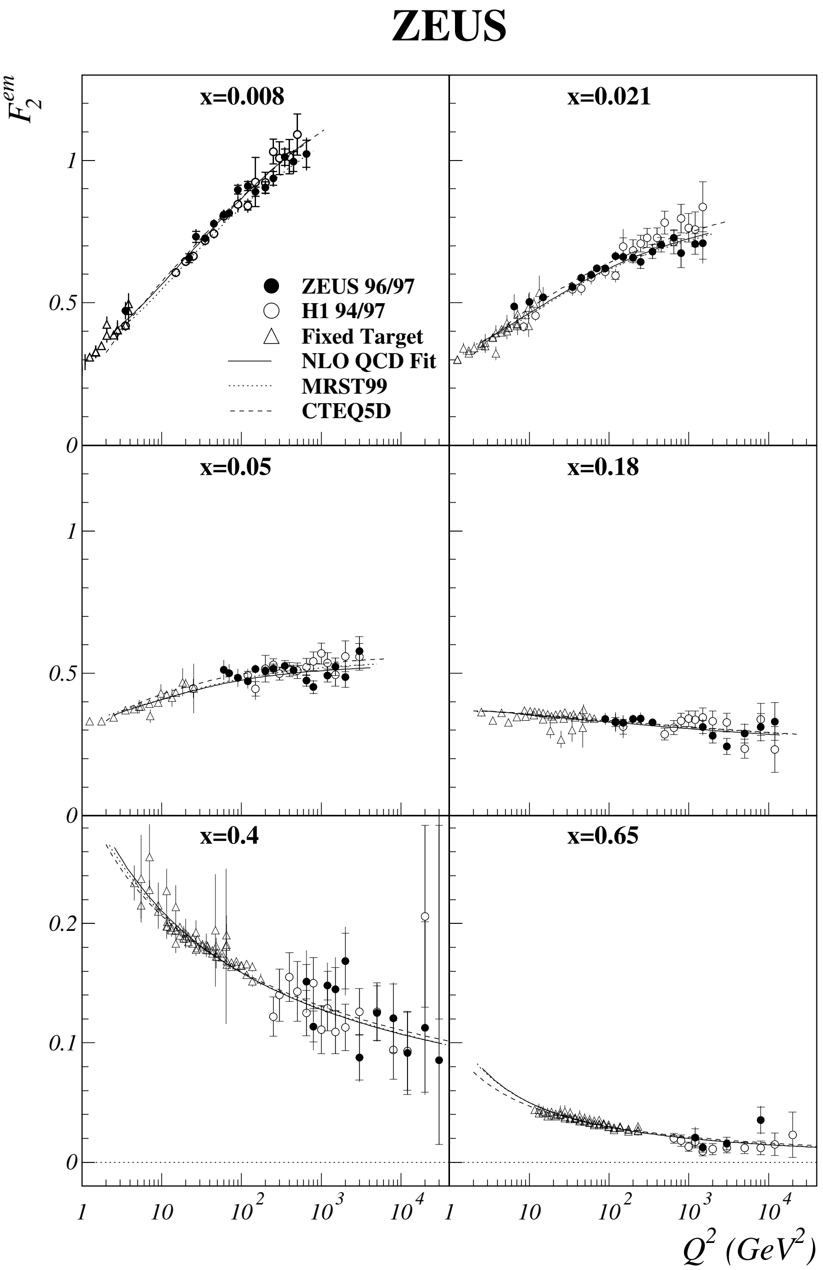

Figure 1.5: Measurements of the ZEUS and H1 Collaborations of the structure function F_2. Scaling violations are clearly visible especially in case of low values of x.

Due to gluon radiation quarks can also have transverse momenta enabling the coupling to longitudinally photons. Therefore the Callan-Gross relation does not longer hold and the structure function F_L can be different from zero.

1.6 Parton Distributions and Evolution Equations

The parton distributions inside the proton or inside hadrons in general depend on long distance and therefore on non-perturbative effects (not calculable by perturbation theory). Thus the structure functions and consequently the cross section can not be calculated from first principles.

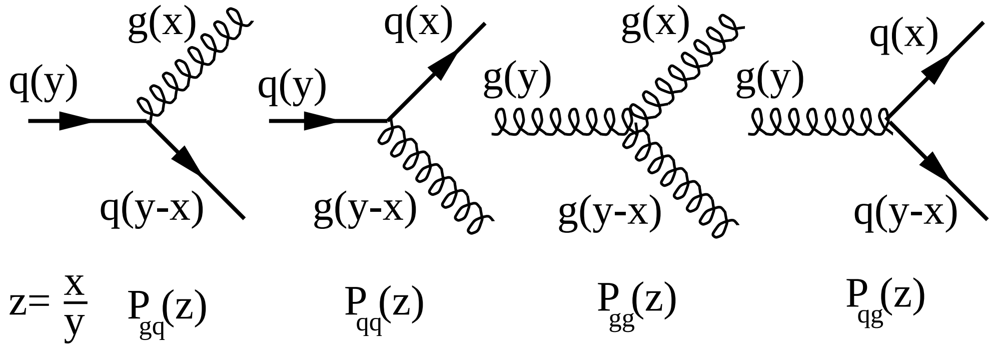

Figure 1.6: The four possible particle splittings corresponding to the functions P_{gq}, P_{qq}, P_{gg} and P_{qg}.

The factorisation theorem separates both contributions by introducing another scale μ_F defining the boundary line between the perturbative region, including the short range hard scattering process (σ_{ei}), and the non-perturbative region:

$$\sigma_{ep}(x,Q^2) = \sum_i \sigma_{ei}(x,Q^2,\mu_F) \otimes f_i(x,\mu_F)\,, \tag{1.25}$$

where i denotes the contributing parton. The latter ($f_i(x,\mu_F)$ is parameterised in the parton density functions (PDFs) which have to be determined experimentally. However, physical observables (as the cross section σ_{ep}) do not dependent on any introduced scale. By using the perturbatively calculated short range interactions, the PDFs can be determined approximately at any point, if they are known at a given starting value. This can be done with the so-called 'evolution equations' starting from different assumptions and therefore valid in different kinematic regions.

The DGLAP[4] [19] evolution equations describe how the quark, antiquark and gluon momentum distributions ($q(x,Q^2)$,$\bar{q}(x,Q^2)$ and $g(x,Q^2)$) evolve with Q^2, if the distributions were parameterized in x at a given scale Q_0^2. This results in ($2n_f$+1) coupled integro-differential equations:

$$\frac{\partial q_i(x,Q^2)}{\partial \ln Q^2} = \frac{\alpha_s(Q^2)}{2\pi}\int_x^1 \frac{\mathrm{d}y}{y}\left[q_i(y,Q^2)P_{qq}(z) + g(y,Q^2)P_{qg}(z)\right]\,, \tag{1.26}$$

$$\frac{\partial \bar{q}_i(x,Q^2)}{\partial \ln Q^2} = \frac{\alpha_s(Q^2)}{2\pi}\int_x^1 \frac{\mathrm{d}y}{y}\left[\bar{q}_i(y,Q^2)P_{qq}(z) + g(y,Q^2)P_{qg}(z)\right]\,, \tag{1.27}$$

$$\frac{\partial g(x,Q^2)}{\partial \ln Q^2} = \frac{\alpha_s(Q^2)}{2\pi}\int_x^1 \frac{\mathrm{d}y}{y}\left[\sum_{i=1}^{n_f}(q_i(y,Q^2)+\bar{q}_i(y,Q^2))P_{gq}(z) + g(y,Q^2)P_{gg}(z)\right], \tag{1.28}$$

where i denotes the flavour of the quark. The splitting functions $P_{ij}(z)$ determine the probability to create a particle i with momentum fraction z relative to the momentum y of the original particle j. The four possible splitting processes are depicted in Figure 1.6, the $P_{ij}(z)$ are calculable in perturbative QCD. The struck quark originates from a cascade of quark and gluon emission in which the momentum x of the daughter particle is always lower than the momentum y of its mother particle. In addition the DGLAP formalism is based on the assumption, that the transverse momentum k_T increases in each emission resulting in the struck quark having

---

[4] Dokshitzer, Gribov, Lipatov, Altarelli and Parisi.

the largest k_T in the cascade. Mathematically this is done by summing up all terms of the form $(\alpha_s \ln Q^2)^n$ to all orders in the so-called Leading Logarithm Approximation (LLA), all other terms are neglected. These assumptions limit the validity of the DGLAP equations to higher values of both Q^2 and especially x. At lower values of x terms $(\alpha_s \ln \frac{1}{x})^n$ are not negligible and have to be taken into account. In the Double Leading Logarithm Approximation (DLLA) these terms are summed up if they are accompanied by $\ln Q^2$ terms $((\alpha_s \ln \frac{1}{x} \ln Q^2)^n)$ leading to a steep rise of the gluon density at small values of x [20].

To describe the parton evolution towards even smaller values of x the BFKL[5] equation [21] can be used. In this formalism $(\alpha_s \ln \frac{1}{x})^n$ terms are summed to all orders by neglecting other terms. The assumption of the ordering in k_T is not necessary but it is replaced by a stronger ordering in x, i.e. the momentum of the daughter particles in the cascade is assumed to be much smaller than the one of the mother particle. The BFKL equation predicts an even stronger rise of the gluon distribution towards smaller values of x. The omission of $\ln Q^2$ term restricts its application to moderate values of Q^2.

Both DLLA and BFKL equations lead to a violation of unitarity in the case of $x \to 0$, therefore the rise of the cross section has to stop at some point. This process in which gluon recombination or annihilation compete with the usual evolution is called saturation. It results in a screening of the gluons by themselves, they do not behave as free particles any more. Various models are discussed at present (i.e. [22]). Up to now no clear evidence of this effect was found in HERA measurements or at other accelerators.

1.7 A Look Beyond the Standard Model: Contact Interactions

The precise measurement of the deep inelastic scattering cross section in the region of high Q^2 provides a strong test of the Standard Model. New physics like the formation of new particles or the existence of a new force at short distance is expected to be most prominent in reactions with high momentum transfers and at high energies. Due to interferences with the photon and the Z^0 boson new phenomena could be indirectly detected even if the centre of mass energy available at HERA $\sqrt{s} = 318\,\mathrm{GeV}$ is too small for a direct observation. Four fermion contact interactions are a very general model to describe the experimental sensitivity to such kind of new physics. A point-like *eeqq* interaction would modify the Standard Model Lagrangian by additional scalar, vector and tensor terms including the different couplings of left and right handed particles. Only the vector contact interactions are of particular interest at HERA, since strong limits have already been placed to the other two contributions [23]. The additional vector term to the Standard Model Lagrangian can be written as:

$$\mathcal{L}_{CI} = \sum_{i,j=L,R} \eta_{ij}^{eq} (\bar{e}_i \gamma^\mu e_i)(\bar{q}_j \gamma^\mu q_j)\,, \tag{1.29}$$

where η_{ij} represents the coupling strength and i and j denote the electron and quark helicity.

---

[5] Balitskii, Fadin, Kuraev and Lipatov.

1.7.1 Compositeness Models

In general compositeness models, the size of a possible substructure of the involved fermions is related to a compositeness scale. This effective mass scale of the contact interaction Λ_{ij} enters into the couplings η_{ij} via:

$$\eta_{ij} = \epsilon \frac{g_{CI}^2}{\Lambda_{ij}^2}, \tag{1.30}$$

where g_{CI} is the coupling strength which is conventionally chosen to $g_{CI} = 4\pi$. Under the assumption of possitive or negative couplings ($\epsilon \pm 1$), parity conservation and equal couplings for up-type and down-type quarks, limits can be derived for the compositeness scale for various models.

1.7.2 Heavy Leptoquarks

Interactions looking like a four fermion contact interaction, could originate by particle exchange in which the particle mass is in the TeV range. A possible source of these type of contact interactions can be the exchange of a heavy leptoquark ($M_{LQ} \gg \sqrt{s}$). Leptoquarks are composed of an electron and a quark or at least carry their quantum numbers. The colour triplet bosons with spin 0 or 1 therefore carry both lepton and baryon number. In the contact interaction model the mass M_{LQ} and the coupling of the leptoquark λ enter in the effective coupling:

$$\eta_{ij} \sim \left(\frac{\lambda_{LQ}}{M_{LQ}}\right)^2 . \tag{1.31}$$

1.7.3 Large Extra Dimensions

Another interesting physics possibly manifesting as contact interactions arises from the existence of large extra dimensions. An attempt to solve the hierarchy problem was proposed by N. Arkani-Hamed, S. Dimopoulos and G. Dvali [24], in which the gravitational and gauge interactions become united at the electroweak scale $M_{EW} \sim 10^3$ GeV. Thus the electroweak scale is assumed to be the only fundamental scale in nature. The usual $(1/M_P)$ strength (with the Planck Mass $M_P \sim 10^{19}$ GeV) of the gravitational force is explained by the existence of n extra compact spatial dimensions. This assumption of the space-time to be $4+n$ dimensional where the Standard Model particles and forces are confined in four dimensions and only the graviton can propagate as spin 2 particle in the extra dimensions results in deviations of the gravitational potential at distances $r \ll R$, with the size of these extra dimensions R. The characteristic scale M_S, which is related to the Planck Mass via:

$$M_P^2 \sim R^n M_S^{2+n}, \tag{1.32}$$

can be of the order of TeV and therefore of the order of M_{EW} if R is large compared to $\sim M_{EW}^{-1}$. This is compatible with available experimental information since gravity has been tested only to distances above $\sim 100\,\mu$m, which could not exclude (in the accessible kinematic range of today's particle colliders) a number of large extra dimensions $n > 2$ up to now. In this way the gravitational interaction can become comparable to the electroweak interaction at very high energies, since the coupling depends on M_S and the number of extra dimensions n [25]: $\sim (2/(n-2))/M_S^4$.

1.7.4 Quark Radius R_q

Furthermore it can be searched for a possible quark substructure by a measurement of the spatial charge distribution of quarks. By the use of a 'classical' form factor of the type:

$$f(Q^2) = 1 - \frac{1}{6}\langle r^2 \rangle Q^2 \,, \tag{1.33}$$

where the radius R of the particle is identified with the root of the mean-square of the electroweak charge distribution, $R = \sqrt{\langle r^2 \rangle}$, the deviation from the Standard Model is given by the equation:

$$\frac{d\sigma}{dQ^2} = \frac{d\sigma^{SM}}{dQ^2} \cdot \left(1 - \frac{R_q}{6} Q^2\right)^2 \,. \tag{1.34}$$

Here the lepton, photon and Z^0-boson are assumed to be point-like.

The results obtained by the analysis described in the following chapters were combined with previous ZEUS data to constrain lower limits on the compositeness scale Λ_{ij}, on M_{LQ}/λ and M_S and upper limits on the quark radius and are presented in chapter 9.

Chapter 2

The ZEUS Experiment at HERA

2.1 The HERA Collider

HERA (Hadron-Electron-Ring-Anlage) is the world wide first lepton-proton storage ring. Located at DESY in Hamburg, Germany, it was built between 1984 and 1990 15 m - 25 m underground mostly under a large park area as can be seen in Figure 2.1. The accelerator is 6.3 km long and consists of four circular and four straight sections (Figure 2.2). In two separate rings the leptons and protons are accelerated by electrical fields and focussed using conventional

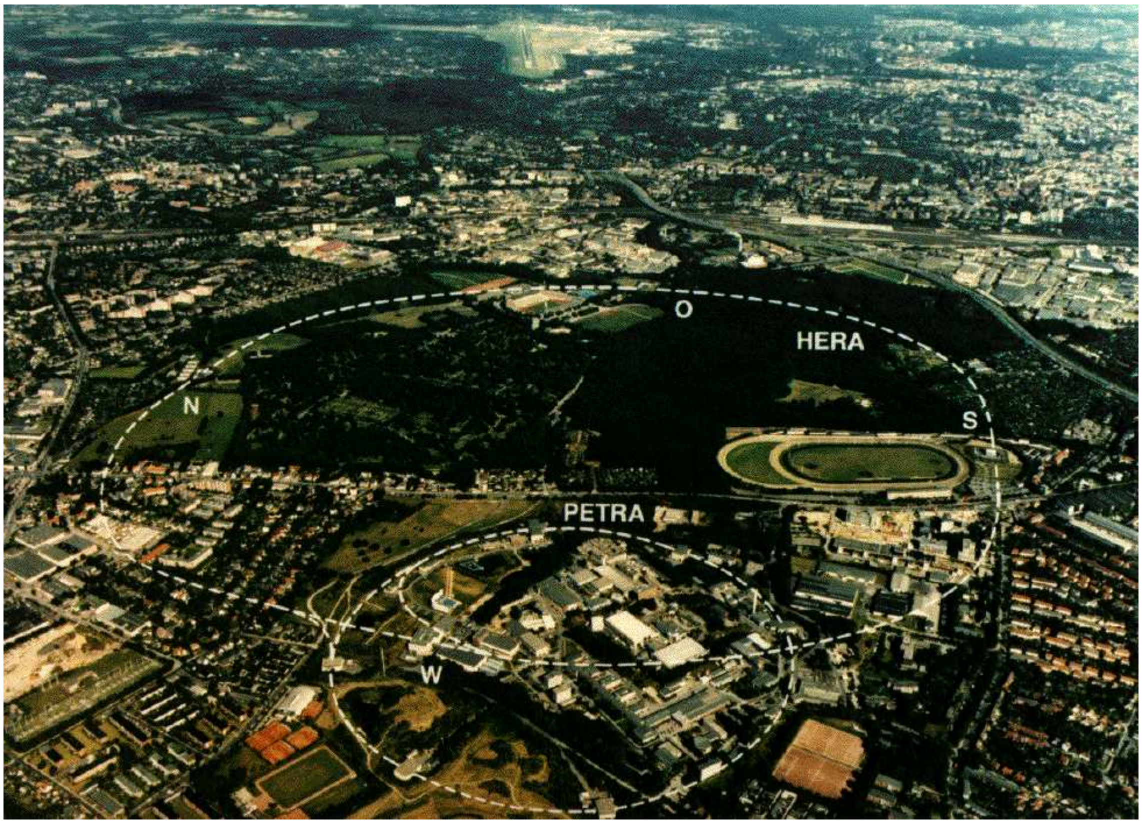

Figure 2.1: View of the DESY area in Hamburg, Germany. The HERA collider is marked with the dashed line. In addition the pre-accelerator PETRA (enclosing the main DESY site) is shown in the foreground.

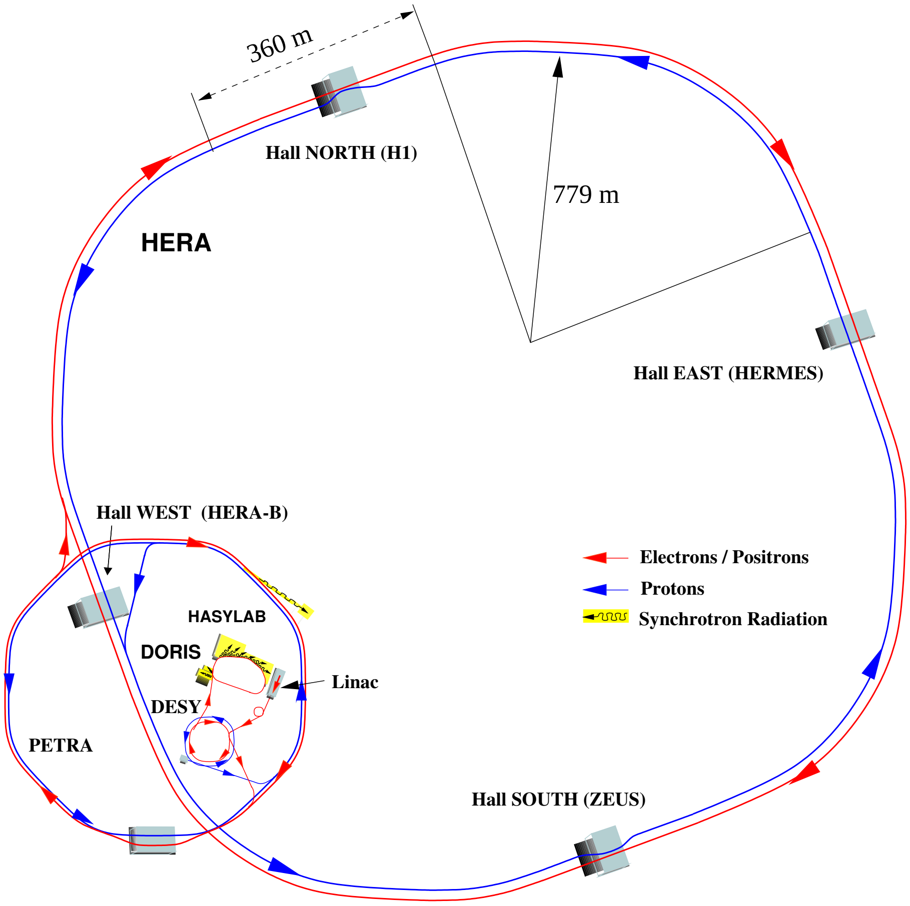

Figure 2.2: Schematic view of the HERA accelerator.

and super-conducting magnets, respectively. The two beams are brought into collision at zero crossing angle in the north and south experimental area, where the two collider experiments H1 and ZEUS are located. The east hall is used by HERMES which makes only use of the lepton beam (which is longitudinally polarised in that area) to study the nucleon spin structure with an internal polarised gas target. In the west hall HERA-B is located. This experiment has been designed to measure $\mathcal{CP}$-violation in the $B^0\overline{B^0}$-system. The B-mesons are produced by collisions of the proton beam halo with a wire target.

HERA was designed to accelerate electrons or positrons to 30 GeV and protons to 820 GeV. The protons are obtained from negative hydrogen ions (H^-) which are accelerated to 50 MeV in a linear accelerator LINAC and then they are injected in the proton storage ring DESY III whereas the electrons are stripped off by traversing a thin foil. When they have reached 7.5 GeV, the protons are filled in the PETRA storage ring where they are further accelerated to 40 GeV and injected in HERA. In a similar way the electrons respectively positrons are accelerated. After they exit a LINAC with an energy of 450 MeV they are accelerated to 7 GeV in DESY II followed by an acceleration to 14 GeV in PETRA from which they are injected in HERA. Colliding protons and leptons are grouped in bunches with $\mathcal{O}(10^{10})$ particles, 210 of these bunches of each particle kind can be filled in HERA. They are spaced by 96 ns. However, in normal running not all of these bunches are filled resulting in unpaired bunches which are used for background studies.

---

[1] non-colliding bunches

HERA parameters	Values of 1999/2000	
	e^+	p
Energy (GeV)	27.6	920
Centre-of-mass energy (GeV)	318	
Number of bunches	174+15[1]	174+6[1]
Time between bunch crossings (ns)	96	
Longitudinal beam size (mm)	8	$\sim$ 200

Table 2.1: HERA parameters during 1999/2000 running.

After the first years of operation the used lepton was changed from electrons to positrons in 1995 since severe lifetime problems were observed for the electron beam[2]. After the installation of new vacuum pumps in winter 1997/1998 the situation improved and electrons were used until in 1999 it was switched back to positrons[3]. Since 1998 the machine is running with a proton beam energy of 920 GeV while the used lepton beam energy is 27.5 GeV. The integrated luminosity delivered by HERA as a function of days of operation is shown in Figure 2.3. The significant progress achieved by the machine group can be seen by the increase of the integrated luminosity in comparison to previous years. Unfortunately not all luminosity can be used for physics analyses since the data-taking of the experiment is not fully efficient ($< 100\%$).

2.2 The ZEUS Detector

The ZEUS detector [26] is a multipurpose detector designed to study various aspects of lepton proton scattering and the structure of the proton. An asymmetric design was implemented taking into account the large difference between lepton and proton beam energy which results in a centre-of-mass system moving in the proton beam direction with respect to the lab-frame system. The ZEUS coordinate system is defined as a right-handed coordinate system with its origin at the nominal interaction point, the X-axis pointing towards the centre of HERA, the Y-axis pointing upwards whereas the Z-axis points in the direction of the outgoing proton, also referred to as forward direction. In 1992 the installation of the detector in the HERA south hall was finished, however, new detector components were added continuously. The main ZEUS detector has a size of $12\,\mathrm{m} \times 10\,\mathrm{m} \times 19\,\mathrm{m}$ and a weight of 3600 tons. An overview of the detector is shown in a view along the beam direction in Figure 2.4 and perpendicular to it in Figure 2.5.

In the following the main components of the detector will be shortly described. A more detailed description of the operational principles is given in the next sections for the components of great importance for the analysis presented in this thesis. The most inner part of the ZEUS detector is the cylindrical drift chamber surrounding the interaction point. This central tracking detector (CTD) is enclosed by a super-conducting magnet providing a field of 1.43 T. The tracking system is completed in the forward direction by three sets of planar drift chambers (FTD) with transition radiation detectors (TRD) in between (together labeled as FDET in Figure 2.4) whereas in the rear direction one planar drift chamber with three layers (RTD) is installed. A

---

[2] The shorter lifetime of the electron beam was presumably caused by the capture of positive charged dust originating from ion getter pumps from the HERA electron vacuum system.

[3] In this thesis expressions as 'electron finder', 'electron method' etc. are used. Here 'electron' is used as a generic expression for the colliding lepton since there are no differences in the methods applied between electron and positron beams.

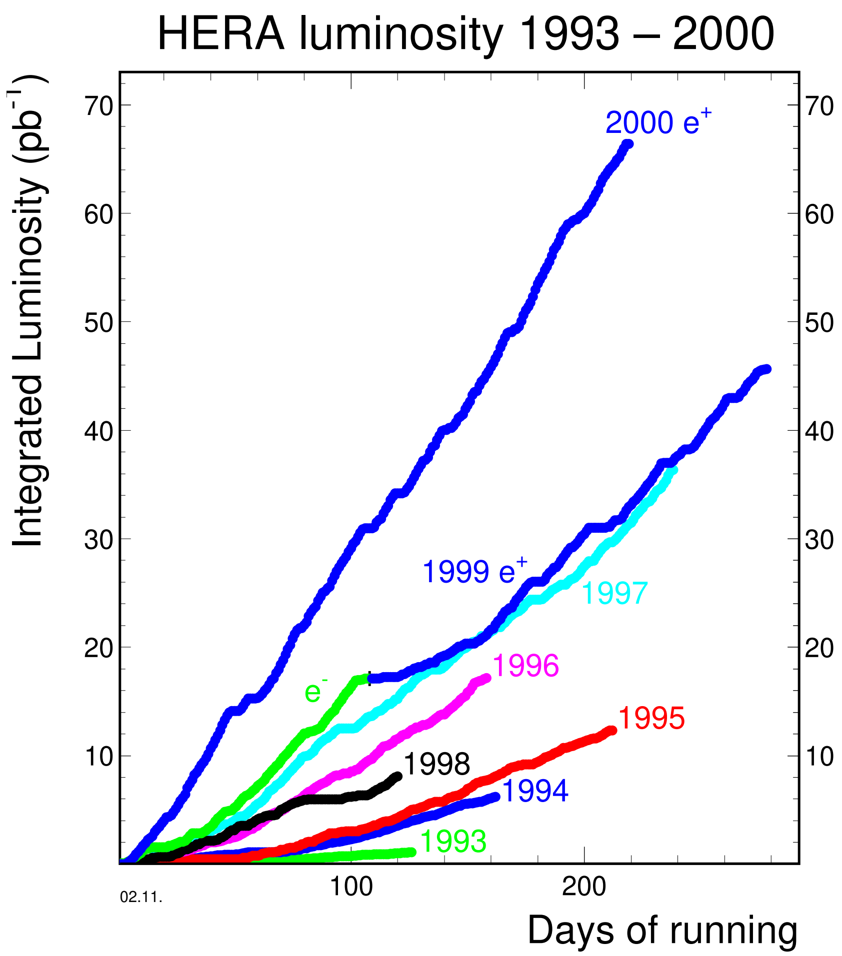

Figure 2.3: Integrated Luminosity delivered by HERA. Positrons were used as colliding lepton in the years 1995-1997 and from summer 1999 until the end of the running period in september 2000.

vertex detector (VXD) located between beampipe and CTD was removed during the shutdown 1995/1996. In 2001 a new Microvertex detector (MVD) was installed at the same place in the ZEUS experiment. This is subject of the next chapter.

The tracking system is surrounded by a high resolution uranium-scintillator calorimeter (UCAL) which is the main device for the energy measurement. It is subdivided into the forward (FCAL), barrel (BCAL) and rear calorimeter (RCAL). Presampler detectors are mounted in front of the calorimeter modules. The UCAL is enclosed by an iron yoke which provides the return path for the solenoid magnetic field flux. In addition it is instrumented with proportional chambers allowing to measure energy leakage of the UCAL and is therefore called backing calorimeter (BAC). Inside and outside of the BAC muon identification chambers (FMUI, BMUI, RMUI and FMUO, BMUO, RMUO) are installed. In the rear direction at Z=-7.3 m the veto wall is located. This is a detector composed of iron and scintillator with the purpose of beam related background rejection. Outside the main detector additional detectors are installed. The six components of the leading proton spectrometer (LPS) are located at distances of 24 m to 90 m away from the interaction point in the forward direction to measure scattered protons with low transverse momentum (< 1 GeV). The detector with the largest distance to the

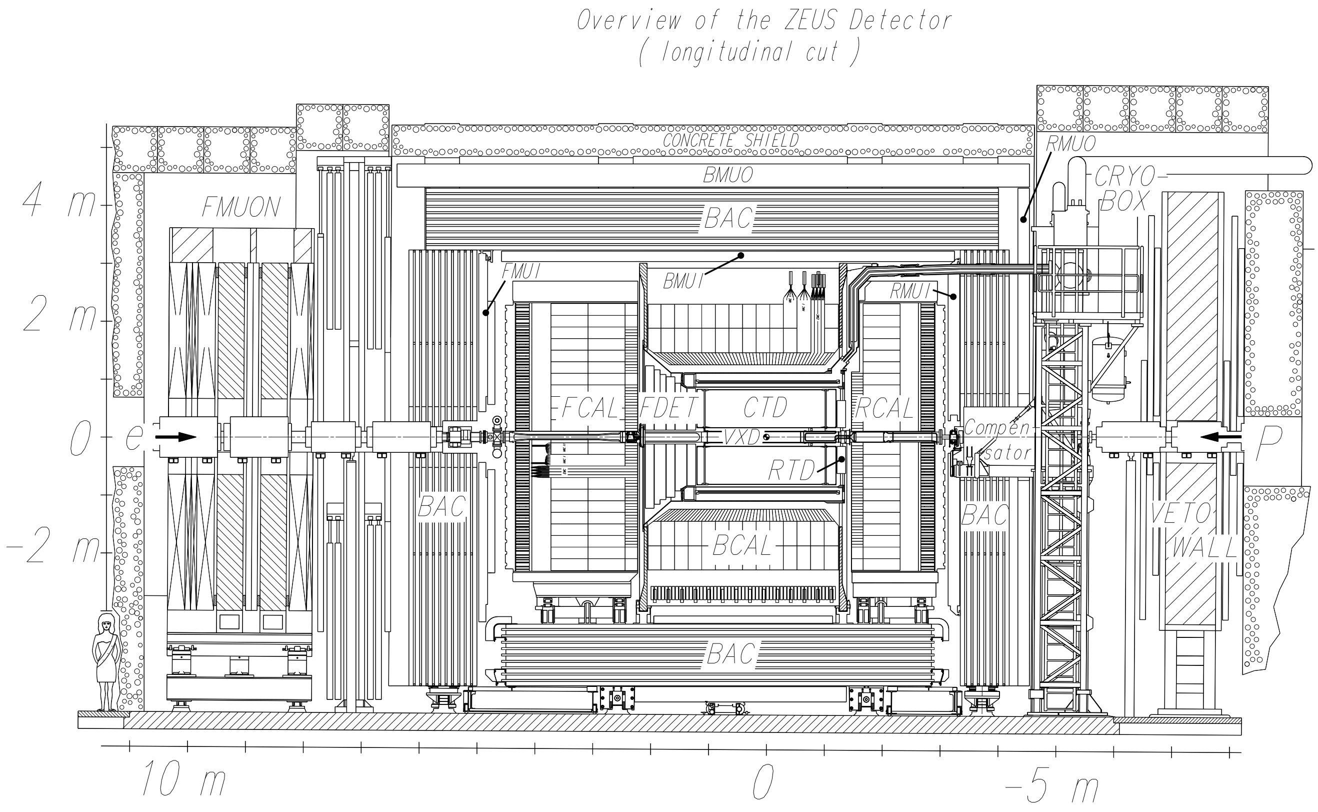

Figure 2.4: Cross section of the ZEUS detector along the beam axis.

interaction point in the forward direction is the forward neutron calorimeter which is located at Z=105.6 m to detect neutrons produced at small forward angles. In the rear direction two small electromagnetic calorimeters (LUMIE and LUMIG) are placed at Z=−34 m and Z=−107 m to measure bremsstrahlung events ($ep \rightarrow ep\gamma$) necessary for the determination of the luminosity and also used for tagging photoproduction events in addition to the taggers at Z=−8 m and Z=−44 m.

2.2.1 The Central Tracking Detector

The central tracking detector [27] is a cylindrical gas-filled wire chamber to measure direction and transverse momentum of charged particles. In addition energy loss dE/dx information provides particle identification.

The detector has a polar angular coverage of $15° < \theta < 164°$ and a complete azimuthal angular coverage. It consists of 72 radial layers organised in 9 superlayers with cells of 8 sensitive wires each (see Figure 2.6). The wires in the odd numbered superlayers are parallel to the detector axis whereas the wires in the even numbered ones are inclined by $\approx \pm\, 5°$ to provide a determination of the Z-position of the hit. In addition the layers 1, 3 and 5 are equipped with a Z-by-timing system (resolution $\sigma_Z \sim 4$ cm), mainly used for trigger purposes. The active volume of the CTD has a length of 205 cm with an inner radius of 18.2 cm and an outer radius of 79.4 cm. It is filled with a mixture of argon, CO_2 and ethane. Traversing charged particles

Figure 2.5: Cross section of the ZEUS detector perpendicular to the beam direction.

ionise the gas mixture along their trajectory (minimal ionising particles ionise 10-20 atoms per centimeter). Whereas the electrons drift to the positive sense wires (velocity $\approx 50\,\mu$m/ns) the positive ions are attracted by the negative field wires. In the field of the sense wire avalanche-like multiplication occurs with an amplification factor of about 10^4. The momentum resolution for tracks (with transverse momentum $p_T > 150\,$MeV) coming from the vertex and passing at least three superlayers was parameterized [28] to

$$\frac{\sigma(p_t)}{p_t} = 0.0058 \cdot p_t \oplus 0.0065 \oplus 0.0014/p_t \ , \tag{2.1}$$

where the symbol $\oplus$ indicates that the three terms are added in quadrature. The first term originates from the position resolution, whereas the other two terms are due to multiple scattering before and inside the CTD, respectively. The event vertex for medium and high multiplicity events can be reconstructed with an accuracy of $< 2\,$mm in the Z-direction (as measured in section 6.4) and $< 1\,$mm transverse to the beam.

2.2.2 The Uranium Calorimeter

The ZEUS uranium calorimeter [29, 30, 31] is a compensating sampling calorimeter consisting of alternating layers of absorbing and scintillating materials. On the one hand 3.3 mm thick depleted uranium (98.1% U^{238}, 1.7% Nb, 0.2% U^{235}) plates wrapped in stainless steal foils and on the other hand 2.6 mm thick plastic scintillator (SCSN38) plates. Whereas the uranium plates act as absorbers reducing the energy of traversing particles resulting in a shower development,

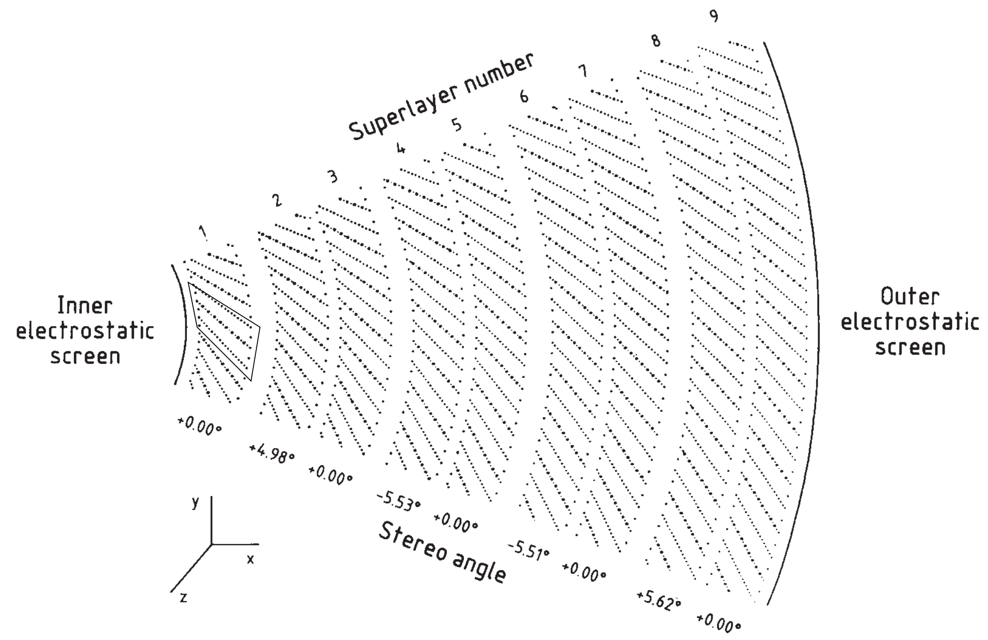

Figure 2.6: Layout of a CTD octant. The CTD consists of nine superlayers. Whereas the wires in the odd numbered superlayers are parallel to the detector axis the ones in the even numbered superlayers are tilted by the angles given in the figure. The superlayers itself consist of cells in which the orientation of the wires is tilted by 45° with respect to the radius to compensate the Lorentz angle. Therefore the electrons drift in the combined electric and magnetic field azimuthally towards the sense wires.

the scintillators measure the energy of these shower particles. The thickness of the layers was chosen to provide compensation, i.e. the energy response to electrons and hadrons is equalised (e/h = 1.00± 0.02), which is particular important for the energy resolution of hadrons. In testbeam measurements the energy resolution of the ZEUS detector was determined for electrons and hadrons to be [26]:

$$\frac{\sigma_e}{E} \approx \frac{18\%}{\sqrt{E(\text{in GeV})}} \quad \text{and} \quad \frac{\sigma_{had}}{E} \approx \frac{35\%}{\sqrt{E(\text{in GeV})}} \,. \tag{2.2}$$

The calorimeter is divided into three parts. The FCAL covers the polar angles from 2.2° to 39.9°, the BCAL from 36.7° to 129.1° and the RCAL from 128.1° to 178.4°. Leaving only space for the beam whole in the forward ($20 \times 20\,\text{cm}^2$) and in the rear direction ($8 \times 20\,\text{cm}^2$). The calorimetric coverage is larger than 99.8% of 4π. Each calorimeter is subdivided into single modules, an FCAL module is shown in Figure 2.7. FCAL and RCAL modules are rectangular whereas the 32 BCAL modules have a wedge shape, since the BCAL encloses the CTD cylindrically.

The modules are transversely divided into so called towers of $20 \times 20\,\text{cm}^2$ which themselves are subdivided longitudinally into one electromagnetic (EMC) and two (only one in RCAL) hadronic sections (HAC1,HAC2). The EMC sections in FCAL and BCAL are further transversally subdivided into four cells, in the RCAL only into two. Each cell is readout on two sides via wavelength shifters by photomultiplier tubes (PMT). Whereas the sum of the signals of both PMTs is independent of the the impact point of the particles, the information about

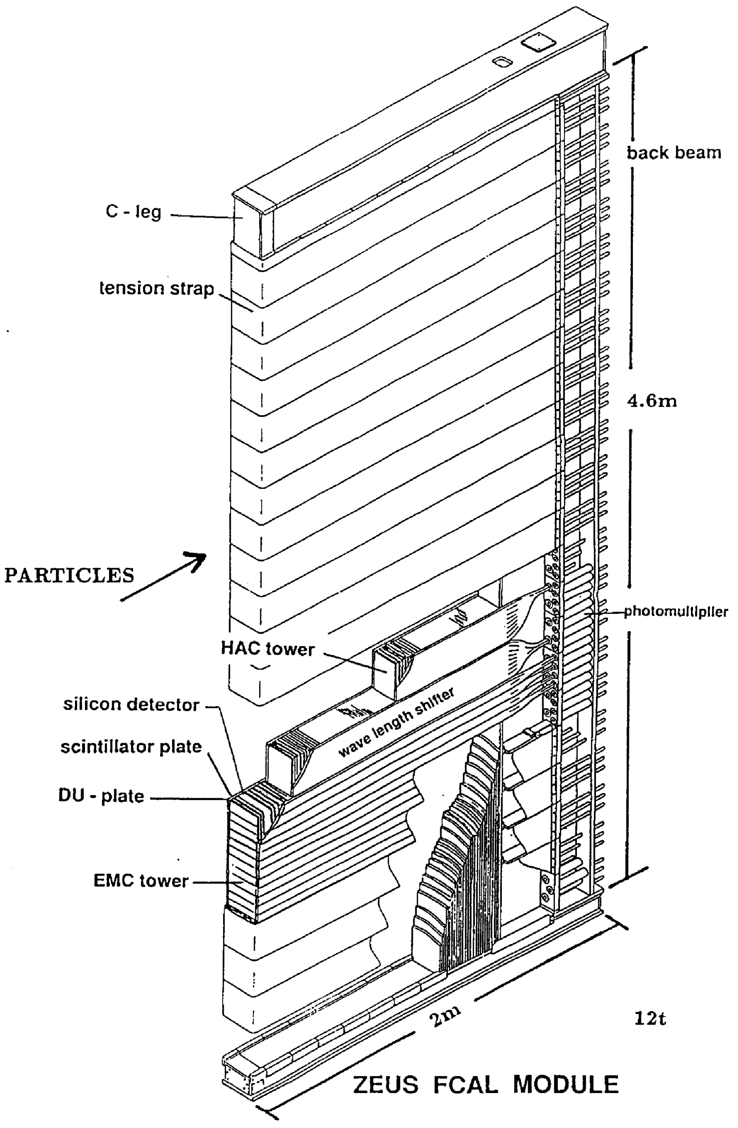

Figure 2.7: Cut-away view of a large FCAL module [26].

the horizontal position can be obtained by a comparison of both signals. Besides the energy measurement of electrons and hadrons the excellent time resolution (< 1 ns for energy deposits larger than 4.5 GeV) of the calorimeter is a powerful tool for background rejection at trigger level.

The calorimeter is calibrated on a daily basis by use of the stable signal from the natural radioactivity of U^{238}. Additional calibration of PMTs and readout electronics are performed by laser, LED and test pulses.

2.2.3 The Presampler

Inactive material in front of the calorimeters cause a worse energy resolution. To improve the energy measurement of the scattered positron a layer of $20 \times 20\,\mathrm{cm}^2$ scintillator tiles is placed in front of the RCAL towers. This presampler (PRES) [32] measures the number of minimum ionising particles (MIPs) which were produced by shower development in front of the

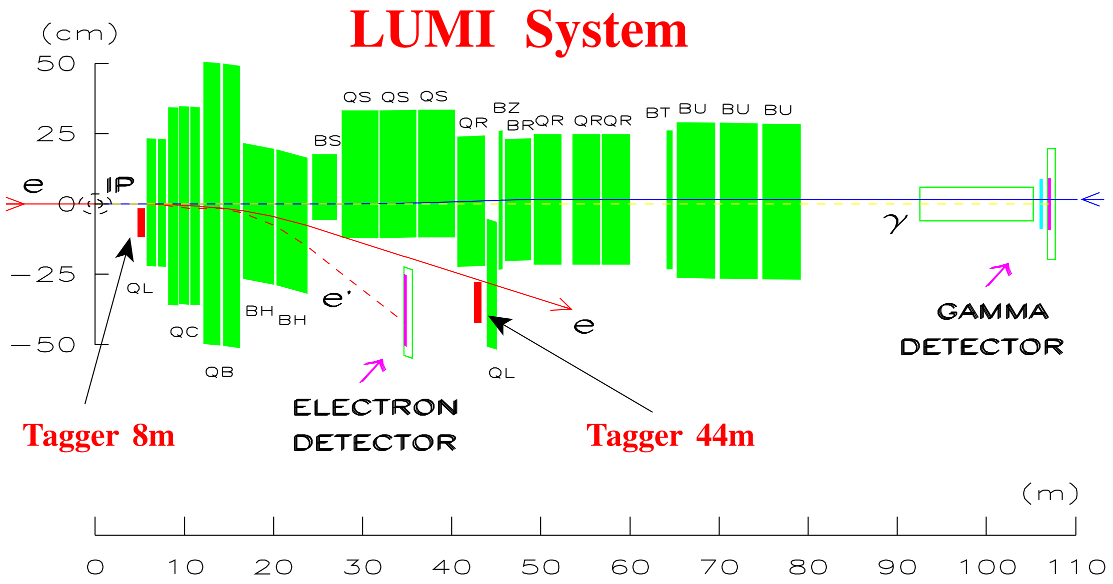

Figure 2.8: The ZEUS luminosity monitoring system. The position of luminosity monitors photon detector (LUMIG) at Z=-106 m and electron detector (LUMIE) at Z=-35 m is shown. Beside the luminosity measurement the LUMI detector together with the taggers at 8 m and 44 m are used for the measurement of the electron when scattered under small angle.

calorimeter. Event-by-event the measured calorimeter positron energy can be corrected by the signal in the presampler to account for the loss in the dead material resulting in an improved energy resolution (see section 6.2).

2.2.4 The Luminosity Monitor

To measure a certain cross section with high precision the time integrated luminosity $\mathcal{L}_{int} = \int \mathcal{L} dt$ has to be known very accurately since it enters directly in the cross section calculation:

$$\sigma = \frac{N}{\mathcal{L}_{int}}, \tag{2.3}$$

with the number of measured events N. The luminosity measurement is performed using a reaction with theoretically well known cross section. In the ZEUS experiment the Bethe-Heitler process (bremsstrahlung) $ep \to e\gamma p$ is chosen. A precise measurement of the rate of the bremsstrahlung photons allows thus a precise determination of the ep-luminosity.

Bremsstrahlung photons propagate inside the proton beam pipe which they can leave through a Cu-Be window at Z=-82 m. Photons emitted with $\theta_\gamma < 0.5$ mrad with respect to the positron beam direction can be detected by a lead/scintillator sampling calorimeter (LUMIG) which is placed at Z=-106 m (Figure 2.8). The detector is shielded by a carbon/lead filter from synchrotron radiation, together with this filter an energy resolution of $23\%/\sqrt{E}$ (with E measured in GeV) was achieved in testbeam measurements. With embedded layers of scintillator fingers in LUMIG the photons impact position can be reconstructed with a resolution of 2 mm. The differential cross section which is used to determine the luminosity can be extracted as a function of the photon energy via the Bethe-Heitler equation [33]. A large background with almost the same experimental signature originates from positron bremsstrahlung on the residual gas. By measuring the bremsstrahlung rate of unpaired positron bunches together with a measurement of the current in both paired and unpaired bunches the background can be subtracted statistically.

The systematic uncertainty of the luminosity measurement originates from uncertainties of the cross section measurements and to a large extend from the calorimeter energy scale.

2.2.5 The ZEUS Trigger and Data Acquisition

The HERA bunch crossing interval of 96 ns provides potentially 10.5 MEvts/s each of them with a total data size of 0.5 MB. Since the writing speed is limited to 0.5 MB/s the data rate and size has to be reduced significantly. For the ZEUS experiment a three-level trigger system was designed to select *ep* physics events which occur with a rate of 1-100 Hz by separating them from a large rate (10-100 kHz) of background events. Background events originate mainly from interactions between protons and gas molecules upstream the detector, furthermore by interactions between positrons and gas molecules as well as by cosmic rays.

The ZEUS trigger system is illustrated in Figure 2.9. Each major detector component has its own first level trigger (FLT), which on a basis of properties such as energy sums, thresholds or timing information provides a fast trigger decision which is passed to the global first level trigger (GFLT) while the event data is stored in logical pipelines. By combining different trigger slots a decision is made by the GFLT after $\sim 4.4\,\mu$s and the accepted events are passed to the second level trigger (SLT). At this stage the data rate should be reduced to less than 1 kHz. The organisation of the second level trigger is similar to the first level one. On the SLT level rough information about vertex, tracking and calorimeter timing is available for the decision. Like many SLT the global second level trigger (GSLT) is based on software running on a network of transputers. After 7 ms a decision is made by the GSLT reducing the event rate to 50-100 Hz. In case of accepted events the data of all components is combined in a single record of ADAMO [34] database tables by the eventbuilder. This is the data format used by the third level trigger (TLT) and all subsequent offline reconstruction and physics analyses. The TLT uses a computer farm to analyse and classify each single event. With the information about more detailed tracking, jet finding and possible candidates of the scattered positron the rate is reduced to 5 Hz. Accepted events (now of a size of $\sim$ 100 kB) are written to tape and offline fully reconstructed by the ZEUS software.

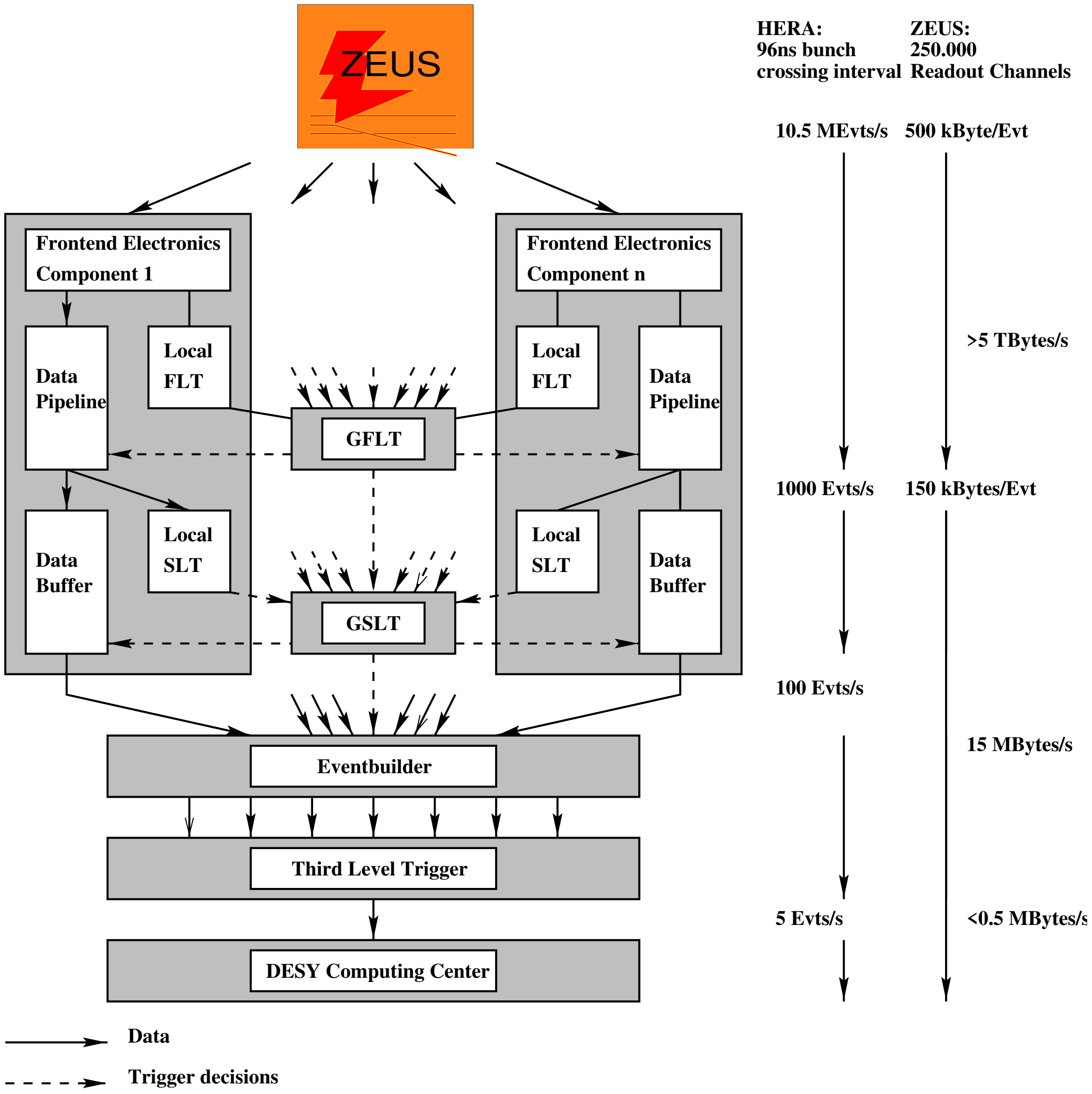

Figure 2.9: The ZEUS trigger and data acquisition system.

Chapter 3

The ZEUS Microvertex Detector

During the shutdown in the years 2000-2001 the HERA collider has been upgraded in order to increase the $e^{\pm}p$ peak luminosity from 1.5 to $7.0\times10^{31}\,\mathrm{cm}^{-2}\mathrm{s}^{-1}$ and to provide in addition longitudinally polarised lepton beams with a polarisation up to 70 % for H1 and ZEUS [35]. To fully profit from the enlarged data sample a silicon microvertex detector (MVD) and an additional forward tracking device, the straw-tube-tracker (STT) [36], were installed in the ZEUS experiment. The new tracking system significantly improves the measurement of particles in the forward direction being of large interest for many physics analyses. In the high Q^2 neutral current analysis the largest advantage will arise from the improved identification of the forward scattered electron whereas the charged current analysis will mostly benefit by a more precise vertex measurement and by a better reconstruction of the forward going tracks of the hadronic system. Furthermore the improved overall tracking system will allow to resolve secondary vertices which will lead to improved measurements of heavy quark production [37]. This chapter will describe the overall layout of the ZEUS MVD, of the chosen silicon sensors and furthermore important results of the testbeam program will be presented.

3.1 The ZEUS MVD Layout

The ZEUS MVD consists of two parts, the barrel (BMVD) and the forward (FMVD) detector. The sketched layout is shown in Figure 3.1.

The BMVD covers cylindrically the interaction point and is placed inside the CTD. It is ~60 cm long and has a diameter of ~31 cm resulting in a polar angular coverage of ~20°-160°. The longitudinal dimension of the BMVD guarantees that the interaction point is covered also in case of extreme values of its longitudinal distribution, which is determined mainly by the proton bunch length (~20 cm) (compare also to 6.4) whereas the diameter is constrained by the inner radius of the CTD. The BMVD consists of three double layers of silicon strip detectors which are assembled in planes on concentric cylinders around the interaction point. Due to the elliptical shape of the beampipe the innermost layer of silicon detectors is not complete. The shape of the beampipe was motivated by the presence of backgrounds mainly from synchrotron radiation in the horizontal plane. An elliptical shape in combination with a shift of the centre of the ellipse with respect to the nominal beam position in the negative X direction (towards the outside of the ring) keeps the background inside the beampipe and ensures that the detectors are not hit by the direct radiation. The beampipe and the assembled bottom half of the BMVD is shown in Figure 3.2.

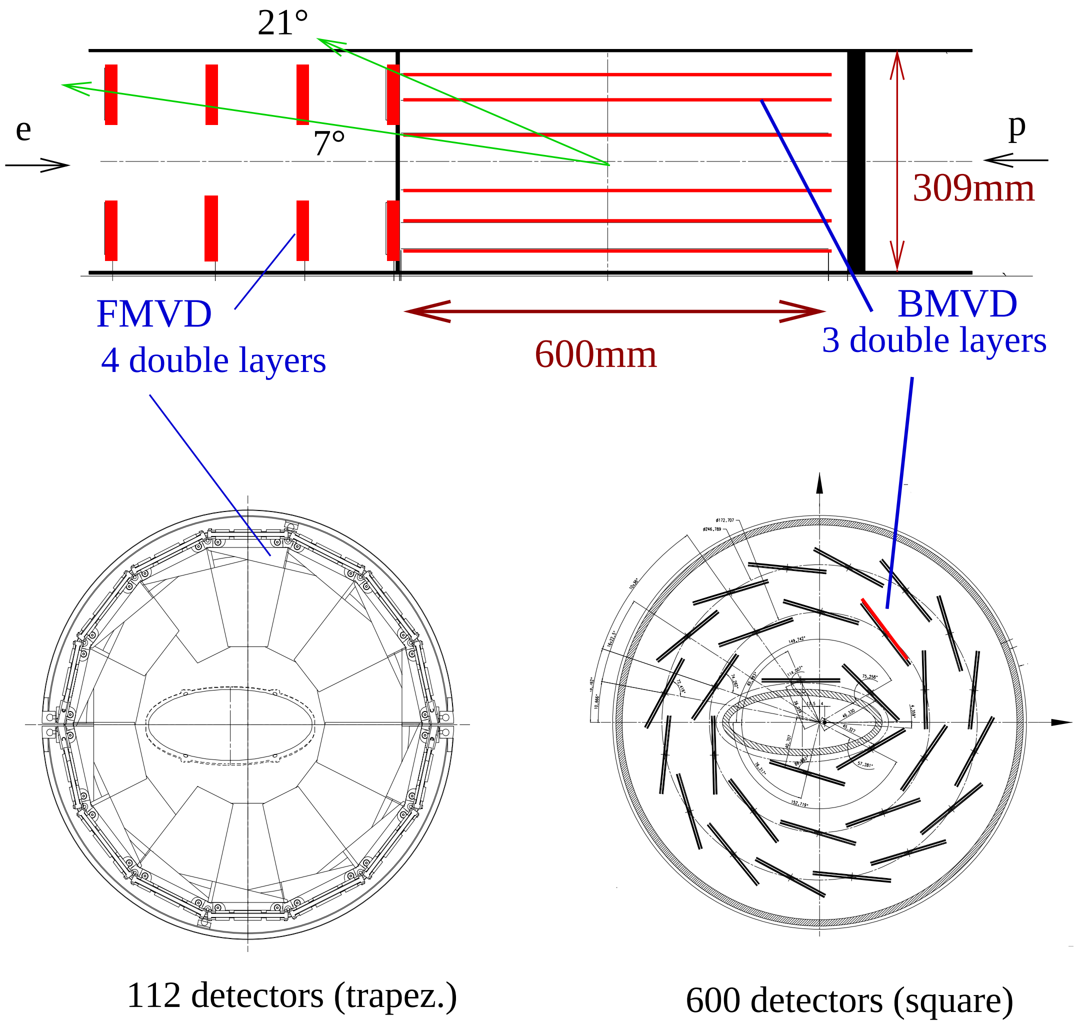

Figure 3.1: A schematic drawing of the MVD along the beam direction (top) and in r-ϕ plane (bottom). The BMVD consists of three double layers which are assembled around the beampipe. The FMVD consists of four double layers which are mounted as wheels in the forward direction of the proton beam.

The BMVD silicon strip detectors have 512 readout channels and a size of $64.2 \times 64.2\,\mathrm{mm}^2$; pairs of them are arranged in a so called 'half-module': two silicon sensors with perpendicular strip orientation are glued together and are electrically interconnected via copper traces (covered by gold) etched on a 35μm thick polyimide foil and are readout by the same front-end electronics. Thus if a signal is measured for one particular channel it cannot be distinguished which of the two connected strips (on the two different sensors) caused the signal. This results in a hit ambiguity which can be resolved by software (by performing the track fit) when the full information of the whole detector is available. Figure 3.3 shows a picture of a half-module on the left, on the right a drawing of a half-module together with its 'mirror image' can be seen. Those two half-modules are mounted on top of each other and form a 'full module'. Five full modules are arranged on a support ladder, which also supports readout electronics, cabling and cooling for the front-end electronics. The BMVD consists of 30 ladders with 150 full modules for a total of 600 silicon sensors with 153600 readout channels altogether.

The FMVD sensors are arranged in four wheels around the beampipe. The wheels are located at z$\simeq$ 31.9, 44.9, 57.9 and 72.9 cm away from the nominal interaction point following the proton

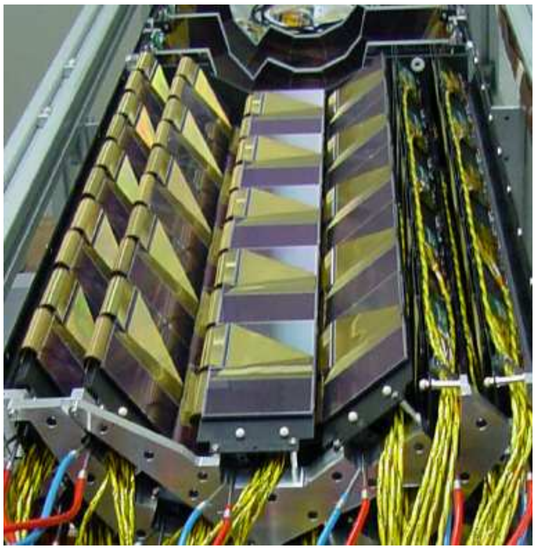

Figure 3.2: Photograph of one half of the BMVD.

beam direction. The FMVD extends the polar angular coverage down to ∼7°. Each wheel consists of 14 FMVD modules which themselves consist of two silicon detectors.

These sensors have a trapezoidal shape, two sides being parallel and two tilted by 13 degrees in opposite directions. As can be seen in Figure 3.1 the sensors are produced in two different lengths to account for the limited space around the elliptical beam pipe. The lengths are 73.5 mm and 48.5 mm respectively, the top side is in both cases 64.2 mm long whereas the width of the bottom side is 30.7 mm in case of the long detectors and 42.0 mm in case of the short ones. The strips are parallel to one of the tilted edges. A module is formed by two detectors assembled back to back resulting in a tilt of 26° between the strips of the two sensors. Because of the trapezoidal shape the 480 readout strips on a FMVD sensor have different length, varying from 6 to 73 mm. A schematic view of a FMVD module is shown in Figure 3.4. In total the FMVD consists of 56 modules with 112 sensors resulting in 53760 readout channels.

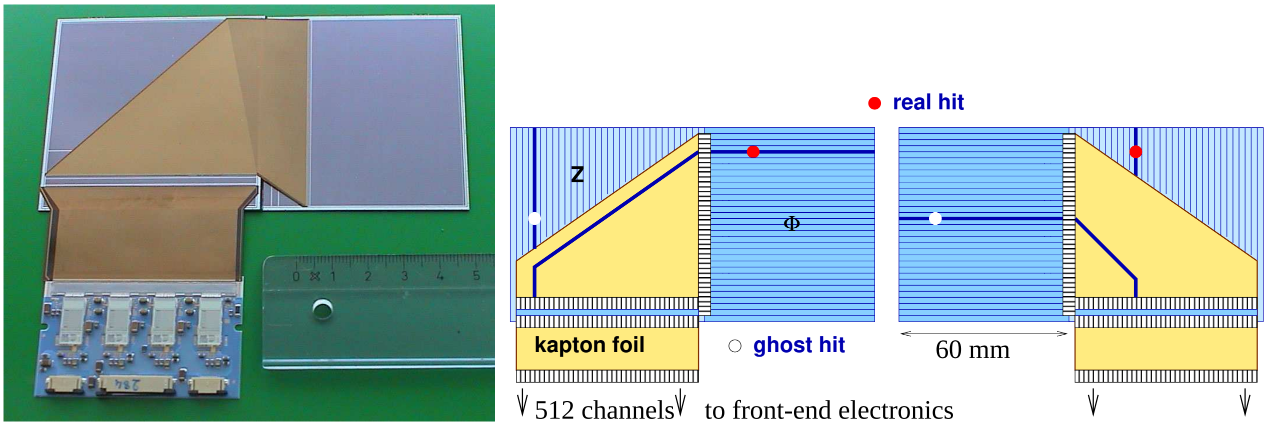

Figure 3.3: A photograph of a BMVD half module is shown on the left. The drawing on the right shows sketches of two half modules forming a full module when assembled on top of each other. Since two detectors always are readout together one traversing, ionising particle causes two hit candidates in a module, the real one and a so called ghost hit.

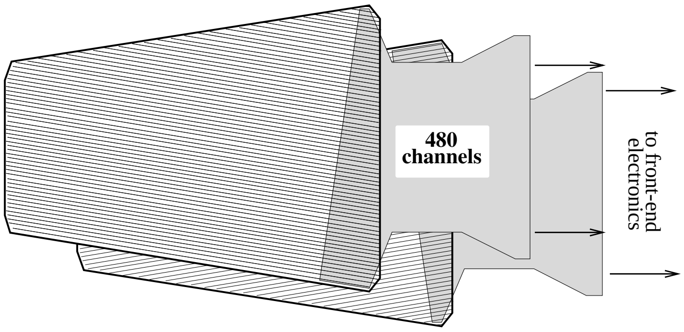

Figure 3.4: Schematic view of a FMVD module. Two detectors with strip directions different by 26° are mounted on top of each other.

3.1.1 Readout Electronics

Each MVD silicon detector is readout by HELIX3.0 chips [38]. Four chips are mounted on a ceramic hybrid which itself is located on the back of the support ladders in the case of the BMVD and perpendicular to the sensors in the case of the FMVD. The HELIX3.0 chip is a modification of an analog chip designed by the ASIC laboratory (Heidelberg, Germany) and manufactured in the $0.8\,\mu$m CMOS process by AMS (Austria). The chip integrates 128 channels with a charge sensitive preamplifier and uses a shaper to form a semi-Gaussian pulse with a peak time of ~60 ns (compare also section 3.4.2). Up to 136 events can be written in a pipeline from which eight can be marked (and therefore protected from overwriting) to wait for the trigger decision. If the event is triggered, all signals are transfered to a serial output readout line where they are digitised by the ADC. Signal thresholds from single strips and from clusters can be defined to select the strips whose signal is written on tape.

3.2 The MVD Silicon Sensors

The MVD silicon sensors are single sided strip detectors consisting of p^+ strips implanted (depth: $\sim 1.5\,\mu$m) on top of a $\sim 330\,\mu$m thick bulk of high resistivity ($3.4\,\mathrm{k}\Omega$cm - $7.9\,\mathrm{k}\Omega$cm) n-type silicon, produced by Hamamatsu Photonics (Japan). A cross section of a MVD silicon sensor is shown in Figure 3.5. The strip pitch is $20\,\mu$m whereas the readout pitch is $120\,\mu$m. In order to reduce the number of readout strips only every sixth p^+ strip is AC-coupled by thin layers of $\mathrm{Si_3N_4}$ and $\mathrm{SiO_2}$ to an aluminium strip ($\sim 1\,\mu$m thick and $\sim 12\,\mu$m wide). All strips are connected to a common bias line with polysilicon resistors ($\sim 1.5\,\mathrm{M}\Omega$). To fully deplete the detectors a bias voltage of 40 V to 93 V, depending on the resistivity, is necessary. A thin layer of $\mathrm{SiO_2}$ covers the detector surface whereas the backside is n^+ doped and aluminised.

If a charged particle traverses the detector ~25000 electron-hole pairs are created along the particle path in the depleted region. In the electric field the electrons drift to the n^+ region whereas the holes move towards the p^+ implantations and cause a change in the induced surface charges resulting in a short current pulse on the electrodes. Due to capacitive charge division [39] a signal is induced on the readout strips. Therefore the charges Ql and Qr measured on the left and right readout strip depend on the relative position s of the particle with respect to the readout strips. The height of the signals and also the amount of loss to the backplane depend on the capacitance between the strips (C_{is}), the capacitance between strip implantations and

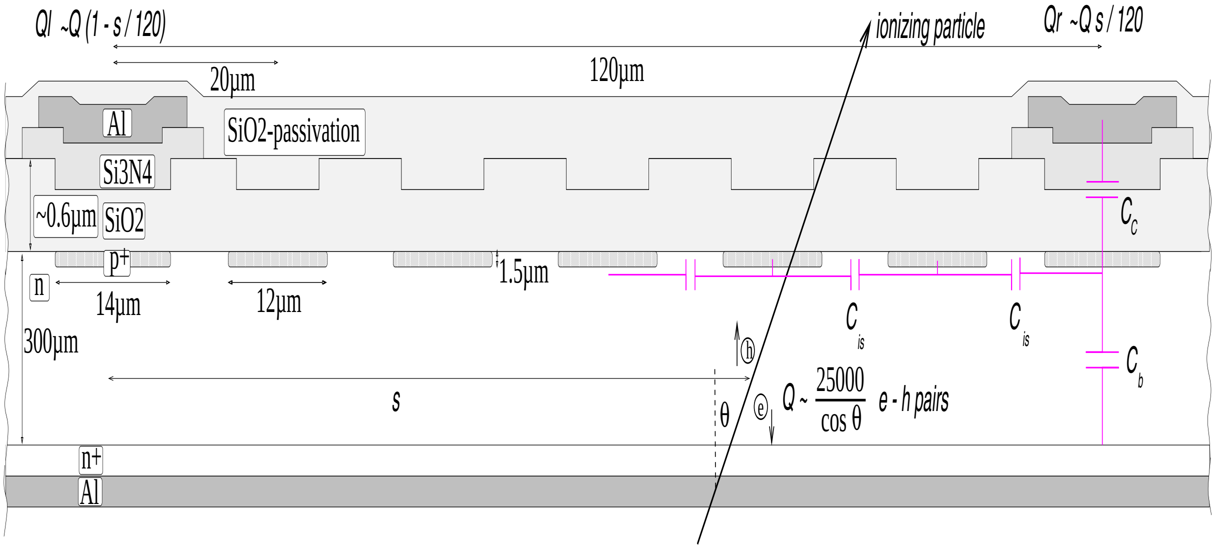

Figure 3.5: Cross section of a MVD silicon sensor between two readout strips. Dimensions of the layers are given in the left part of the picture. On the right side a simplified picture of the capacitive network is shown.

backplane (C_b) and the capacitance between read-out strips and the aluminium (C_c). From electrical measurements the capacitances were determined to be $C_c \approx$30 pF/cm, $C_{is} \approx 1$ pF/cm and $C_b \approx 0.07$ pF/cm.

Before the installation in the ZEUS experiment an extensive program was undertaken to test the performance and proof the functionality of both the silicon sensors and the whole system. In the next section testbeam measurements with BMVD prototype sensors are presented (see also [40]). Similar measurements and analyses were performed also with FMVD detectors [41]. Information about electrical measurements and quality control can be found elsewhere [42],[43].

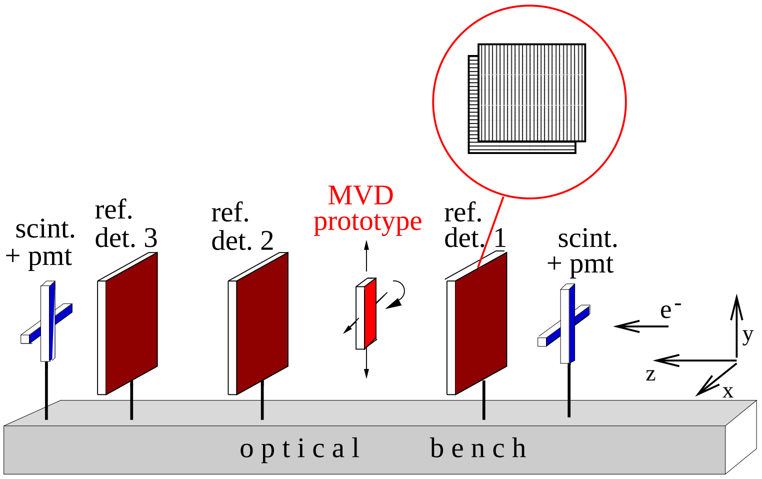

Figure 3.6: Schematic drawing of the testbeam setup. The MVD prototype sensor is placed between three reference detectors which form the beam telescope. The prototype can be rotated with a motor controller. Scintillator fingers are used for triggering.

3.3 Testbeam Setup

A schematic drawing of the testbeam setup is shown in Figure 3.6. A photo of the setup is shown in Figure 3.7. The testbeam program was performed at the DESY testbeam facility where an electron beam in the energy range of 1-6 GeV is made available. To study the performance of a prototype detector the position of the traversing particle has to be known with higher precision than expected from the prototypes, therefore a beam telescope consisting of three reference detectors was used. The prototype, to be investigated, was placed between two of these reference detectors on linear and rotational positioners used to examine different detector regions and effects of inclined particle tracks. For triggering purposes two small plastic scintillators were placed both in front and behind the beam telescope. All components were mounted on an optical bench placed on a metal table.

3.3.1 Beam Telescope and Alignment

Each of the three reference detectors (development of CERN [44]) consists of two high precision single sided silicon strip sensors (size: $32\times32\times0.3\,\mathrm{mm}^3$) measuring the vertical and horizontal position. These two sensors are assembled close to each other ($\sim$2 mm) with their strips orthogonal (as sketched in fig. 3.6) in an electric shielded metal box with very thin aluminium windows ($\sim30\,\mu$m). The detectors have a strip pitch of $25\,\mu$m and a readout pitch of $50\,\mu$m. During the whole time of operation the beam telescope sensors worked stable with a high signal to noise ratio [1] ($\sim$80) and a very low fraction of dead strips ($<0.1\%$).

Before performing high precision measurements the telescope and the prototype have to be aligned properly. The alignment procedure takes for each strip plane an offset perpendicular to the strip direction, an angle around the beam axis and an angle around the strip axis as free parameters into account. This results in six alignment constants for each two plane detector. They are determined by a χ^2-fit minimising the distances between predicted and measured

---

[1] See explanation in section 3.4.1

Figure 3.7: Photograph of the testbeam setup. The MVD prototype sensor is located in the cylindrical box between two reference detectors of the beam telescope.

positions. The procedure aligns first the reference detector #1 with respect to reference detector #2. Then detector #3 and the prototype are aligned on the extrapolated position determined from detectors #1 and #2. Since the prototype has strips only in one direction the second (not measured) coordinate is replaced by the predicted one in the alignment fit [45]. The achieved precision of the alignment procedure is $< 1\mu$m. This introduces a systematic error in the analysis which is so small that it can be neglected.

To be able to determine later the position resolution of the MVD prototypes the position resolution of the beam telescope has to be known. The position resolution depends on multiple Coulomb scattering and therefore on the amount of material in the particle path and on the intrinsic resolution of the telescope detectors. For this measurement the prototype was removed from the optical bench and the position predicted by detector #1 and #3 was compared to the one measured by detector #2. Since the effect of multiple Coulomb scattering is proportional to the inverse squared particle energy, the intrinsic resolution can be determined with measurements at different beam energies. The result of this analysis is shown in Figure 3.8. The intrinsic resolution of the reference detectors was determined to be $2.8 \pm 0.1\,\mu$m in both vertical and horizontal plane. The same procedure was also used for the prototypes and will be explained in more detail later (section 3.4.7). More information about other properties of the reference detectors can be found elsewhere [40].

3.4 Testbeam Measurements and Results

This section summarises several measurements performed at the DESY testbeam with one of the first BMVD prototypes. The used detector was previously irradiated by low energy photons from a ^{60}Co-source ($E_\gamma \approx 1.2\,$MeV) with a total dose of 2 kGy, but without bias voltage applied. Whereas electrical measurements showed some effects on the detector surface [42], testbeam measurements with a non-irradiated detector showed a similar detector performance (see section

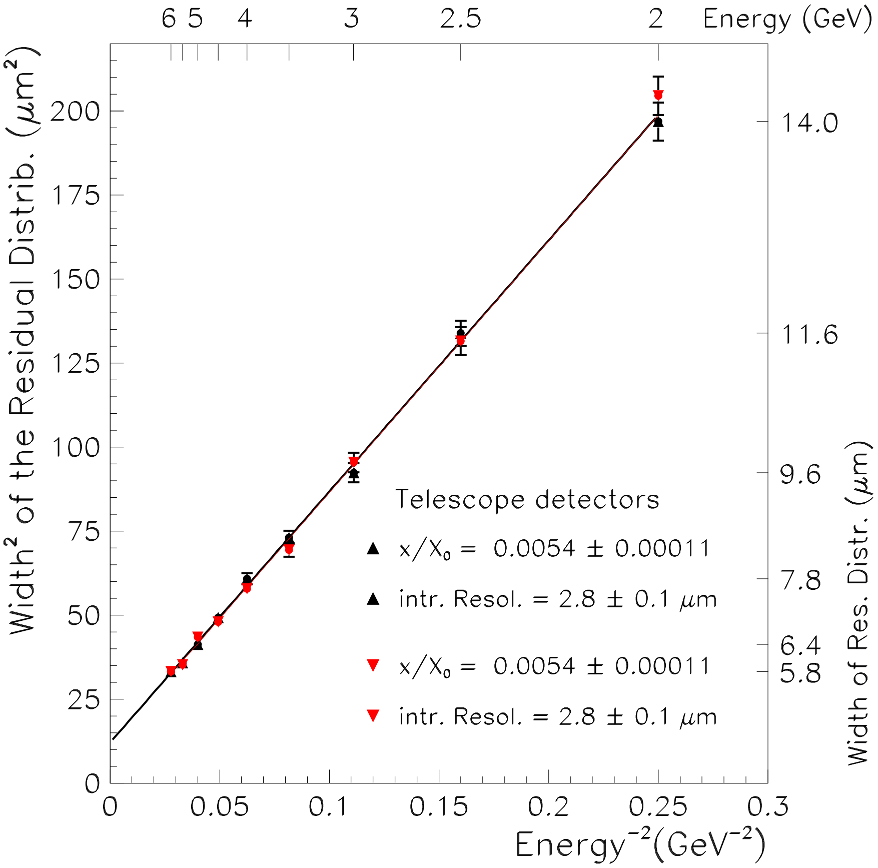

Figure 3.8: Squared width of the residual distribution measured by the beam telescope as a function of the inverse squared electron energy in vertical and horizontal direction (different orientated triangle symbols).

3.4.10).

3.4.1 Signal and Noise

For each event (i) and for all prototype readout channels (k) the voltage outputs are stored in digitised ADC counts (Q_i^k). The measured value Q_i^k is a superposition of the true signal S_i^k, the pedestal P^k (a DC offset on the voltage output), the individual strip noise N_i^k and the common mode noise C_i (CMN), which is an offset assumed to be common to all strips of a readout chip, changing event by event:

$$Q_i^k = S_i^k + P^k + N_i^k + C_i \tag{3.1}$$

Before every measurement the individual strip pedestals and noise levels were obtained by special runs of $\sim$ 100 random triggered events (S_i^k=0). To determine the pedestals the common mode offset (for each event and for the 128 channels of one readout chip) has also to be subtracted :

$$C_i = \frac{1}{128} \sum_{k=1}^{128} Q_i^k \tag{3.2}$$

The pedestal can then be defined as the mean of the common mode subtracted output for all events:

$$P^k = \frac{1}{N_{events}} \sum_{i=1}^{N_{events}} (Q_i^k - C_i) \,. \tag{3.3}$$

For a given event the individual strip noise N_i^k cannot be determined because it is randomly distributed event by event for each strip separately. Nevertheless an estimation of this quantity can be obtained from all events by the variance (rms) of the pedestal distribution, which is Gaussian distributed and centred at zero. This strip individual noise level N_{rms}^k is defined as follows:

$$N_{rms}^k = \frac{1}{N_{events} - 1} \sqrt{\sum_{i=1}^{N_{events}} (P^k - Q_i^k - C_i)^2} \,. \tag{3.4}$$

In case of a measurement with ionising particles the pedestal P^k and common mode noise C_i can be subtracted from the ADC output to extract the signal S_i^k whereas the individual noise N_i^k cannot and therefore is included in S_i^k in the following. To avoid including signal clusters in the CMN determination, in contrast to the case of random events the CMN is determined in a two step procedure. The mean and the variance of the pedestal subtracted ADC output $(Q_i^k - P^k)$ are determined for all strips on a chip. Then, those strips whose $Q_i^k - P^k$ is more than two standard deviations away from the average are excluded and the average value is redetermined using all others. This average is used as an estimate for the CMN and is subtracted for all strips on the chip under consideration:

$$S_i^k = Q_i^k - P^k - C_i \,. \tag{3.5}$$

The ionisation of a charged particle traversing the detector is usually measured on more than one strip. These strips with a measured signal form a cluster. The total measured pulse height of that cluster depends on the cluster algorithm, i.e. the definition which strips belong to the cluster. In the standard analysis in case of particles traversing the detector perpendicular to the strip plane the strip h with the highest signal is searched. Dependent on whether the left or right neighbour strip of h has the higher signal, this neighbour strip n is chosen to form a cluster together with strip h. The pulse height caused by the traversing particle is determined by the charges on the strips belonging to the cluster (consisting only of two strips in this case), given by:

$$Q_i^{cluster} = S_i^h + S_i^n \,. \tag{3.6}$$

For many particles traversing the detector perpendicular to the strip plane the $Q_i^{cluster}$ is plotted in Figure 3.9 resulting in the typical energy loss distribution which is well fitted by a Landau curve[2]. The most probable value for the energy loss divided by the averaged noise level of the used readout chip defines the signal to noise ratio (S/N) .

The performance of the MVD prototypes in terms of signal, noise and related quantities is summarised in following:

- Pedestal: the variation of the strip pedestal within one readout chip was of the order of the pulse height $(Q_i^{cluster})$. Since the pedestal is subtracted for each single strip separately

---

[2] For the fit the following parametrisation is used:

$$f(x, P_1, P_2, P_3) = P_1 \cdot \exp\left[-\frac{1}{2} \cdot \lambda + \exp(-\lambda)\right] \quad \text{where} \quad \lambda = \mathrm{P_3 \cdot (x - P_2)} \tag{3.7}$$

The P_i are adjustable parameters, x is the actual value of $Q_i^{cluster}$

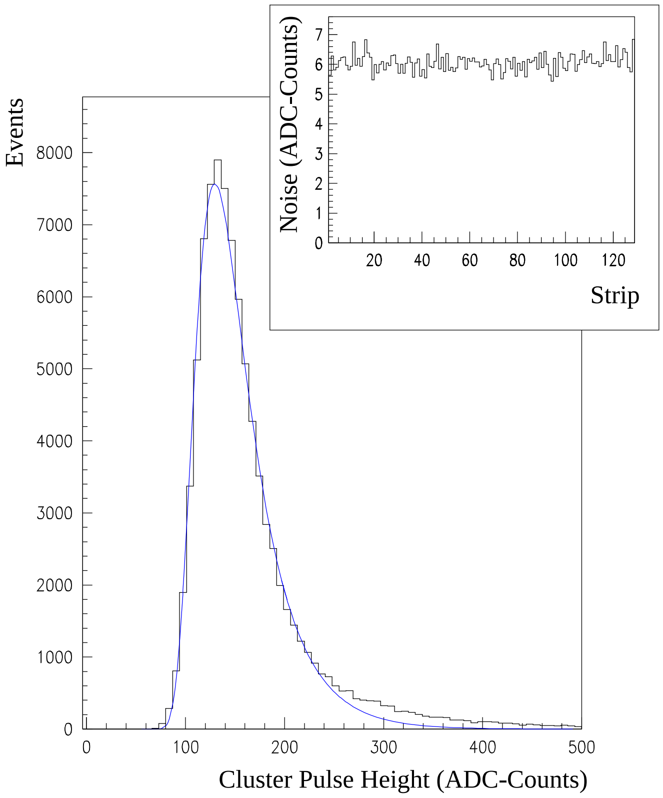

Figure 3.9: Pulse height distribution fitted by a Landau curve. In the top right corner the noise level of all strips within the used readout chip are shown.

this causes no problems. The pedestal was determined at least once a day. Although the observed changes in the value of the pedestal for single strips (for example due to changes of temperature) are small, their permanent monitoring improves the accuracy of the measurements.

- Noise: the noise was found to be uniform for all strips of one detector and stable in time.
- Signal to Noise Ratio: S/N values of ~ 22 were obtained for all four readout chips.
- CMN: the common mode was found to be Gaussian distributed with an rms of similar size to the noise level.
- Detector efficiency: the detector efficiency is defined as the ratio between on the one hand the number of events with the presence of one strip with a signal larger than five times the value of the noise in a region of ± 10 strips around the predicted position and on the other hand the number of predicted events by the telescope. In addition this method was restricted to events with only one cluster in each silicon plane. The detector efficiency was found to be very high (>99.95% [41]).

3.4.2 Front-end Pulse Shape

Each HELIX chip can be adjusted by setting the front-end bias voltages and currents to an operation point defining signal height, noise level, peak time and undershoot for the shaped

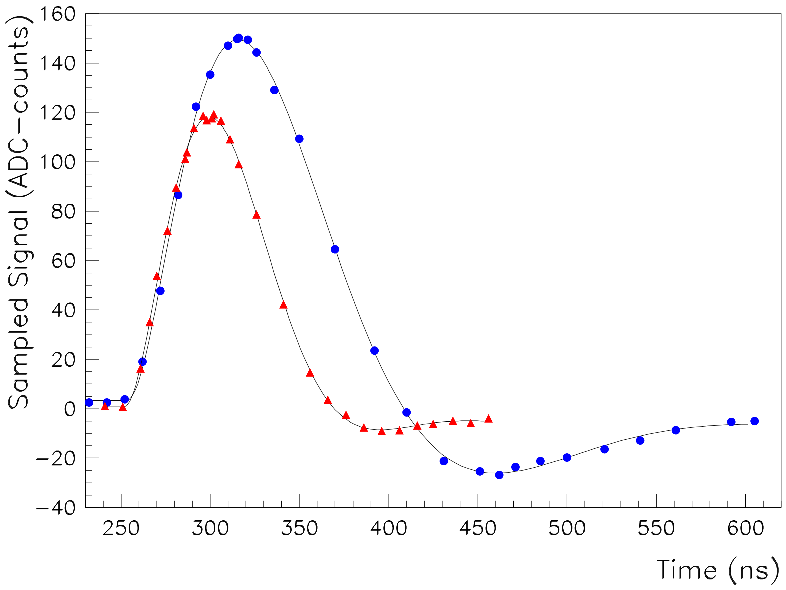

Figure 3.10: Pulse shaped signal for two different front-end operation modes, resulting in a peaking time of 48 ns and 62 ns, respectively. The data points are fitted with an analytical transfer function.

pulse. For optimum performance the shaped signal has to be sampled at its maximum height. Therefore a time scan was performed by shifting the falling edge of the sampling clock with respect to the trigger signal. Due to irradiation the behaviour of the chip will change and will make a change of the chip settings necessary resulting in a change of the peaking time during the years of operation. To study the effect of different settings measurements with two different operation modes for the HELIX chip were performed. The results are shown in Figure 3.10.

It can be seen that the two operation modes result in a different peaking time (48 ns and 62 ns, respectively) and a difference in maximum pulse height of 25%. The measurement showed that the overall noise level scales with the same factor and thus the S/N value stays unchanged. For all following measurements the output pulse was sampled at its maximum and the operation mode with the longer shaping time was used.

3.4.3 Strip Calibration

Variations of the strip gains (response of a strip and the electronics to a given input charge) can cause a systematic bias in the analysis of the testbeam data in particular in the reconstruction of the particles impact position. For example a particle traversing the detector perpendicular to the strip plane and in the middle between two readout strips is expected to cause signals of similar height on both readout strips. In case of large differences in the strip gains the signals would also differ a lot and the position cannot be reconstructed precisely without correcting for the different gains. Therefore the strip-to-strip gain variation was determined.

This is done using a matrix method in which rows and columns of the matrix are the strips of the detector under consideration and therefore resulting in a 512×512 matrix. For each event the strip k with highest ADC signal (h_k) is searched for and filled in the matrix at row k and column k. In addition the signals on the left l_k and right r_k neighbour strip are filled in the

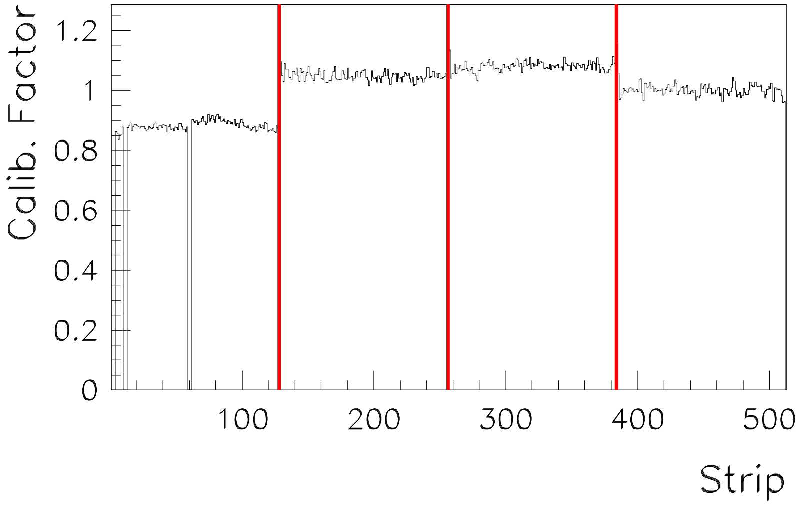

Figure 3.11: Strip calibration constants for 512 strips of one detector readout by four Helix chips. The strip regions readout by different chips are separated by the vertical lines.

same row in columns $k-1$ and $k+1$, respectively.

$$\begin{pmatrix} h_1 & r_1 & & & & \\ l_2 & h_2 & r_2 & & & \\ & l_3 & h_3 & r_3 & & \\ & & \dots & \dots & \dots & \\ & & & & l_{512} & h_{512} \end{pmatrix}_{512\times 512}$$

The whole detector was illuminated such that each strip was found to have the highest signal at least 1200 times, all events were added in the matrix. Each row is then divided by the number of contributing events. In the next step the resulting averaged values of a column are added $\epsilon_k = r_{k-1} + h_k + l_{k+1}$. The individual strip calibration constants c_k are obtained as the ratio of ϵ_k and the averaged value of ϵ_k over-all columns:

$$c_k = \frac{\epsilon_k}{\epsilon_{ave.}} \quad \text{with} \quad \epsilon_{\mathrm{ave.}} = \frac{1}{512}\sum_{\mathrm{k=1}}^{512} \epsilon_{\mathrm{k}} \tag{3.8}$$

The strip calibration constants for one detector are shown in Figure 3.11, the mean value and the rms of each chip are given in table 3.1. The first and the last strip (which have only one neighbour) as well as all the broken strips and their direct neighbour strips are excluded and their calibration constants are set to zero in the calibration procedure. The strips #2, #11 and #60 were found to be broken in the particular detector used (see Figure 3.11)

BMVD prototype	**chip 1**	**chip 2**	**chip 3**	**chip 4**
Mean value	0.884	1.050	1.081	1.001
RMS value	0.016	0.017	0.016	0.017

Table 3.1: Average chip calibration constants and their rms for a BMVD prototype detector.

The fluctuations of the strip gains inside one chip are smaller than 2% and comparable with the statistical uncertainty of the determination of the gain calibration ($\sim$ 1%), whereas the calibration constants differ from chip to chip up to 20 % and therefore they have to be taken into account in the analyses to avoid systematic biases.

3.4.4 Cross Talk Effects

An asymmetric cross talk effect was observed by measurements on the readout chip (HELIX2.2 and following versions). When pulsing a channel n with an external test pulse a fraction of the charge is found on the next or previous channel, dependent of n being an even or odd number. By use of a high statistics data sample (done for the strip calibration) the quantitative size of this effect was determined to be 4.9%. All testbeam data were corrected for this effect. An asymmetry in the chip pipeline layout is presumably the cause for this effect. Details of the analysis can be found in [40]. Any kind of symmetric cross talk (affecting all strips and their neighbours) cannot be separated from the symmetric charge sharing features of the detector itself (see next section), which leads also to an improvement of the detectors resolution. Therefore no corrections are applied for these effects.

3.4.5 Charge Division

The property of charge division of the MVD prototypes with five intermediate strips (see section 3.2) was studied using the testbeam data.

In Figure 3.12 the charge collected on the two readout strips closest to the particle incident point (strips l and r) is shown as a function of the predicted position (by the telescope). In each bin, the most probable value of the collected charge obtained by fitting the distribution to a Landau curve is plotted. The sum of the signals of these two readout strips is also shown. The sum of the most probable energy loss on strips l and r in case of position $0\,\mu$m is used as normalisation.

It can be seen that the principle of charge division works as expected. When a particle crosses the detector between two readout strips (l and r) the charge collected on the intermediate strips induces charges on the readout ones. Due to capacitive couplings between the strip implants the fraction of charge collected by strip r is not negligible ($\sim$ 10%) even for the case of particles crossing the detector exactly underneath readout strip l (positions x=0 in Figure 3.12) and vice versa. The charge collected by the next neighbour to the closest readout strip (left neighbour of strip l and right neighbour of strip r) is shown in the bottom plot of fig. 3.12. The total charge collected on the two readout strips (l and r) is smaller for particles traversing the detector in the central region between two readout strips in comparison to the regions close to them. The fraction of charge loss is larger in the central part due to the backplane coupling. On its way from the central part to the readout strips the capacitances between each intermediate strip implantation to the backplane cause some charge loss. Only $\sim$ 84% of the charge can be collected compared to particles crossing the detector exactly underneath a readout strip. Because of additional capacitances between not neighbouring strip implantations, charge is also induced on not closest readout strips (neighbours of neighbours). The charge collected by the next to next neighbouring readout strip is shown in the bottom plot of Figure 3.12. Although the used position reconstruction algorithm, described in the next section, works very successfully with neglecting the amount of charge collected by the next neighbours, they had to

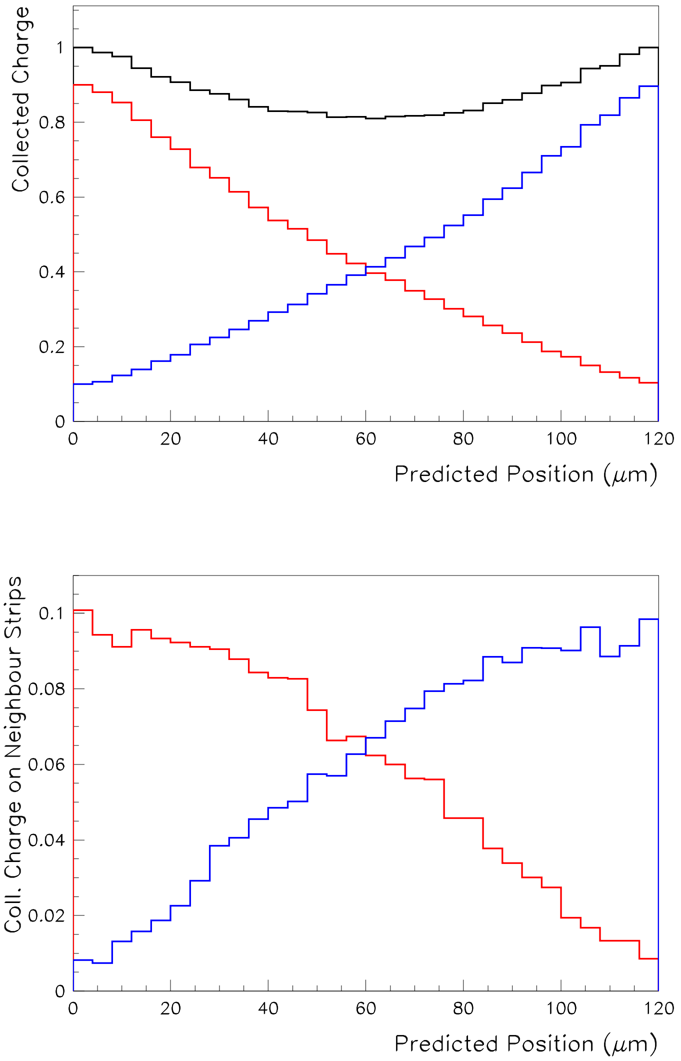

Figure 3.12: Top: collected charge by the left (falling from the left (x=0) to the right (x=120)) and right (falling from the right (x=120) to the left (x=0)) readout strip with respect to the impact position as a function of the predicted position. The sum of both signals is also shown. Bottom: charge collected by the next left (right) neighbour of left (right) readout strip used in top plot (please note the change of scale).

be considered in the simulation (see section 3.4.9). The measurement confirms the observation that a simple model considering only capacitances to neighbouring strip implantations resulting in charge collected on the two neighbour strips only is not satisfactory [43].

3.4.6 Position Reconstruction for Small Incident Angles

In the case of small incident angles almost all charge is collected by the two readout strips close to the incident point. Only these two strips are used in the reconstruction. As can be seen in Figure 3.12 the charge sharing is not linear. To correct for these non-linearities the η-algorithm

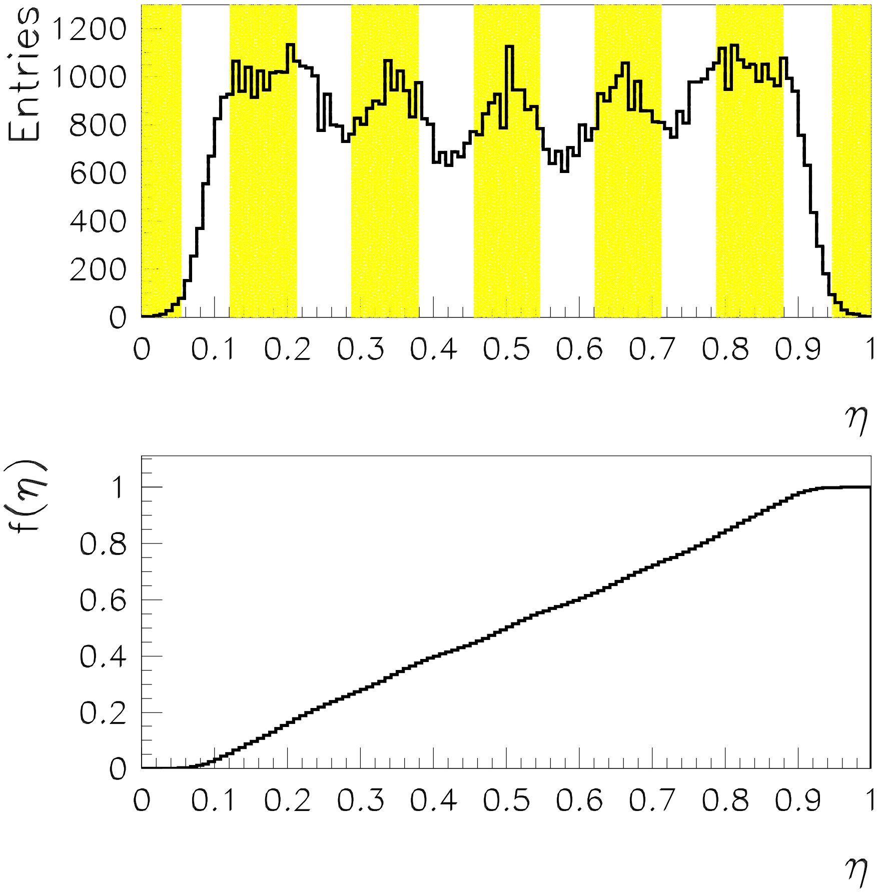

Figure 3.13: η distribution for the high statistics data sample (90000 events). The shadowed regions mark the positions of the strip implantations. In the bottom plot the function $f(\eta)$ is shown.

[46] was used to reconstruct the particle position. The variable η is defined as:

$$\eta = \frac{Q_{right}}{Q_{left} + Q_{right}} \tag{3.9}$$

where Q_{right} (Q_{left}) is the collected charge on the right (left) readout strip next to the particle impact position. The variable η represents the position relative to the readout strips using linear interpolation. The η distribution is shown in Figure 3.13 for a uniformly illuminated detector. Due to the properties of the electric field, especially the fact that all field lines end on a strip implantation, positions on the intermediate strips are reconstructed more often than positions between them. In addition positions on the readout strips are not reconstructed correctly since this would require no charge on the second considered strip. Due to the charge coupling between the strips and noise effects always a neighbouring strip with a charge larger than zero is found [3].

To correct for these biases, a function $f(\eta)$ is defined as follows:

$$f(\eta) = \frac{\int_0^{\eta} n(\hat{\eta})d\hat{\eta}}{\int_0^{1} n(\hat{\eta})d\hat{\eta}} \tag{3.10}$$

---

[3] In case of a decreased value of S/N it could happen that both neighbouring strips have a signal below zero.

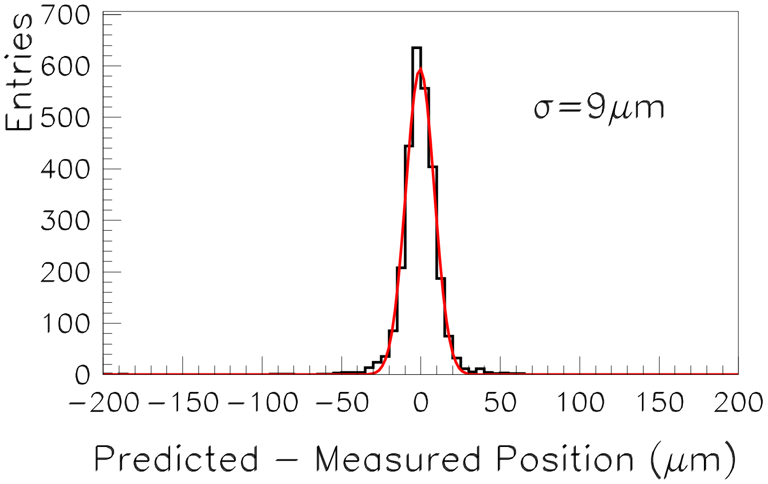

Figure 3.14: Residual distribution for data taken at electron beam energy of E=6 GeV.

where $n(\eta)$ is the event density as a function of η as obtained from the data. The corrected reconstructed hit position x_{rec} is then given by:

$$x_{rec} = p \cdot f(\eta) + x_{left} \tag{3.11}$$

where p is the readout pitch (120 μm) and x_{left} the position of the left (previous) strip.

3.4.7 Position Resolution

To measure the best possible position resolution of the MVD prototype sensor the used event sample was slightly reduced. For this analysis all events with an energy loss larger than 1.7 times the most probable value were excluded. These events have the signature of so called δ-rays (see section 3.4.11) which can spoil the position resolution and which were therefore not considered in this particular measurement. The residual distribution, defined as the difference between the position predicted by the telescope modules and the position reconstructed by the MVD-prototype (both obtained with the η-algorithm) was fitted with a Gaussian as shown in Figure 3.14.

The width of this residual distribution depends on the intrinsic resolution of the MVD-prototype, the intrinsic resolution of the telescope detectors, multiple Coulomb scattering effects on all material layers along the particle path (Si-detectors and aluminium foils) and on the relative distances of these different layers (defined in Figure 3.15):

$$\sigma_{resid.} = \sqrt{\sigma^2_{intr.,mvd} + k_1 \cdot \sigma^2_{intr.,tele.} + k_2 \cdot \theta^2_{c,mvd} + k_3 \cdot \theta^2_{c,alu_{mvd}} + k_4 \cdot \theta^2_{c,tele} + k_5 \cdot \theta^2_{c,alu_{tele}}} \tag{3.12}$$

The following approximation was used for the width of the multiple Coulomb scattering distribution [47]:

$$\theta_c = \frac{13.6 MeV}{\beta \cdot c \cdot p} \cdot \sqrt{\frac{x}{X_0}} \cdot (1 + 0.038 \cdot \ln(\frac{x}{X_0})) \tag{3.13}$$

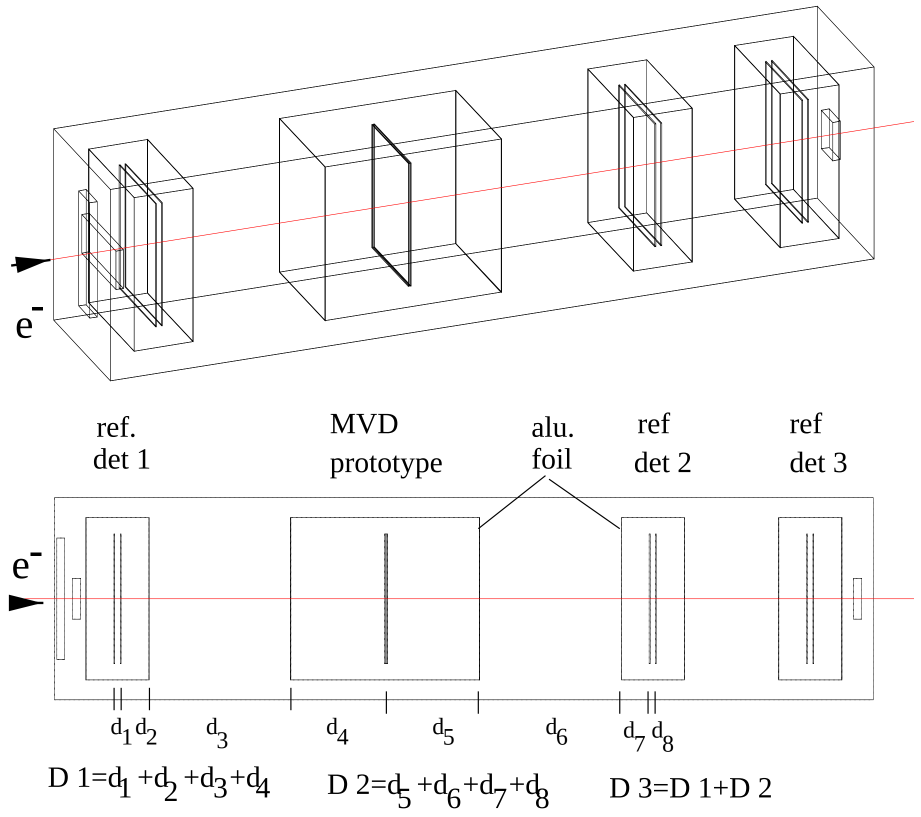

Figure 3.15: Two views of the testbeam setup in the GEANT simulation. The distances d_1-d_8 are needed for calculating multiple Coulomb scattering effects.

in which x is the thickness of the material and X_0 is the radiation length, p and βc are momentum and velocity of the particle. The geometrical factors (k$_i$) depend on the distances between the telescope modules and the MVD-prototype and on the thickness of their support boxes:

$$k_1 = \frac{D1^2 + D2^2}{D3^2}; \; k_2 = \frac{D1^2 \cdot D2^2}{D3^2}; \; k_3 = \frac{d_2^2 \cdot D2^2 + D1^2 \cdot (d_7 + d_8)^2}{D3^2}; \tag{3.14}$$

$$k_4 = \frac{d_7^2 \cdot D1^2}{D3^2}; \; k_5 = \frac{(d_2 + d_3)^2 \cdot D2^2 + D1^2 \cdot (d_6 + d_7 + d_8)^2}{D3^2} \tag{3.15}$$

Taking into account the intrinsic resolution of the telescope detectors ($2.8\,\mu m$) and the given geometry of the setup, the intrinsic resolution of the MVD-prototype can be obtained from a set of measurements at different beam energies (from 2 to 6 GeV) determining the multiple Coulomb scattering contribution, i.e. the ratio between detector thickness and radiation length x/X_0. The result is shown in Figure 3.16.

The calculated intrinsic resolution of the MVD-prototype is $7.2 \pm 0.19\,\mu$m at $0°$ incident angle and the ratio x/X_0 is determined to be 0.38 ± 0.02 %. The multiple scattering contribution was also estimated by means of a detector simulation as will be described in the next section.

I. Examination of multiple scattering effects with a GEANT simulation

The method to disentangle the intrinsic resolution from multiple scattering effects used in the previous section was tested using the simulation program GEANT [48]. In the simulation

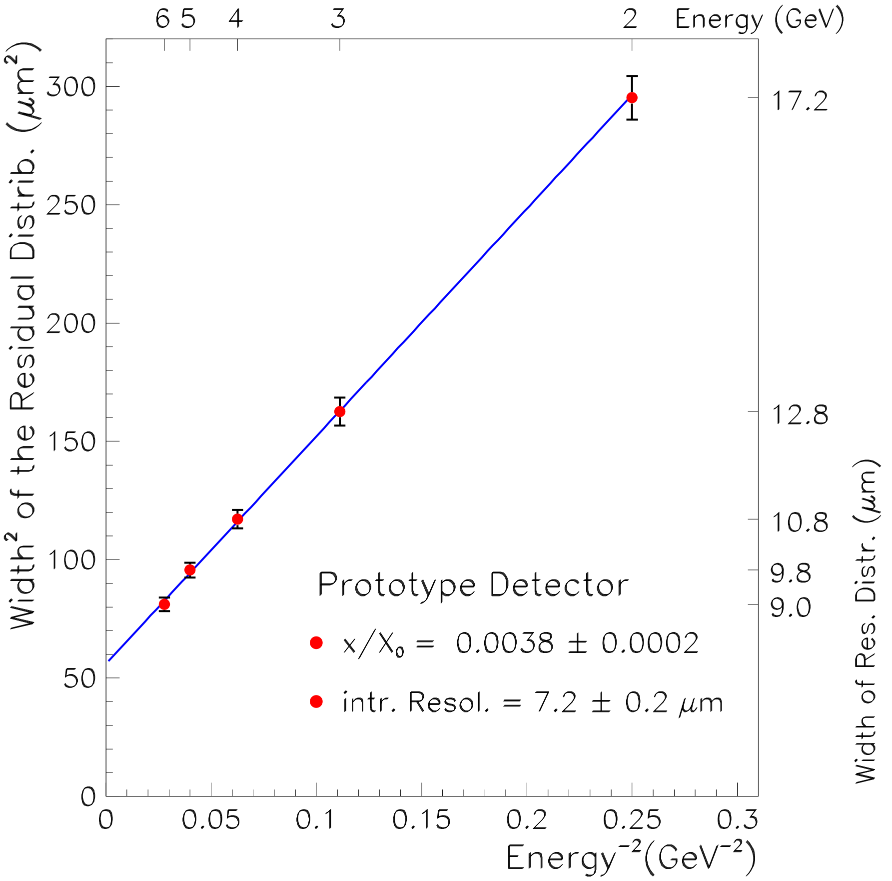

Figure 3.16: Squared width of the residual distribution as a function of the inverse squared electron energy.

the intrinsic resolution of all detectors was set to zero in order to study the effect due to multiple scattering only. The complete geometry of the testbeam set up was implemented in the simulation program (see Figure 3.15).

The same procedure of the determination of the residual distributions applied to the testbeam data was repeated for simulated events (see Figure 3.17).

The obtained value of 0.369 ± 0.005 % is in good agreement with the measured one of 0.38 ± 0.02 %. This confirms the reliability of the method used for the extraction of the intrinsic resolution. Note, the value obtained is different from the one quoted in literature ($\sim$ 0.33 % [47]). This discrepancy can be attributed to bremsstrahlung effects of the beam electrons. A simulation using muons was able to reproduce the value in the literature.

3.4.8 Position Resolution as a Function of the Interstrip Position

The measured resolution was studied as a function of the interstrip position. The telescope prediction was used to define spatial intervals (bins) according to the particle incident position between two readout strips. The size of these bins corresponds to the size of the strip implantations and the sizes of the intermediate regions respectively. The width of the residual distribution determined using the η algorithm as a function of the interstrip position is shown in Figure 3.18.

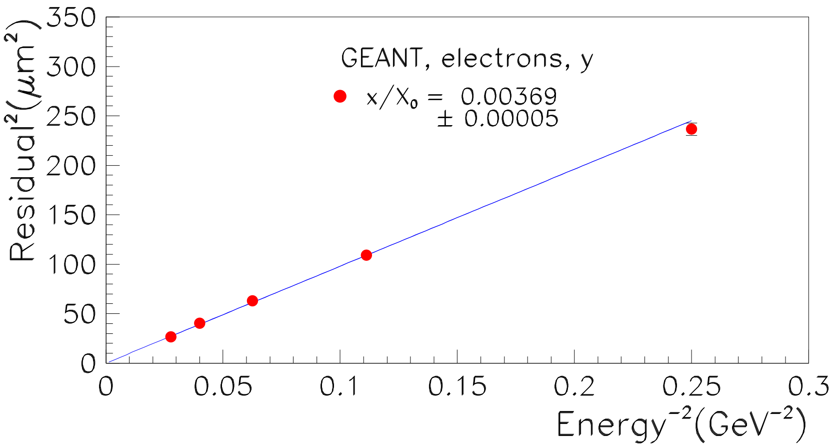

Figure 3.17: GEANT simulation: squared width of the residual distribution as a function of the inverse squared electron energy. All intrinsic resolutions are set to zero.

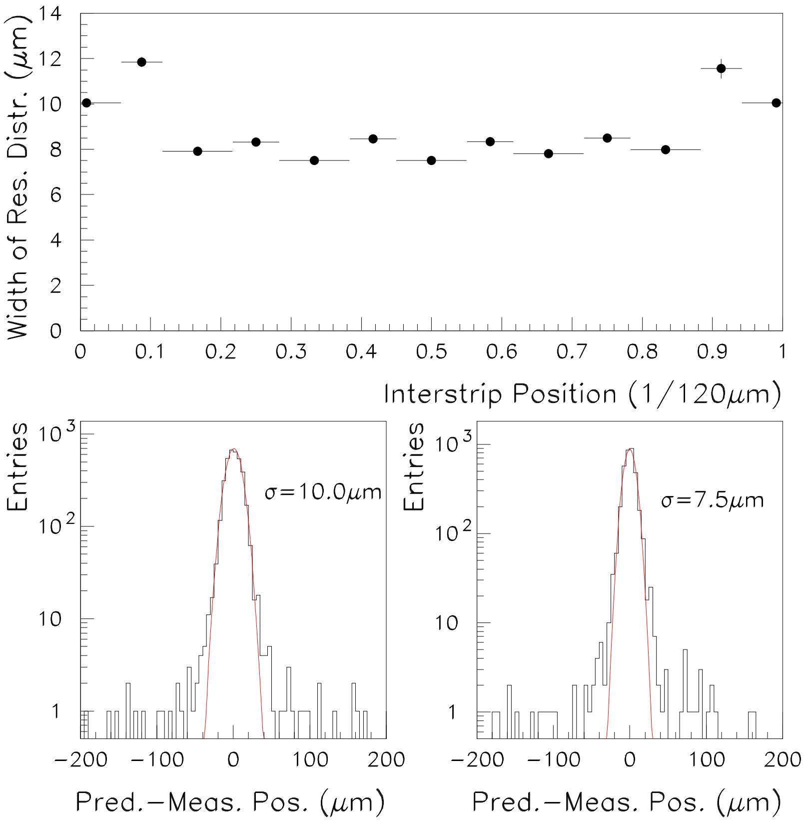

Figure 3.18: Top: width of the residual distribution as a function of interstrip position. The η algorithm was used to reconstruct the particle position. Bottom: residual distributions for particles crossing the detector underneath a readout strip (first and last bin in the upper Figure) and in the centre between the two readout strips at interstrip position x=0.5.

The η algorithm works better in the central region between two readout strips, where the charge division is more effective. In addition the result for particles traversing the detector underneath strip implantations is slightly better ($\sim 1\,\mu$m) than for particles crossing the detector between them. When a particle is found underneath a readout strip the charge expected on the two neighbouring strips is equal and only due to noise fluctuations one of them is chosen as the second strip used by the η algorithm. These random shifts to the left and to the right increase the width of the residual distribution. The worst resolution is found for particles between readout and first intermediate strip. Here the shifts are not random but systematic to one side.

3.4.9 Simulation of the MVD Prototype Response

To gain a better understanding of the MVD prototypes their response was compared to a detector simulation program, based on the program developed by G. Bashindzhagyan and N. Korotkova, described in [50]. Diffusion, ionisation fluctuations, noise and charge division were simulated. For the latter transfer coefficients were extracted using the testbeam data. The different effects and components in the program are detailed in the following.

I. Diffusion

To calculate the diffusion, the particle path inside the detector is divided into several (20) sections. For each of these different detector depths, the electric field is calculated and thus the drift time of the holes generated at this particular depth is determined. The charge carriers distribution resulting from the diffusion process is obtained by solving the continuity equation in the plane perpendicular to the electric field:

$$\frac{\partial p}{\partial t} = D \cdot (\frac{\partial^2 p}{\partial x^2} + \frac{\partial^2 p}{\partial y^2}) \tag{3.16}$$

where $p = p(x, y, t, z_0)$ is the distribution of holes generated at a depth z_0 in (x,y) plane[4] at the time t. The diffusion constant, D, depends on the temperature. Therefore its change during the drift time due to heating up is also taken into account. To get the total number of holes collected by one strip the charge distribution is integrated along the strip (y-axis). In the simulation, it is furthermore assumed that once the holes have reached the detector surface they are collected by the closest strip implantation.

II. Ionisation Fluctuations

For simulating the ionisation fluctuations the particle path is divided into different sections, with respect to the crossed readout cell (region between the third strip implantation left from a readout strip to the third implantation on the right). In each of these sections the ionisation fluctuation is assumed to have Landau shape independent on the section length. On the other hand the full width on half magnitude (FWHM) depends on the section length and is parameterized from other measurements with silicon detectors.

---

[4] This plane is equivalent to the strip plane, x direction orthogonal and y direction parallel to the strips.

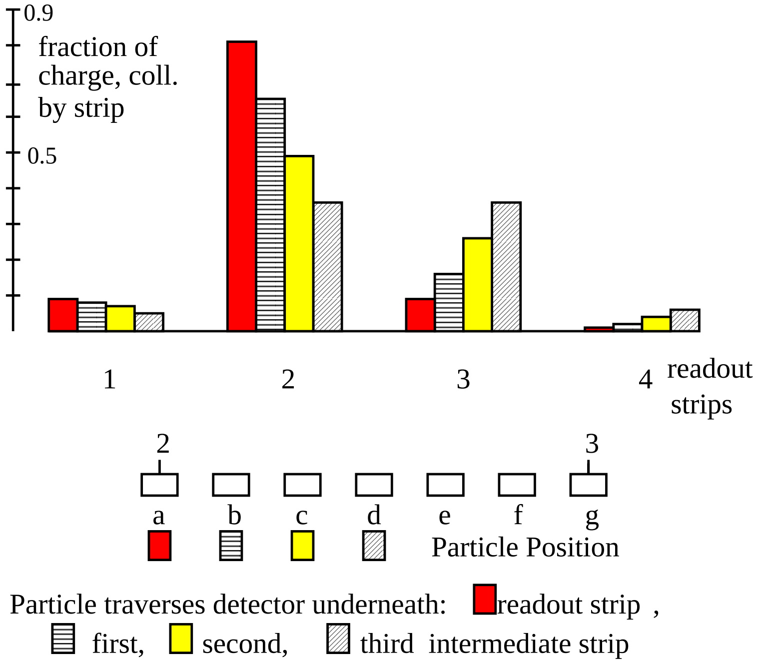

Figure 3.19: Relative charge collected by the four readout strips surrounding the particles position. The position of the particle is changed between readout strip #2 and #3, represented by different symbols. Only positions underneath strip implantations are considered, a symmetric detector performance was assumed.

III. Charge Transfer

After the charges were collected on the strip implantations they have to be transferred to the readout strip. The capacitive network is more complicated than the simple sketch in Figure 3.5, since also capacitances to next to next or to strip implantations even further apart have to be taken into account [43]. Thus a phenomenological description was obtained determining the charge transfer from testbeam measurements. The charge transfer coefficients give the fraction of charge on a strip implantation which is transferred to the surrounding readout strips. To measure these coefficients only tracks crossing the detector exactly underneath strip implantations (as predicted by the telescope, bin width $5\,\mu$m) were used. The collected charge (most probable value of the Landau distribution) on four readout strips (numbered from #1 to #4) is measured as a function of the particle positions: #a underneath strip #2, #b underneath the first intermediate strip (between strip #2 and #3), #c underneath the second intermediate strip, #d underneath the third intermediate strip and so on until #g underneath strip #3. Since the detector response is symmetric the charges measured on strip #2 and #3 are the same as also on strip #1 and #4 at particles position #d, also positions #a and #g, #b and #f, #c and #e are equivalent by exchanging the charges measured on strip #2 and #3 and on strip #1 and #4. In case of positions #a and #g the measured sum of charges on all four readout strips has its maximum and is therefore used as normalisation. The results of this measurement is shown in Figure 3.19. Each considered particle position (#a to #d) is represented by a different symbol, the fraction of charge collected by the particular readout strip is drawn in the top of the Figure.

In the simulation all charges collected on a strip implantation are transferred to the four surrounding readout strips using these measured coefficients (fractions smaller than 4% were neg-

	Charge frac. coll. by readout strip				
Part. Pos.	#1	#2	#3	#4	sum
#a: strip 2	0.090	0.810	0.090	0.004	1.000
#b: 1. interm.	0.082	0.655	0.158	0.021	0.915
#c: 2. interm.	0.076	0.486	0.256	0.041	0.859
#d: 3. interm.	0.058	0.363	0.363	0.058	0.842
#e: 4. interm.	0.041	0.256	0.486	0.076	0.859
#f: 5. interm.	0.021	0.158	0.655	0.082	0.915
#g: strip 3	0.004	0.090	0.810	0.090	1.000

Table 3.2: Fraction of charge collected by four readout strips surrounding the particle position. The particles cross the detector perpendicular to the strips and directly underneath strip implantations. The position of the particle is varied between readout strip #2 and #3.

lected).

IV. Noise Fluctuations

For every readout channel an additional signal according to Gaussian distributed noise was simulated. The width of the Gaussian was chosen in such a way that a comparison between the most probable simulated energy loss and the simulated noise results in the equivalent S/N -ratio than measured in testbeam data.

The agreement between data and simulation was studied in terms of the intrinsic detector resolution as a function of the angles of the traversing particle and will be discussed in the next section.

3.4.10 Position Reconstruction for Larger Incident Angles

In case of large incident angles θ of the particle direction in the plane perpendicular to the strip direction (θ is defined in Figure 3.5) the length of the particle path increases. The ionising particle traverses the detector underneath more than one readout strip. Therefore the generated charge is collected by many strips. The two strips around the hit position do not contain position information and the position resolution using the η-algorithm worsens as the angle increases. A head-tail-algorithm [49] is preferable for large incident angles. This method uses only the first (tail) and the last strip (head) of a cluster. The cluster is defined by all consecutive strips with a signal above the threshold of three times the noise level. The reconstructed position is given by:

$$x_{rec} = \frac{x_t + x_h}{2} + \frac{Q_h - Q_t}{2 \cdot Q_{ave}} \cdot p \qquad (3.17)$$

where $x_t(x_h)$ is the position of the first (last) strip above the threshold, $Q_t(Q_h)$ is the collected charge on this strip whereas Q_{ave} is the average charge collected by the strips in the cluster.

For the study of large incident angles a set of data at different angles in the range of 0° and 70° has been used. Figure 3.20 shows the energy loss distribution at various incident angles.

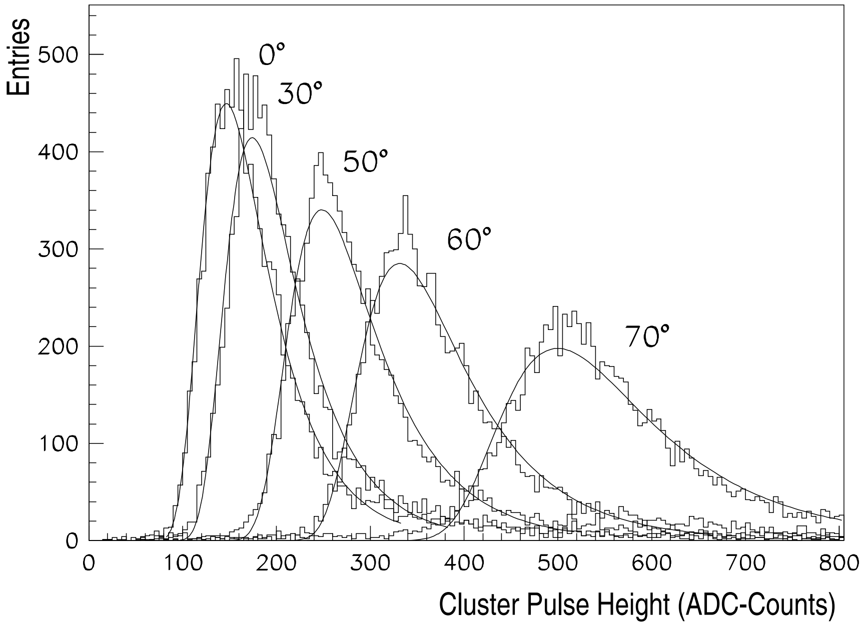

Figure 3.20: Energy loss distribution at different incident angles θ (0°, 30°, 50° and 70°).

By increasing the angle θ the most probable value of the energy loss distribution is shifted to higher values due to the increased track length. The resolution results obtained by using the η- and head-tail-algorithm are compared in Figure 3.21. The intrinsic resolution as a function of the incident angle is shown not only for the detector used for all other measurements (det. #1) but for comparison the result is also shown for a second detector (det. #2) which was not irradiated (see section 3.4). The behaviour of both detectors is similar over the whole angular region. The only exception is the result for small angles obtained with the head-tail algorithm. The difference is due to a better signal to noise ratio of det. #2 which makes the performance of the head-tail algorithm in this region even worse[5]. Above $\sim$ 32° the head-tail algorithm is seen to perform better than the η algorithm. Reconstruction algorithms applicable in the whole angular range (with and without the information on the particle incident angle) have been studied. A promising result of such an algorithm is discussed in [40].

Figure 3.21 shows in addition the results for the simulation as open points connected with lines. The simulation is able to describe the data over the whole angular region and for both different reconstruction algorithms. The S/N of det. #1 was used in the simulation which explains the slightly better agreement with this detector. Since no δ-rays (see next section) are taken into account the simulated intrinsic resolution is found to be better than the one obtained from testbeam data especially at small incident angles.

3.4.11 Impact of δ-rays on Position Resolution

When a particle crosses the detector sometimes a large fraction of the energy is transferred to an electron of the silicon lattice. This so called δ-electron may create electron hole pairs in a different direction as the incoming particle. This results in two effects sketched in Figure 3.22.

---

[5] The head-tail algorithm is not thought to be an alternative for small angles and it would be easy to modify this algorithm to work better for that angular range. The points are only shown for completeness.

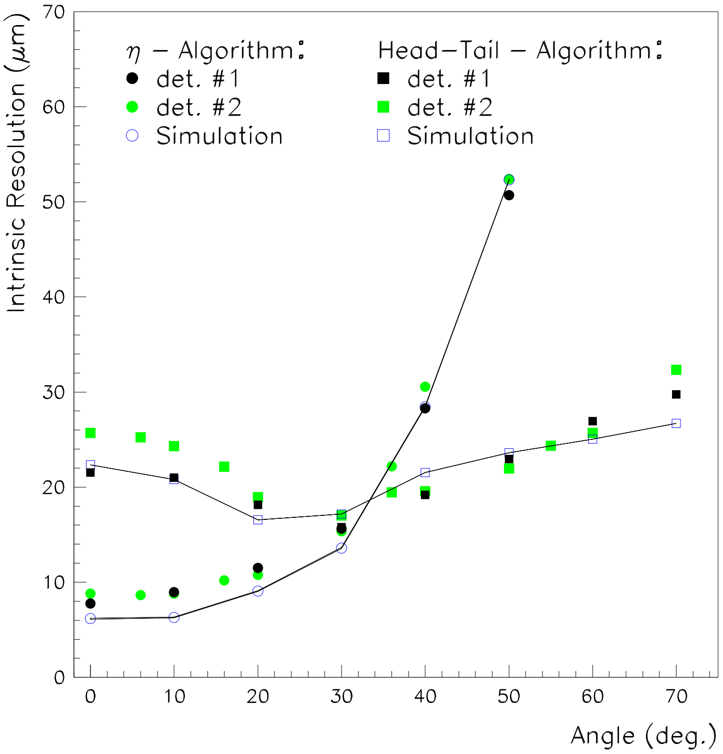

Figure 3.21: Resolution as a function of incident angle. The resolution was obtained using the η-algorithm (dots) and the head-tail algorithm (squares). The dark points correspond to the detector which was also used for all other measurements presented here whereas the lighter ones belong to an unirradiated detector. The results of the detector simulation are shown with open symbols connected with lines.

The sum of the charges collected by the two readout strips increases. In addition the relation between them is changed which leads to a spoiled position reconstruction precision.

For an analysis of the impact of delta rays on the position resolution the energy loss distribu-

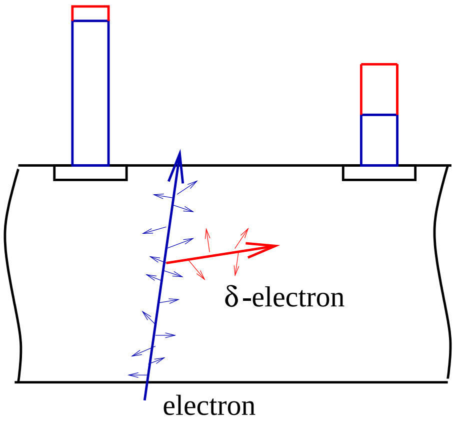

Figure 3.22: Sketch of the effects of delta rays. The total amount of charge collected by two readout strips increases and the relative pulse height relation between them changes.

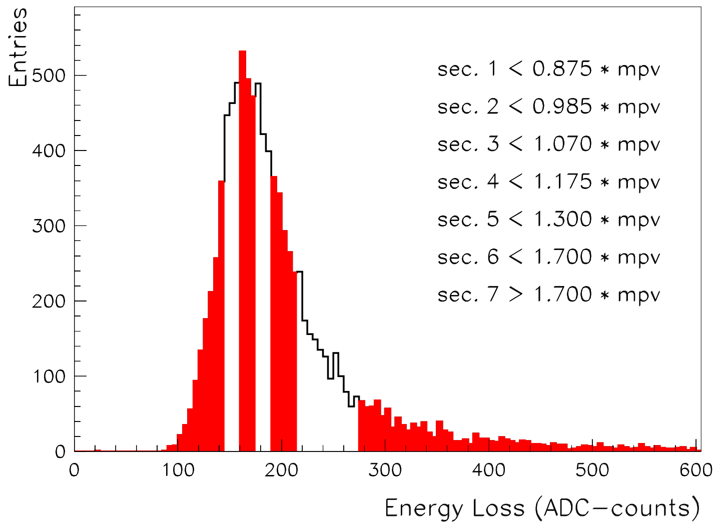

Figure 3.23: Energy loss distribution at an incident angle of 30°. Shown are the seven bins of collected charge in respect to the most probable value.

tion (for different incident angles) was sliced in sections of comparable statistics. The charge collected by two readout strips (in case of incident angles up to 30°) or by all strips with signal higher than three times the noise level (in case of angles larger than 30°) was added and seven bins with a similar number of entries were chosen. The bin boundaries with respect to the most probable value are given in Figure 3.23. The number of events per bin at all incident angles is of the order of 1000.

Figure 3.24 shows the width of the residual distribution in the seven bins for incident angles between 0° and 70°. The position was reconstructed using the η-algorithm up to angles of 30°, whereas for higher incident angles the head-tail algorithm was used.

For all measured incident angles and for both reconstruction algorithms the resolution for events with large cluster pulse height was found to be significantly worse than for events with moderate energy loss. Whereas the dependency of the resolution on the pulse height is small for the other bins in case of incident angles up to 30°, the precision in position resolution decreases with increasing energy loss for data analysed with the head-tail algorithm. Although the resolution is worse, events with large signal cluster cannot be excluded in the tracking reconstruction for the MVD, because the loss in reconstruction efficiency would be too high. However, it would be possible to assign different weights to the found hits when performing the track fit for particles traversing several layers of the MVD.

3.4.12 Summary of Testbeam Measurements

The behaviour and performance of BMVD silicon sensors together with their readout electronics were studied using a testbeam facility at DESY. The following main results have been obtained:

- Performance: the studied detector worked stably over the whole measurement period, with a high efficiency (>99.95%), uniformly distributed noise levels and a S/N -ratio of ~22.

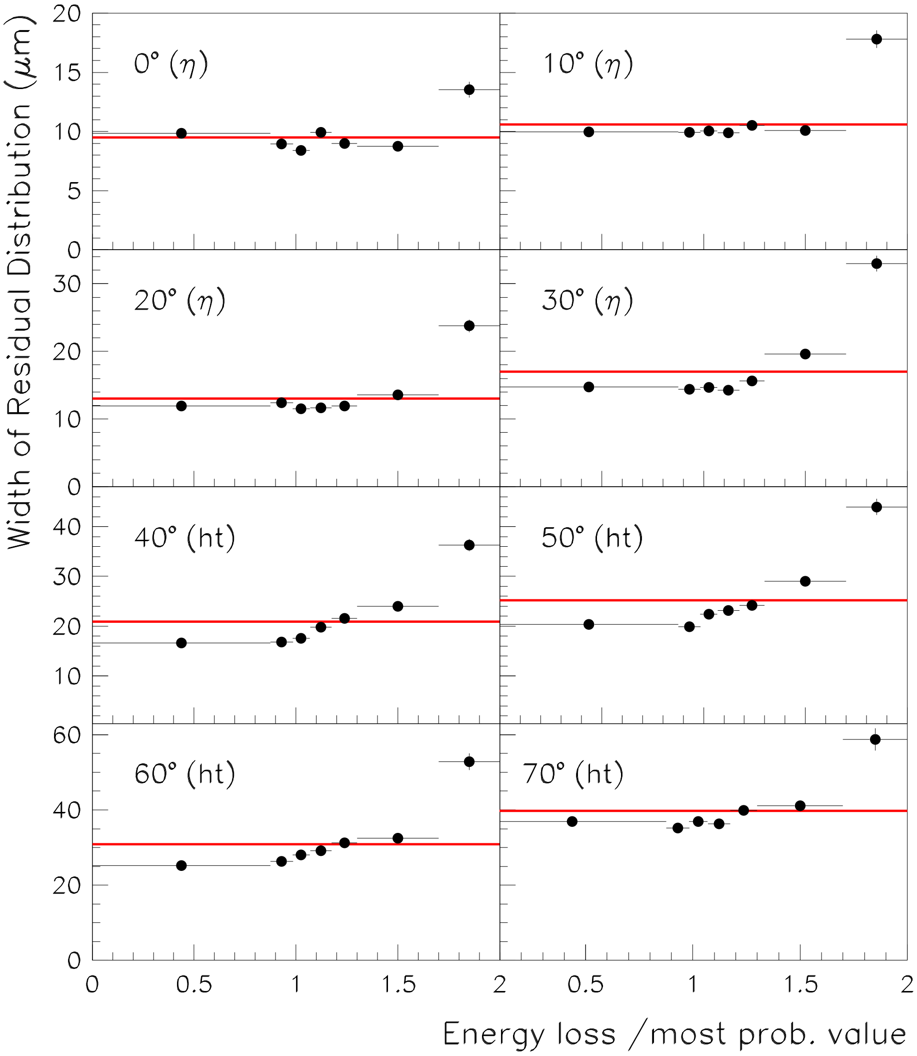

Figure 3.24: Width of the residual distribution in seven bins of energy loss for incident angles between 0° and 70°. The line marks the level of the overall resolution in each angular bin.

- Strip calibration: the gain variations of strips read out by one HELIX chip were determined to be not larger than 2%, whereas amplification variations up to 20% for different readout chips were observed.

- Charge division: the charge division was studied in detail. The expected charge sharing between the strip implantations was confirmed.

- Position resolution: the η-algorithm was used to reconstruct the particles position for small incident angles. For perpendicular tracks (and by excluding events with energy depositions larger than 1.7 times the most probable value) the intrinsic detector resolution was determined to be $\sigma_{intr.,mvd}$=7.2±0.2 μm. To obtain this value the effect of multiple Coulomb scattering was subtracted by taking advantage of its energy dependence. The method used was cross-checked with a GEANT-simulation. In case of larger incident angles the head-tail-algorithm was used which is able to improve the position resolution significantly.

- Simulation of the detector response: the charge transfer between strip implantations and readout strips was parameterized and implemented in a detector simulation program. Good agreement for the position resolution between data and simulation was obtained.
- Impact of δ-rays: δ-rays cause a deterioration of the position resolution. Since they cannot be excluded from the MVD data, the hit positions used for a track fit should be weighted according to their pulse height.

Chapter 4

Monte Carlo Simulation

Due to the complexity of the possible systems of outgoing particles from an electron proton interaction it is impossible to calculate analytically the acceptance and resolution of the ZEUS detector. Therefore Monte Carlo (MC) techniques are used to simulate the event topology and the detector response.

In the MC procedure a physics event generator is used which models the underlying physics process. It returns the four momenta of all outgoing particles. In a second step a simulation of the detector response is performed. The data format of this simulation is the same as for the real data. This has the advantage that the same event reconstruction and physics analysis chain can be used for data and MC events. This chapter introduces the used physics event generators, gives an overview of the detector simulation and summarises the total amount of generated Monte Carlo events.

4.1 DIS Monte Carlo Simulation

Deep inelastic lepton-proton scattering (DIS) is simulated by the event generator DJANGOH 1.2[1] [51]. In the leading logarithmic QCD approximation (LLA) corrections from QED/electroweak theory and QCD can be factorised allowing two different programs to describe these effects. The DJANGOH event generator contains the Monte Carlo program HERACLES [52] and an interface to LEPTO [53].

HERACLES includes electroweak calculations for initial and final state radiation, vertex and propagator corrections and exchange of two different bosons. The colour dipole model (CDM) implemented in ARIADNE 4.10 [54] and interfaced to LEPTO was used to simulate the QCD parton cascade. The Lund string fragmentation as implemented in the program JETSET [55] was used to model the fragmentation into hadronic final states.

As input for the parametrisation of the structure functions the parton distribution function (PDF) CTEQ5D [56] was used. CTEQ5D makes use of fixed target data and previous F_2 measurements at HERA by both H1 [57] and ZEUS [58, 80].

---

[1] DJANGOH comprises the programs (formerly kept separately) DJANGO6, version 2.5, and HERACLES, version 4.6.2

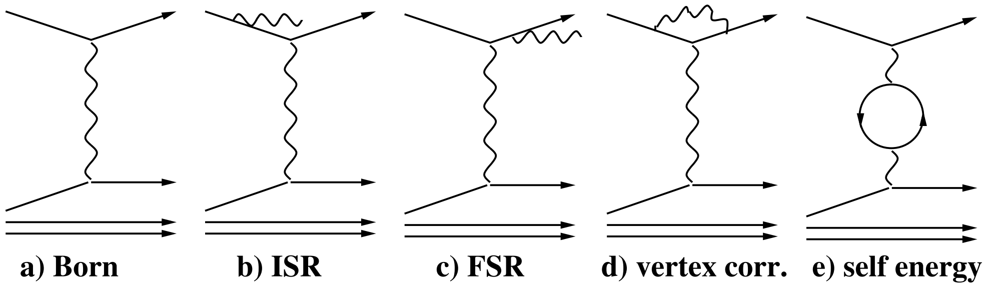

Figure 4.1: Feynman diagrams showing the NC *ep* process on Born level and the LO QED corrections.

4.1.1 Electroweak Corrections at the Lepton Vertex

At the Born level the neutral-current positron proton cross section can be described by a single boson exchange between the positron and the proton; this process is shown in diagram 4.1a and can be calculated with e.g. LEPTO. Higher order QED corrections, as the radiation of a photon in the initial or final state (diagram 4.1b and c) can change the event kinematics significantly. The real photon modifies the energy and the angle of the positron which results in a shift of the reconstructed variables. In order to compare the measurement with a simulation these effects have to be taken into account. For this purpose the program HERACLES is used which includes the leptonic corrections as well as the complete one-loop virtual corrections (see diagrams 4.1b - e).

HERACLES separately treats the Born term and three parts of the leptonic QED correction: initial and final state radiation and a part called QED Compton. This is a purely technical division of three parts corresponding to different pole terms of the differential cross section. Whereas the ISR and FSR peak correspond to photons emitted collinearly with the initial positron and collinearly to the scattered positron respectively, the QED Compton peak originates from a $Q^2 = 0$ interaction in which the positron-photon pair gains a large invariant mass and the photon is emitted at relatively large angles.

Figure 4.2 shows the polar angles of scattered positrons and radiated photons. In the left part of the figure the ISR events can easily identified peaking at $\theta_\gamma = \pi$ whereas FSR events peak at $\theta_\gamma = \theta_e$. The angular distribution of the QED Compton events (which are a minor fraction of the events) is shown separately in the right part of the figure.

HERACLES uses the Quark Parton Model not containing any QCD effects. The events are described by the flavour of the scattered quark and the four-momenta of the final positron, the final quark and the potentially radiated photon.

4.1.2 QCD Cascade and Hadronisation

The situation on the proton side is more complicated due to the structure of the proton and the confinement of the quarks. In a typical DIS event a quark is struck out of the proton. Since both the struck quark and the proton remnant are coloured objects a QCD cascade develops between them. This cascade can result in the production of particles. In the experiment this colour flow causes the deposition of energy in the detector region between the quark jet and the proton remnant. In the simulation the ARIADNE program was used to model the QCD cascade.

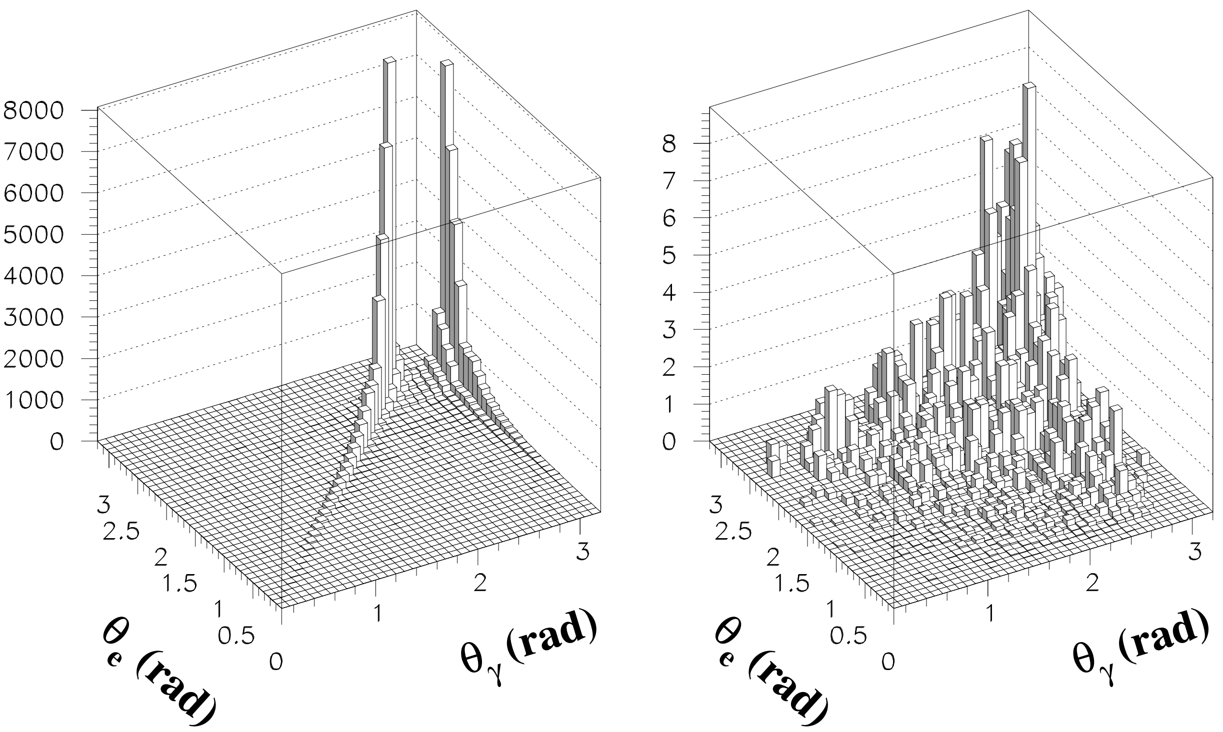

Figure 4.2: Distribution of scattered positron and photon polar angle as simulated in HERACLES. On the left side all emitted photons are considered whereas the plot on the right side shows the angular distribution of only the QED Compton photons.

ARIADNE uses the colour dipole model, regarding the emission of a gluon as a radiation of a colour dipole between two coloured objects. Then the emission of a second (softer) gluon is treated as radiation from two independent dipoles, one between struck quark and first gluon, the other between that gluon and the proton remnant. Subsequent (even softer) gluon emission is treated as radiation of even more dipoles. In the boson-gluon-fusion process (BGF), in which the virtual boson interacts with a gluon out of the proton forming a quark anti-quark pair, no obvious dipole between the struck quark and the proton remnant is available. Therefore the probability of this process has to be included by hand based on the leading order matrix element. A conservative estimate of the uncertainty introduced by the used model of the QCD cascade can be achieved by using a different model as a systematic check. In that case the model MEPS implemented in LEPTO is used. The calculated matrix elements (ME) in first order (α_s) are supplemented by parton showers (PS) which approximate the parton emission at higher orders. The calculation of the parton showers is based on the DGLAP equations in the Leading Logarithm Approximation (LLA) (cf. 1.6).

After the development of the QCD cascade the coloured quarks are transformed into colour neutral hadrons. This process is called hadronisation or fragmentation; in the simulation it is modeled by the Lund string model in JETSET. Here each quark-anti-quark pair is connected with a string. When such pair moves apart the potential energy in the string increases linearly which finally results in the breaking of the string producing a new quark-anti-quark pair. This procedure ends when only on-mass-shell hadrons remain. Further decays of unstable hadrons are also taken into account.

4.2 Diffractive Monte Carlo Simulation

An important result of HERA was the observation of a class of events with no energy deposition in the angular region between the proton remnant (which is not seen in the detector) and the direction of the struck quark [59, 60]. By comparing these so called diffractive events with usual DIS events a significant difference is therefore observed in the variable η_{max}:

$$\eta_{max} = -\ln(\tan(\theta_{min}/2)) , \tag{4.1}$$

where θ_{min} denotes the polar angle of the most forward energy deposition greater than 400 MeV. In addition diffractive events typically have lower hadronic mass and particle multiplicity with respect to non-diffractive events.

Diffraction is usually explained as the exchange of a colour-neutral object (sometimes called Pomeron) between the proton and the photon. In some models this object (in its simplest form) is thought to consist of two gluons which compensate each other in colour.

The RAPGAP2.08/06 [61] event generator (developed with the help of HERA measurements) was used to simulate diffractive events. RAPGAP makes also use of HERACLES, ARIADNE and JETSET but in contrast to DJANGOH where all events a generated with a colour flow between struck particle and proton remnant, here all events are generated with an interacting colourless object. Since the measured cross section contains both types of events a mixing of the two MC samples is necessary.

4.2.1 Mixing of DJANGOH and RAPGAP MC Sample

Since the diffractive cross section is not known very precisely the events from both generators can not be combined by simply using the predicted cross sections. Instead the η_{max} distribution was used to determine the fraction of diffractive MC. After reweighting both MC samples separately to the data luminosity by using the cross sections given by DJANGOH, MC and data η_{max} distributions are normalised separately. Thus the mixing is done only by the different shape of the distributions which leaves the over-all normalisation between them unchanged in the mixing procedure. Then a fit was performed in bins of η_{max} to obtain the fraction f of RAPGAP events needed to describe the data:

$$N_{data} = f \times N_{RAPGAP} + (1-f) \times N_{DJANGOH} . \tag{4.2}$$

To give a good description in the low η_{max} regions the fit was restricted to $\eta_{max} < 3$. A fraction of $f = 6.4\%$ was obtained, the data distribution together with the weighted MC samples is shown in Figure 4.3.

The data distribution at low η_{max} is after mixing well reproduced by the diffractive events generated by RAPGAP. However, the method used assumes a similar behaviour in x and Q^2 of the RAPGAP and DJANGOH cross section. Since this is not completely true the obtained mixing fraction f was varied by ±50% in the performed systematic studies (see section 9.4).

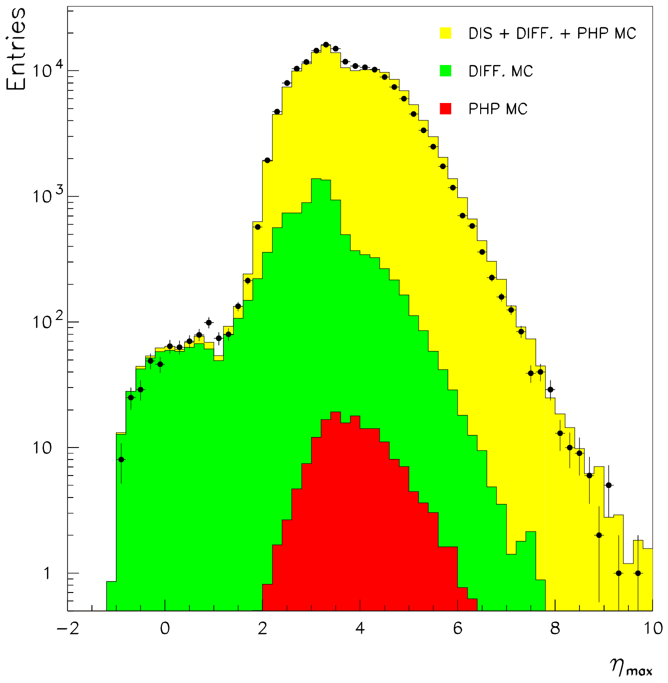

Figure 4.3: The η_{max} distribution of the sum of DJANGOH DIS, RAPGAP diffractive and HERWIG photoproduction Monte Carlo samples after mixing DJANGOH and RAPGAP events. The data is shown as points.

4.3 Photoproduction Monte Carlo Simulation

Photoproduction (PHP) events defined by $Q^2 \approx 0\,\mathrm{GeV}^2$ are events in which the positron is scattered under very small scattering angles escaping undetected through the beam hole. These events are a source of background even for this high Q^2 analysis when another particle is wrongly identified as scattered positron. In leading order QCD PHP can be divided in two processes. In the direct process the exchanged photon participates in the hard scattering whereas in the resolved contribution it acts as a source of partons. One parton emitted by the photon takes part in the hard scattering process. Both direct and resolved events were simulated with the event generator HERWIG 6.1 [62]. To reduce the number of to be generated events a filter at the generator level was used. The events were required to have either missing transverse momentum $P_t(had) > 6\,\mathrm{GeV}$ or a total transverse energy $E_t(had) > 30\,\mathrm{GeV}$ [2]. Both quantities are calculated excluding particles close to the beampipe, the polar angle of the considered particles had to be in the range $0.038\,\mathrm{rad} < \theta_{particle} < 3.081\,\mathrm{rad}$. Since the generation cuts and the cross section normalisation introduce some uncertainty a systematic check is assigned to the number of photoproduction events (cf. 9.4).

---

[2] The restriction in $E_T(had)$ is the important cut for NC analyses, the $P_T(had)$ cut was set because of a CC analyses using the same MC samples

Generator	Q^2 range (GeV^2)	Events	Luminosity $\mathcal{L}_{int}$ (pb^{-1})
DJANGOH	100-400	804790	115
	400-1250	205366	211
	1250-2500	49684	360
	2500-5000	17864	405
	5000-10000	24318	2000
	10000-20000	26162	10500
	20000-30000	22391	87000
	30000-40000	13470	310000
	40000-50000	12419	1400000
	>50000	14961	7000000
RAPGAP	100-400	84169	12.1
	400-1250	111721	115
	>1250	100724	500
HERWIG dir.	0	1100000	~450
HERWIG res.	0	3570000	~450

Table 4.1: Generated MC samples.

4.4 Detector Simulation

In order to compare the MC events produced by the previously described physics generator programs with the measured data the MC events were passed to a simulation of the ZEUS detector. The program MOZART simulates the response of all different detector components taking into account the exact geometry and inactive (dead) material. MOZART is based on the GEANT [48] package and was previously tuned with testbeam data and later enhanced with performance studies of the running ZEUS experiment. After MOZART the events are passed to ZGANA which simulates the three level trigger described in section 2.2.5. MC as well as data events are reconstructed with the ZEPHYR program resulting in the same format for both. ZEPHYR contains the reconstruction codes of the different components, at this stage physics objects like tracks (from single hits) are built and calibrations are applied.

4.5 Generated Event Sample

Table 4.1 shows the total amount of used Monte Carlo events for the e^+p analysis. The DJANGOH and the RAPGAP sample are divided into samples with different ranges of Q^2. In this way the MC statistical uncertainty becomes very small in higher Q^2 bins without producing a huge amount of events with low Q^2. The combination of these samples, produced in different Q^2 regions, is done by a reweighting procedure in terms of the generated luminosity with respect to the data luminosity.

Chapter 5

Trigger Preselection and Data Sample

The main uncertainty in the measurement of high Q^2 ($Q^2 > 800\,\mathrm{GeV}^2$) NC DIS cross section originates from the limited statistics in this kinematic range. Therefore a high efficiency of the trigger system is essential. NC DIS events are characterised by an isolated scattered positron in the detector. The main aim of the trigger is to identify this positron and reject background events. In this chapter the selection at the three trigger levels is discussed. The last section gives information about the used run range and the total amount of data used.

5.1 First Level Trigger

In the First Level Trigger (FLT) a decision, whether the event is a NC DIS candidate, is mainly done by checking energy thresholds. Depending in which calorimeter the positron is scattered different calorimeter requirements have to be fulfilled. In case the positron is scattered into the RCAL, it is triggered if the energy in the RCAL EMC (REMC) is larger than 3.4 GeV outside the first inner calorimeter ring (60 cm × 60 cm) or if the total RCAL EMC energy is larger than 3.75 GeV.

For larger scattering angles the positron ends up in the BCAL. Here events are triggered if the BCAL EMC (BEMC) energy is larger than 4.78 GeV. Since these positrons must have passed through large parts of the CTD a track is required in addition (at this stage tracks are reconstructed in a fast but not very sophisticated way). In this way backgrounds from halo muons are reduced. Halo muons are produced by collisions between protons and residual gas in the beampipe. Muons produced upstream of the detector move parallel to the proton beam axis and can enter the BCAL without passing through the CTD.

Positrons in the FCAL are triggered in a different way because of the more frequent energy depositions (by the colour flow between proton remnant and struck quark). These events can be triggered in two different ways: either by the high E_T trigger which requires a high calorimeter transverse energy E_T ($E_T > 30\,\mathrm{GeV}$ or $E_T > 11.6\,\mathrm{GeV}$ in combination with a track in the CTD) or by a total calorimeter EMC energy larger than 10 GeV. These different requirements ensure a high trigger efficiency in the whole ZEUS detector acceptance region.

The efficiency of the REMC (BEMC) trigger was determined with a sample of events which pass the high E_T trigger and all analysis cuts. For a sub-sample of events the scattered positron is found in the RCAL (BCAL) and therefore are expected to fulfil the requirements of the REMC

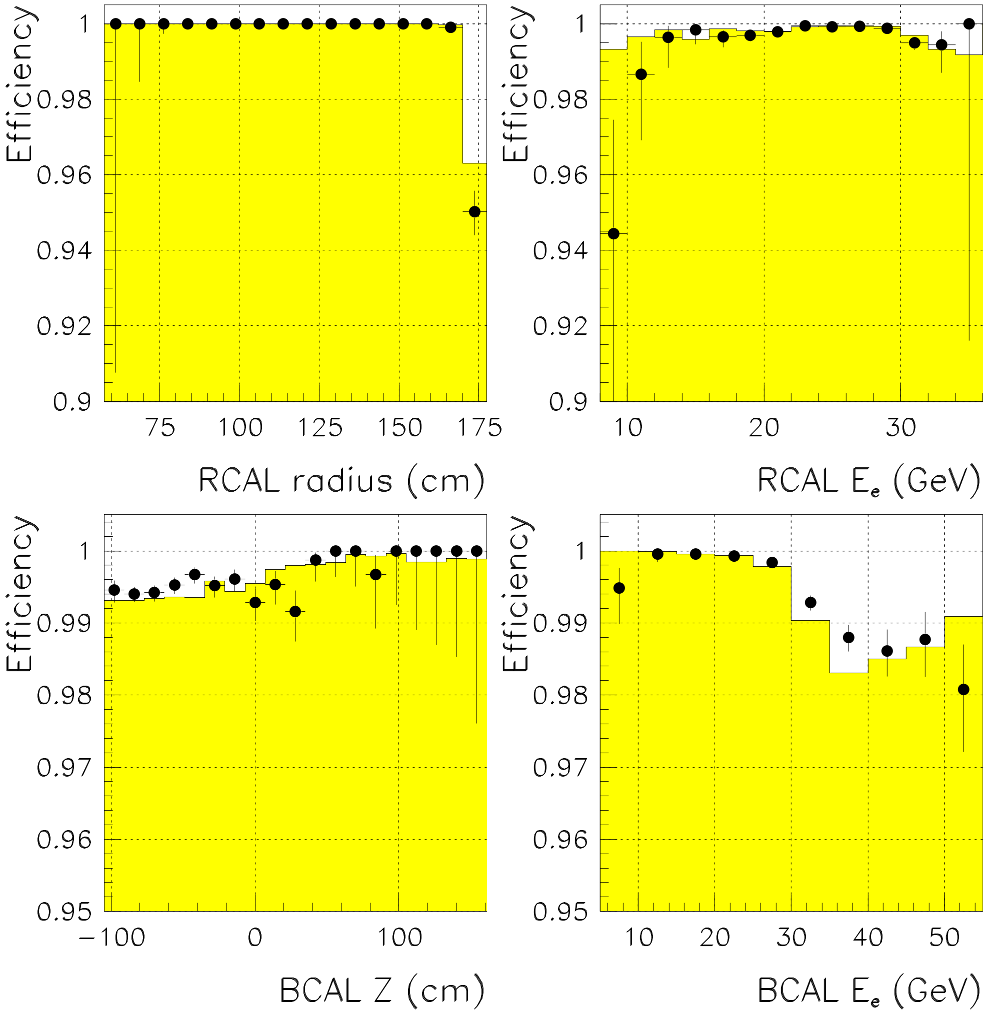

Figure 5.1: The two plots at the top show the efficiency of the REMC trigger versus the RCAL radius and the electron energy whereas the two bottom plots show the efficiency of the BEMC trigger versus the BCAL Z position and the electron energy. The data is shown as points whereas the MC is plotted as a histogram.

(BEMC) trigger. These events provide an unbiased sample to measure the REMC (BEMC) trigger efficiency shown in Figure 5.1 as a function of RCAL radius (BCAL Z position) and electron energy.

It can be seen from the figures that the agreement between data and MC in case of the EMC triggers is better than 1% in the whole region of RCAL as well as of BCAL and for electron energies above 10 GeV. At higher RCAL radii (radius > 175 cm) the trigger efficiency drops. Since the effect is larger in the data the final event sample is restricted to events with RCAL radius < 175 cm to ensure a good agreement between data and MC. More detailed trigger studies can be found in [64].

5.2 Second Level Trigger

On the Second Level Trigger (SLT) level a more detailed trigger selection is possible, since the full calorimeter information is available now. By use of the energy and momentum conservation a cut is applied on $E - p_Z$, the difference between the measured energy and the Z component of the momentum of all particles involved. The $E - p_Z$ in the initial state is given by:

$$(E - p_Z)_{initial} = 920\,\mathrm{GeV} + 27.5\,\mathrm{GeV} - (920\,\mathrm{GeV} - 27.5\,\mathrm{GeV}) = 55\,\mathrm{GeV}\,. \tag{5.1}$$

The value of $E - p_Z$ is conserved: $(E - p_Z)_{final} = (E - p_Z)_{initial}$. However, the measured $E - p_Z$, defined as:

$$(E - p_Z)_{meas.} = \sum_{i=1}^{Cal.Cells} E_i \times (1 - cos(\theta_i))\,, \tag{5.2}$$

where E_i and θ_i are the energies and polar angles (assuming the nominal vertex) of energy deposits in the calorimeter cells, can decrease if not all outgoing particles are detected. Whereas particles escaping through the forward detector beam hole have an $E - p_z$ value close to zero, particles leaving the ZEUS experiment through the rear beam hole reduce the measured $E - p_Z$ significantly. This is important for positrons scattered at low angles as well as for ISR photons radiated parallel to the incoming positron direction (see section 4.1). The SLT rejects events without a scattered positron, but keeps the ISR events by applying the cut:

$$(E - p_Z)_{meas.} + 2 \times (E_{\gamma,LUMIG}) > 29\,\mathrm{GeV}\,, \tag{5.3}$$

where the measured photon energy, $E_{\gamma,LUMIG}$, in the luminosity photon detector LUMIG (cf. section 2.2.4) is taken into account.

In addition the SLT applies several timing cuts in order to further reduce the amount of background events. Particles from proton beam gas interactions, which hit the RCAL before the protons have reached the interaction point, are cut out by demanding RCAL time larger than -8 ns (events from interactions in the centre of the detector occur at 0 ns, proton beam gas interactions peak at -10 ns [63]). Further the difference between FCAL and RCAL has to be smaller than 8 ns and all events with FCAL time larger 8 ns are cut out. Cosmic ray events hit the upper half of the detector 12 ns before hitting the bottom half. A cut at -10 ns on the asymmetry between up and down calorimeter time removes these events.

5.3 Third Level Trigger

At the level of the Third Level Trigger (TLT) the $(E - p_Z)_{meas.}$ is calculated again. This time the real event vertex determined by the CTD is used improving the resolution. Here a cut is placed at:

$$(E - p_Z)_{meas.} + 2 \times (E_{\gamma,LUMIG}) > 30\,\mathrm{GeV}\,. \tag{5.4}$$

Electron finding algorithms (similar to the one used offline, see 6.1) select events with high probability positron candidates. Only events with positron candidates of an energy larger than 7 GeV are triggered. In addition a box cut of $40 \times 40\,\mathrm{cm}^2$ in RCAL is applied to remove low Q^2 events.

5.4 DST Bit Selection

After the trigger selection further cuts are applied to the remaining sample. Only events with $Q^2_{DA} > 80\,\mathrm{GeV}^2$ and $y_E < 0.95$ are selected and used in this analysis. The indices DA and E denote the used reconstruction method, described in chapter 8. For all events which pass these additional cuts a special bit is set (DST bit12) to achieve an easy and fast identification.

5.5 The Data Sample

The e^+p data used in this analysis was taken in the years 1999 and 2000 and covers the run range 33125 to 37715. Some runs were excluded either by the standard ZEUS data quality routine EVTAKE or if in the data quality monitoring of the ZEUS Structure Functions/Electroweak working group a problem with a detector component was found which could cause a bias in the analysis. The used data set corresponds to an integrated luminosity of $63.2\,\mathrm{pb}^{-1} \pm 2.25\%$ [65]. As a comparison and for an extraction of the structure function xF_3 also the e^-p data taken in the years 1998 and 1999 was analysed. The e^-p analysis covers the run range 30768 to 32906 corresponding to an integrated luminosity of $15.9\,\mathrm{pb}^{-1} \pm 1.9\%$ [65].

Chapter 6

Measurement of Event Variables

This chapter summarises all event quantities and variables which have to be measured to reconstruct the kinematics of the event.

Figure 6.1 shows a typical candidate of a NC high Q^2 event visualised in ZEUS event display. To analyse the event the scattered positron has to be found first. In the shown event it is scattered back in the forward part of the BCAL. The algorithm for finding the electromagnetic cluster corresponding to the scattered positron is described in the first section. In the second section the measurements of positron energy, scattering angle and position are discussed. The remaining energy in the calorimeter not originating from the scattered positron belongs to the hadronic system. This consists of the current jet originating from the struck quark, the proton remnant which mainly escapes through the forward beam-hole and particles produced in the colour flow between the struck quark and the remnant. The hadronic event variables such

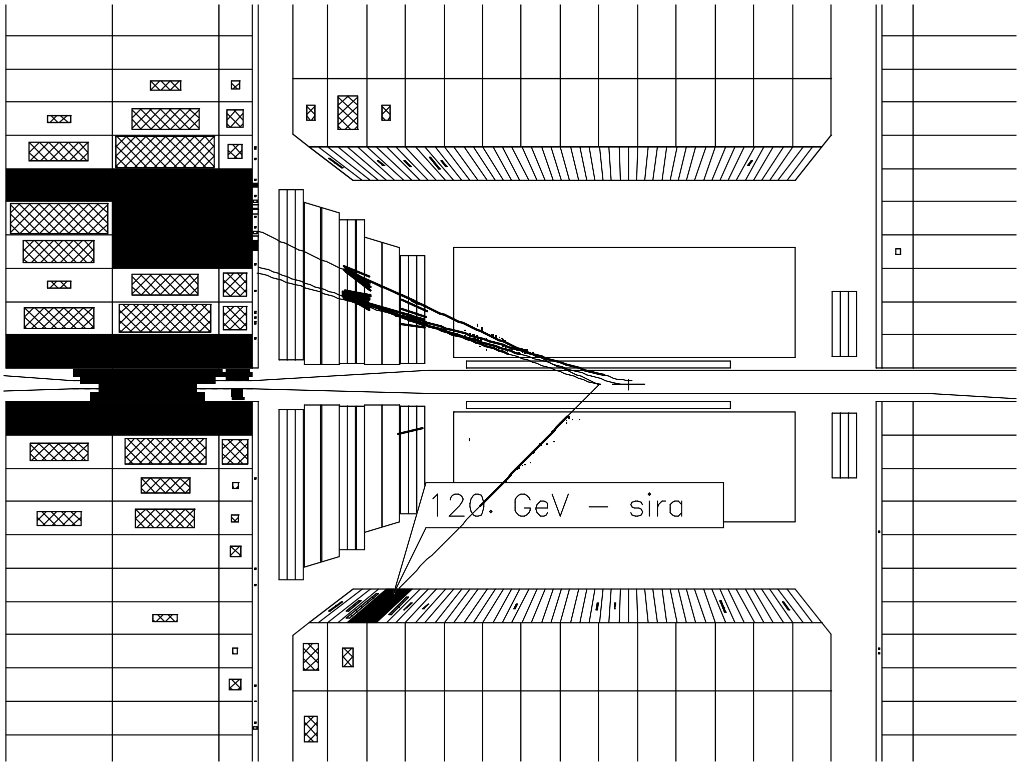

Figure 6.1: NC event ($Q^2 \approx 12000\,\mathrm{GeV}^2$) in the ZEUS detector as visualised by the event display.

as the four momentum of the whole hadronic system and the angle γ_h, which corresponds to the polar angle of the struck quark in the naive quark parton model, are subject of the third section. A precise reconstruction of the longitudinal interaction position (Z-vertex) is vital for the determination of the polar angles of the scattered positron as well as of the current jet. The measurement of the Z-vertex is the topic of the last section.

6.1 The Electron Finder

The scattered positron[1] is characterised by a localised energy deposition mainly in the electro-magnetic part of the calorimeter with little energy leakage into the hadronic part. In contrast, hadronic showers are usually transversely much broader and longitudinally much deeper. In addition usually the positron is well separated from the hadronic system, since due to energy and momentum conservation they balance each other in transverse momentum resulting in an azimuthal back-to-back event topology. Nevertheless the identification of the positron can be rendered more difficult by the presence of particles in the hadronic system with similar signature as the positron in the detector. The major background contribution comes from pions. The neutral ones mainly decay into two photons resulting in electro-magnetic clusters only slightly broader than the ones from positrons. In rare cases also charged pions can mimick an electro-magnetic energy deposition. Furthermore, possible interactions of the positron with inactive material between the interaction point and the calorimeter can cause the positron shower to become broader and more hadronic like. In this analysis the electron finder Sinistra95 [66] was used. After merging of neighbouring energy deposits into islands a neural net based program converts these islands into a probability for being a positron by analysing the shower shapes. The probability varies from zero (cluster is of hadronic origin) to one (cluster stems from positron). Within the CTD acceptance region an additional track requirement (an extrapolated track has to be found within 20 cm around the cluster position) is used in this analysis to increase the purity of the electron finder.

The probability distribution from Sinistra95 is shown for data and MC events in figure 6.2. The probabilities found in data are slightly smaller to the ones found in MC due to small differences in the shower development and shower shape. To reduce the number of background events all used events were required to have a probability $P_{si} > 0.9$.

6.1.1 Sinistra95 Efficiency of Isolated Tracks

A method was developed to study the efficiency of the electron finder Sinistra95 for isolated tracks [63]. In this method a sample of events triggered independent of any electron finder is used. High momentum isolated tracks in this sample are assumed to be the scattered positrons and therefore can be used to estimate the efficiency of the electron finder.

- Trigger Requirements. The used event sample was triggered by the FLT high E_T trigger (see section 5.1), by a trigger requiring a $Z_{vtx} < 60\,\text{cm}$ and $E - p_Z > 12\,\text{GeV}$ at the SLT level and by a trigger requirement of the transverse energy in the calorimeter (excluding the two inner rings in FCAL) above 25 GeV at the TLT, which ensures a selection independent of the electron finder.

---

[1] The electron finder identifies electromagnetic clusters belonging to the scattered lepton in case of both electrons or positrons. The name 'electron finder' is only historical.

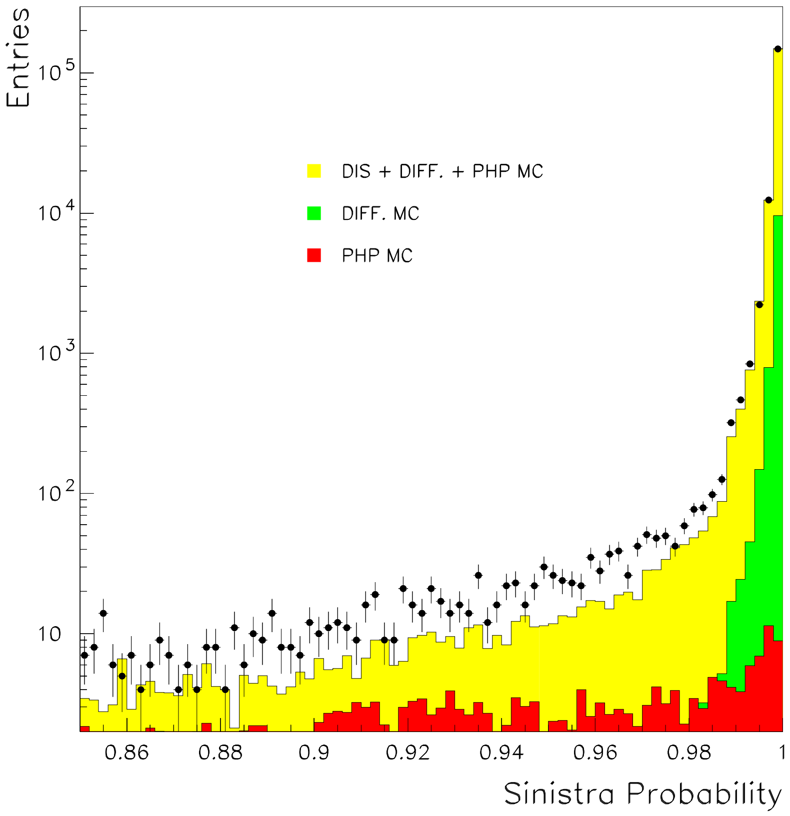

Figure 6.2: The electron probability calculated from Sinistra95. The data is shown as points whereas the MC is represented as histograms.

- Offline Requirements. Background events were rejected by excluding events with $E - p_Z < 44\,\mathrm{GeV}$ and $E - p_Z > 65\,\mathrm{GeV}$. Furthermore events with energies in the first three inner rings of RCAL above $0.464\,\mathrm{GeV}$ were excluded to ensure that no low Q^2 positron was in the rear direction. Events with exactly two electro-magnetic clusters were assumed to be QED Compton events and were therefore rejected.

- Track Isolation Requirements. In a first step only events with exactly one track with momentum greater $4\,\mathrm{GeV}$ and no other track within 90° in θ and ϕ with momentum greater than $0.5\,\mathrm{GeV}$ were selected. Furthermore it was required that no track is within 30° in θ and ϕ with momentum greater than $0.1\,\mathrm{GeV}$ of the found track.

The isolated track in the events passing the above criteria is assumed to be the positron. Obviously, the correctness of this assumption is vital for the determination of the electron finder efficiency. Therefore MC was used to study the purity of the isolated track sample. The purity is defined as the fraction of isolated track events in which this track is the positron and all isolated track events.

In Figure 6.3 the purity is shown as a function of the polar angle and the momentum of the track. Purities above 99.5% are achieved for high momentum tracks ($P > 15\,\mathrm{GeV}$) and polar angles between 1.0 rad and 2.6 rad. The positron found by the electron finder was considered the same, if the isolated track and Sinistra95 positron were within a cone of 30° of each other. In addition only Sinistra95 candidates with high probability $P_{si} > 0.9$ were used.

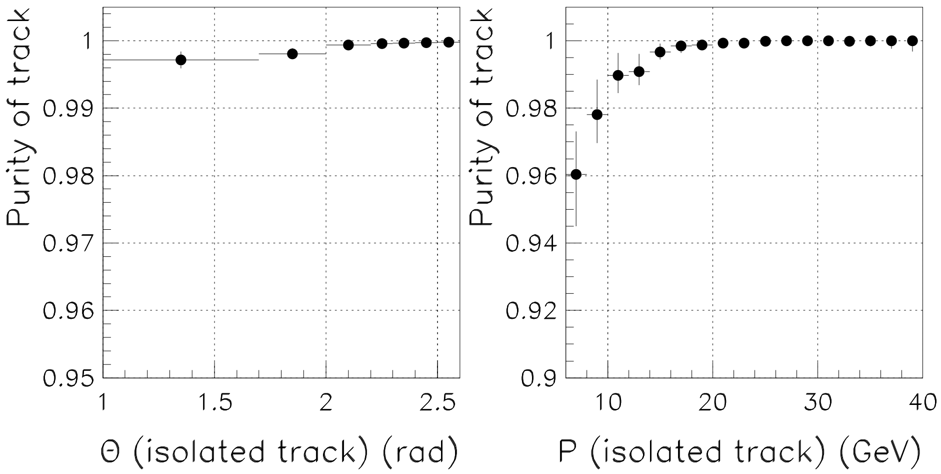

Figure 6.3: The purity of the isolated track event sample versus track θ and track momentum.

The efficiency of Sinistra95 versus the polar angle and the momentum of the isolated track is shown in Figure 6.4. In the range $1.0\,\text{rad} < \theta < 2.6\,\text{rad}$ and for momentum above 10 GeV the efficiency is determined to be larger than 99 %. Furthermore the agreement between data and MC is better than 0.5%.

Additional studies concerning Sinistra95 including also comparisons to other electron finder can be found in [67].

6.2 Energy, Angle and Position of the Scattered Positron

The energy of the measured final state positron can not only be used for kinematic reconstruction (see section 8.1), but is in addition used in the final event selection. Therefore its precise measurement and a good MC description of the data is necessary.

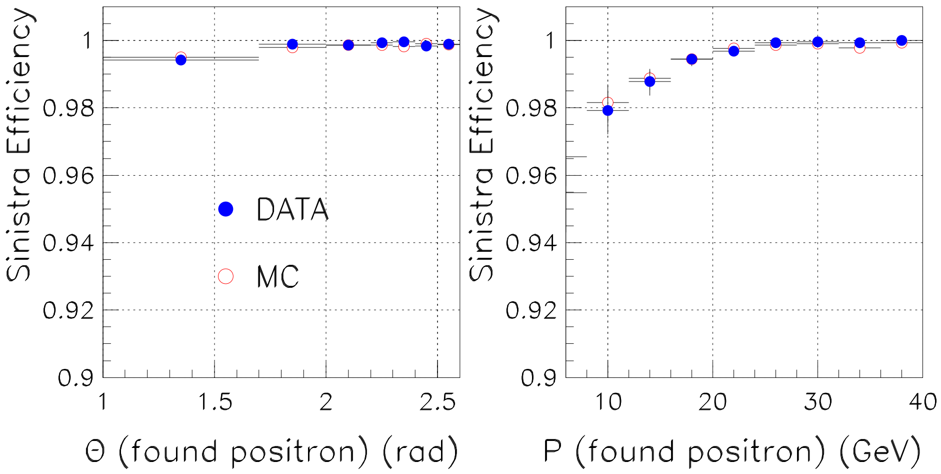

Figure 6.4: Efficiency of Sinistra95 in terms of polar angle and momentum of the isolated track.

To compare results of data and MC the energy scales have to agree. An energy measurement of a particle with a given energy should result in a similar effect in data and MC. Previous ZEUS analyses showed that the data had to be scaled up by 5% in case of energy depositions in BCAL and 2.2% in case of energy depositions in RCAL. This is done by the routine RCALCORR before any further analysis.

6.2.1 RCAL Corrections

In the majority of the events ($\approx 72\%$) used in this analysis the scattered positrons end up in the RCAL. Interactions with inactive material, such as the beampipe, screws and cables, between the interaction point and the calorimeter surface can create a shower of secondary particles and thus a part of the positron energy can be lost. The presampler (see 2.2.3) is used to correct for this effect in RCAL. The secondary particles deposit energy in the presampler (E_{pres}). This energy is measured in terms of the number of traversing minimal ionising particles (Mips), which is proportional to the energy loss. A correction to the raw calorimeter energy ($E_{e,raw}$) of the following form can be applied:

$$\begin{aligned} E_{e,corr} &= E_{e,raw} + E_{pres} \cdot C_{pres} \\ &= E_{e,raw} \cdot (1 + \frac{E_{pres}}{E_{e,raw}} \cdot C_{pres}) \\ &= E_{e,raw} \cdot C_{PRES} \,. \end{aligned} \tag{6.1}$$

The correction factors C_{pres} and C_{PRES} depend on the position in RCAL and are determined for data and MC separately. This was done in a previous analysis taking into account also events with lower values of Q^2. The method uses kinematic peak events where $E'_e \approx E_e$ and is described in [68].

The effect of the presampler correction is shown in Figure 6.5. Both data and MC distributions are shifted to the expected value. Since the energy resolution is worse in data, the measured MC energy was smeared in the whole UCAL region according to the data after all corrections in the following way:

$$E_{e,corr} = E_{e,raw} + rnd_{Gauss} \cdot (0.03 \cdot E_{e,raw}) \,, \tag{6.2}$$

where rnd_{Gauss} is a random number, distributed according to a Gaussian with width one. With smearing and presampler correction good agreement between data and MC is achieved. Since the electron energy is not used in this analysis for kinematic reconstruction, the slight remaining systematic difference between the corrected and the true energy in the MC was not further investigated.

6.2.2 BCAL Corrections

In approximately 28% of all events the positron is scattered into the BCAL. The fraction is indeed lower than in RCAL, but since these events represent higher values of Q^2 they are even more important in this analysis. The structure of the BCAL causes non-uniformities in the detector response. Cracks between towers and cells are less sensitive regions resulting in a loss of some energy fraction. On the other hand cracks between the 32 BCAL modules are more sensitive regions causing an overestimation of the energy. The scattered positron travels here parallel to the cracks depositing its energy mainly in the wavelength shifters. The effect of

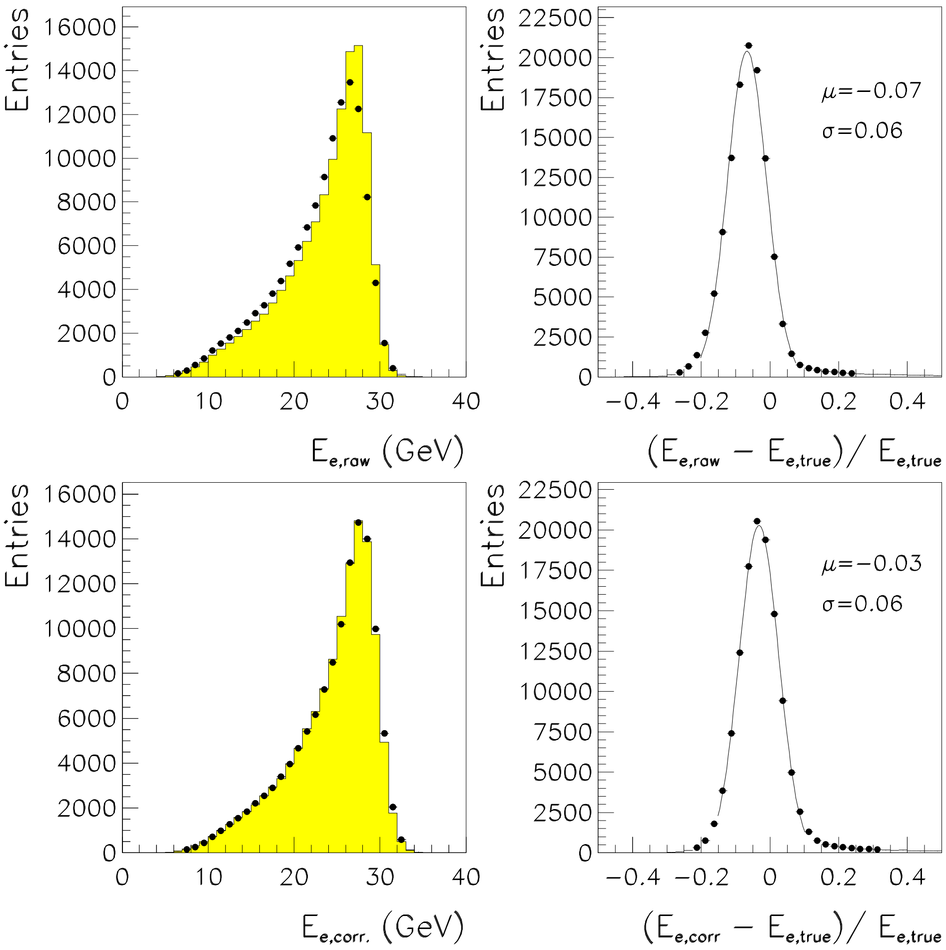

Figure 6.5: The measured energy of the scattered positron and the resolution in MC before and after applying presampler correction and energy smearing are shown. The plots on the left show the data as points whereas the MC is represented as a histogram. On the right the resolution of the energy is shown in MC. The values μ and σ denote the overall percental difference between the corrected measured and the true energy and the resolution respectively.

the non-uniformities depends on the inactive (dead) material in front of the calorimeter, since the shower of secondary particles smears the gap effect and a correction can only worked out taking into account both non-uniformities and inactive material. Such a correction procedure was developed using testbeam data together with MC studies [69]. The method uses the predicted (by the matched CTD track) calorimeter impact position to calculate the distances to the calorimeter cracks and applies a correction accordingly. A map containing the amount of inactive material was extracted from the MC and is used in both MC and data. The large number of positrons scattered into the BCAL due to the high luminosity used in this analysis allows a detailed check of this energy correction.

A non-uniformity independent way to measure the positron energy is E_{DA}, since only the scattering angles enter (see formula 8.9). E_{DA} is used to check the measured energy, the ratio between the raw measured calorimeter energy E_{raw} and E_{DA} is shown in Figure 6.6 as a

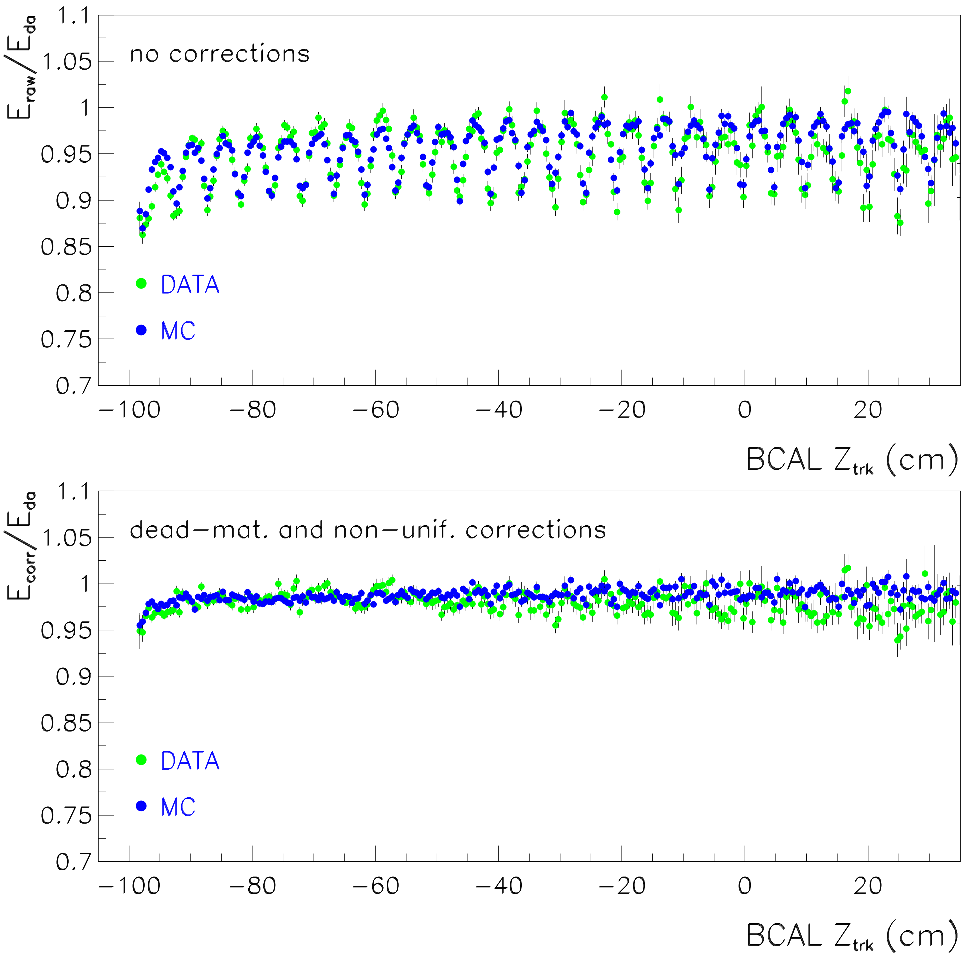

Figure 6.6: Effect of non-uniformities and their correction in BCAL versus the longitudinal impact position as determined from the track. The MC points are shown in black compared to the grey data points.

function of the longitudinal impact position in the BCAL. This position Z_{trk} was obtained by extrapolating the corresponding track to the surface of the calorimeter to avoid biases caused by the non-uniformities under study.

The cell cracks every 5 cm are clearly visible in the plot for both data and MC. Applying the correction routine results in a constant value of E_{raw}/E_{DA} close to one over the entire Z range of impact positions and data and MC agree well. The correction routine was not optimised in the region $-97\,\text{cm} < Z < -92\,\text{cm}$ since a lot of dead material in front of the calorimeter makes the correction very difficult. In this region the measured energy in data was scaled up by additional 2% to agree with the MC.

The measured energy of positrons in the module cracks is overestimated by $\sim 10\%$ as can be seen in Figure 6.7. The correction works very well for both data and MC and a constant value of E_{raw}/E_{DA} is achieved versus ϕ.

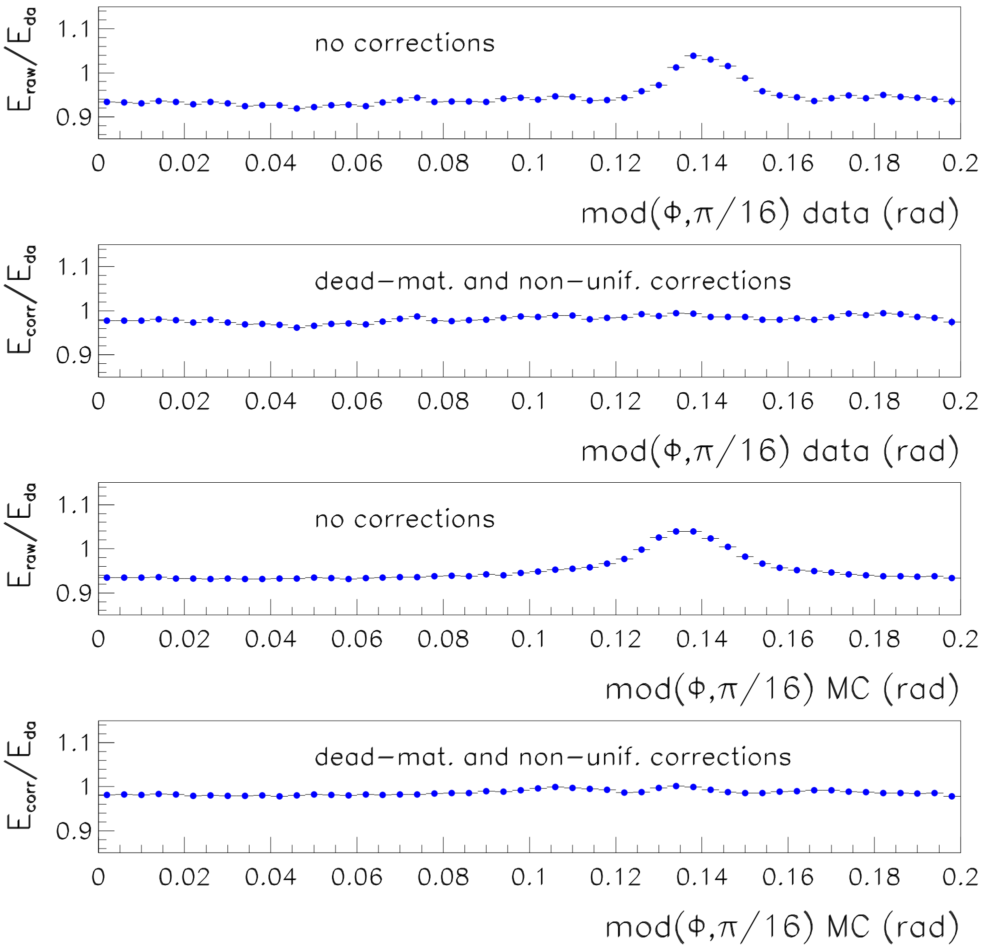

Figure 6.7: Effect of module cracks and their correction in BCAL versus the azimuthal positron scattering angle ϕ. The whole angular range 2π was divided into 32 sections of $\pi/16$ which are plotted on top of each other. The two plots on the top show the effect of module cracks and their correction in the data whereas the plots at the bottom show the MC.

6.2.3 Energy Scale Uncertainty

After applying all corrections an uncertainty in the knowledge of the energy scale is still expected. The way to determine this uncertainty is obtained by fitting distributions of $1 - E_{raw}/E_{DA}$ in bins of the BCAL Z position and E_{DA} with a Gaussian and comparing the mean values of the fit in data and MC. Figure 6.8 shows the result.

The comparison in bins of E_{DA} shows the agreement between data and MC to be better than 1% in the entire energy region. Nevertheless a detailed look in bins of the BCAL Z position confirms this good agreement in the case of higher positron energies ($E_{corr.} > 20\,\mathrm{GeV}$), but in the case of lower energies larger deviations are observed in the centre of the BCAL. An energy scale uncertainty of 1% for $E_{corr.} > 20\,\mathrm{GeV}$ and 1.5% for $E_{corr.} < 20\,\mathrm{GeV}$ seems therefore reasonable. These values are used in the systematic checks described in section 9.4.

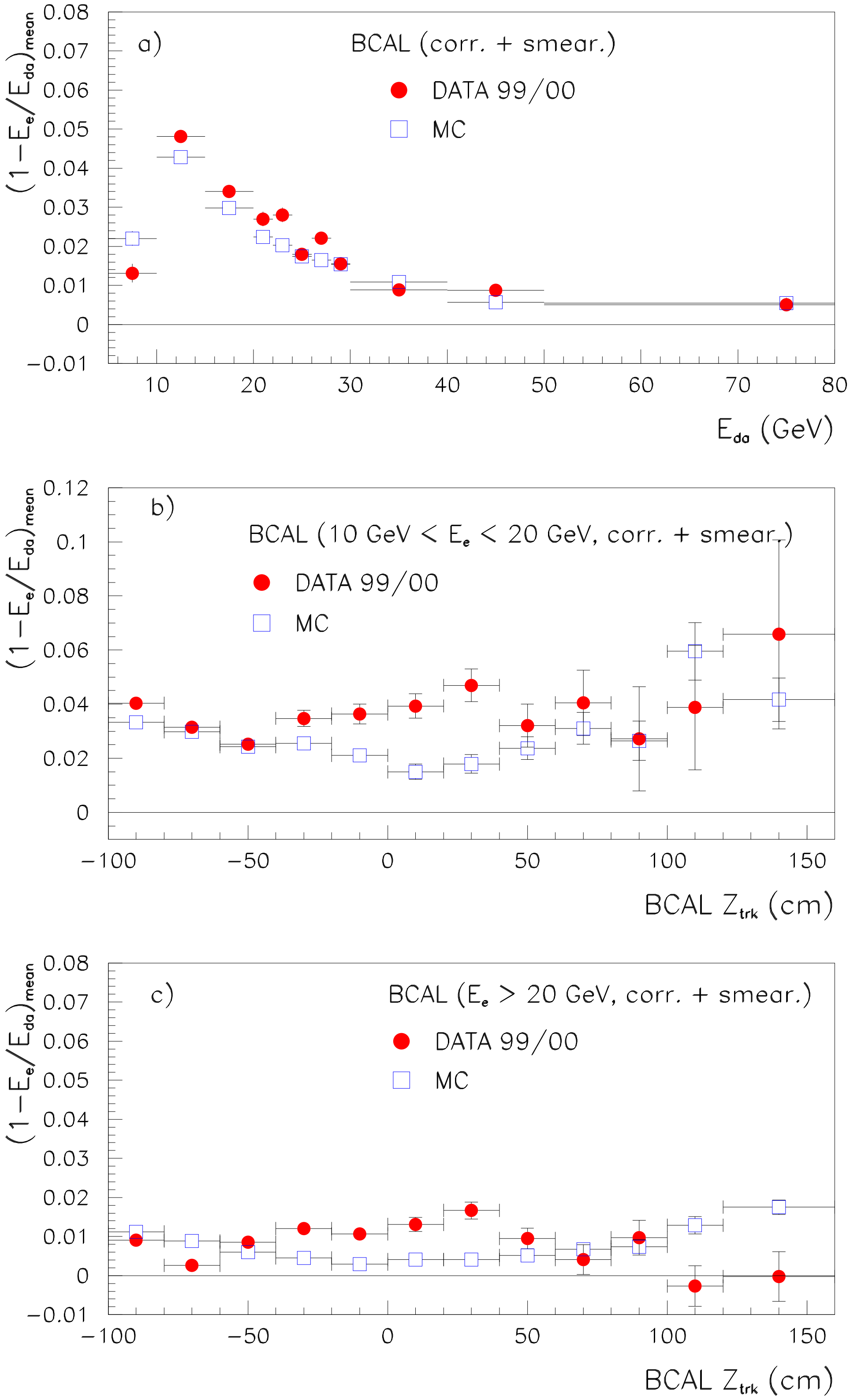

Figure 6.8: The mean value of a Gaussian fit to the distributions of $1 - E_{raw}/E_{DA}$ in bins of the BCAL Z position (shown for low (b) and high measured energies (c) separately) and E_{DA} (a) in data (points) and MC (squares).

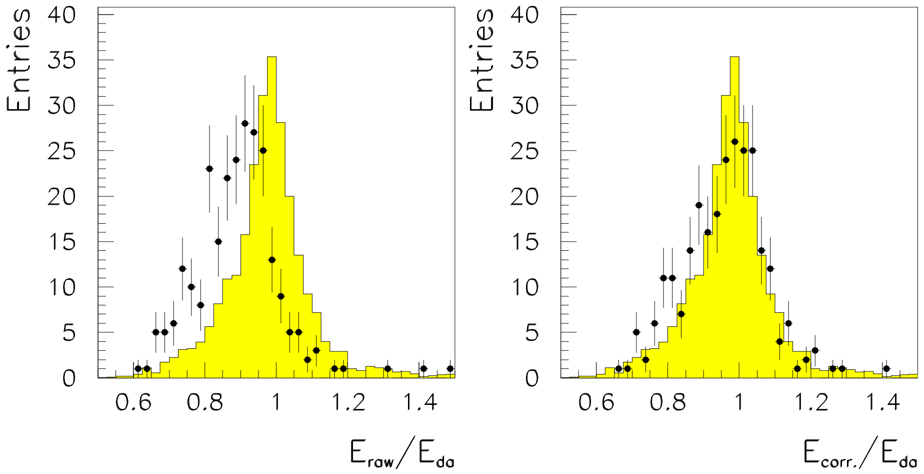

Figure 6.9: Ratio of E_{raw}/E_{DA} in FCAL for data and MC before and after scaling up the measured energy by 8.3% in data.

6.2.4 FCAL Corrections

Only in a very small fraction of the events ($\approx 0.15\%$) the positron is scattered into the FCAL. Due to the small number of events only a rough energy correction can be determined.

The distribution of E_{raw}/E_{DA} in the FCAL is shown in Figure 6.9 before and after scaling up the measured energy by 8.3% in data. This correction factor was obtained with a subsample of the events. Tighter cuts ($P_{si} > 0.99, DCA < 5\,\mathrm{cm}, P_{trk} > 15\,\mathrm{GeV}$ and $E_{CONE} < 2\,\mathrm{GeV}$, all selection cuts are discussed in section 7.5) as used in the usual event selection were applied to select events with a very clean signature. In this way biases in the calculation from background events i.e. photoproduction are avoided.

6.2.5 Positron Position

All scattered positrons were selected by requiring a track in the CTD (within the CTD acceptance). Usually this track is used to determine the scattering angles. Only in cases where the track was reconstructed with hits in three or less superlayers the calorimeter position was used to calculate the angles. The calorimeter position is determined by the routine ELECPO [70, 71]. The energy weighted position from the photomultipliers on the two sides of the cell is used to determine the X position whereas the Y position is reconstructed by the energy sharing between neighbouring cells. Before using the position reconstructed from the calorimeter a proper alignment of the calorimeters had to be performed. An extensive analysis was done for the 98/99 e^-p data period [72]. The obtained results were used also in this analysis since no changes in the positions are expected. Indeed a nice agreement in the positions of the calorimeter cracks can be seen in Figure 6.6 confirming a good alignment of the BCAL.

The reconstructed positron polar angle is shown in Figure 6.10. The data are very well described by the MC. The dips in the distribution at $\theta = 0.7\,\mathrm{rad}$ and $\theta = 2.3\,\mathrm{rad}$ originate from the supercrack cut explained in section 7.5.

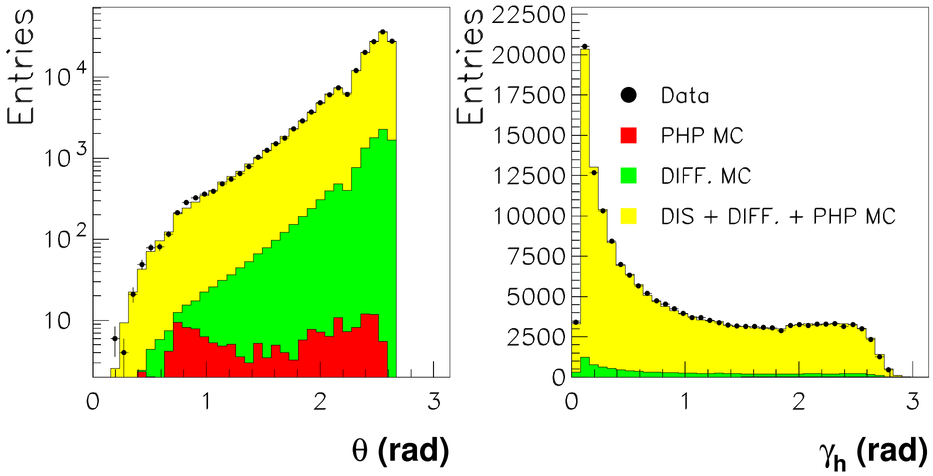

Figure 6.10: The left plot shows the reconstructed polar angle of the scattered positron. On the right the polar angle of the hadronic system γ_h is shown for data and MC.

6.3 Hadronic Event Variables

All calorimeter cells not belonging to the identified positron are regarded as belonging to the hadronic system. For the reconstruction at first noisy cells are removed. This is done on the one hand according to a given noisy cell list [73] containing all noisy cells for a given run number[2] and on the other hand by excluding all energy deposits less than 140 MeV in HAC sections and less than 80 MeV in EMC sections. In addition both photomultipliers reading out a calorimeter cell are checked for sparks. If both signals differ very much the corresponding cell is removed, since this is a signature of sudden, non particle related discharges in one of the photomultipliers. The remaining calorimeter cells are used for the calculation of the hadronic variables.

In the simplest possible approach the energies of all cells are added together. Caused by the scattering in inactive material in front of the calorimeter energy is lost. In addition the shower shape gets broader and therefore the energy is distributed over several cells which causes energy losses in cracks. This results in a worse resolution of the energy and the angle.

In this analysis a more sophisticated method is used in which the cells are clustered together in a two step procedure as described in detail in [74]. In each calorimeter and in each section (EMC, HAC1, HAC2) separately the cells are connected to the highest energy neighbouring cell. These so-called 'cell islands' are the input to the second stage where the 'cell islands' are merged into three dimensional 'cone islands' or just islands. The procedure of merging is based on the probability that the two considered 'cell islands' originate from one particle. This probability depends on the angular separation of the 'cell islands' and was extracted from single pion MC. The clustering is done from the outside towards the inside of the calorimeter allowing also the merging of EMC islands. Even a combination of cell islands in different calorimeter parts is possible if the particle traversed the BCAL before hitting the RCAL or FCAL.

The found calorimeter islands are used to determine the four momentum of the hadronic system after applying corrections for three different effects. The first effect concerns positions of the

---

[2] The noisy cell list is determined with random triggered runs.

energy depositions which are shifted from the original particle direction by the detector itself. Particles which are back-scattered from the calorimeter surface and thus are hitting a different part of the calorimeter are called backsplash. Backsplash as well as scattering and showering in inactive material in front of the calorimeter can cause energy depositions far apart from the original direction of the particle. These islands would cause an overestimation of γ_h and have to be excluded. The applied correction method [75] excludes low energy islands ($< 3\,\mathrm{GeV}$) if their polar angles are larger than a threshold value γ_{max}. γ_{max} is a function of γ_h and was derived using MC. Since the variation of γ_{max} changes γ_h, an iterative procedure is necessary which is continued until the changes in γ_h are small enough.

The second effect which is corrected for is the energy loss due to interactions in the inactive material in front of the calorimeter. The correction is applied as a function of the passed number of radiation length X_0 in front of the found island. Therefore the dead material maps, which were mentioned in the previous section concerning positron energy, are used. Finally a correction for energy loss in calorimeter cracks is applied.

The reconstructed γ_h is shown in Figure 6.10. The data is well described by the MC in the whole angular range.

6.4 Measurement of the Longitudinal Interaction Point

The interaction point along the Z-axis, the so-called Z-vertex, enters in the determination of both positron scattering angle θ and the angle of the hadronic system γ_h and therefore has to be reconstructed as precise as possible. The origin of the Z-vertex distribution can be explained by HERA machine parameters which is described in the first of the following paragraphs. After that the vertex finding and reconstruction is presented. The measurement of the vertex depends on the calorimeter acceptance which is itself a function of the longitudinal interaction point. To achieve a good MC description the acceptance-corrected and therefore unbiased vertex distribution has to be determined and used as an input to the MC. This procedure is described in the last paragraph.

6.4.1 The Origin of the Z-Vertex Distribution

The accelerator is filled with 210 bunches of each positrons and protons. The particles in the bunches are approximately Gaussian distributed. However, the longitudinal widths are different, $\sigma_{Z,P} \approx 170\,\mathrm{mm}$ in the proton case compared to only $\approx 8\,\mathrm{mm}$ for positron bunches. When both bunches are collided with similar velocities it is expected that the Z-vertex distribution is also Gaussian like with a width of $\approx 0.5 \cdot \sigma_{Z,P}$ centred at the nominal interaction point. In addition the beam structures give reason for other interaction points as described in the following.

The accelerating radio frequency for the proton (positron) bunches is 20 (48) times higher than the interaction frequency of 10.42 MHz (corresponding to the interaction rate of 96 ns). This causes a bucket structure in which only one of the 20 (48) buckets is filled with the proton (positron) particle bunch. Since each bucket is in the same phase, it is accelerated in the same way. Therefore particles which accidently entered in neighbouring buckets in the filling procedure of the storage ring, precede or follow the nominal bunch with a distance of $d_{pro} \approx 96\,\mathrm{ns}/20 \cdot c \approx 144\,\mathrm{cm}$ for the protons and $d_{pos} \approx 96\,\mathrm{ns}/48 \cdot c \approx 60\,\mathrm{cm}$ for positrons.

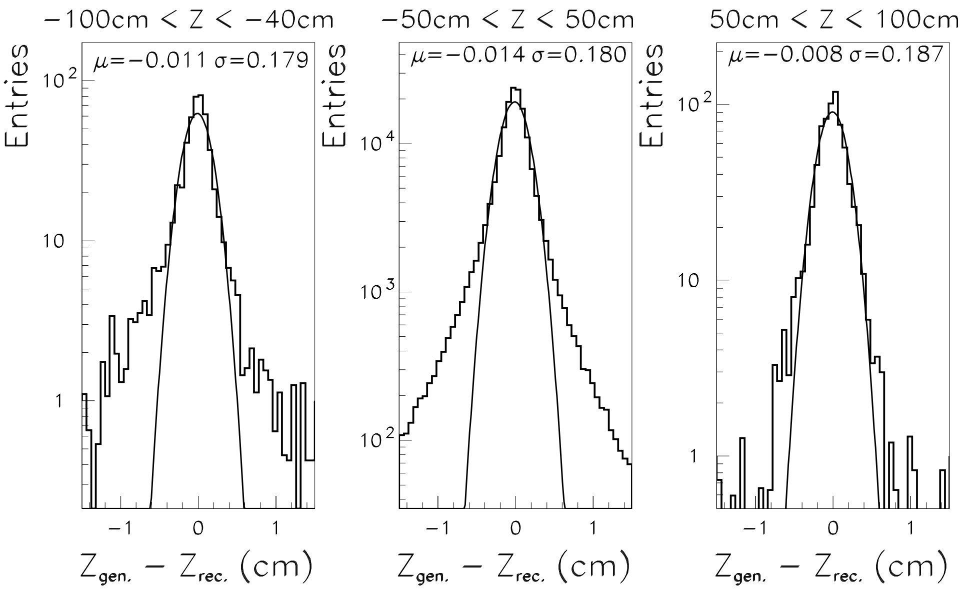

Figure 6.11: Z-vertex resolution of the CTD in three bins of the generated longitudinal interaction point. Shown is the difference between generated Z-vertex position ($Z_{gen.}$) and the reconstructed one ($Z_{rec.}$). Each distribution was fitted with a Gaussian, mean (μ) and width (σ) of the fit is also shown in the plots.

These so-called satellite bunches can collide with the nominal bunches causing interactions in Z-direction around $\pm 0.5 \cdot d_{pro}$ and $\pm 0.5 \cdot d_{pos}$. Since the densities in the satellite bunches are much smaller than in the nominal ones these kind of collisions are rare and a collision of two satellite bunches is even more seldom.

Compared to the longitudinal dimensions, the transverse sizes are very small for both proton and positron bunches. The width of the vertex distribution in X and Y are $< 1.5\,\mathrm{mm}$.

6.4.2 Vertex Finding and Reconstruction

All reconstructed tracks in the CTD are used to obtain the vertex position by using a fit. Some modifications from the simplest approach of fitting all tracks to one vertex had to be done to improve the resolution. Particles coming from the interaction point can create a bunch of particles by interacting with the beampipe wall or the inner wall of the CTD . The tracks of these secondary particles will point to the beampipe causing a large variation from the original vertex. To account for this the fitting procedure allows more than one vertex. First the proton direction (positive Z axis) is used as a seed to a vertex fit then all tracks which did not improve the fit are excluded. These excluded tracks are used for a second vertex fit. Another modification concerns the positron. When the scattered positron, which has to come from the vertex, is found, its track is used as a seed for the primary vertex. This improves the vertex resolution especially in cases where the tracks of the hadronic system are short or have low polar angles. This analysis demands a good vertex, when no vertex fit was successful the event is excluded.

The Z-vertex resolution of the CTD, as modelled in the MC, is shown in Figure 6.11 in rear, central and forward region. In all parts a similar resolution of 1.8 mm was found.

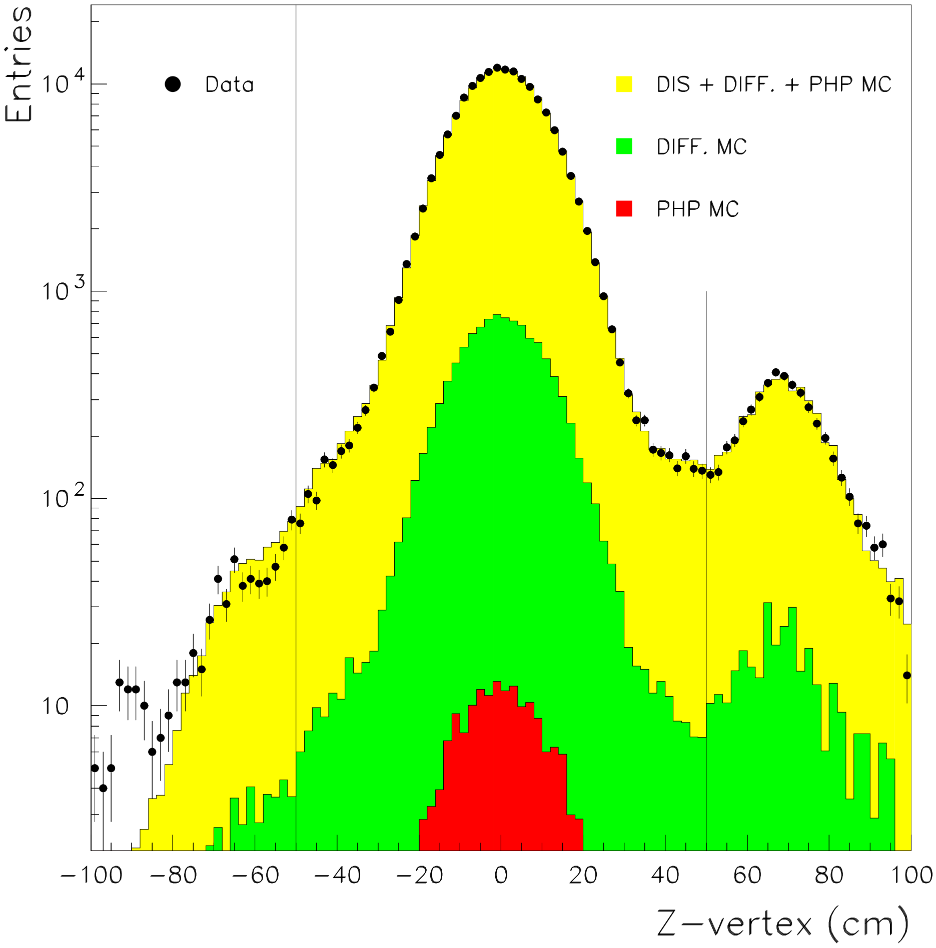

Figure 6.12: Distribution of the measured Z-vertex in data and MC. The contributions from different event types in MC are shown with different colours. The lines indicate the region of events used in this analysis.

The data and MC Z-vertex distribution can be seen in Figure 6.12. The distribution shows the dominating main peak centred at the nominal interaction point, but also contributions from satellite bunches are visible (most obvious at $Z = \pm 70\,\mathrm{cm}$). Very good agreement between data and MC was obtained. Although only events in the region $-50\,\mathrm{cm} < Z < 50\,\mathrm{cm}$ are used in this analysis a good MC description is also needed in the main satellite peaks due to the luminosity measurement. The luminosity measurement considers not only events originating from the central peak. Therefore a difference in the height of the satellites would cause normalisation problems. The small number of data events at very low Z positions not described by MC are wrongly reconstructed low Q^2 events. The usage of MC samples with lower Q^2 cut would fill this tiny gap.

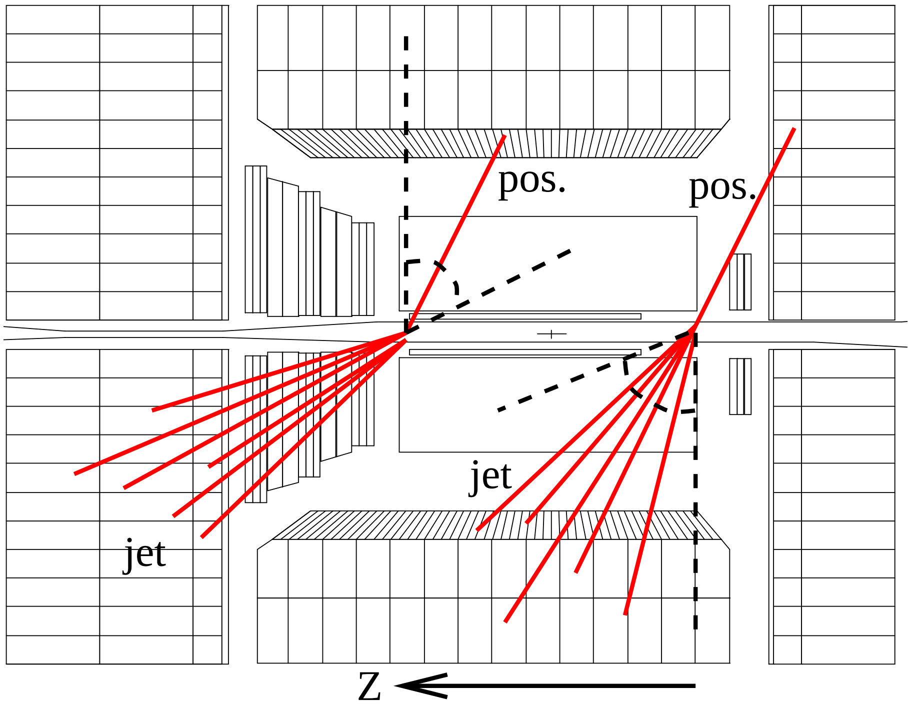

Figure 6.13: Schematic sketch of DIS events in different CTD acceptance regions. Shown are the tracks from the positron (pos.) and the jet. The dashed lines indicate the used angular ranges for θ (event on the left) and γ_h (event on the right).

6.4.3 The Monte Carlo Event Vertex Distribution

The shape of the Z-vertex distribution, as seen in Figure 6.12, depends on the used run range since the beam conditions, i.e. the filling of neighbouring buckets, may change in time. Therefore the MC distribution has to be derived from the used data sample. However, detector and therefore also trigger acceptance depend on the Z-vertex resulting in a biased measurement of this quantity. Thus the true, underlying vertex distribution is different from the measured one. This section describes a method to extract an unbiased vertex distribution from the data which was used as an input to the MC. Only in this way the acceptances can be examined and a comparison of data and MC is meaningful.

The presented method was already used in previous analyses [63]. Analysis cuts were placed in a way to achieve a data subsample with a selection efficiency independent from the Z-vertex. Besides demanding an electron energy above 10 GeV and a value of $E-p_Z$ in the range between 35 GeV and 65 GeV to ensure high trigger acceptance and the event to be DIS like ($E-p_Z$ close to 55 GeV), the main selection is done via the positron polar scattering angle θ and the polar angle of the hadronic system γ_h. The chosen angular ranges are shown in case of two extreme values in Figure 6.13 in the ZEUS detector.

Essential for a precise measurement of the vertex are first of all tracks in the CTD. In addition tracks perpendicular to the CTD wires will give a better precision than almost parallel tracks. To make sure that tracks are in the CTD even if the event vertex is close to the forward end of the CTD acceptance, the angle of the scattered positron was restricted to:

$$90^\circ < \theta < 146^\circ, \tag{6.3}$$

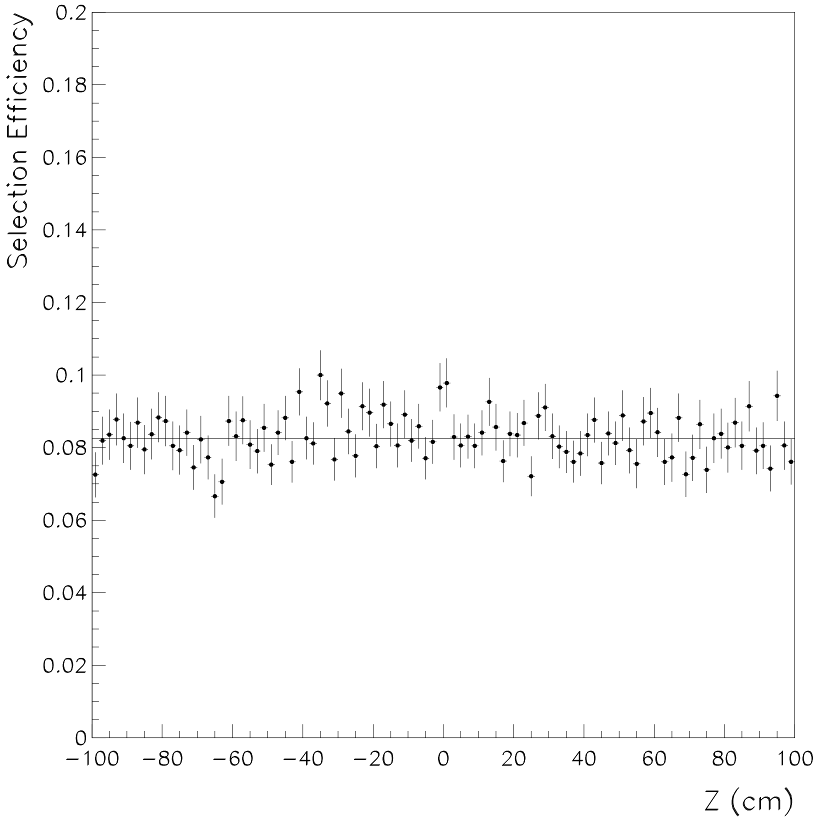

Figure 6.14: Selection efficiency of the applied cuts (explained in the text) as a function of the generated Z-vertex for the extraction of the unbiased vertex distribution. The line represents the average value.

(compare to the left event in Figure 6.13). On the other hand tracks in the CTD also at very low Z-vertices are guaranteed by the selection:

$$27.5^\circ < \gamma_h < 90^\circ. \tag{6.4}$$

This time the tracks belong to the hadronic jet (compare to the event on the right in Figure 6.13). A MC sample, generated with a uniform Z-vertex distribution was used to check if the selection efficiency of the events passing the cuts described above is independent of the Z-vertex.

Figure 6.14 shows that the selection efficiency is uniform along the Z direction, no large deviations are observed for different CTD regions proving the applicability of the method. After extracting the underlying Z-vertex distribution in the data a fit taking into account five Gaussians and one common offset was performed to extract a smooth curve for the MC generation. Both data and the corresponding fit[3] are shown in Figure 6.15.

The distribution fitted by five Gaussian reflects nicely the expected distribution (comp. section 6.4.1). Besides the main peak at $Z = 0\,\mathrm{cm}$, the additional peaks originating from the satellites bunches can be identified. The obtained curve is used as an input in the ZEUS MC generation

---

[3] The fit was done with 14 free parameters. The inner two and the outer two satellites were fitted with the same width.

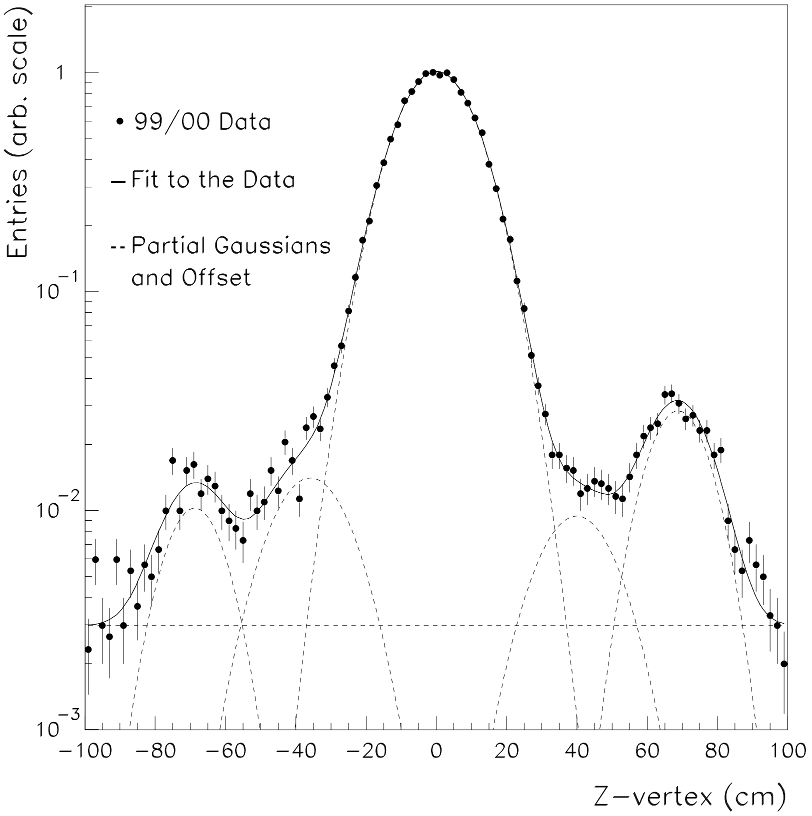

Figure 6.15: The underlaying data Z-vertex distribution was fitted with five Gaussians and one offset. Shown is the data with the resulting fit which was used as an input to the MC simulation.

for the 1999/2000 data period since January 2001. Since the MC used in this analysis was generated earlier a reweighting routine is used to modify the previously generated MC distribution to the one determined here.

The applied procedure introduces a systematic uncertainty of the vertex distribution which is now included in the MC. As a check the fit is systematicly changed, the satellites on the right (left) are scaled up (down) by three σ of their fitted height, corresponding in a change in height by $\approx 15\%$ for the highest satellite (located at $Z = 69\,\mathrm{cm}$) and $\approx 26\%$ for the others. For each of the systematic changes the other three Gaussians are fitted again resulting in slightly different fitted Z-vertex distributions. These curves are used to estimate the systematic uncertainty.

Chapter 7

Background Suppression and Event Selection

After the description of the trigger preselection and the explanation of the measurement of the event variables this chapter presents the final event selection. The selection is done by applying analysis cuts which should remove or at least reduce the background events. Background events usually occur when particles are wrongly identified as the scattered positron. After a description of several sources of background events the chapter ends with a presentation of the applied analysis cuts, designed to improve the purity of the data sample or, if possible, to reject background events completely.

7.1 Photoproduction Events

Photoproduction events are the most serious source of background. They are defined as events with $Q^2 \approx 0$ with an exchanged photon almost on mass shell. The positron is therefore scattered with very low angles (large θ) and escapes the detector through the rear beam-hole. These events are selected when a photon or a pion is misidentified as a positron. Because of its Q^{-4} dependence (see equation 1.8) the cross section is very high in case of these lowest Q^2 events. Therefore the background contamination is potentially high and its determination has to be done with great care. An effective way to reduce the amount of events originating from photoproduction is to exclude events with a low value of $(E - p_Z)$. As already discussed in section 5.2 the expected value of 55 GeV is reduced when the positron is not detected in the calorimeter by two times the positron energy. In addition cuts on the probability derived from the electron finder to be a positron and the measured energy of the chosen positron candidate can further reduce photoproduction events. Usually both probability and energy are lower than for DIS events. Nevertheless a certain fraction of photoproduction events can not be distinguished from DIS events. MC (cf. section 4.3) is used to estimate the number of photoproduction events in the data sample which are then statistically subtracted. The normalisation between data and MC is determined with the positron taggers outside the main ZEUS detector. For such an analysis the acceptance of the tagger is the crucial parameter. The detailed study of the photoproduction normalisation in the 99/00 data is described in [64]. The assigned systematic error reflects its uncertainty (cf. section 9.4).

7.2 Background from Cosmic Rays

Cosmic rays, mainly high energetic protons, produce pions in the atmosphere of the earth which decay into muons. These muons are a source of background in the used event sample. By crossing the BCAL the muon can deposit some energy in the EMC section e.g. by radiating a photon and together with the created track in the CTD this is wrongly reconstructed as a scattered positron. The hadronic system is reconstructed on the basis of the energy deposits in the calorimeter which are deposited after the muon has crossed the whole CTD. Although this kind of events is usually rejected in the SLT by timing requirements (see section 5.2) some events still pass the trigger. However, the muon energy deposits are asymmetrically in the top and bottom halves of the BCAL and therefore in contrast to the balance of transverse momentum in DIS events the vector sum $p_{T,tot}$ of all $p_{T,i}$ of all energy deposits i is large compared to the scalar sum $E_{T,tot}$ of $p_{T,i}$.

$$p_{T,tot} = \sqrt{(\sum_i p_{X,i})^2 + (\sum_i p_{Y,i})^2} \tag{7.1}$$

$$E_{T,tot} = \sum_i \sqrt{p_{X,i}^2 + p_{Y,i}^2} \tag{7.2}$$

Thus a restriction to low values on $p_{T,tot}/E_{T,tot}$ or $p_{T,tot}/\sqrt{E_{T,tot}}$ (taking into account the calorimeter energy resolution dependence on $1/\sqrt{E_{T,tot}}$) can be used to reject background originating from cosmic rays. The remaining contamination is negligible.

7.3 Beam Related Background

The positron or proton beam can interact with gas molecules in the beampipe (beam gas)[1]. Proton beam gas interactions are not similar to DIS events and usually are not selected due to a low value of $E - p_Z$. Positron beam gas events cannot be distinguished from DIS events in general due to the presence of the scattered positron. Nevertheless the low available centre of mass energy of these events prevents them to have a high enough value of Q^2 to be considered in this analysis. This was confirmed by looking for events originating from positron pilot bunches, in which a positron bunch collides with an almost empty ($< 1\,\mathrm{mA}$) proton bunch.

57 events were found in this analysis but all looking DIS like, originating from a collision with one of the few protons still in the bunch. These events were excluded because the luminosity measurement does not take pilot bunches into account. No proton pilot bunch events were found. Overlay events (in which the detected energies correspond to two events) usually have a very high value of $E - p_Z$ and an upper limit of the accepted $E - p_Z$ range removes such events.

7.4 QED Compton Events

Radiative processes as ISR and FSR are calculable by QED and are included in the MC (see section 4.1.1 and 9.2). Nevertheless a specific class of radiative events has to be removed from

---

[1] The pressure in the beampipes is about 10^{-9} bar.

the data sample since they are a source of background which is not simulated in the MC. The emission of a hard photon not collinear with the emitting positron (see Figure 4.2) can change the reconstruction of the kinematic variables dramatically. Therefore such QED Compton events have to be considered as a source of background also in a high Q^2 analysis although the QED Compton cross section peaks at $Q^2 = 0\,\mathrm{GeV}^2$. The events can be elastic or quasi elastic whereby there is no proton dissociation or at least no measured energy in the forward parts of the calorimeter. On the other hand the events can be inelastic with energy deposition in the calorimeter originating from the proton. The hard photon is falsely considered to belong to the hadronic system which causes usually a migration of the hadronic angle γ_h to higher values. Elastic and quasi elastic QED Compton events are efficiently excluded by searching for two electromagnetic clusters balancing each other in transverse momentum and only small additional energy deposition in the calorimeter ($< 3\,\mathrm{GeV}$, such events are absent in MC). The energy deposit of the dissociated proton makes an efficient identification of inelastic events more difficult and therefore the events can not be easily separated from usual DIS events. Similar to ISR and FSR events the exclusion of such events is not necessary, if the inelastic QED Compton events in the used MC (generated with HERACLES) describe the data. The performed study is shortly described in the next section.

7.4.1 Inelastic QED Compton Events in Data and MC

To separate the small number of QED Compton candidates (their fraction in the MC is less than 0.5%) events were selected in which the electron finder found two electromagnetic clusters with probabilities $P_{si} > 0.85$. The sample was further restricted to events where only for one of these candidates (the scattered positron) a corresponding track was found. Therefore regions close to the beampipe had to be excluded since there tracks can not be measured. Thus only particles which passed the CTD within a radius of at least 35 cm were considered. Additional selection cuts are necessary to improve the purity of the considered event sample (with still reasonable efficiency).

- Usually the photon polar angle is large (cf. Figure 4.2). Events were required to have $\theta_{photon} > 1.0\,\mathrm{rad}$.
- Photon and positron are separated in the azimuthal angle. Events with $\phi_{e-photon} < 2.5\,\mathrm{rad}$ were excluded.
- The majority of the QED Compton events has only one good track (passing more than 3 superlayers) which is the track of the positron. Only these events are used in this study.
- The sum of the energies of the two electromagnetic candidates E_{sum} is usually close to or larger than 27.5 GeV. Therefore a lower energy threshold was introduced at $E_{sum} = 25\,\mathrm{GeV}$.

In Figure 7.1 the energy and angular distributions used for the event selection are shown. The selected sample has the following properties:

- Purity: 76% of the selected MC events are QED Compton events. Additional 18% are ISR events. These events have a similar signature as the QED Compton events, they originate from the transition region between ISR and QED Compton MC definition.

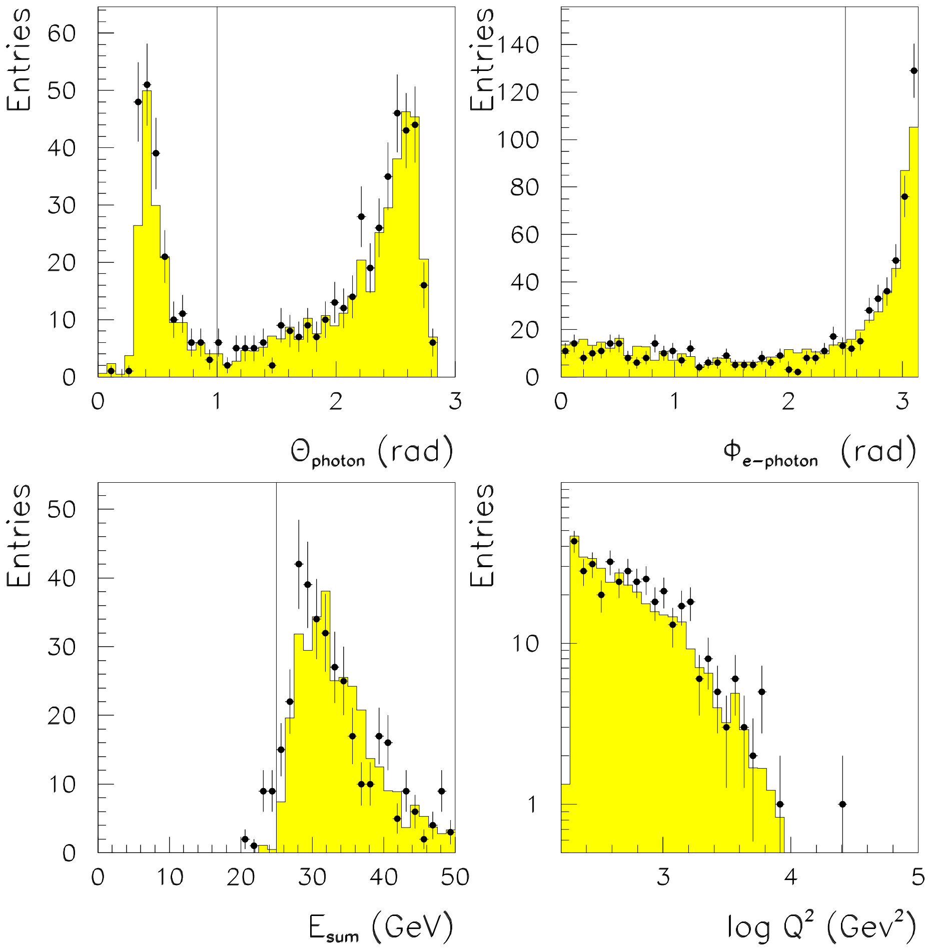

Figure 7.1: QED Compton candidates in data and MC. Shown are the polar angle of the photon θ_{photon}, the difference in the azimuthal angle $\phi_{e-photon}$, the energy sum of the two electromagnetic candidates E_{sum} and the distribution in Q^2 of the selected events in data (points) and DJANGOH MC (histograms). The lines indicate the selection cuts which are needed to improve the purity of the event sample as discussed in the text.

- Efficiency: 50% of all MC QED Compton events in the here presented high Q^2 analysis are selected with the cuts described above.

- Comparison between data and MC: the data are reasonably described by the MC (the normalisation was done in the usual way according to data and MC luminosity). The difference in the number of the selected events is $\sim 5\%$ which is within the statistical uncertainty. One event in the data with a reconstructed value of $Q^2 = 27300\,\mathrm{GeV}^2$ was found not predicted by the MC. This event has to be regarded as a statistical fluctuation.

Since this subsample shows a reasonable agreement between data and MC QED Compton candidates, it is not necessary to exclude these events.

7.5 Final Event Selection

After the preselection (discussed in chapter 5) and the measurement of the event variables including the applied corrections (see chapter 6) the final event sample is selected. Most of these restrictions were motivated in the previous chapters and sections. They were chosen to increase the purity and quality of the selected sample. The events considered in this analysis had to fulfil following criteria:

- Electron finder probability $P_{si} > 0.9$. Below this threshold the fraction of photoproduction events dominates (see Figure 6.2)
- Positron energy: $E_e > 10\,\mathrm{GeV}$. This guarantees a high trigger and electron finder efficiency (see Figures 5.1 and 6.4) and further reduces background from photoproduction.
- Energy not assigned to the positron in an $\eta - \phi$ cone of radius 0.8 around the found positron $E_{CONE} < 5\,\mathrm{GeV}$. This cleans the sample from events where the positron is wrongly identified in a hadronic energy cluster. The pseudo-rapidity $\eta = -\ln(\tan(\theta/2))$ is used since differences in η are invariant to boosts along the Z-direction. In addition this cut removes effects of remaining noisy cells which were not yet corrected.
- Position of the vertex in the central region of the CTD: -50 cm< Z < 50 cm. This selection restricts the events to occur in a region where CTD and calorimeter acceptance are well understood.
- Ratio of vector and scalar sum of transverse momenta $p_T/\sqrt{E_T} < 4\sqrt{\mathrm{GeV}}$. This cut reduces background mainly from cosmic rays.
- Rejection of quasi elastic and elastic QED Compton events (cf. section 7.4).
- Radius of the positron position if it is found in the RCAL: $R < 175\,\mathrm{cm}$. The simulation of the RCAL region which is shadowed by the BCAL does not describe the data satisfactory mainly due to a different trigger acceptance in data and MC (see Figure 5.1).
- Rejection of events in the supercracks. Scattered positrons which are reconstructed on the edges of the BCAL ($-98.5\,\mathrm{cm} < Z < -104\,\mathrm{cm}$ and $164\,\mathrm{cm} < Z < 174\,\mathrm{cm}$) or for which the corresponding track is extrapolated to that region are excluded. The MC description is poor in that region because of the large amount of inactive material.
- $y_E < 0.95$. Very high values in the reconstructed kinematic variable y_E (see section 8.3) are excluded because of a large photoproduction contamination. These events are caused mainly by photons from π^0 decays which are wrongly identified as the scattered positron. This happens mainly in photoproduction, since there no scattered positron can be found in the detector, and predominantly in the forward direction, since the proton remnant is a large source of π^0 particles. The low energy assigned to the positron candidate results in a high value of y_E.

In addition positrons scattered in the forward region of the calorimeter were treated differently from the ones scattered backwards. Forward scattering means low values of θ corresponding to high values of Q^2. The measurement in this region suffers because of the low statistics of these events in combination with the high hadronic activity in the forward region. That results in a higher misidentification probability and therefore the cuts were chosen differently.

If the measured polar angle of the scattered positron is less than 0.3 rad the event has to pass the following criteria:

- $p_{T,e} = E_e \sin(\theta) > 30\,\text{GeV}$. Similar to the y_E restriction this cut removes the background with low positron energy.
- $44\,\text{GeV} < E - p_Z < 65\,\text{GeV}$. The $E - p_Z$ cut is essential to reduce the photoproduction background.

In case the positron was scattered with $\theta > 0.3$ rad the events were selected by following cuts:

- Track match: DCA $< 10\,\text{cm}$. The difference between the extrapolated position from the found track to the calorimeter surface and the position reconstructed by the calorimeter (distance of closest approach, DCA) has to be small to exclude wrongly identified positrons.
- Momentum of the positron track $P_{trk} > 5\,\text{GeV}$. This cut makes sure that the identified track belongs to the found positron and low energy positron candidates are removed.
- $38\,\text{GeV} < E - p_Z < 65\,\text{GeV}$. The $E - p_Z$ cut is slightly relaxed in comparison to the events with a forward scattered positron. The probability of a misidentification of the scattered positron is smaller in the barrel and rear part of the calorimeter. The restriction to values less than 65 GeV removes background with overlays, i.e. usual DIS events in combination with a proton beamgas interaction.

In total 165917 (42621) e^+p (e^-p) events pass the cuts described above. Figure 7.2 shows distributions of variables which are used for cuts indicated as lines. Plotted are all events which pass the event selection together with the events failing only the particular requirement shown. Overall the data are well described by the MC. The distribution of DCA differs between MC and data, because the shower development and therefore the number of energy cells is systematicly smaller in MC, resulting in a better agreement between track and calorimeter cluster position measurement.

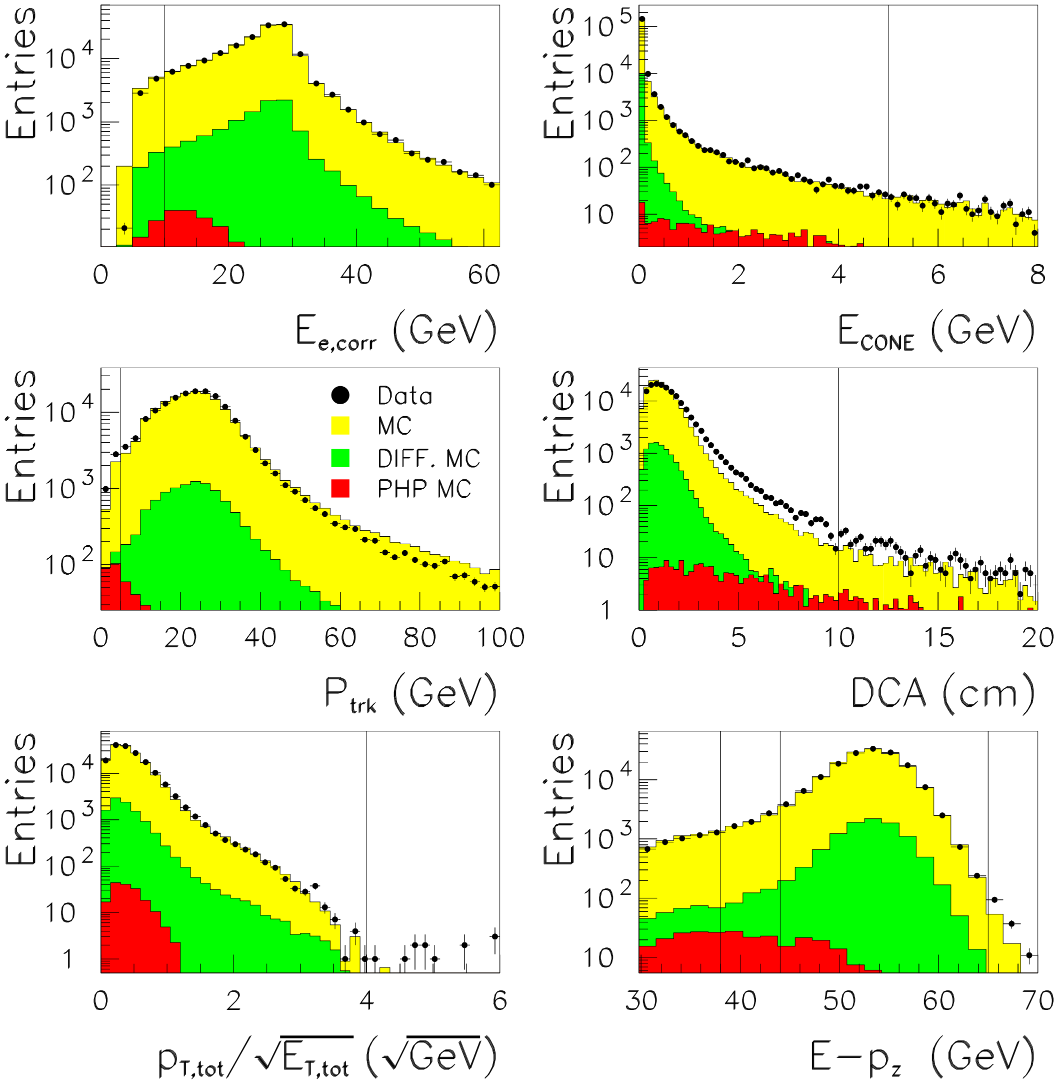

Figure 7.2: Data and MC control plots in the variables used for analysis cuts. Shown are the positron energy ($E_{e,corr}$), the energy not belonging to the positron in a cone around the positron (E_{CONE}), the momentum of the positron track (P_{trk}), the distance of closest approach between reconstructed positron track and calorimeter position (DCA), the ratio between total transverse vectorial energy and the square root of the total transverse scalar energy ($p_{T,tot}/\sqrt{E_{T,tot}}$) and the $E - p_z$ distribution of the events. The position of the lines indicate the applied cuts.

Chapter 8

Kinematic Reconstruction

A precise cross section measurement depends on accurate reconstructed kinematic variables. Only two of the four measured quantities: positron scattering angle and energy as well as hadronic scattering angle and energy, are needed to calculate Q^2, x and y. This chapter presents the most common reconstruction methods and compares their advantages and disadvantages. The Monte Carlo is used to study the resolution of the kinematic reconstruction.

8.1 Electron Method

The electron method is usually used in fixed target experiments where the hadronic system can not be fully reconstructed but is also used by some ZEUS analyses. Since the angle and energy of the scattered lepton are used to reconstruct the kinematics this method is applicable where these quantities can be measured very precisely (or if the measurement of the hadronic system is poor). Together with the equations given previously (see section 1.1) and the four momentum of the initial (inital positron beam energy E_e^{beam}) and scattered positron (scattered positron energy E_e), given by:

$$k = \begin{pmatrix} E_e^{beam} \\ 0 \\ 0 \\ -E_e^{beam} \end{pmatrix} \quad \text{and} \quad \mathrm{k}' = \begin{pmatrix} E_e \\ E_e \sin\theta\cos\phi \\ E_e \sin\theta \sin\phi \\ E_e \cos\theta \end{pmatrix}, \tag{8.1}$$

with θ and ϕ denoting the polar and azimuthal angle, respectively, the kinematic variables can be derived as follows:

$$\begin{aligned} Q_E^2 &= 2E_e^{beam} E_e(1+\cos\theta)\,, & (8.2) \\ y_E &= 1 - \frac{E_e}{2E_e^{beam}}(1-\cos\theta)\,, & (8.3) \\ x_E &= \frac{Q_E^2}{s y_E}\,. & (8.4) \end{aligned}$$

Thus the kinematics depend only on E_e and θ and their relation is shown in Figure 8.1. Here the contours of constant polar angle and energy of the scattered positron in the $x - Q^2$-plane, used for this analysis, are shown. It can be seen that events with low energy of the scattered positron

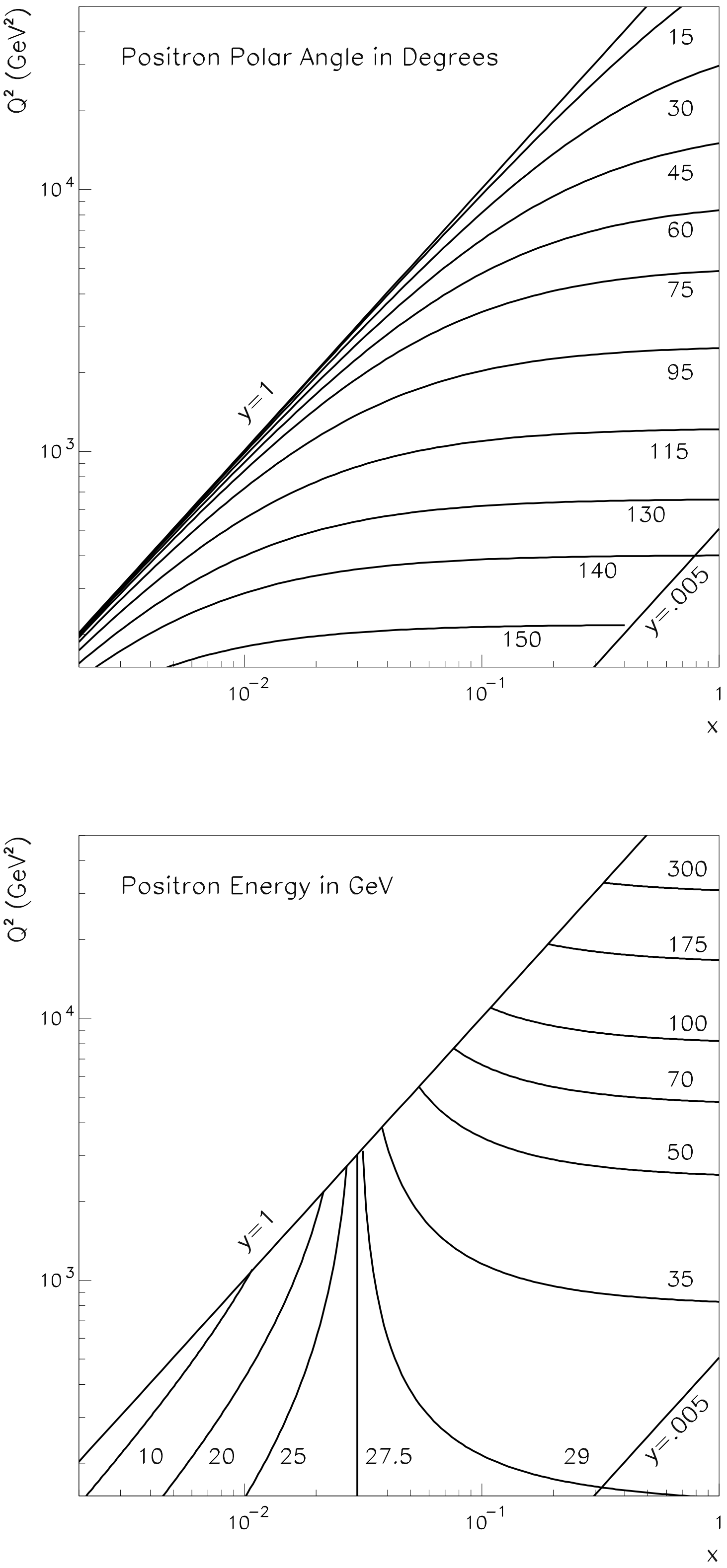

Figure 8.1: The lines of constant positron scattering polar angle in the x, Q^2-plane is shown in the top plot whereas the lines of constant lepton energy are shown in the bottom plot.

($E_e < E_e^{beam}$) result in high y values whereas high energies and large scattering angles (low θ) yield high values of Q^2. Similar values well separated from each other (isolines far apart from each other) indicate regions in which large migrations can occur due to small uncertainties in the determination of the quantity under estimation. These migrations cause events belonging to one x, Q^2-bin to be reconstructed in another. Therefore regions of good resolution are indicated by isolines close to each other. Good resolutions with the electron method are obtained at lower values of Q^2 in regions of high y and at high Q^2. On the other hand the resolution at high x is worse, because here the isolines of energy and angle are almost parallel easily resulting in larger migrations. The behaviour of the relations shown in Figure 8.1 is, of course, not only valid when the electron method is used but is general.

8.2 Jacquet-Blondel Method

In contrast to the electron method only the hadronic system is used in the method developed by Jacquet and Blondel [76]. The usage of this method is motivated by the fact that the HERA detectors ZEUS and H1 have almost full angular coverage and a basically complete measurement of the hadronic system is possible. However, when the hadronic event variables are chosen for reconstruction it has to be ensured that any influence of the final state parton radiation and thus subsequent fragmentation and details of the topology of the hadrons (like rapidity distribution) is negligible. In addition, the effect of undetected particles escaping through the forward beampipe hole has to be small. The quantities satisfying these requirements are the transverse momentum $p_{T,h} = \sqrt{p_{X,h}^2 + p_{Y,h}^2}$ and the difference of energy and longitudinal momentum $\delta_h = (E - p_Z)_h$. With the four momentum of the total hadronic final state

$$p = \begin{pmatrix} E_h \\ E_h \sin\gamma_h \cos\phi_h \\ E_h \sin\gamma_h \sin\phi_h \\ E_h \cos\gamma_h \end{pmatrix}, \tag{8.5}$$

where γ_h and ϕ_h are the hadronic scattering polar and azimuthal angle, the kinematic variables can be reconstructed as follows:

$$\begin{aligned} y_{JB} &= \frac{E_h(1-\cos\gamma_h)}{2E_e^{beam}} = \frac{(E-p_Z)_h}{2E_e^{beam}}, && (8.6)\\ Q^2_{JB} &= \frac{p^2_{T,h}}{1-y_{JB}}, && (8.7)\\ x_{JB} &= \frac{Q^2_{JB}}{s y_{JB}}. && (8.8) \end{aligned}$$

Since the sum over all final state particles excluding the scattered positron is approximated by the sum over all calorimeter entries excluding the ones assigned to the scattered positron, a bias is introduced. Responsible are not only geometrical effects such as cell size and calorimeter granularity, but also the noise from the uranium calorimeter itself. This causes a limitation in resolution at high values of y and in general a worse resolution in Q^2. Nevertheless in case of charge current reactions, in which the neutrino escapes the experiment undetected, the Jacquet-Blondel method is the only way to reconstruct the kinematic variables.

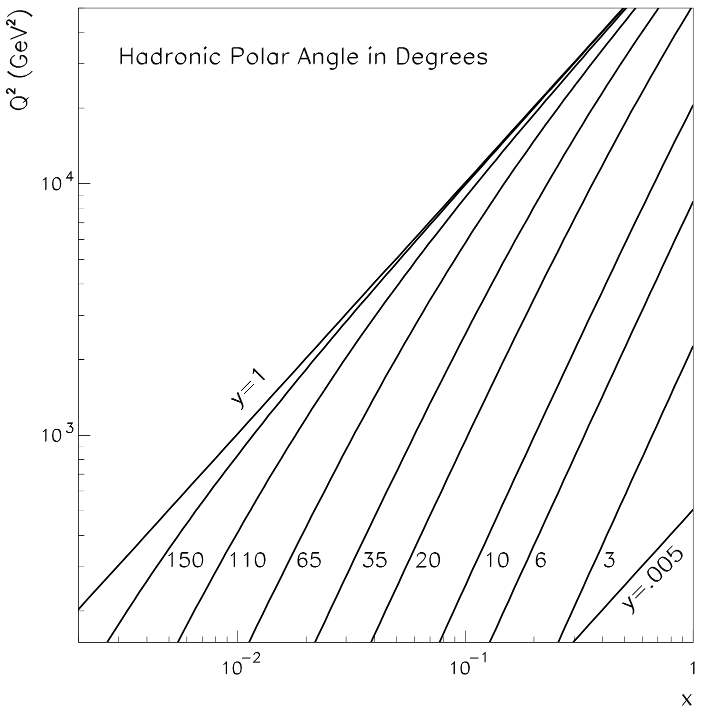

Figure 8.2: Lines of constant hadronic polar angle in the x, Q^2-plane.

8.3 Double-Angle Method

Scattering angles are measured usually more precisely than energies due to the higher accuracy of the tracking devices compared to the calorimeter, which in addition often are affected by correction procedures (introducing further uncertainties). In this analysis the double-angle method [77] is applied which relies on a precise angular measurement. The method uses the lepton scattering polar angle θ as well as the hadronic polar angle γ_h and is therefore to first order independent of the calorimeter energy scale. With $Q^2_E = Q^2_{JB}$ and $y_E = y_{JB}$ the energy of the scattered electron E_e can be expressed as a function of the two scattering angles:

$$E_{da} = E_e^{beam} \frac{\sin\gamma_h}{\sin\gamma_h + \sin\theta - \sin(\theta+\gamma_h)} . \tag{8.9}$$

By substitution of E_e by E_{DA} in equations 8.2, 8.3 and 8.4, the double-angle reconstruction is obtained:

$$\begin{aligned} Q^2_{da} &= (2E_e^{beam})^2 \frac{\sin\gamma_h(1+\cos\theta)}{\sin\gamma_h + \sin\theta - \sin(\theta+\gamma_h)} , && (8.10) \\ y_{da} &= \frac{\sin\theta(1-\cos\gamma_h)}{\sin\gamma_h + \sin\theta - \sin(\theta+\gamma_h)} , && (8.11) \\ x_{da} &= \frac{E_e^{beam}}{E_p^{beam}} \frac{\sin\gamma_h + \sin\theta + \sin(\theta+\gamma_h)}{\sin\gamma_h + \sin\theta - \sin(\theta+\gamma_h)} . && (8.12) \end{aligned}$$

In the double-angle method the electron angle contributes most to the determination of Q^2

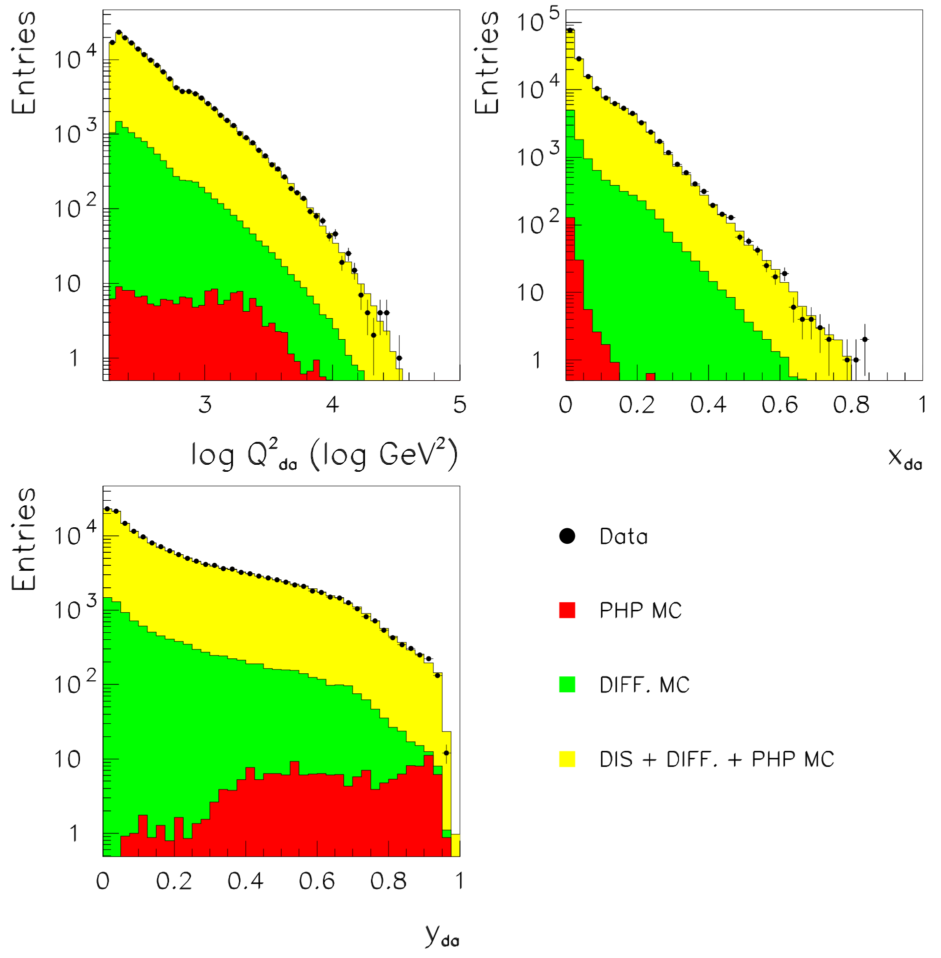

Figure 8.3: Q^2, x, y distributions reconstructed with the double-angle method for data and MC.

whereas the γ_h determines the value of x as can be seen from Figures 8.1 and 8.2. The isolines for both angles become parallel to the $y = 1$-line resulting in a worse resolution at high y.

The reconstructed kinematic variables for data and MC can be compared in Figure 8.3. For all three variables the data is well reproduced by the MC.

8.4 Resolution of the Kinematic Variables

The resolution in a certain kinematic variable, v, can be defined as

$$res. = \frac{v_{meas.} - v_{true}}{v_{true}}, \tag{8.13}$$

for $v = Q^2, x$ and y. Figures 8.4, 8.5 and 8.6 show the resolution of these variables in nine x, Q^2 bins for all three reconstruction methods discussed. The true value is obtained taking the radiative effects into account. In comparison with the different methods the advantage of the double-angle method is clearly visible. The resolution obtained with the double-angle method displayed as a histogram was fitted with a Gaussian. In the whole kinematic range of this analysis the systematic shifts introduced by the reconstruction method are small. The resolution at high Q^2 ($Q^2 > 1300\,\mathrm{GeV}^2$) is better than $\sim 5\%$ in all variables.

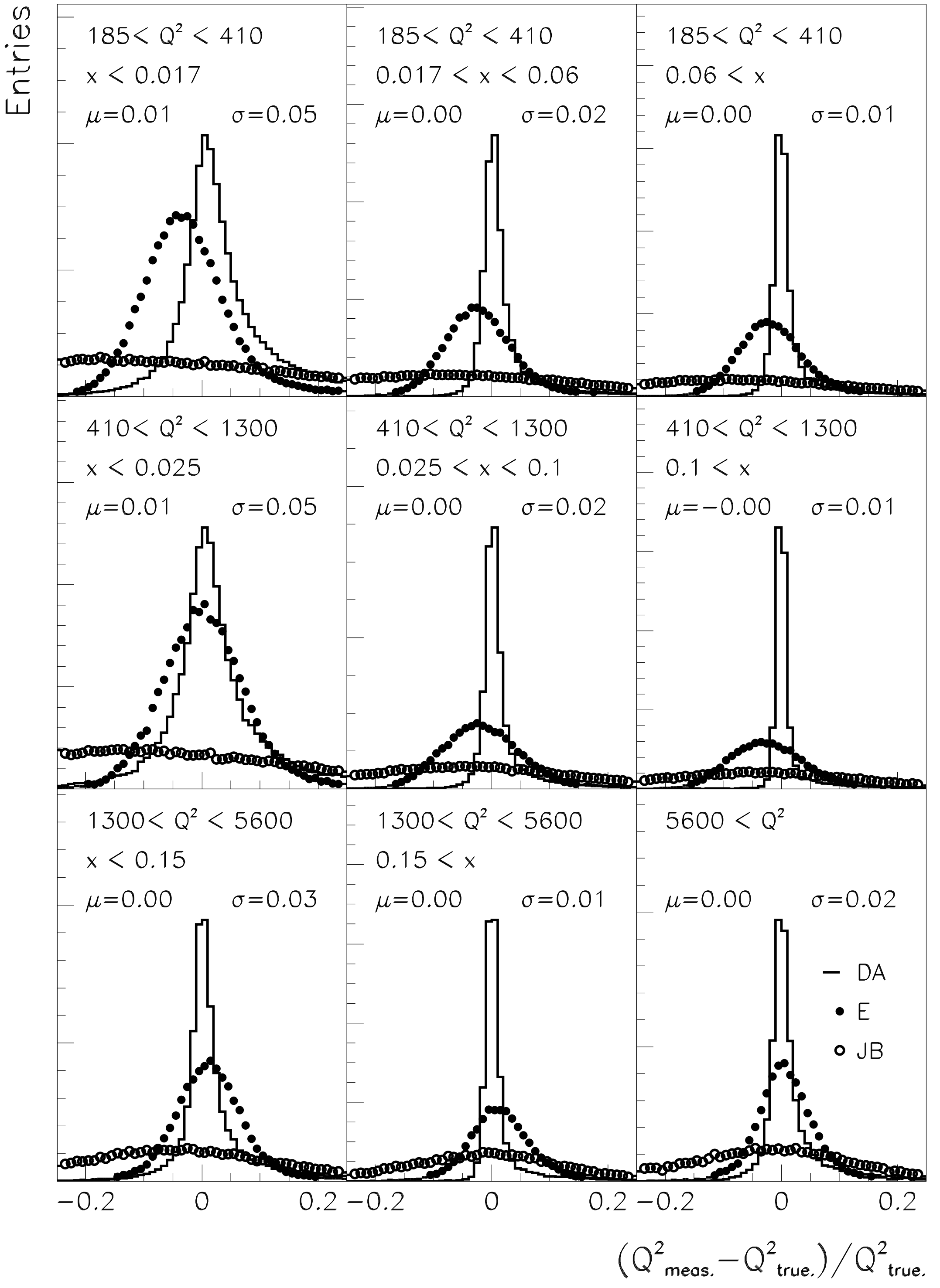

Figure 8.4: Resolution in Q^2 is shown in different bins of x and Q^2 obtained by the double-angle (DA), electron method (E) and Jacquet-Blondel (JB) reconstruction. The value of Q^2 is given in GeV. The DA distributions are fitted with Gaussians, their mean μ and sigma σ is also given in the plot.

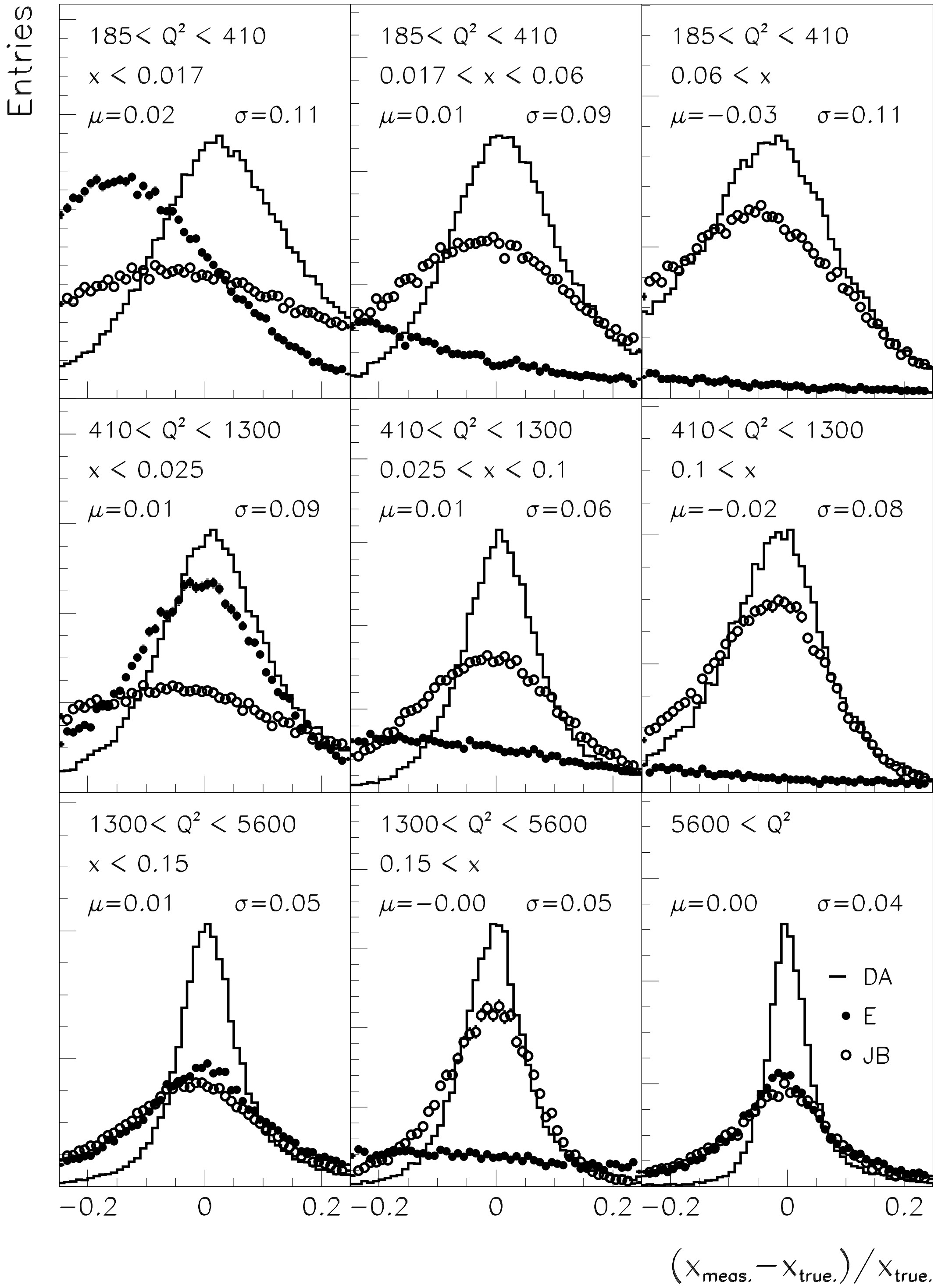

Figure 8.5: Resolution in x is shown in different bins of x and Q^2 obtained by the double-angle (DA), electron method (E) and Jacquet-Blondel (JB) reconstruction. The value of Q^2 is given in GeV. The DA distributions are fitted with Gaussians, their mean μ and sigma σ is also given in the plot.

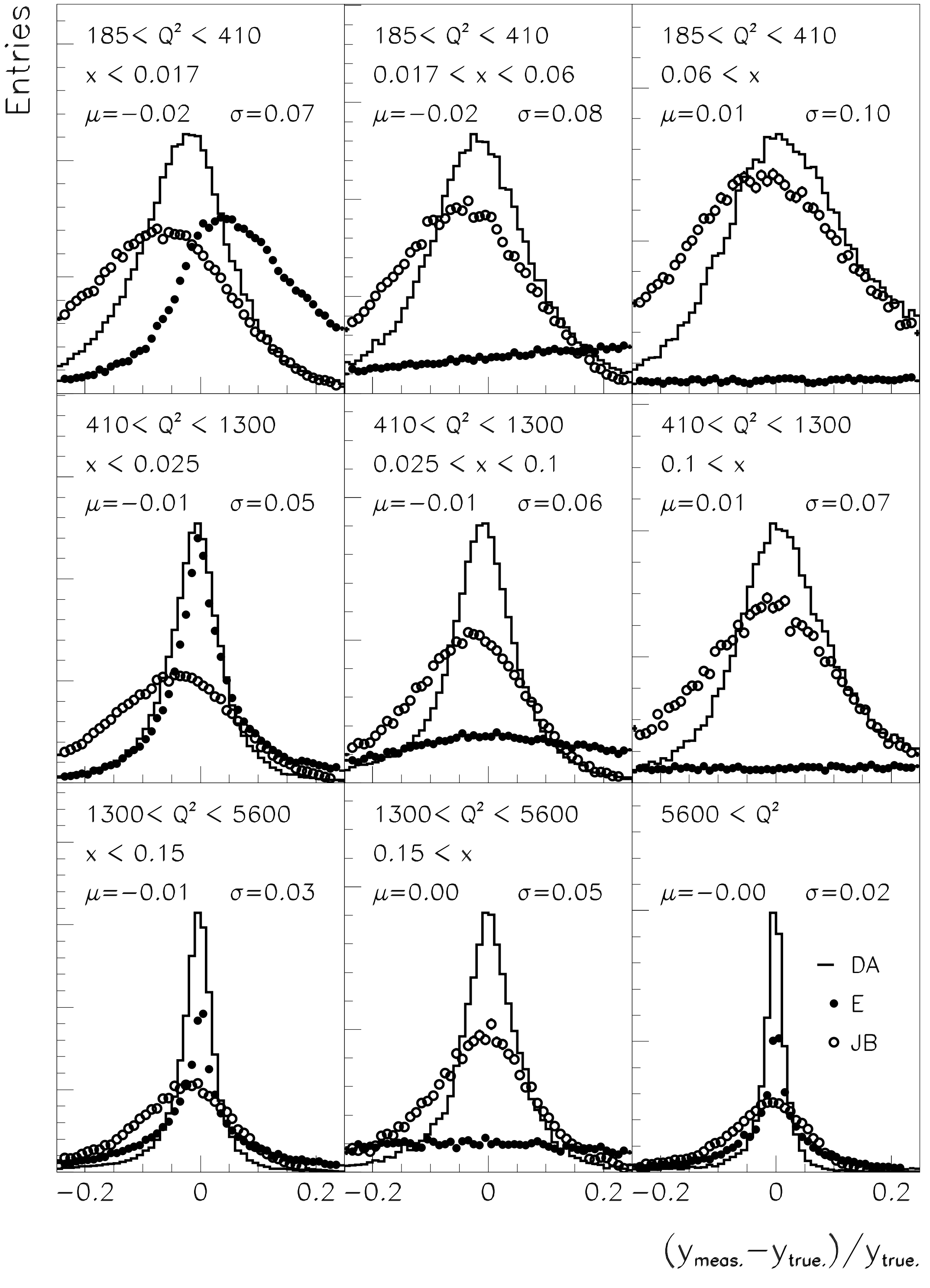

Figure 8.6: Resolution in y is shown in different bins of x and Q^2 obtained by the double-angle (DA), electron method (E) and Jacquet-Blondel (JB) reconstruction. The value of Q^2 is given in GeV. The DA distributions are fitted with Gaussians, their mean μ and sigma σ is also given in the plot.

Chapter 9

The Cross Section Measurements

In this chapter the results of the cross section measurements are presented. The main emphasis lies on the first analysis of the 1999/2000 e^+p data sample. In addition the 1998/1999 e^-p data sample[1] was analysed to point out the general differences in e^+p and e^-p cross sections and to extract the proton structure function xF_3. Besides the measurement of the reduced cross sections, defined in equation 1.9, single differential cross sections were determined by integrating the double differential cross section over x resulting in a measurement of $d\sigma/dQ^2$ and integrating over Q^2 yielding $d\sigma/dx$. The latter was done for the case of different lower integration boundaries of Q^2 ($400\,\mathrm{GeV}^2$, $2500\,\mathrm{GeV}^2$ and $10000\,\mathrm{GeV}^2$) to test the x dependence of the cross section in different kinematic regions. Furthermore the cross section can be expressed in terms of y instead of x and therefore an integration over Q^2 results in $d\sigma/dy$.

Before presenting the measured cross sections the bin definition and the cross section unfolding procedure is explained. In the following sections the statistical and systematic uncertainties are discussed.

The measured double differential cross section in both e^+p and e^-p data permit the extraction of the proton structure function xF_3 as described in a separate section. The measurement of $d\sigma^{e^+p}/dQ^2$, as presented in this thesis, in combination with measurements from previous run periods was used in a study searching for physics beyond the Standard Model. Some results of that analysis are presented in the last section of this chapter.

9.1 Bin Definition

A measurement of physics cross sections is performed in particular ranges of the kinematic variables. This allows the study of the shape of the underlying PDFs versus the kinematic variable used and in addition enables the possibility to exclude kinematic regions which are not accessible or result in bad measurements due to the detector geometry and performance. Therefore, the accessible phase space is divided into so-called bins. By defining the bins (binning) two different requirements have to be considered. On the one hand a large number of bins provides the maximum information on the shape of the cross section (and therefore of the proton structure). On the other hand a large number of bins corresponds to small bin sizes leading to increasing statistical uncertainties and larger migration effects. Migration is caused by the

---

[1] The complete analysis of the e^-p data sample including all comparisons between data and MC can be found in [72].

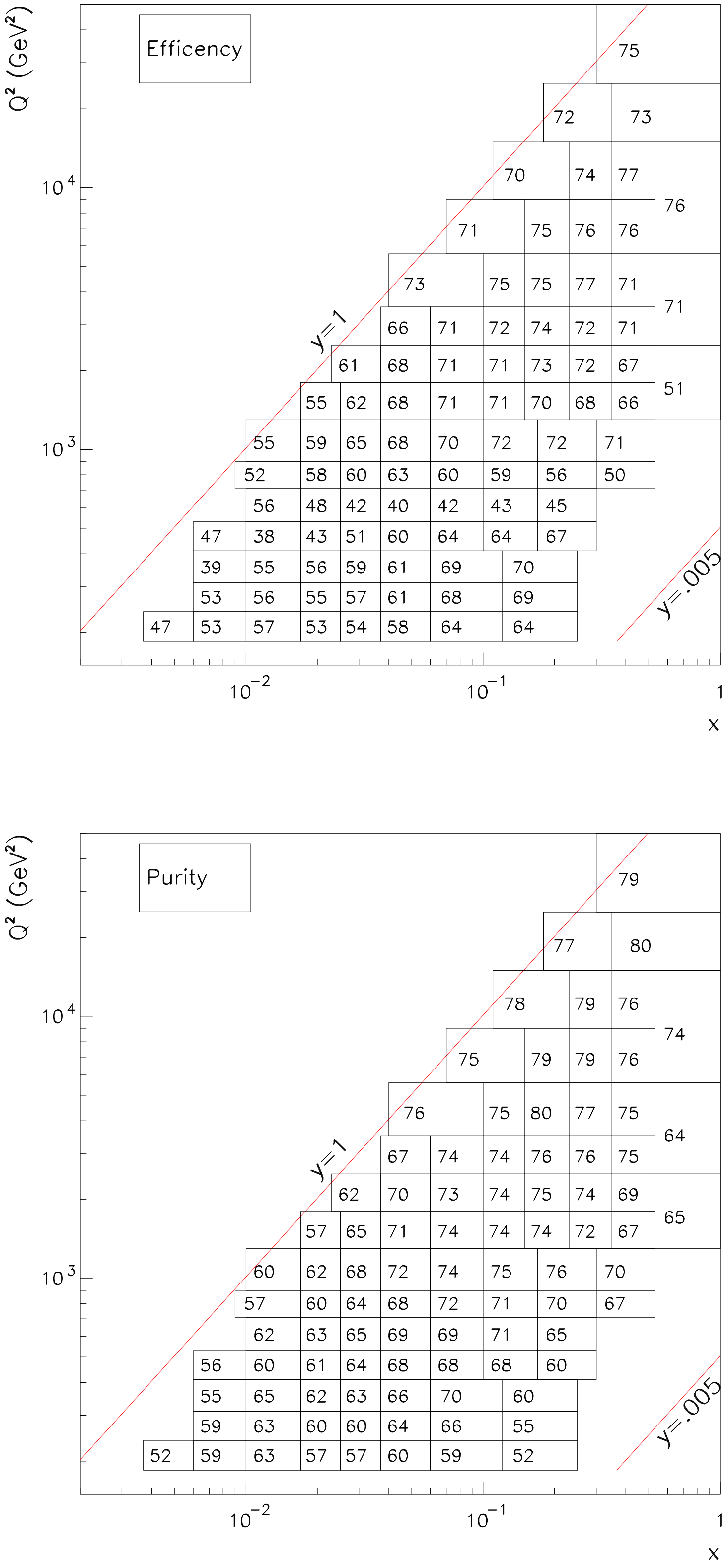

Figure 9.1: Efficiency and purity of the double differential cross section bins. The numbers are given in percent.

limited experimental resolution of the observable to be measured. As a compromise between the two requirements the bin sizes have to be well adapted to the experimental resolution, i.e. the bins should be at least of similar size to the resolution of the kinematic variable in the particular bin (which is necessary for the unfolding procedure discussed in the next section).

The binning used in this analysis was taken from previous ZEUS NC measurements [68] to simplify a combination or a comparison of different data sets. The quality of the bins can be expressed in terms of efficiency and purity (calculable with MC events), defined as follows:

$$\text{Efficiency} = \frac{\#\text{events generated and measured in bin } i}{\#\text{events generated in bin } i}\,, \tag{9.1}$$

$$\text{Purity} = \frac{\#\text{events generated and measured in bin } i}{\#\text{events measured in bin } i}\,. \tag{9.2}$$

The efficiency is reduced by the analysis cuts, by trigger and by detector acceptances and is affected by the resolution which is also strongly correlated to the purity.

The efficiencies and purities of the bins used for the double differential cross section measurements are illustrated in Figure 9.1 (efficiencies and purities of all other presented cross sections can be found in the appendix). The efficiency was required to be larger than 35% in all bins. The regions which are not used in the analysis because the positron is scattered into the area of the supercrack or into the outer areas of the RCAL ($Q^2 \approx 600\,\text{GeV}^2$) are reflected by lower values of the efficiency ($\sim 40\%$). The purities are larger than 50% in all bins, they are increasing towards higher values of Q^2.

9.2 Cross Section Unfolding

This section describes the procedure used to obtain a cross section measurement from the number of selected events in the bins previously defined. Due to the effects of limited resolution, analysis cuts, detector and trigger acceptance the number of measured events m_i in a particular bin i does not have to be equal to the number of true events g_i (in case of MC corresponding to the number of generated events) in that bin. In general the measured events can be related to the true ones by a transfer matrix T_{ij}:

$$m_i = \sum_j (T_{ij}) g_j\,. \tag{9.3}$$

Taking into account only net event migrations from or into a bin, the matrix can be simplified to a diagonal one, therefore the correlation between bins ($i \neq j$) vanishes, m_i and g_i are related by a constant A_i:

$$m_i = \mathcal{A}_i \cdot g_i\,. \tag{9.4}$$

The acceptance $\mathcal{A}_i$ is determined by the MC,

$$\mathcal{A}_i = \frac{\#\text{events measured in bin } i}{\#\text{events generated in bin } i} = \frac{N^{MC}_{meas,i}}{N^{MC}_{gen,i}}\,, \tag{9.5}$$

and can be used to unfold the measured number of events in data to the underlying true number of data events. This so-called bin-by-bin unfolding method is used in this analysis. Crucial for its applicability is a very good description of the data by the MC in all phase space regions.

Differences in resolution or efficiency between data and MC resulting in different shapes of the observable distributions will lead to shifts of the unfolded number away from the true value.

The measurement of a cross section in a bin i is therefore given by the measured number of data events after background subtraction, $N_i^{data} = N_i^{meas} - N_i^{photopr.}$, divided by the luminosity $\mathcal{L}^{data}$ and the acceptance $\mathcal{A}_i$, which was calculated by the MC:

$$\sigma_i = \frac{N_i^{data}}{\mathcal{A}_i \cdot \mathcal{L}^{data}} = \frac{N_i^{data}}{\mathcal{L}^{data}} \cdot \frac{N_{gen,i}^{MC}}{N_{meas,i}^{MC}} \,. \tag{9.6}$$

Both data and MC include electroweak radiative effects. To obtain a cross section at Born level without these effects another correction is necessary. This correction can be determined also by using the MC, in particular by using the ratio between the predictions of a MC at Born level and the DJANGOH MC. The measured cross section at Born level is then given by this equation:

$$\sigma_i^{Born} = \sigma_i \cdot \frac{N_{gen,i}^{MC,Born}}{N_{gen,i}^{MC}} = \frac{N_i^{data}}{\mathcal{L}^{data}} \cdot \frac{N_{gen,i}^{MC,Born}}{N_{meas,i}^{MC}} \,. \tag{9.7}$$

Furthermore the cross section measurement is compared to the differential theoretical cross section at a particular point ν_{quote} of the bin. This point is usually taken in the (logarithmic) middle of the bin. With the assumption that the shape of the cross section is well described in theory, the following bin centre correction (centre of gravity) of the differential cross section of the kinematic variable ν (Q^2, x, y; the argumentation is the same in the case of double differential cross sections) can be applied:

$$\frac{d\sigma^{Born}}{d\nu}(\nu_{quote}) = \sigma_i^{Born} \cdot \frac{\frac{d\sigma^{SM,Born}}{d\nu}(\nu_{quote})}{\int_{bin\, i} \frac{d\sigma^{SM,Born}}{d\nu}(\tilde{\nu})d\tilde{\nu}} \,. \tag{9.8}$$

The correction is obtained by the predicted Standard Model (SM) cross section. By using the same parametrisation of the PDFs the integral of the SM cross section in a bin i is given by the number of generated events in the MC $N_{gen,i}^{MC,Born}$ divided by the MC luminosity $\mathcal{L}^{MC}$. Since the MC events are reweighted such that $\mathcal{L}^{MC} = \mathcal{L}^{data}$ the measured cross section can finally be unfolded in the following way:

$$\frac{d\sigma^{Born}}{d\nu}(\nu_{quote}) = \frac{N_i^{data}}{N_{meas,i}^{MC}} \cdot \frac{d\sigma^{SM,Born}}{d\nu}(\nu_{quote}) \,. \tag{9.9}$$

The last term is obtained by numerically integrating equation 1.8 over the bin i with fixed $\alpha = 1/137, M_Z = 91.1882\,\mathrm{GeV}$ and $\sin^2\theta_W = 0.23147$ [78]. In this way the cross section is corrected for all selection cuts and furthermore is extrapolated to the full kinematic range, in particular beyond the y region restricted by the y_E cut. This is done to allow comparisons to previous analyses although the PDFs are not well constrained at high y and the uncertainty is therefore large in these regions.

The SM Born level cross section strongly depends on the PDFs which are used as input and therefore the measurement done in the described manner depends on them, too. The PDFs used (compare to section 4.1) are extracted from previous measurements mainly done at lower momentum transfers. Since the measurements presented here have a higher statistical precision than previous analyses the PDFs could differ and deviations between measurement and theory could be observed. The bin-by-bin unfolding procedure can be performed in an iterative way. New PDFs can be extracted from the obtained cross section and can be put in the MC leading to a modification of the measurement. The method can be repeated since the modification of the measurement is small. Since the measured cross section is well described by the one obtained using the CTEQ5D PDF, an iterative procedure as was done in previous analyses would result in a negligible change of the measurement.

9.3 Statistical Uncertainties

The measured cross section is proportional to the ratio of measured data and MC events (cf. equation 9.9). Its statistical uncertainty is given by the statistical uncertainty of both numbers. The MC events are reweighted to the data luminosity. Therefore to each MC event k a weight w_k is assigned and the number of MC events in a bin i is the sum of the weights in that bin. The statistical uncertainty of the number of MC events is given by:

$$\Delta N_i^{MC} = \sqrt{\sum_k w_k^2} \,. \tag{9.10}$$

In this way the uncertainty is not calculated from the number of weighted MC events but from the total number of MC events. As can be seen from table 4.1 the MC luminosity exceeds the data luminosity by far. This results in weights much smaller than one and a small statistical uncertainty. The statistical uncertainty of the data events, ΔN_i^{data}, in bin i is given by:

$$\Delta N_i^{data} = \sqrt{(\Delta N_i^{obs})^2 + (\Delta N_i^{photopr.})^2} \,, \tag{9.11}$$

where $\Delta N_i^{photopr.}$ is calculated like ΔN_i^{MC} and Gaussian uncertainties of the observed events $\Delta N_i^{obs} = \sqrt{N_i^{obs}}$ are used in case $N_i^{obs} > 12$. Otherwise the uncertainty was calculated using Poisson statistics. Therefore the relative statistical uncertainty of the measured cross section is given by:

$$\frac{\Delta\sigma_i}{\sigma_i} = \sqrt{\left(\frac{\Delta N_i^{data}}{N_i^{data}}\right)^2 + \left(\frac{\Delta N_i^{MC}}{N_i^{MC}}\right)^2} \,. \tag{9.12}$$

9.4 Systematic Uncertainties

The systematic understanding of a measurement is vital for the significance of its physics interpretation. Numerous systematic checks were performed to achieve a good estimation of the systematic uncertainty. The large statistics data sample of the run period 99/00, which exceeds the luminosity of previous ZEUS high Q^2 analyses by almost a factor two (in case of double differential measurements), was of large importance to the determination of the systematic uncertainty. Especially the energy calibration between data and MC could be studied in more detail which improves the understanding of the detector leading to the developement of best suited systematic checks and a reduction of the amount of systematic checks to be considered in the future.

The systematic checks performed can be divided into two groups. The first group concerns the systematic effects of the selection cuts. In these checks the analysis was repeated with one modified selection criterium for both data and MC[2]. The other group includes all systematic

---

[2] Limited statistics can increase the effect of a systematic variation artificially.

studies concerning the variation of the calibration factors or distributions as well as the effect of using a different fragmentation model. In general the analysis was repeated for each single systematic study. The difference between the cross section resulting from the systematic check and the nominal one is taken as systematic uncertainty. All systematic uncertainties which result in an increase of the cross section are added in quadrature to form the total, squared positive uncertainty and vice versa in case of the negative contributions. The size of the systematic variation is motivated by the differences in the data and MC distributions and are treated very conservatively at this stage of the analysis.

The sizes of the systematic uncertainties, discussed in the following, are shown in Figures 9.2 and 9.3 in case of the measurement of the single differential cross section $d\sigma/dQ^2$.

The considered systematic uncertainties are:

- The variation of the $E - p_Z$ selection cut. The cut was varied by $\pm 2\,\mathrm{GeV}$. It changes the cross section $d\sigma/dQ^2$ by up to 10% at high values of Q^2, the cross section $d\sigma/dx$ ($Q^2 > 2500\,\mathrm{GeV}^2$) is changed by up to 20% at high x. In addition it has large impact on the low statistics bins of $d\sigma/dx$ ($Q^2 > 10000\,\mathrm{GeV}^2$) at low x ($\sim 15\%$) and high x ($\sim 100\%$).

- The variation of the P_{trk} selection cut. Changes of $\pm 5\,\mathrm{GeV}$ in this selection cut result in a variation of the cross section $d\sigma/dQ^2$ by up to 10% at high values of Q^2 and of the cross section $d\sigma/dy$ at high values of y by the same amount. Consequently it affects also $d\sigma/dx$ at low values of x by $\sim 2\%, \sim 8\%$ and $\sim 5\%$ for $Q^2 > 400\,\mathrm{GeV}^2$, $Q^2 > 2500\,\mathrm{GeV}^2$ and $Q^2 > 10000\,\mathrm{GeV}^2$, respectively.

- The variation of the DCA selection cut. The cut was lowered from 10 cm to 8 cm. It affects the cross section $d\sigma/dQ^2$ by up to 4%.

- The variation of the y_E selection cut. This cut is changed from $y_E > 0.95$ to $y_E > 0.90$. It has large impact on the high Q^2 bins of $d\sigma/dQ^2$ ($\sim 10\%, 80\%$ in highest Q^2 bin which is affected in addition by large statistical uncertainties). The effect on $d\sigma/dy$ at high values of y is 5% whereas $d\sigma/dx$ at high values of Q^2 and low x is changed by up to 10%.

- The variation of the E_{CONE} selection cut. Variations of $\pm 2\,\mathrm{GeV}$ cause only small differences, such as 2% on $d\sigma/dy$ at high values of y and $d\sigma/dx$ ($Q^2 > 2500\,\mathrm{GeV}^2$) at low values of x.

- The variation of the RCAL radius selection cut. The cut was varied by ±15 cm. Its effect is limited to regions of lower values of Q^2. The effect is up to 4.5% in the double differential cross section.

- The variation of the $p_{T,tot}/\sqrt{E_{T,tot}}$ selection cut. A change by $\pm 1\,\sqrt{\mathrm{GeV}}$ results in very small variations of the cross sections ($< 0.5\%$).

- The variation of the electron energy scale. The electron energy calibration between data and MC was changed by a variation of the energy in the MC by ±1.5% for energies below 20 GeV and by ±1.0% in case of higher energies (cf. section 6.2). The effect on all cross section measurements is small, the largest difference was found on $d\sigma/dy$ at high values of y ($\sim 2\%$).

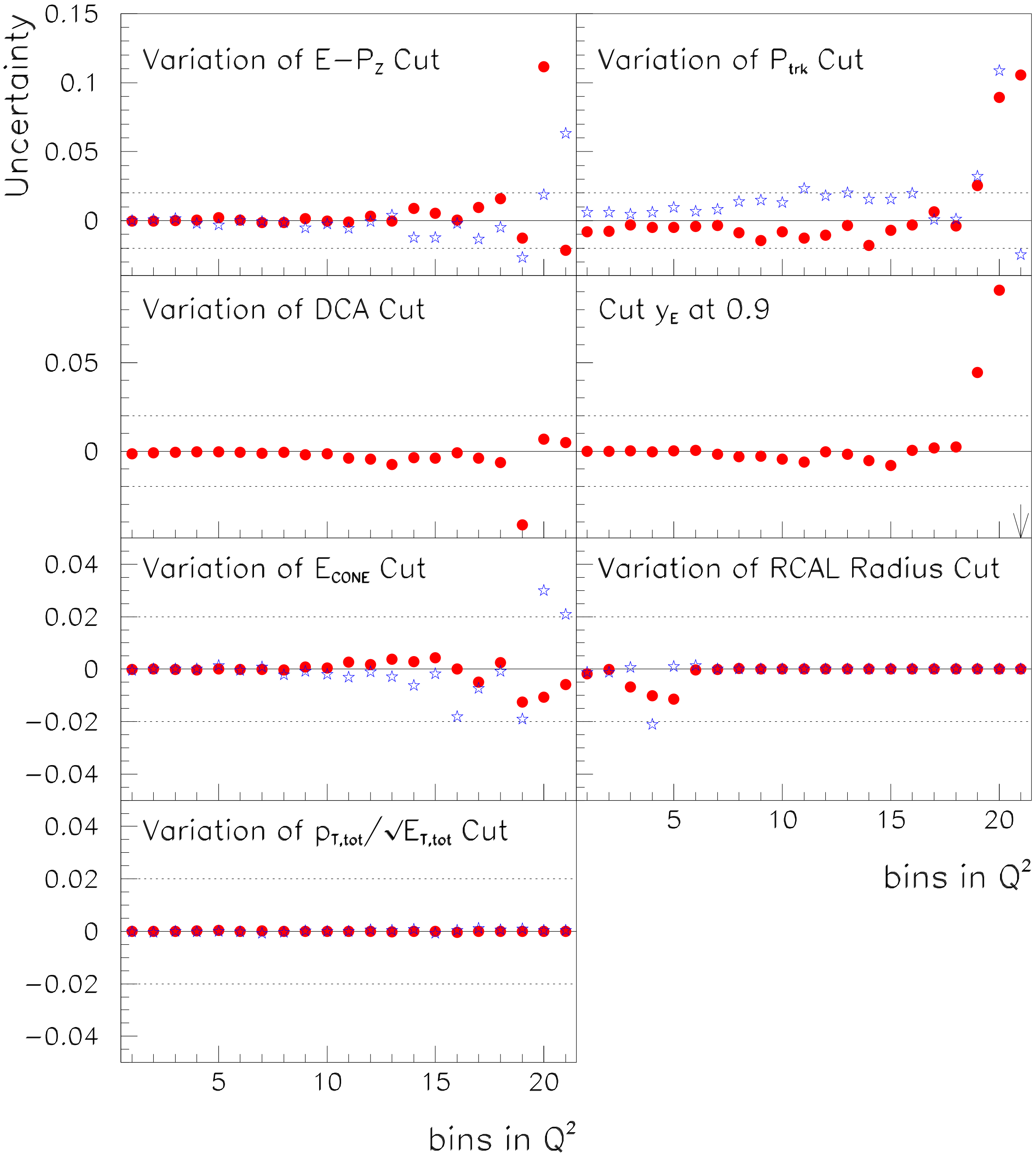

Figure 9.2: Systematic uncertainties for the measurement of $d\sigma^{e^+p}/dQ^2$. Most of the systematic studies were done by changing the analysis cuts in both directions represented by the two different symbols. The scale of the y-axis differs for the plots, the lines indicate the uncertainties of 2%, 0.% and −2%.

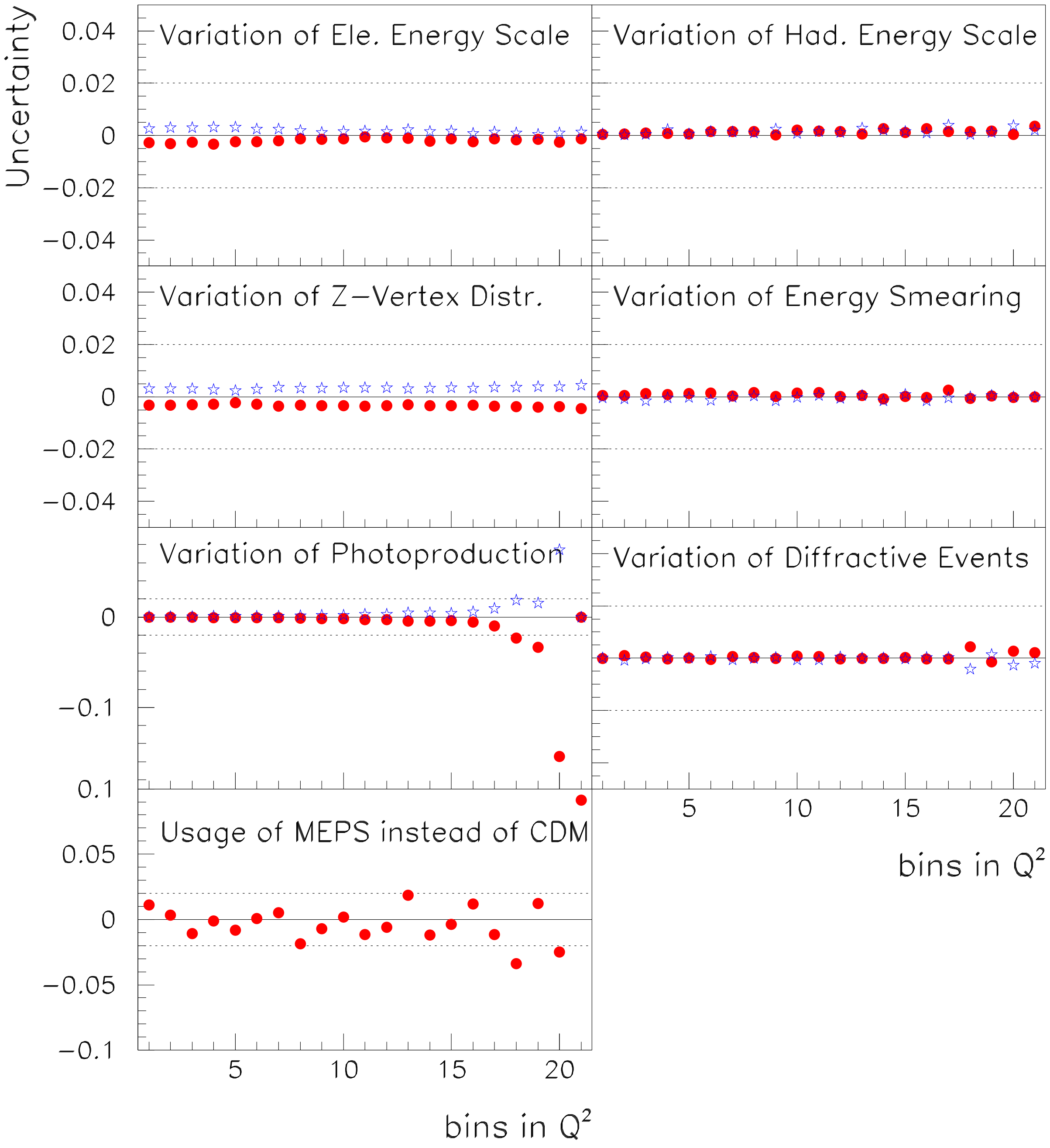

Figure 9.3: Systematic uncertainties for the measurement of $d\sigma^{e^+p}/dQ^2$. Most of the systematic studies were done by changing the standard analysis in two different directions represented by the two symbols. The scale of the y-axis differs for the plots, the lines indicate the uncertainty of 2%, 0.% and −2%.

- The variation of the hadronic energy scale. The response to hadronic energy deposition between data and MC was varied in MC for each calorimeter (FCAL,BCAL and RCAL) and for the hadronic (HAC) and the electromagnetic section (EMC) separately. FCAL HAC and BCAL HAC were varied by ±1.0%, FCAL EMC and BCAL EMC by ±1.5% and RCAL EMC and RCAL HAC by ±2.0%. The values were obtained for the first time with this high precision by an analysis using the large statistic sample of 99/00 data [81]. The effect of the different variations is small for all cross section measurements ($\sim 0.5\%$).

- The variation of the Z-vertex distribution. A change of the MC input Z-vertex distribution as described in section 6.4.3 causes uncertainties up to 0.5% in the cross section measurements.

- The variation of the energy smearing. The smearing of the electron energy was changed from 3% to 4.5% and to zero (no smearing). At most changes of 1% can be observed for cross section measurements of $d\sigma/dy$ at high y and $d\sigma/dx$ at high x.

- The variation of the number of subtracted photoproduction events. The number of photoproduction events which has to be subtracted from the data was obtained by MC. The number was varied by $\pm 3\sigma$ to account for the normalisation uncertainty. This systematic check has large impact on $d\sigma/dQ^2$ and the double differential cross section at high Q^2 (up to 20% and 10% respectively). In addition the measurement of $d\sigma/dx$ ($Q^2 > 10000\,\mathrm{GeV}^2$) is changed up to 10% at low x.

- The variation of the fraction of diffractive events. A variation of the fraction of diffractive events by ±50% results in changes in the cross sections by less than 0.5%.

- The usage of a different fragmentation model. The MEPS fragmentation model was used instead of the CDM model of ARIADNE to account for differences in the forward energy flow[3]. This variation causes the largest systematic uncertainties for $d\sigma/dQ^2$ at low Q^2 ($1-3\%, 10\%$ at highest Q^2), for the double differential cross section measurement (up to 8% at low Q^2 , up to 10% at higher Q^2) and $d\sigma/dy$ at moderate y (up to 6%).

9.5 Cross Section Results

This section summarises the results of the different cross section measurements obtained by analysing the e^+p data of the run period 1999/2000. As a comparison the e^-p data of the run period 1998/99 was analysed with the same analysis framework and with the same systematic investigations and corresponding uncertainties. In this way the different contribution of the γ–Z^0 interference to the e^+p and e^-p cross section can be investigated for large values of Q^2. All measured cross sections are compared to the Standard Model predictions using the CTEQ5D parton distributions. In the following the results of the individual cross section measurements are discussed. The exact values of the plotted points can be found in [79].

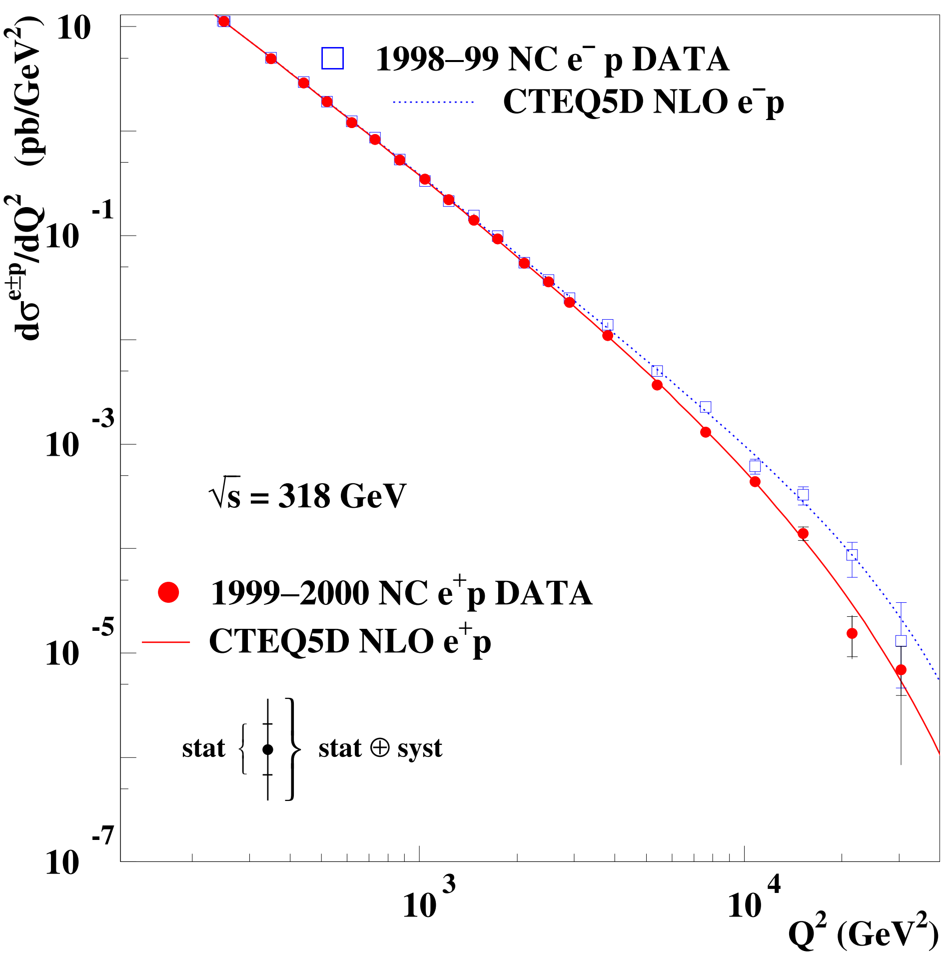

Figure 9.4: The single differential cross section $d\sigma^{e^\pm p}/dQ^2$ (full dots (e^+p) and open squares (e^-p)) and the Standard Model predictions obtained by using the CTEQ5D parton distributions (solid and dotted lines).

9.5.1 The Single Differential Cross Section $d\sigma^{e^\pm p}/dQ^2$

The measurement of the single differential cross section $d\sigma/dQ^2$ is shown in Figure 9.4. The e^+p cross section is found to decrease by six orders of magnitude from $Q^2 = 200\,\mathrm{GeV}^2$ to $Q^2 = 30000\,\mathrm{GeV}^2$ as expected from the Q^{-4} dependence of the cross section (cf. equation 1.8). The event with the highest measured Q^2 in the data sample has a value of $Q^2 \approx 32000\,\mathrm{GeV}^2$ ($Q^2 \approx 37500\,\mathrm{GeV}^2$ in case of e^-p). For $Q^2 \leq 1000\,\mathrm{GeV}^2$ the cross section is dominated by photon exchange causing e^+p and e^-p cross sections to be similar. At larger values of Q^2 the exchange of the Z^0-boson becomes more important and the destructive contribution to the e^+p cross section due to the γ–Z^0 interference can be distinguished from the constructive one in case of the e^-p cross section.

---

[3] The MC using MEPS results in general in a worse description of the data except in the energy depositions in the forward detector region. The forward energy flow is currently under investigation. Besides the aim of a better understanding a better suited systematic check will be developed which will replace the systematic use of MEPS.

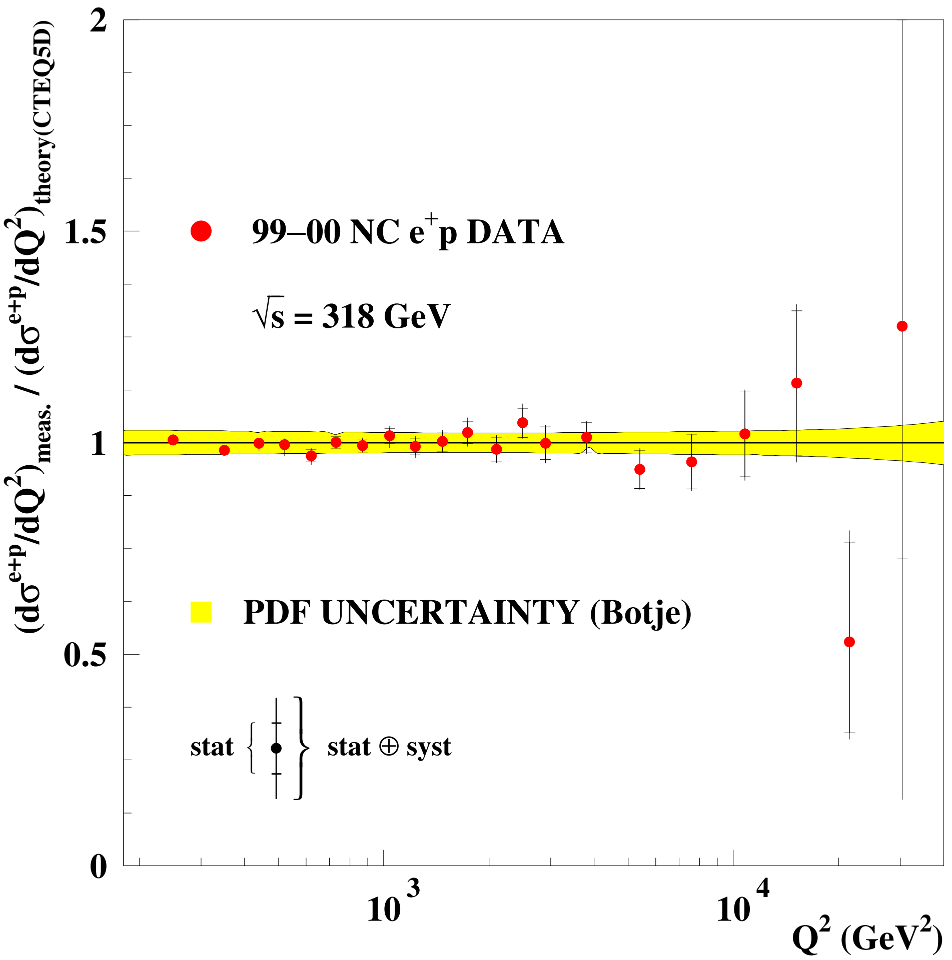

Figure 9.5: The ratio of the measured $d\sigma^{e^+p}/dQ^2$ and the Standard Model computed using CTEQ5D. The shaded band gives the PDF uncertainty as calculated by Botje.

The increased luminosity in comparison to previous ZEUS single differential cross section measurements by 30% results in a very high precision of the e^+p cross section most prominent in the ratio plot in Figure 9.5. Furthermore the large data sample does not only decrease the statistical uncertainty but also improves the systematic understanding of the whole measurement and therefore leads to smaller systematic uncertainties as well. The Standard Model prediction as obtained by using the CTEQ5D PDFs is able to describe the data up to the highest values of Q^2 and therefore at shortest distances ($\sim 1/1000$ of the proton radius). Besides data from other experiments (mainly at low Q^2) previous HERA analyses with much lower statistics at high values of Q^2 were used as input to extract the CTEQ5D PDFs. The good description also at highest Q^2 is a remarkable success of the DGLAP evolution equations. The PDF uncertainty as given by Botje [80] is shown as a shaded band in the figure. The largest systematic uncertainty at low Q^2 in the data originates from the usage of a different fragmentation model. At high Q^2 the variation of the y_E cut contributes most.

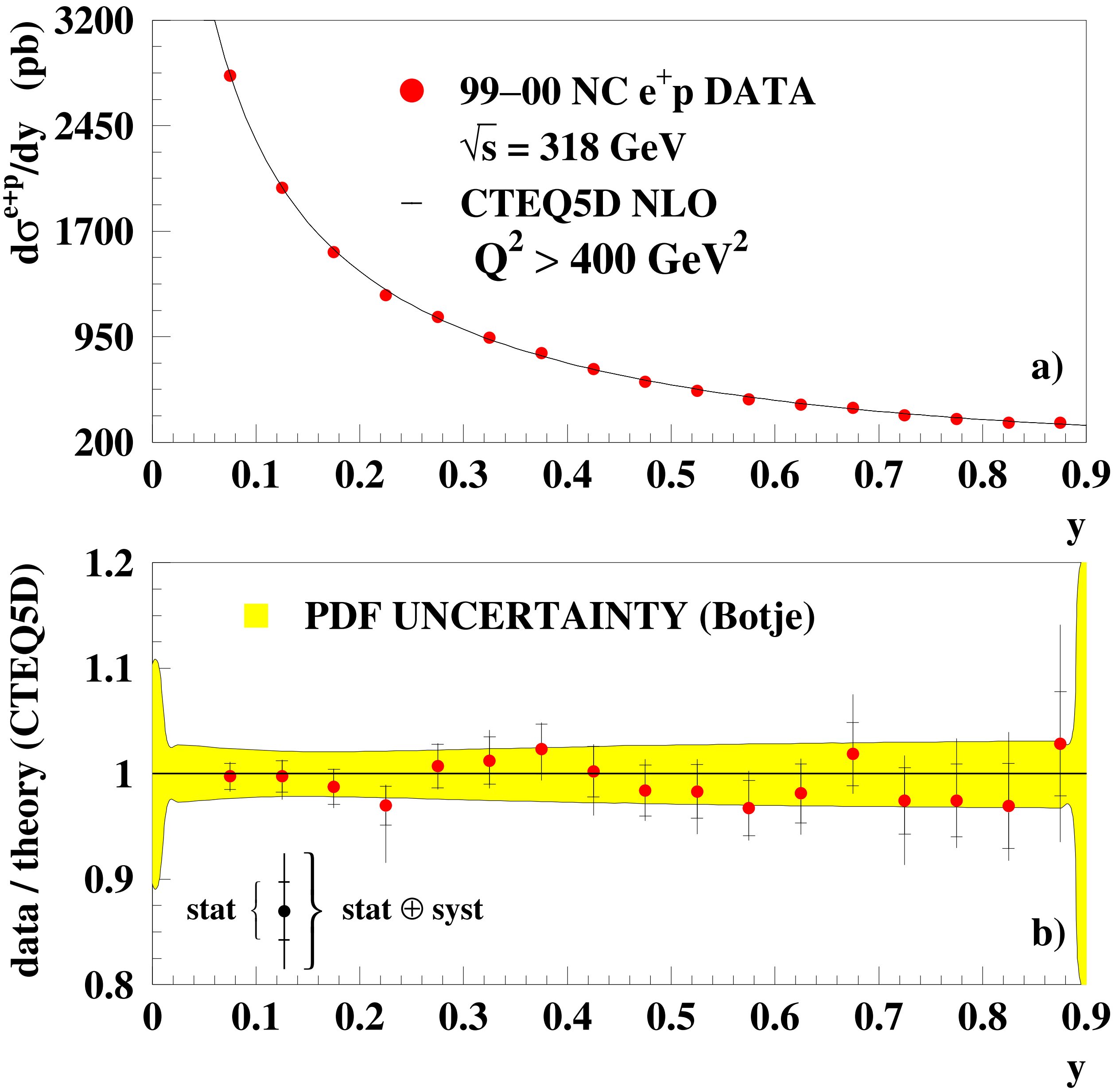

Figure 9.6: a) The single differential cross section $d\sigma^{e^+p}/dy$ for $Q^2 > 400\,\mathrm{GeV}^2$ and the Standard Model prediction obtained by using the CTEQ5D parton distributions (solid line). b) The ratio of the measured $d\sigma^{e^+p}/dy$ to the cross section obtained using CTEQ5D PDF. The shaded band gives the PDF uncertainty as calculated by Botje.

9.5.2 The Single Differential Cross Sections $d\sigma^{e^+p}/dy$ and $d\sigma^{e^+p}/dx$

The single differential cross section measurements of $d\sigma/dy$ and $d\sigma/dx$ (in different regions of Q^2) were performed to investigate the x and y dependence of the cross section. In addition these measurements prove the very good understanding of the analysed data in more than one variable.

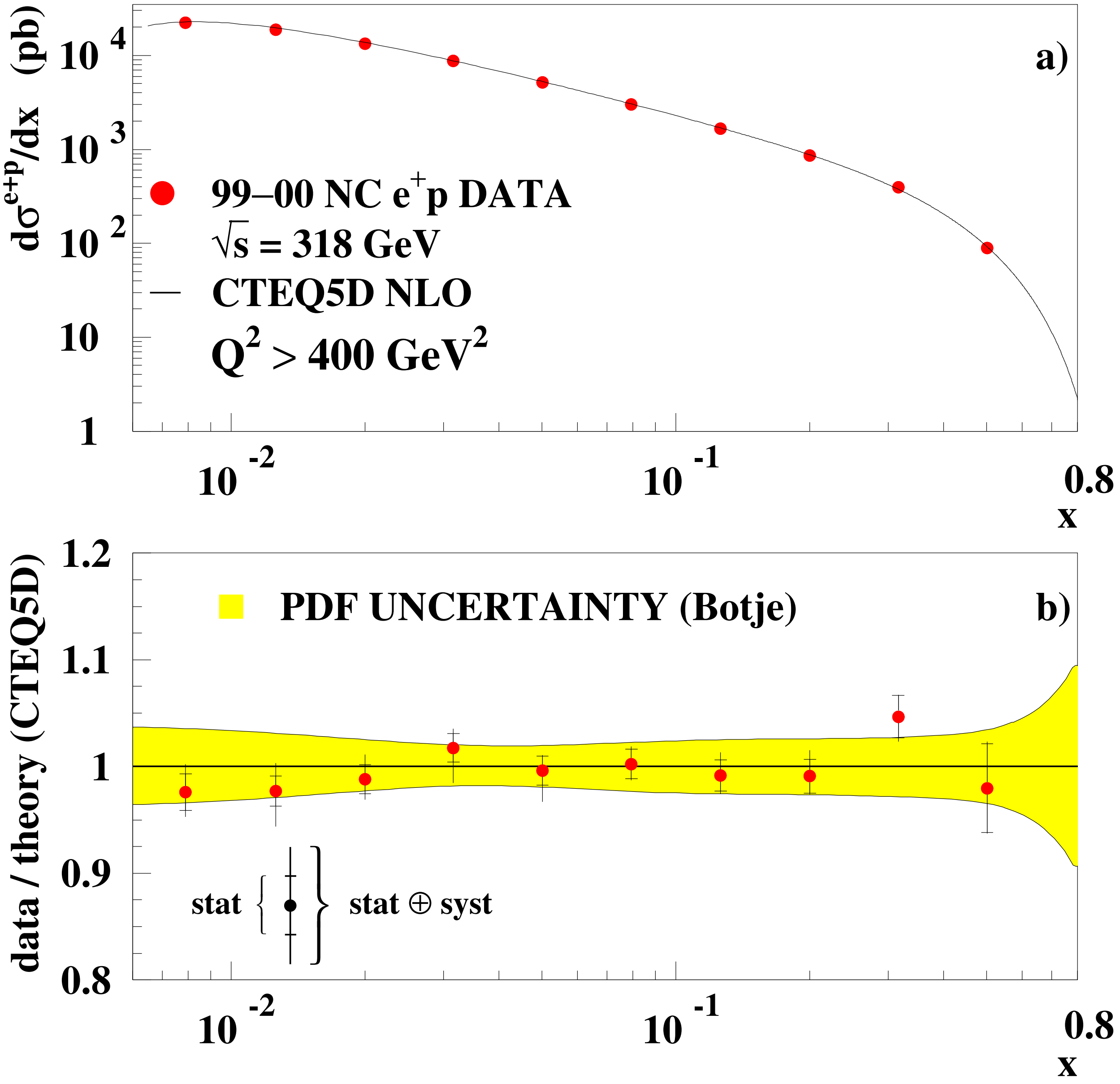

Figure 9.7: a) The single differential cross section $d\sigma^{e^+p}/dx$ for $Q^2 > 400\,\mathrm{GeV}^2$ and the Standard Model prediction obtained by using the CTEQ5D parton distributions (solid line). b) The ratio of the measured $d\sigma^{e^+p}/dx$ to the cross section obtained using CTEQ5D PDF. The shaded band gives the PDF uncertainty as calculated by Botje.

In Figure 9.6 the measurement of the cross section $d\sigma^{e^+p}/dy$ is shown. The majority of the events are found at low values of y. The cross section falls towards high y by one order of magnitude. The cross section is well described by the Standard Model prediction. The different fragmentation models constitute the main systematic uncertainty at lower y whereas at higher values the cut variations and the number of photoproduction events become significant.

The cross section $d\sigma^{e^+p}/dx$ was measured at three different minimum Q^2 values. The meas-

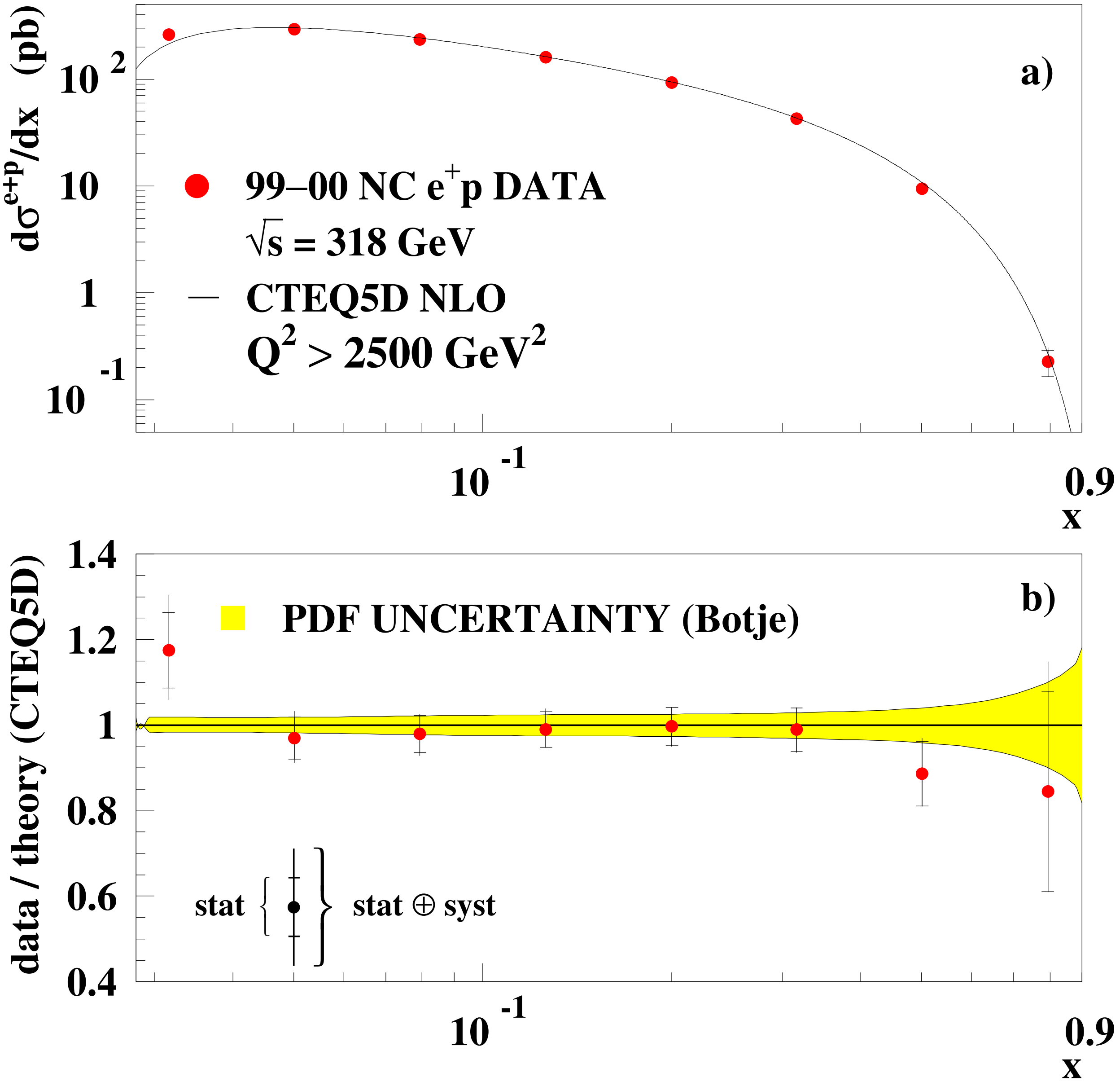

Figure 9.8: a) The single differential cross section $d\sigma^{e^+p}/dx$ for $Q^2 > 2500\,\mathrm{GeV}^2$ and the Standard Model prediction obtained by using the CTEQ5D parton distributions (solid line). b) The ratio of the measured $d\sigma^{e^+p}/dx$ to the cross section obtained using CTEQ5D PDF. The shaded band gives the PDF uncertainty as calculated by Botje.

urement of $d\sigma^{e^+p}/dx$ ($Q^2 > 400\,\mathrm{GeV}^2$) is shown in Figure 9.7. Over two orders of magnitude in x the cross section decreases also by two orders of magnitude towards higher x. A similar behaviour is observed for $d\sigma^{e^+p}/dx$ ($Q^2 > 2500\,\mathrm{GeV}^2$), shown in Figure 9.8. This reflects the low probability of hitting a quark with very high momentum (x close to one) at such large values of Q^2. The data is well described by the Standard Model in both cases.

If the selection cut is increased to ($Q^2 > 10000\,\mathrm{GeV}^2$) the measurable range of x is limited to

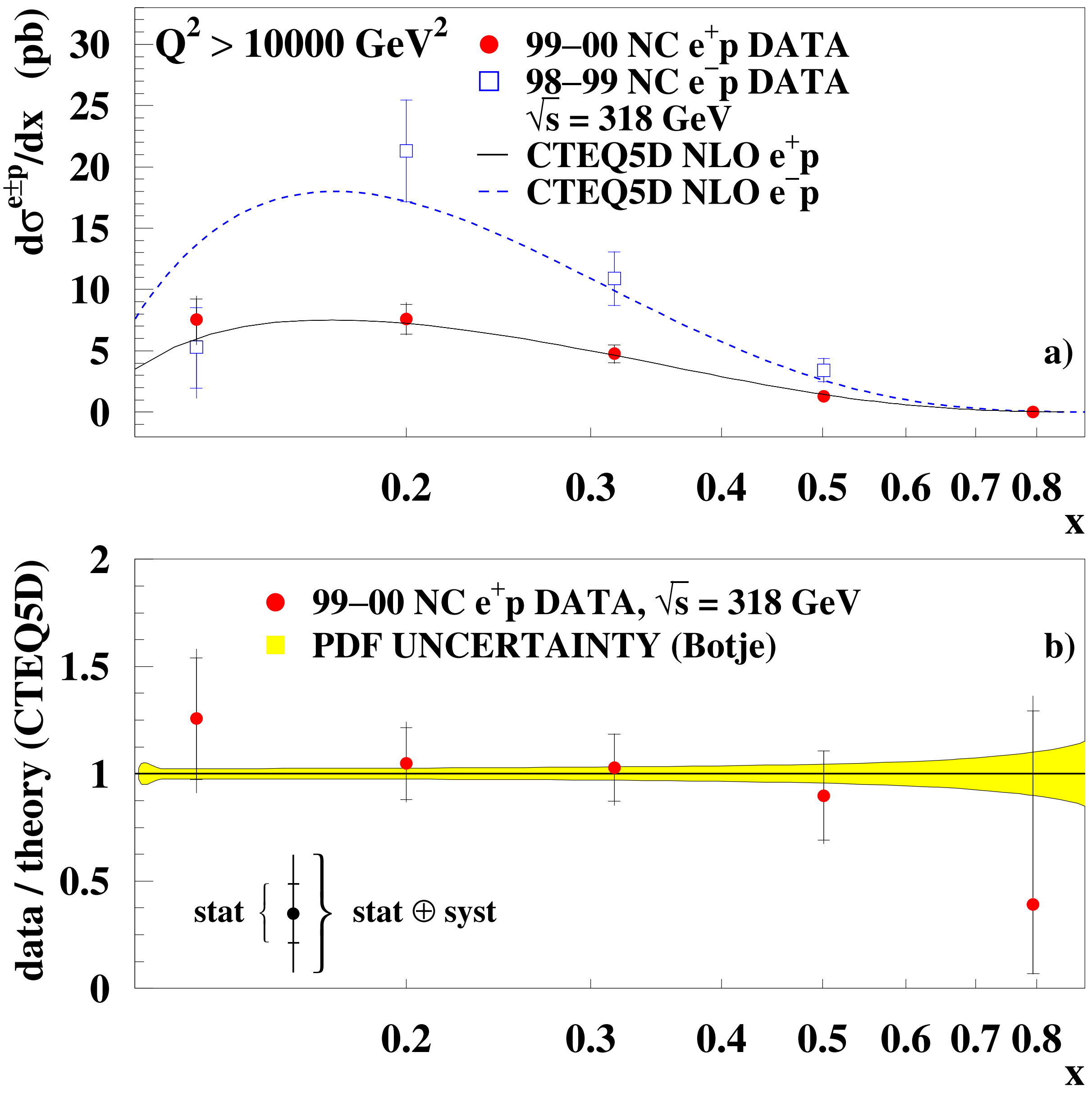

Figure 9.9: a) The single differential cross section $d\sigma^{e^{\pm}p}/dx$ ($Q^2 > 10000\,\mathrm{GeV}^2$) (full dots and open squares) and the Standard Model predictions obtained by using the CTEQ5D parton distributions (solid and dotted lines). b) The ratio of the measured $d\sigma^{e^{+}p}/dx$ ($Q^2 > 10000\,\mathrm{GeV}^2$) to the cross section obtained using CTEQ5D PDF. The shaded band gives the PDF uncertainty as calculated by Botje.

$x > 0.1$ due to kinematics. In this kinematic region the exchange of the Z^0 boson has to be taken into account. The measured cross sections $d\sigma^{e^{\pm}p}/dx$ as shown in Figure 9.9 are separated due to the different contribution of the γ–Z^0 interference. The measurement is dominated by statistical uncertainties for both e^+p and e^-p data.

9.5.3 The Double Differential Cross Section

The measurement of the double differential cross section is presented as a measurement of the reduced cross section, which has a much weaker kinematic dependence (cf. equation 1.9). The measurement presented here uses more luminosity than the previous ZEUS publication by a factor of two. Figure 9.10 shows $\tilde{\sigma}^{e^{\pm}p}$ at fixed values of Q^2 in the range between 200 GeV^2 and 1500 GeV^2 versus x whereas Figure 9.10 covers the Q^2 range between 2000 GeV^2 and 30000 GeV^2. Up to $Q^2 \approx 1000\,\mathrm{GeV}^2$ both cross sections are very similar and cannot be distinguished. The steep rise towards lower x values can be seen at each value of Q^2. With increasing Q^2, and approaching the squared mass of the Z^0 boson, the exchange of the Z^0 boson becomes visible by its destructive and constructive interference with the photon exchange to the e^+p and e^-p cross section respectively. The high precision of the e^+p analysis becomes very obvious in comparison to the e^-p data.

The same data can be plotted at fixed x versus Q^2 as shown in Figure 9.12. The different behaviour of the two cross sections towards higher values of Q^2 can be seen even more explicitly.

Furthermore by plotting $\Phi_{NC}^{e^{\pm}p}$, defined as

$$\Phi_{NC}^{e\pm p} = Y_{(+)} \cdot \tilde{\sigma}_{NC}^{e\pm p} = (F_2^{NC} \mp xF_3^{NC}) + (1-y)^2(F_2^{NC} \pm xF_3^{NC}) - y^2 F_L^{NC}\,, \qquad (9.13)$$

the effect of Z^0 exchange can be seen as a function of y as shown at fixed values of x in Figure 9.13. At low y and $(1-y)^2 \approx 1$ the term Φ_{NC} is proportional to $2F_2^{NC}$ and therefore $\Phi_{NC}^{e^+p}$ and $\Phi_{NC}^{e^-p}$ are the same. Assuming the F_L^{NC} contribution to be negligible at high Q^2 the term $\Phi_{NC}^{e^{\pm}p}$ approaches $F_2^{NC} \mp xF_3^{NC}$ towards higher values of y and therefore lower values of $(1-y)^2$. Due to the large contribution from photon exchange and therefore couplings to all type of quarks, an intuitive interpretation as in the case of charged current (CC) exchange is not possible. In CC the term Φ_{CC} depends in e^-p mainly on the u-quark content at $(1-y)^2 = 0$ and on the other hand is driven in e^+p by the d-quark content at $(1-y)^2 = 1$.

Independent of the variable chosen to present the data, the Standard Model is able to describe the measurement very well. This reflects the good agreement with the CTEQ5D PDFs. As already pointed out these PDFs were obtained mainly by low Q^2 HERA data (in addition to results from other experiments) and a good agreement at high Q^2 need not be observed. It is therefore a great success of the DGLAP evolution equations, that data at low Q^2 can successfully extrapolated to high values of Q^2.

The analysis of the double differential cross section of the previous e^+p data set taken in 1996/1997 is used by the ZEUS collaboration for a ZEUS NLO QCD fit [82]. Similar to the CTEQ approach, the parton densities are parametrised at some input scale Q_0^2 (7 GeV^2) as a function of x, are evoluted to higher values of Q^2 by QCD in terms of solving the DGLAP equations and are then fitted to the data. This fit considers only ZEUS data supplemented with DIS results from fixed target experiments and allows the extraction of the gluon and quark densities of the proton. In future the analysis presented in this thesis will also be used in the ZEUS NLO QCD fit. Since this analysis is restricted to high values of Q^2 and therefore also high values of x the measured cross sections are most sensitive to the valence quark distribution, due to the proton content (uud) in particular to the u valence quark distribution. The improvements in statistical as well as systematic uncertainties will allow precise determination of the u valence quark distribution from ZEUS data alone. This can then be compared in detail to the one obtained from fixed target experiments at the same values of x but much smaller values of Q^2. This cross check is not only important to test the Q^2 evolution of the parton densities but also

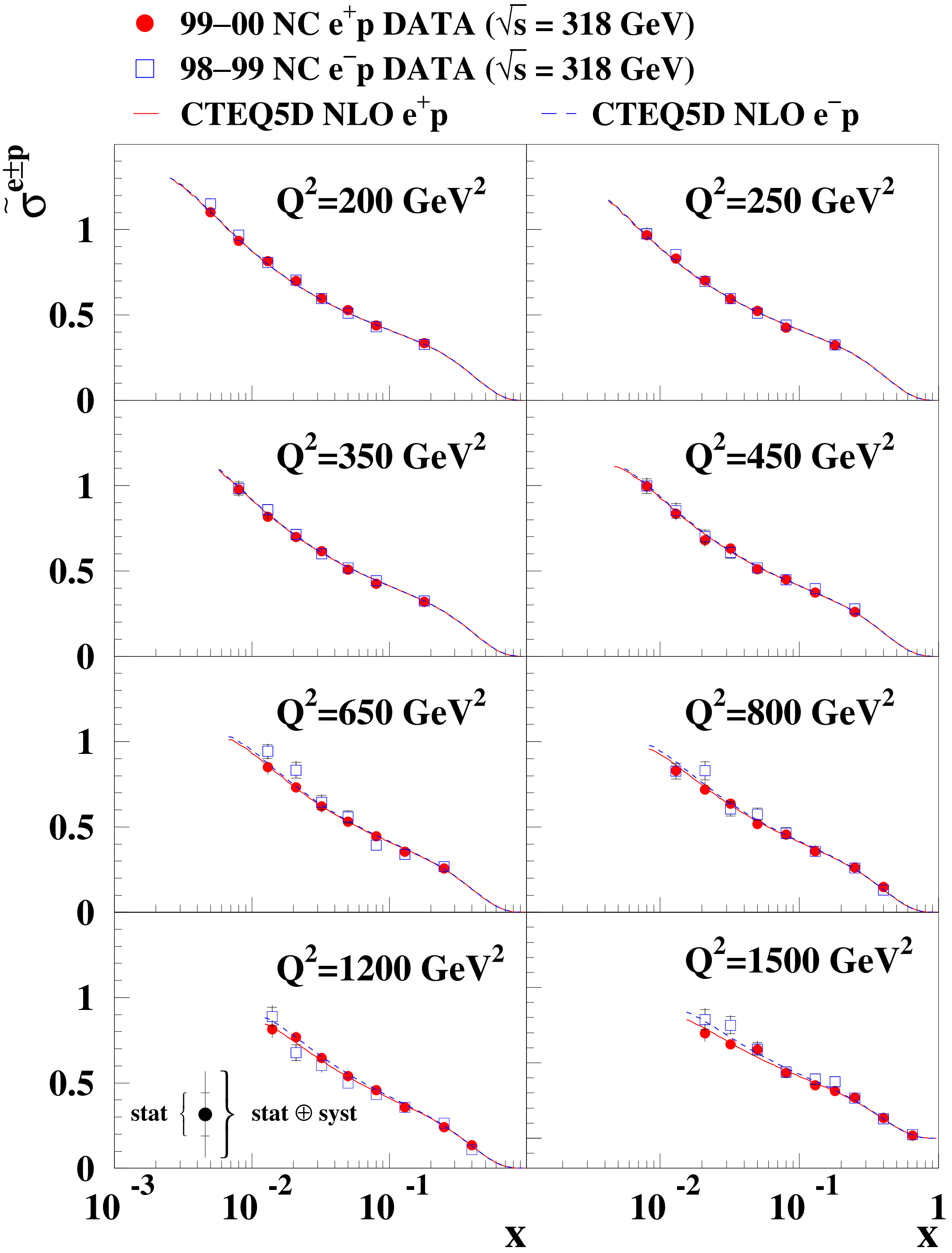

Figure 9.10: The reduced cross section $\tilde{\sigma}^{e^\pm p}$ (full dots (e^+p) and open squares (e^-p)) and the Standard Model predictions obtained by using the CTEQ5D parton distributions (solid (e^+p) and dotted lines (e^-p)) plotted at fixed Q^2 between 200 GeV^2 and 1500 GeV^2 as a function of x.

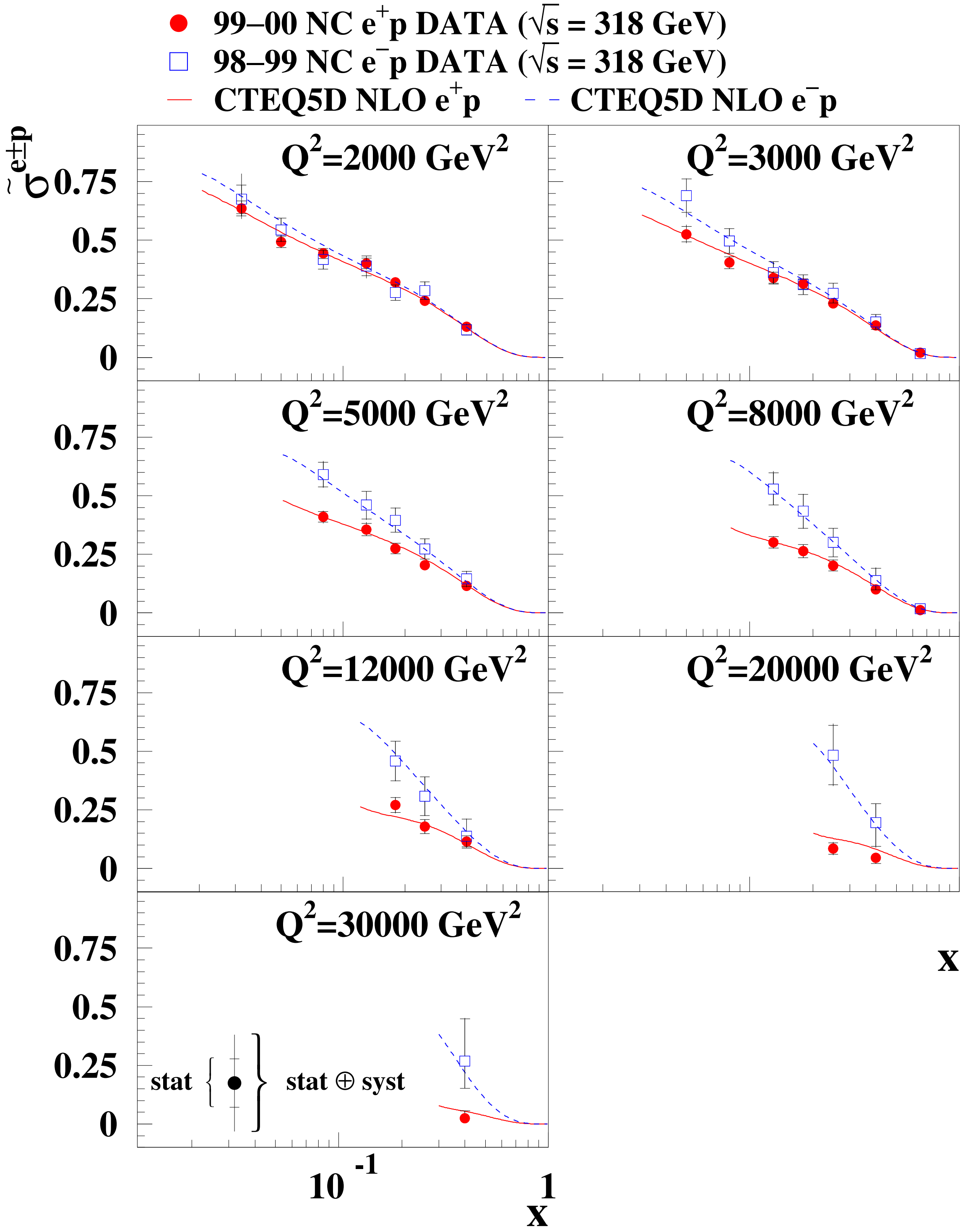

Figure 9.11: The reduced cross section $\tilde{\sigma}^{e^{\pm}p}$ (full dots (e^+p) and open squares (e^-p)) and the Standard Model predictions obtained by using the CTEQ5D parton distributions (solid (e^+p) and dotted lines (e^-p)) plotted at fixed Q^2 between 2000 GeV^2 and 30000 GeV^2 as a function of x.

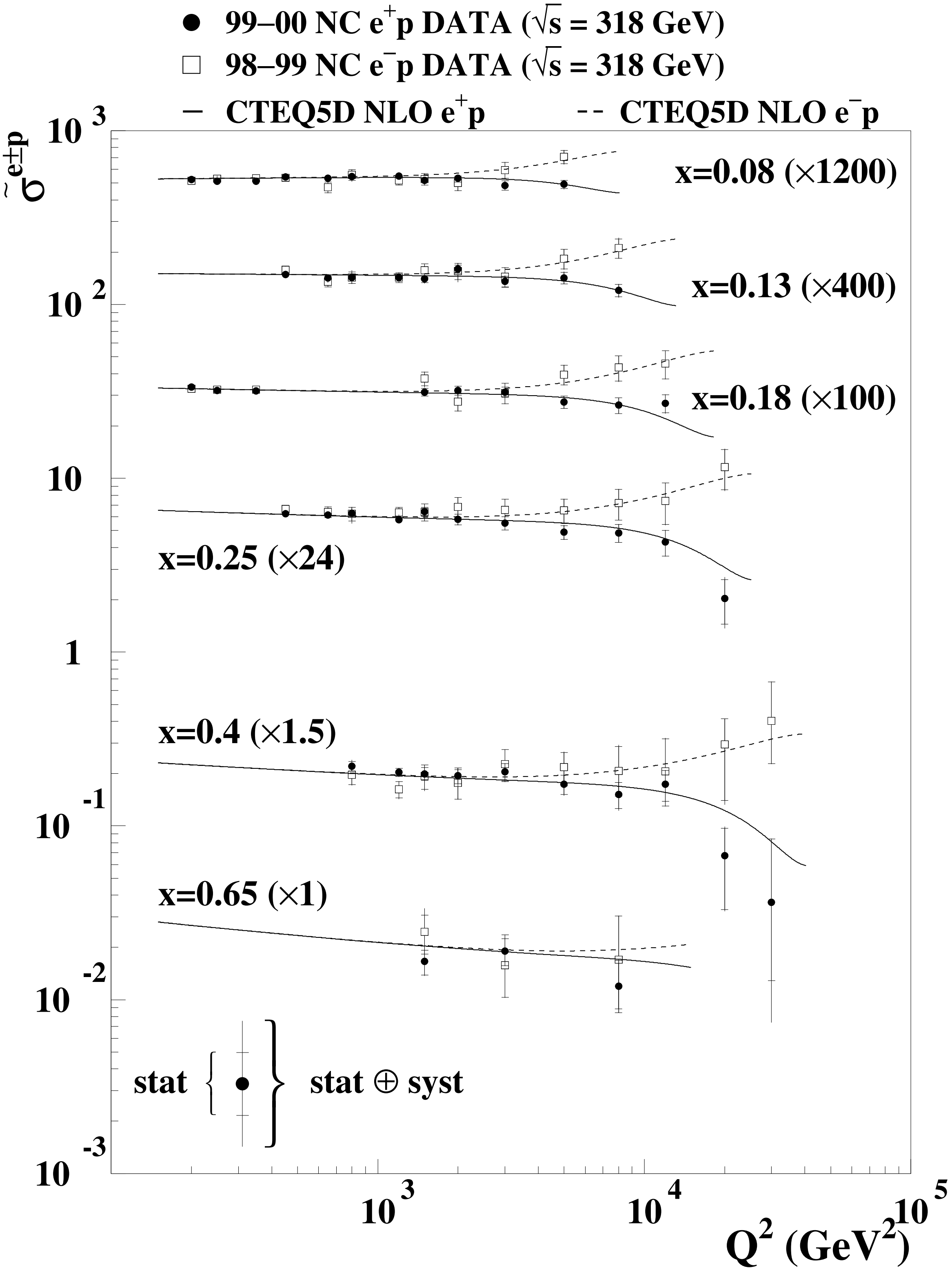

Figure 9.12: The reduced cross section $\tilde{\sigma}^{e^{\pm}p}$ (full dots (e^+p) and open squares (e^-p)) and the Standard Model predictions obtained by using the CTEQ5D parton distributions (solid (e^+p) and dotted lines (e^-p)) plotted at fixed x as a function of Q^2.

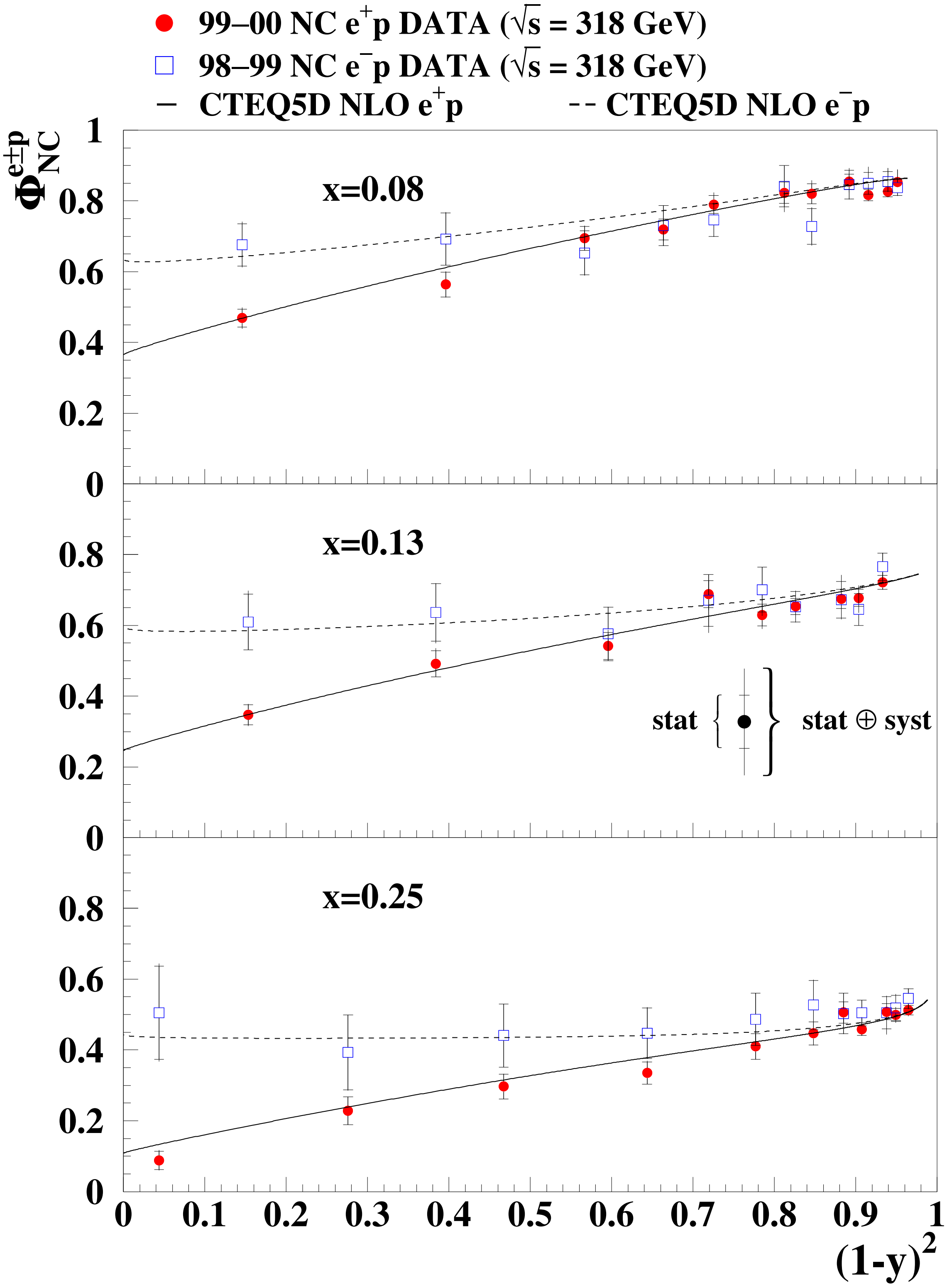

Figure 9.13: The cross section term $\Phi^{e^\pm p}_{NC}$ (full dots (e^+p) and open squares (e^-p)) and the Standard Model predictions obtained by using the CTEQ5D parton distributions (solid (e^+p) and dotted lines (e^-p)) plotted at fixed x as a function of $(1-y)^2$.

because the HERA data need in contrast to fixed target data no nuclear correction for which only phenomenological models can be used.

Moreover the precise knowledge of the cross section with unpolarised leptons is important for structure function measurements after the HERA upgrade. Cross sections will then be measured with different electron/positron longitudinal polarisations. Combinations of several polarised measurements can be used to test the reproducibility of the unpolarised measurement presented here. Any new physics effect will become evident when this measurement cannot be reproduced.

The different contribution of the interference term to the e^+p and e^-p cross section offers the possibility of an extraction of the structure function xF_3 from both data sets. This is discussed in more detail in the next section.

9.6 Extraction of the Proton Structure Function xF_3

Previous analyses of the structure function xF_3 were performed using beams of neutrinos or muons on targets of heavy nuclei such as iron. The neutrino measurements used charged current exchange where the effect of the structure function xF_3 is measurable also at moderate values of Q^2 ($1.3\,\mathrm{GeV}^2 < Q^2 < 199\,\mathrm{GeV}^2$) [12]. The measurability of xF_3 with charged lepton beams is made difficult by the dominant photon exchange. Nevertheless due to the different weak couplings to left and right handed particles, polarised beams enable a measurement at moderate values of Q^2. Polarised muons were used to extract one measurement in the range $40\,\mathrm{GeV}^2 < Q^2 < 180\,\mathrm{GeV}^2$ [13]. Both measurements were performed on fixed targets containing protons and neutrons which made a nuclear correction necessary.

At HERA a measurement of the proton structure function xF_3 was not possible until the machine changed the operation mode from e^+p to e^-p collisions in the run period 1998/1999 (in coincidence with an increase of the proton beam energy). For the first time an extraction with a proton target and at much higher momentum transfers compared to previous measurements was possible using the new e^-p data and previous e^+p data (96/97). However, the different proton beam energies in the two run periods had to be taken into account.

In this thesis the measurement of the e^+p data set of the run period 99/00 is used together with e^-p data for an extraction of the structure function xF_3. This has the advantage of a simpler mathematical extraction since the same kinematic factors are involved and profits from the improved systematic understanding gained with the e^+p data set of the run period 99/00. However, the measurement is dominated by statistical uncertainties mainly due to the limited amount of e^-p data.

9.6.1 Extraction Method

The measured NC DIS double differential cross sections in e^+p and e^-p collisions can be used to extract the structure function xF_3^{NC}. As can be seen from equation 1.9 the structure function xF_3^{NC} can be expressed by the difference of the reduced cross sections:

$$xF_3^{NC} = \left(\frac{Y_{(+)}}{2Y_{(-)}}\right)\left[\tilde{\sigma}_{NC}^{e^-p} - \tilde{\sigma}_{NC}^{e^+p}\right] \quad \text{with } Y_{(\pm)} = 1 \pm (1-y)^2\,, \tag{9.14}$$

where the other structure function terms cancel due to the same kinematic factors in the used analyses.

9.6.2 Measurement of the Structure Function xF_3

The parity violating term of the reduced cross section $\tilde{\sigma}_{NC}$ becomes visible at $Q^2 > 1000\,\mathrm{GeV}^2$, but starts to be significant at higher values $Q^2 \approx 3000\,\mathrm{GeV}^2$ (cf. Figures 9.10,9.11). Therefore the measurement was restricted to high momentum transfers $Q^2 \geq 3000\,\mathrm{GeV}^2$. In addition the number of bins was reduced to increase the statistical precision. The reduced cross section in these bins is shown in Figure 9.14.

I. Determination of the Uncertainties

The statistical uncertainty was derived using error propagation of the statistical uncertainties from the two reduced cross sections. It is therefore given by:

$$\Delta xF_3^{NC} = \left(\frac{Y_{(+)}}{2Y_{(-)}}\right)\sqrt{(\Delta\tilde{\sigma}_{NC}^{e^-p})^2 + (\Delta\tilde{\sigma}_{NC}^{e^+p})^2}\,. \tag{9.15}$$

Although the dominant uncertainty of this measurement is statistical the systematic uncertainty was carefully studied as well. The structure function xF_3 was re-calculated with each systematic variation in the same way as the systematic uncertainty was obtained in the cross section measurement (cf. 9.4). All variations resulting in a larger value of xF_3 contribute to the upper systematic uncertainty and vice versa. The largest contributions originate from the variation of the number of photoproduction background events and the different fragmentation scheme.

II. Result of the Structure Function xF_3

The determination of the structure function xF_3 is shown in Figure 9.15. In five bins of Q^2 ($3000\,\mathrm{GeV}^2 < Q^2 < 30000\,\mathrm{GeV}^2$) the dependence on x is shown. The measurement of xF_3 reflects the valence quark distribution. It is zero at $x \approx 1$ and grows for lower values of x until $x \approx 0.1$. Although the measurement is dominated by statistical uncertainties a value no longer compatible with zero is clearly observed at lower x. The presence of the valence quarks in the proton is proven.

The limitation of the statistical precision is related to the small e^-p data sample corresponding to an integrated luminosity of $15.8\,\mathrm{pb}^{-1}$ in comparison to the four times larger luminosity of the e^+p data. A further combination with previous ZEUS e^+p data can not improve the statistical uncertainty significantly.

As discussed in section 1.4 the structure function xF_3 is dominated by the γ–Z^0 interference term $xF_3^{\gamma Z}$. Therefore $xF_3^{\gamma Z}$ can be obtained by simply multiplying xF_3 with a kinematic factor:

$$xF_3^{\gamma Z}(x, Q^2) \approx \frac{8(Q^2 + M_Z^2)\sin^2\theta_W\cos^2\theta_W}{Q^2} \cdot xF_3(x, Q^2)\,. \tag{9.16}$$

The result is shown in Figure 9.16 at different values of Q^2 as a function of x. The Q^2 dependence of the $xF_3^{\gamma Z}$ Standard Model prediction is very weak as can be seen from the small

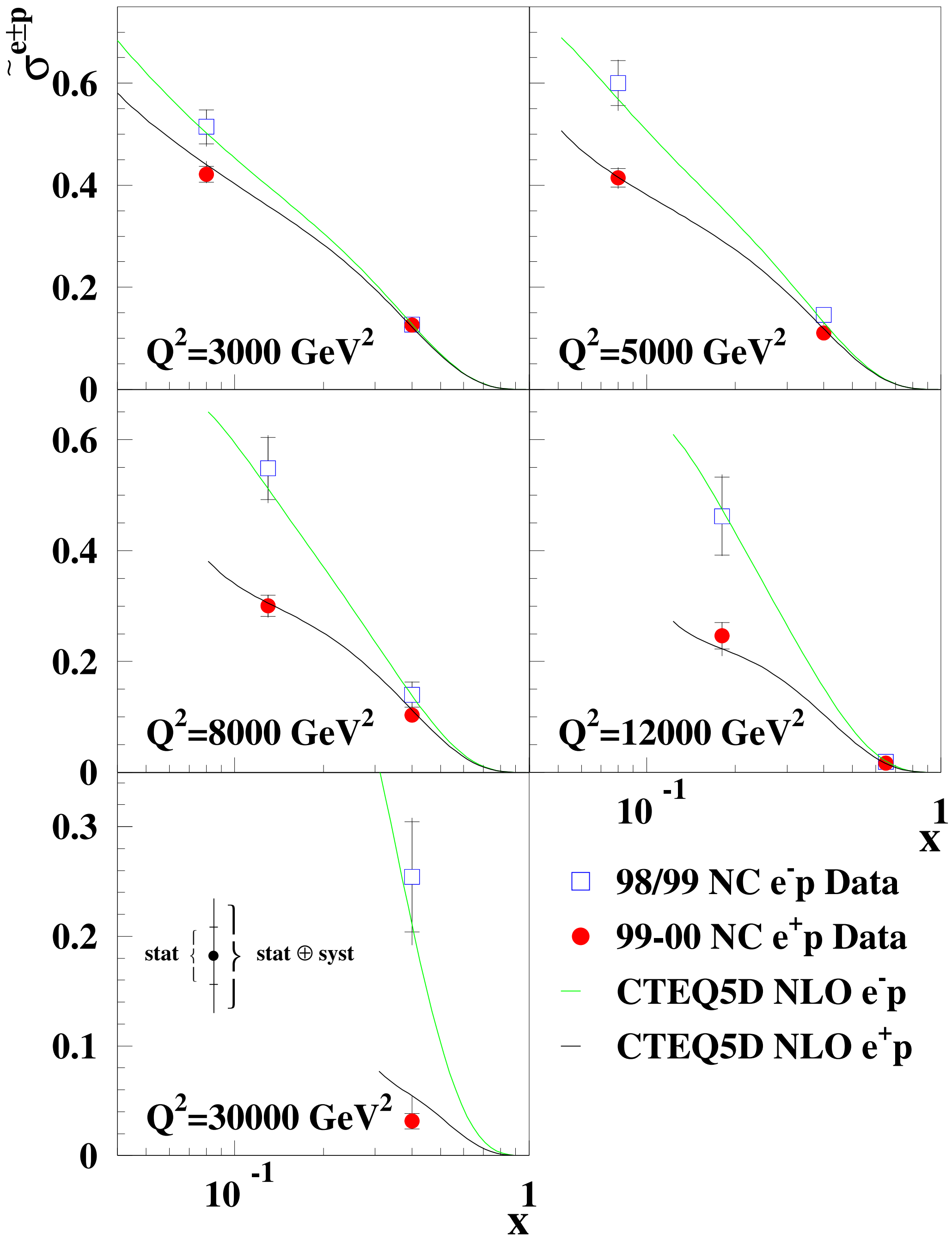

Figure 9.14: The reduced cross section $\tilde{\sigma}^{e^{\pm}p}$ (full dots and open squares) and the Standard Model predictions obtained by using the CTEQ5D parton distributions (solid and dotted lines) plotted at fixed Q^2 between $3000\,\mathrm{GeV}^2$ and $30000\,\mathrm{GeV}^2$ as a function of x in the binning used for extraction of the structure function xF_3.

differences between the plotted lines. The data are in agreement with the prediction, however, the statistical uncertainty is large. Additional studies concerning ZEUS xF_3 measurements can be found in [83]. Similar to the shape of xF_3, $xF_3^{\gamma Z}$ increases towards lower values of x and reaches a maximum at $x \approx 0.1$ in agreement with the expectation for the valence quark

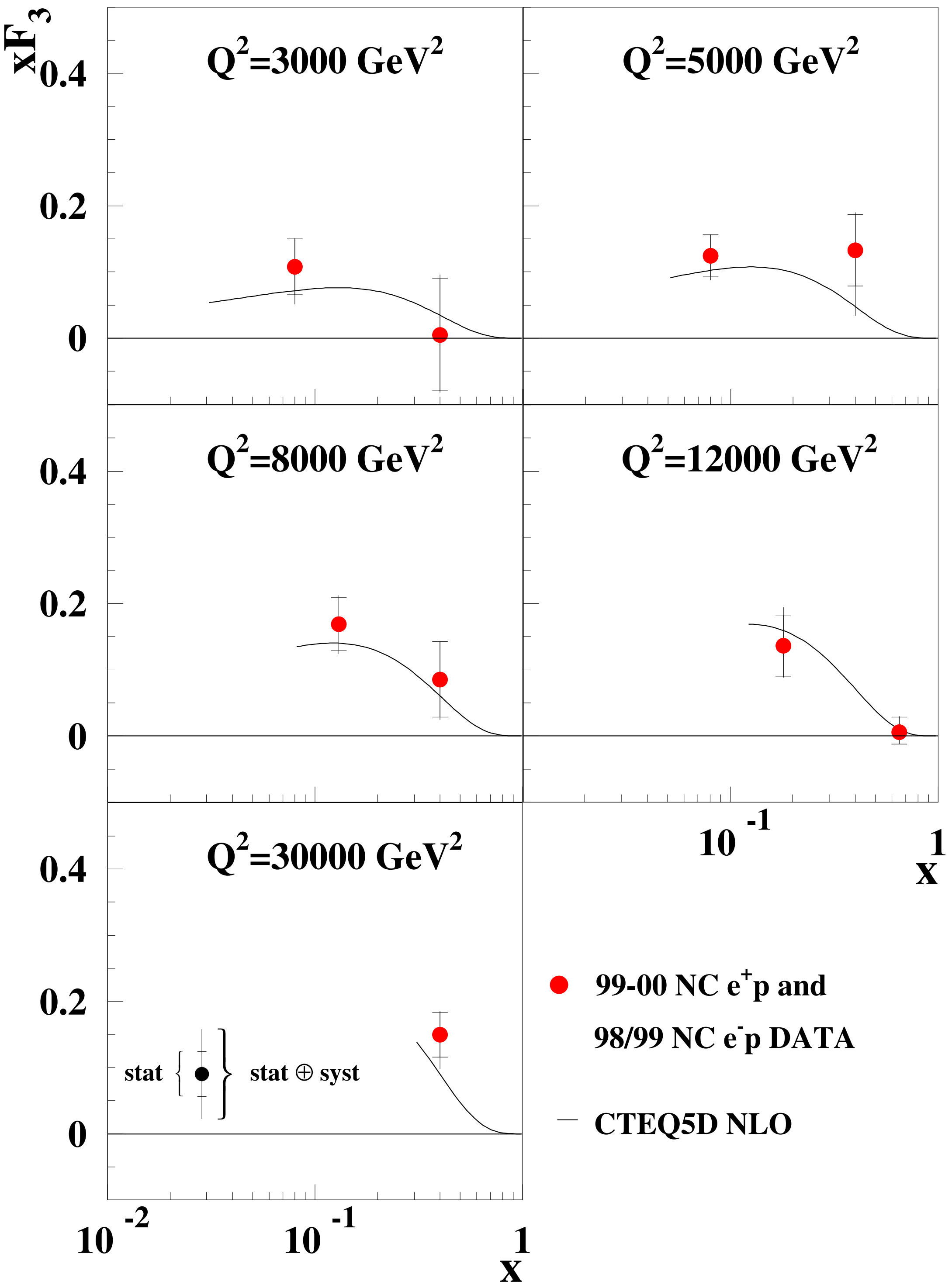

Figure 9.15: The structure function xF_3 (full dots) and the Standard Model predictions obtained by using the CTEQ5D parton distributions (solid lines) plotted at fixed Q^2 between $3000\,\mathrm{GeV}^2$ and $30000\,\mathrm{GeV}^2$ as a function of x.

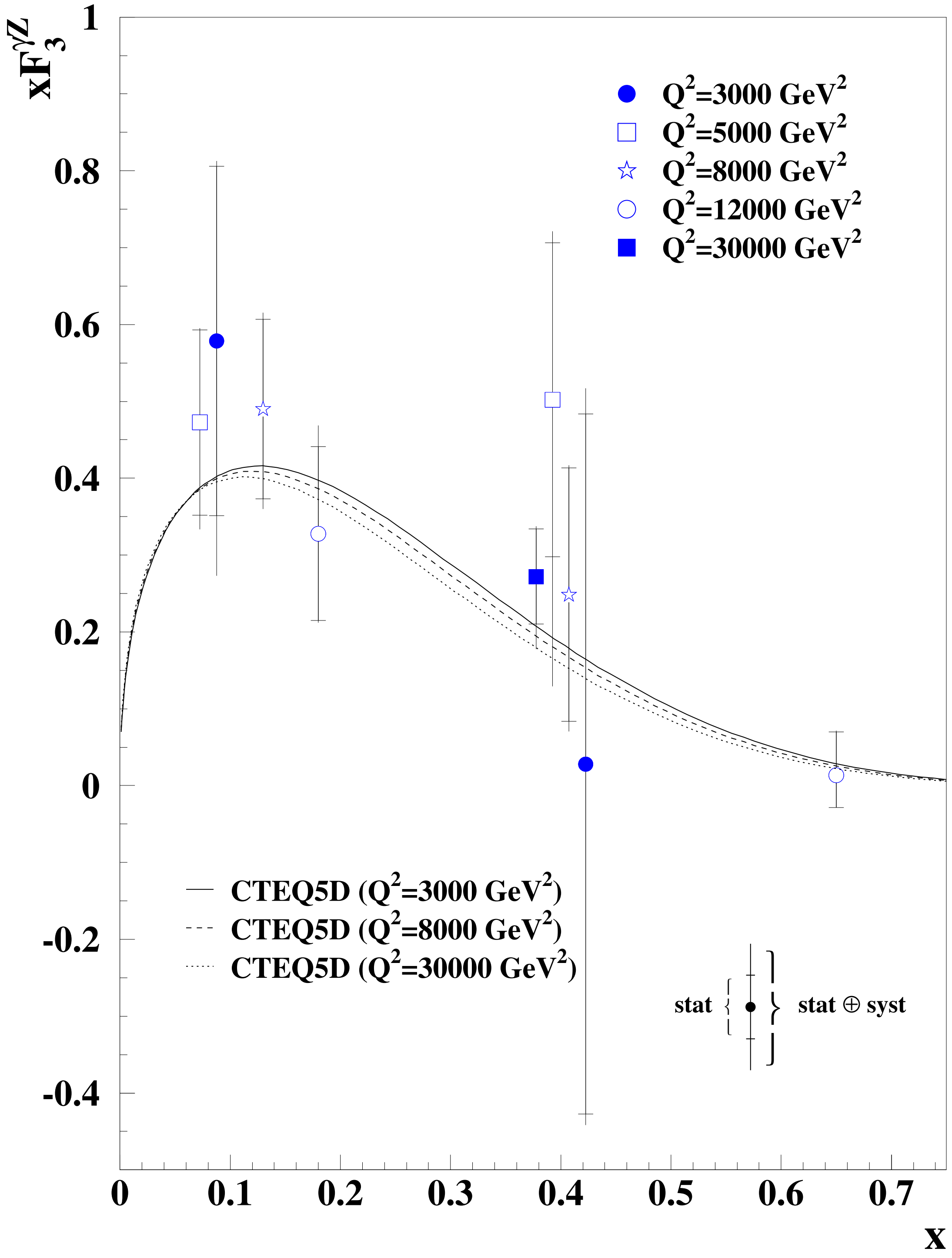

Figure 9.16: The structure function term $xF_3^{\gamma Z}$ and the Standard Model predictions at different values of Q^2 obtained by using the CTEQ5D parton distributions (lines) plotted for Q^2 between 3000 GeV^2 and 30000 GeV^2 as a function of x (The first two points both belong to $x = 0.08$ and are separated for comparison as well as the four points close $x = 0.4$).

distribution. The drop to very small values of x could not been measured. A more precise measurement will be possible after the HERA upgrade in 2002, if e^-p data are collected. After collecting $150\,\mathrm{pb}^{-1}$ (corresponding to approx. one year data taking period) e^-p data and the same amount of e^+p data the statistical uncertainties could be more than halved. Further improvements can be achieved with polarised lepton beams which will also be available after the HERA upgrade.

9.7 Searches for Contact Interactions

A preliminary result[4] of the here presented measurement of the single differential cross section $d\sigma^{e^+p}/dQ^2$ was used by the ZEUS collaboration in combination with previous ZEUS data sets to search for physics beyond the Standard Model in terms of signatures of contact interactions. Since the Standard Model is able to describe the data very well and no significant deviations were observed, the analysis can only set limits on the minimum value of the mass scale where new physics sets in. The results [84] for different contact interaction models (cf. section 1.7) are briefly discussed in the following paragraphs.

9.7.1 General Models

In the general case (compositeness model) the analysis covers 15 models assuming different helicity structures which fulfil the parity conserving relation:

$$\eta^{eq}_{LL} + \eta^{eq}_{LR} - \eta^{eq}_{RL} - \eta^{eq}_{RR} = 0\,. \tag{9.17}$$

Limits on the minimum mass scale Λ are derived for each model in two scenarios, $\eta < 0$ (denoted with Λ^-) and $\eta > 0$ (denoted with Λ^+). The limit setting is based on so-called MC experiments in which the measurement is simulated a lot of times with one particular input model (a similar method was used by the LEP experiments to derive their limits on the mass of the Higgs boson). In this method all models which result in a worse agreement with the Standard Model prediction than the measurement of the data in more than 95% of the MC experiments are excluded on 95% confidence level (CL).

Table 9.1 contains the lower limit on Λ^+ and Λ^- in the 15 considered models. The range of the obtained limits on the mass scale Λ are in the range between 2.6 TeV to 7.0 TeV. This result is compatible with the measurement of the H1 collaboration (limits between 1.3 TeV to 5.5 TeV, including only e^+p data at a centre of mass energy $\sqrt{s} \approx 300\,\mathrm{GeV}$) [87] and with measurements at the TEVATRON, where via Drell-Yan production limits between 2.5 TeV to 6.0 TeV were achieved [89]. The most stringent limits were obtained at LEP (between 3.0 TeV to 10.0 TeV) [88].

9.7.2 Limits on Leptoquark Mass

The analysis of the minimum mass of a heavy leptoquark (i.e. $M \gg \sqrt{s}$) considers 14 possible leptoquark states according to a general classification [91]. The effective contact interaction

---

[4] The ZEUS preliminary result presented at the DIS Workshop in Bologna in May 2001 was used in this study.

ZEUS (prel.) 1994-2000 $e^{\pm}p$										
	Coupling structure								95% CL [TeV]	
Model	η^{ed}_{LL}	η^{ed}_{LR}	η^{ed}_{RL}	η^{ed}_{RR}	η^{eu}_{LL}	η^{eu}_{LR}	η^{eu}_{RL}	η^{eu}_{RR}	Λ^-	Λ^+
VV	$+\eta$	$+\eta$	$+\eta$	$+\eta$	$+\eta$	$+\eta$	$+\eta$	$+\eta$	7.0	6.5
AA	$+\eta$	$-\eta$	$-\eta$	$+\eta$	$+\eta$	$-\eta$	$-\eta$	$+\eta$	5.3	4.6
VA	$+\eta$	$-\eta$	$+\eta$	$-\eta$	$+\eta$	$-\eta$	$+\eta$	$-\eta$	3.4	3.3
X1	$+\eta$	$-\eta$			$+\eta$	$-\eta$			4.0	2.7
X2	$+\eta$		$+\eta$		$+\eta$		$+\eta$		4.7	4.7
X3	$+\eta$			$+\eta$	$+\eta$			$+\eta$	4.3	4.2
X4		$+\eta$	$+\eta$			$+\eta$	$+\eta$		5.6	5.6
X5		$+\eta$		$+\eta$		$+\eta$		$+\eta$	4.8	4.8
X6			$+\eta$	$-\eta$			$+\eta$	$-\eta$	2.6	3.9
U1					$+\eta$	$-\eta$			4.1	3.6
U2					$+\eta$		$+\eta$		5.8	5.3
U3					$+\eta$			$+\eta$	5.8	5.2
U4						$+\eta$	$+\eta$		6.4	5.9
U5						$+\eta$		$+\eta$	6.0	5.5
U6							$+\eta$	$-\eta$	2.8	3.7

Table 9.1: Table of the 95% confidence level limits of the mass scale in general contact interaction models [84].

coupling can be expressed via:

$$\eta^{eq}_{ij} = a^{eq}_{ij} \cdot \left(\frac{\lambda_{LQ}}{M_{LQ}}\right)^2 \tag{9.18}$$

in which M_{LQ} is the mass of the leptoquark, λ_{LQ} is the coupling of it and a^{eq}_{ij} depends on the leptoquark type and is given in table 9.2.

The analysis is restricted to leptoquarks which couple to the electron and the first generation of quarks (u, d). The results on the 95% CL limit on the ratio of M_{LQ}/λ_{LQ} is given in table 9.2. The limits on the ratios were found to be in the range between 0.31 TeV and 1.42 TeV. Similar limits are obtained by the H1 collaboration.

9.7.3 Limits on the Large Extra Dimension Scale and Quark Radius

The 95% CL lower limits on the effective Planck mass scale in models with large extra dimensions were determined to be M_S^+ =0.81 TeV in case of positive couplings and M_S^- =0.82 TeV in case of negative couplings. This is in good agreement with the limits determined by the H1 collaboration (M_S^+ =0.63 TeV and M_S^- =0.93 TeV). In comparison limits above 1 TeV were derived in $p\bar{p}$ collisions by measuring e^+e^- and $\gamma\gamma$ production [85] and in e^+e^- collisions, taking into account all final states [86].

The ZEUS measurements of NC DIS Q^2 distributions are compared to possible effects of graviton exchange are shown in Figure 9.17.

In addition the limit on the quark radius are shown. By combining all ZEUS data from 1994-2000 a quark radius bigger than $0.73 \cdot 10^{-16}$ cm could be excluded at the 95% CL (assuming the probing electron or positron to be pointlike). This limit is smaller by a factor of two

ZEUS (prel.) 1994-2000 $e^{\pm}p$

	Coupling structure								95% CL [TeV]
Model	a^{ed}_{LL}	a^{ed}_{LR}	a^{ed}_{RL}	a^{ed}_{RR}	a^{eu}_{LL}	a^{eu}_{LR}	a^{eu}_{RL}	a^{eu}_{RR}	M_{LQ}/λ_{LQ}
$S^L_\circ$					$+\frac{1}{2}$				0.75
$S^R_\circ$								$+\frac{1}{2}$	0.69
$\tilde{S}^R_\circ$				$+\frac{1}{2}$					0.31
$S^L_{1/2}$						$-\frac{1}{2}$			0.91
$S^R_{1/2}$			$-\frac{1}{2}$				$-\frac{1}{2}$		0.69
$\tilde{S}^L_{1/2}$		$-\frac{1}{2}$							0.50
S^L_1	$+1$				$+\frac{1}{2}$				0.55
$V^L_\circ$	-1								0.69
$V^R_\circ$				-1					0.58
$\tilde{V}^R_\circ$								-1	1.03
$V^L_{1/2}$		$+1$							0.49
$V^R_{1/2}$			$+1$				$+1$		1.15
$\tilde{V}^L_{1/2}$						$+1$			1.26
V^L_1	-1				-2				1.42

Table 9.2: The 95% CL lower limit on M_{LQ}/λ_{LQ} for different models of scalar and vector leptoquarks and their coupling coefficients a^{eq}_{ij}. Empty entries correspond to $a^{eq}_{ij} = 0$ [84].

in comparison to the limit obtained by the H1 collaboration ($R_q < 1.7 \cdot 10^{-16}$ cm) [87] and similar to the limit obtained by the CDF collaboration ($R_q < 0.79 \cdot 10^{-16}$ cm) [89]. A stronger limit was recently published by the L3 collaboration based on quark pair production at LEP2 ($R_q < 0.3 \cdot 10^{-16}$ cm) [90].

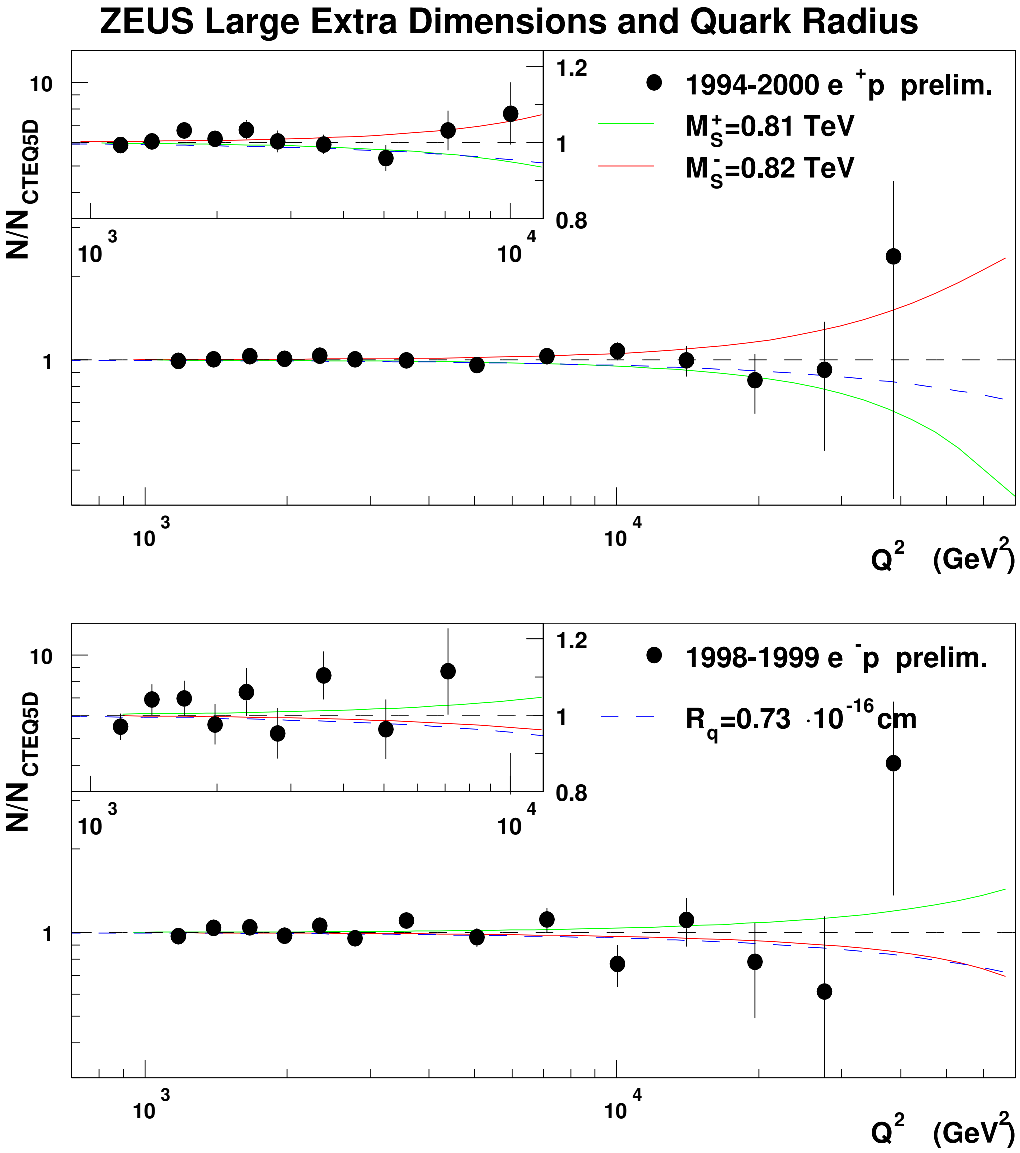

Figure 9.17: ZEUS data compared to possible effects of graviton exchange with effective Planck mass scales M_S^+ and M_S^- [84]. In addition the upper limit on the quark radius R_q is shown. The limits on M_S^+, M_S^- and R_q are shown in the ZEUS e^+p data (top) and in ZEUS e^-p data (bottom).

Summary and Outlook

This thesis has presented the first measurement of high Q^2 ($> 185\,\mathrm{GeV}^2$) neutral current cross sections in e^+p data taken with the ZEUS detector at a centre of mass energy of $\sqrt{s} \approx 318\,\mathrm{GeV}$. Besides the enlarged centre of mass energy the integrated luminosity of $63\,\mathrm{pb}^{-1}$ used for the measurement of the double (single) differential cross section was increased by $\sim 100\%$ ($\sim 30\%$) with respect to previous ZEUS analyses.

The large data set offers the most precise study of the proton structure at length scales $\mathcal{O}\,(1/1000)$ of the proton radius so far. The high statistical precision leads not only to an accurate measurement of the cross section but also improves the understanding of both the detector itself and the deviations between data and MC. Of great interest were the positron energy corrections in the BCAL and the determination of the corresponding systematic uncertainty. Furthermore, a precise measurement of the underlying longitudinal vertex distribution was performed. This forms a basis of the MC production for all ZEUS analyses of that data sample.

The data was compared with MC predictions combining all relevant physics processes. A bin-by-bin unfolding procedure was used to extract the single and double differential cross sections. The measurement is in good agreement with the Standard Model prediction derived from the CTEQ5D parametrisation of the PDFs. Since the CTEQ5D PDFs were mainly determined with low Q^2 data, the good description at shortest distances is a remarkable success for the NLO DGLAP evolution formalism extrapolating the PDFs from low to high values of Q^2. Moreover, this analysis can be used in QCD fits to adjust the PDFs to the data and to reduce their uncertainties. The precise knowledge of the structure of the proton is vital for both present (TEVATRON) and future hadron colliders like LHC.

The good description of the data by the Standard Model allows the determination of upper limits on the coupling strength of new physics phenomena, which may occur as contact interactions. Results from this analysis were used in combination with analyses of previous data sets to study the coupling strength of new physics phenomena in the framework of different theoretical models. New interactions with coupling strength up to $\mathcal{O}\ 1\,\mathrm{TeV}$ can be excluded at 95% C.L. depending on the concrete model used.

To study the high Q^2 effects resulting from the exchange of the Z^0-boson an additional analysis was performed on the e^-p data sample, which corresponds to an integrated luminosity of $15.8\,\mathrm{pb}^{-1}$. The comparison between both data sets makes explicit the constructive and destructive character of the γ–Z^0-interference to the e^-p and e^+p cross sections respectively. An extraction of the structure function xF_3 was possible by combining both data samples and therefore the contribution of the valence quarks alone to the cross section became visible. However, the uncertainty of the measurement is statistically dominated.

A more precise measurement will be possible after the upgrade of the HERA collider. Starting in 2002 HERA will deliver an integrated luminosity of $\sim 150\,\mathrm{pb}^{-1}$ per year. Additional improvements can be achieved by exploiting the longitudinally polarised lepton beams, which will be available after the upgrade. Since the weak interaction depends on the helicity, the couplings of the $W^{\pm}$ and Z^0 bosons can be studied in more detail.

To fully benefit from the new experimental conditions, the ZEUS detector was upgraded by an improved tracking system consisting of a straw-tube-tracker and a microvertex detector. The silicon strip sensors used in the microvertex detector were extensively tested and studied before their installation. A complete understanding of the sensors and their performance is crucial for an optimal use of the new device. Key parameters as the intrinsic resolution of the detectors, the dependence of the resolution on the track angle and the charge couplings between strip implantations were determined.

Although analyses of heavy quarks and charged current measurements will profit most from the improved tracking capabilities future neutral current analyses will also benefit from the improved measurement of the scattered electron track (mainly in the forward direction, outside the CTD acceptance region) and better vertex reconstruction. In addition higher statistics and smaller systematic uncertainties will offer a more precise insight into the structure of the proton at shortest distances.

Appendix A

Efficiencies and Purities of the Single Differential Cross Section Measurements

The efficiencies and purities of the cross section measurements $d\sigma/dQ^2$ and $d\sigma/dy$ ($Q^2 > 400\,\mathrm{GeV}^2$) are shown in Figure A.1. The purity of $d\sigma/dQ^2$ is in all bins larger then 70%. A change in the bin widths cause the distribution to be discrete between bin 14 and bin 15. In general the efficiency distribution follows the one of the purity of $d\sigma/dQ^2$ except in the low Q^2 region, where the supercrack cut and the RCAL radius cut lead to a reduction of the efficiency.

The purity and efficiency of $d\sigma/dy$ is in all bins higher than 40% except in the two bins at highest y where the efficiency drops below 30%. This is mainly due to radiative events which cause the event to be reconstructed in other bins of y.

In the measurement of $d\sigma/dx$ ($Q^2 > 400\,\mathrm{GeV}^2$) and ($Q^2 > 2500\,\mathrm{GeV}^2$) purities and efficiencies above 50% are achieved as can be seen in Figure A.2. The only exception is the highest x bin in $d\sigma/dx$ ($Q^2 > 400\,\mathrm{GeV}^2$), where losses due to the forward beam hole become important.

The cross section $d\sigma/dx$ ($Q^2 > 10000\,\mathrm{GeV}^2$) is measured with efficiencies and purities above 55% in all bins.

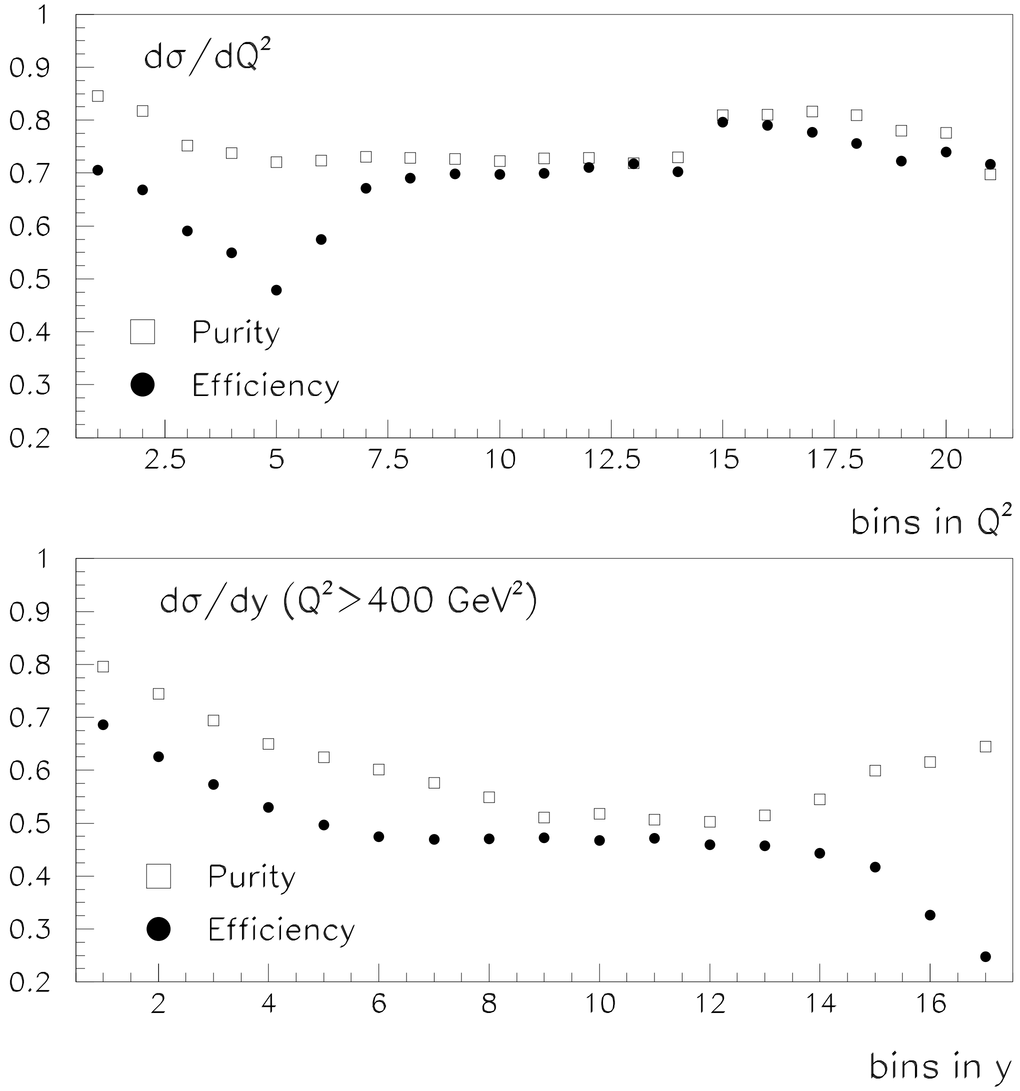

Figure A.1: Efficiencies and purities of the cross section measurements $d\sigma/dQ^2$ (top) and $d\sigma/dy$ ($Q^2 > 400\,\mathrm{GeV}^2$) (bottom).

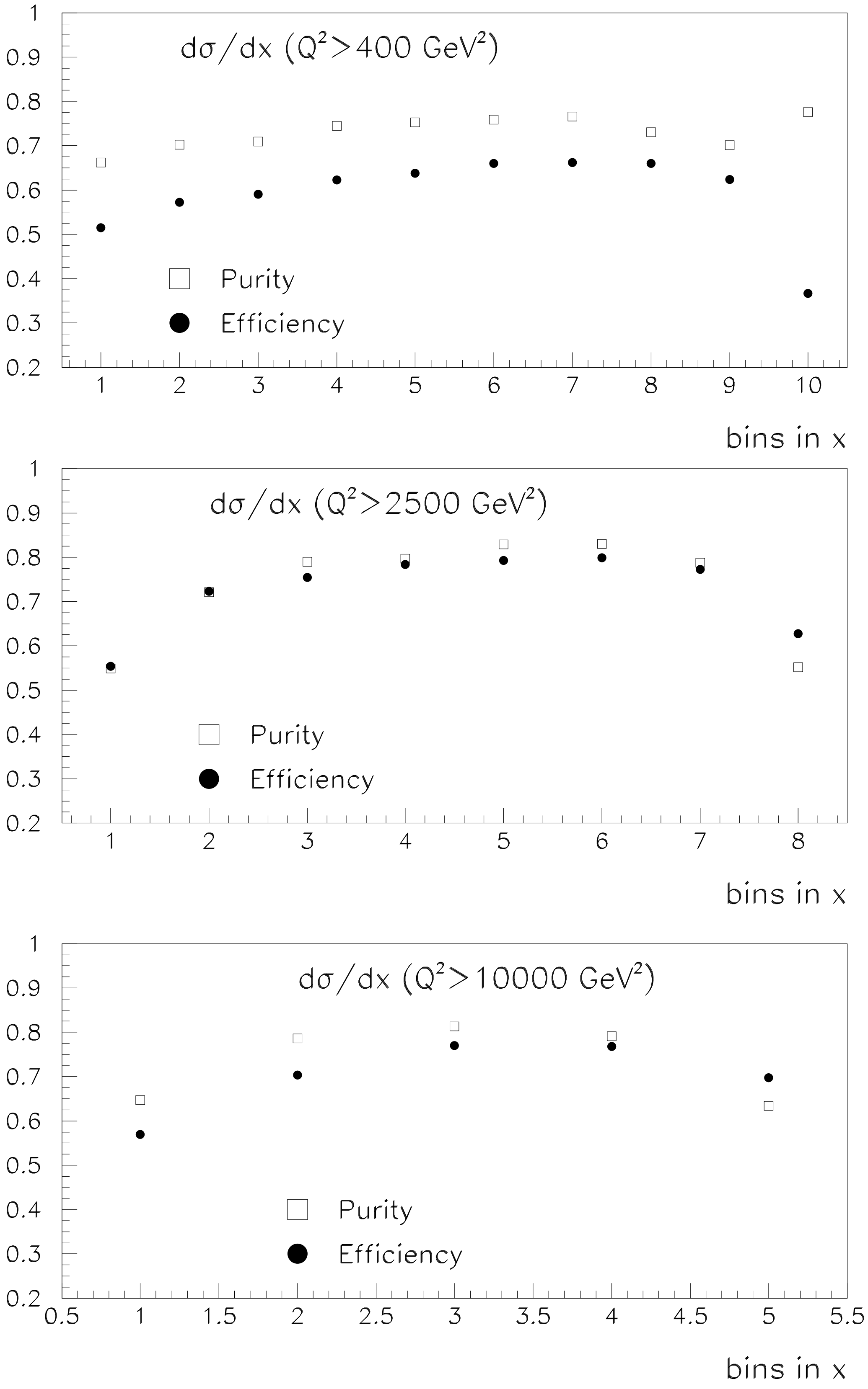

Figure A.2: Efficiencies and purities of the cross section measurements $d\sigma/dx$ ($Q^2 > 400\,\mathrm{GeV}^2$) (top), $d\sigma/dx$ ($Q^2 > 2500\,\mathrm{GeV}^2$) (middle) and $d\sigma/dx$ ($Q^2 > 10000\,\mathrm{GeV}^2$) (bottom).

Bibliography

[1] J.I. Friedmann, H.W. Kendall, R.E. Taylor, *Rev. Mod. Phys.*, **63**, 573,597,615 (1991).

[2] J.D. Bjorken, *Phys. Rev.*, **179**, 1547 (1969).

[3] R.P. Feynman, *Phys. Rev. Lett.*, **23**, 1415 (1969).

[4] C.G. Callan and D.J. Gross, *Phys. Rev. Lett.*, **22**, 156 (1969).

[5] M. Gell-Mann, *Phys. Lett.*, **8**, 214 (1964).

[6] T. Eichten et al., *Phys. Lett.*, **B46**, 274 (1973).

[7] S. Weinberg, *Rev. Mod. Phys.*, **52**, 515 (1980), A. Salam, *Rev. Mod. Phys.*, **52**, 525 (1980), L. Glashow, *Rev. Mod. Phys.*, **52**, 539 (1980).

[8] P.W. Higgs, *Phys. Lett.* **12**, 132 (1964), *Phys. Rev. Lett.* **13**, 508 (1964), *Phys. Rev.* **145** 1156 (1966), F. Englert and R. Brout, *Phys. Rev. Lett.* **13**, 321 (1964), G.S. Guralnik et al., *Phys. Rev. Lett.* **13**, 585 (1964).

[9] G. 't Hooft and M. Veltman, *Nucl. Phys.* **B44**, 189 (1972).

[10] K. Bethge, U.E. Schroeder, *Elementarteilchen und ihre Wechselwirkungen*, Wissenschaftliche Buchgesellschaft, Darmstadt (Germany), (1986).

[11] R.J. Cashmore et al., *Measurement of Weak Neutral Current Couplings of Quarks at HERA*, in Proc. Workshop on Future Physics at HERA, eds. G. Ingelmann, A. De Roeck, R. Klanner, Vol. 1, 163, Hamburg (Germany), (1996).

[12] W.G. Seligman et al., *Phys. Rev. Lett.*, **79**, 1213 (1997).

[13] A. Argento et al., *Phys. Lett.,*, **B140**, 142 (1984).

[14] F. Halzen and A.D. Martin, *Quarks & Leptons: An Introductory Course in Modern Particle Physics*, John Weley and Sons, New York (USA), (1984).

[15] R.K. Ellis, W.J. Stirling and B.R. Webber, *QCD and Collider Physics*, Cambridge University Press, Cambridge (United Kingdom), (1996).

[16] A. Quadt, *Measurement and QCD Analysis of the Proton Structure Function F_2 from the 1994 HERA Data Using the ZEUS Detector*, DESY-Thesis-1998-007, RAL-TH-97-004, Hamburg (Germany), (1998).

[17] ZEUS Collaboration, S. Chekanov et al., *Eur. Phys. J.*, **C21**, 443 (2001)

[18] H1 Collaboration, C. Adloff et al., *Eur. Phys. J.* **C13** 609 (2000), H1 Collaboration, C. Adloff et al., *Eur. Phys. J.* **C 21** 33 (2001).

[19] V.N. Gribov and L.N. Lipatov, *Sov. J. Nucl. Phys.*, **15**, 438 (1972);
G. Altarelli and G. Parisi, *Nucl. Phys.*, **B126**, 298 (1977);
Yu.L. Dokshitzer, *Sov. Phys. JETP*, **46** 641 (1977).

[20] A. De Rujula et al., *Phys. Rev.*, **D10**, 1649 (1974)

[21] L.N. Lipatov, *Sov. J. Nucl. Phys.*, **23**, 338 (1976), E.A. Kuraev, L.N. Lipatov and V.S. Fadin, *Sov. Phys.* and *JETP*, **45** 199 (1977), Y.Y. Balitskii and L.N. Lipatov, *Sov. J. Nucl. Phys.*, **28**, 822 (1978).

[22] A.H. Mueller, *Nucl. Phys. B (Proc. Suppl.)*, **18C**, 125 (1990).

[23] P. Haberl, F. Schremp and H.-U. Martyn, *Contact Interactions and New Heavy Bosons at HERA*, in Proc. Workshop Physics at HERA, eds. W. Buchmüller and G. Ingelmann, Vol. 2, 1133, Hamburg (Germany), (1991).

[24] N. Arkani-Hamed, S. Dimopoulos and G. Dvali, *Phys. Lett.*, **B429**, 263 (1998), and *Phys. Rev.*, **D59**, 086004 (1999), I. Antoniadis et al., *Phys. Lett.*, **B463**, 257 (1998).

[25] K. Cheung, *Phys. Lett.*, **B460**, 383 (1999).

[26] ZEUS Collaboration, *The ZEUS Detector, Status Report 1993*, U. Holm ed., Hamburg (Germany), (1993).

[27] B. Foster et al., *Nucl. Instrum. and Methods*, **A338**, 254 (1994).

[28] R. Hall-Wilton et al., *The CTD Tracking Resolution*, internal ZEUS-Note, 99-024 Hamburg (Germany), (1999).

[29] A. Andresen et al. (ZEUS Calorimeter Group), *Nucl. Instr. and Meth.* **A309**, 101 (1991).

[30] M. Derrick et al., *Nucl. Instr. and Meth.*, **A309**, 77 (1991).

[31] A. Bernstein et al., *Nucl. Instr. and Meth.*, **A336**, 23 (1993).

[32] A. Bamberger et al. (ZEUS Presampler Group) *Nucl. Instrum. and Methods*, **A382**, 419 (1996).

[33] H. Bethe and W. Heitler, *Proc. Roy. Soc.*, **A146**, 83 (1934).

[34] S.M. Fisher et al. (Programming Techniques Group, ECP Division, CERN) *ADAMO Entity-Relationship Programming System: Version 3.3 : User's Guide* CERN, Geneva (Switzerland), (1993).

[35] U. Schneekloth *The HERA Luminosity Upgrade*, DESY-HERA 98-05 Hamburg (Germany), (1998).

[36] I. Brock and V. Bashkirov *A Straw-Tube Tracker for ZEUS*, internal ZEUS note, 98-046 Hamburg (Germany), (1998).

[37] ZEUS Collaboration, J. Breitweg et al.,*A Microvertex Detector for ZEUS* , DESY-PRC 97/01 (1997), The ZEUS MVD Group, E. Koffeman and H. Tiecke, *Mechanical Design and Construction of the ZEUS Microvertex Detector*, internal ZEUS note, 2000-028 Hamburg (Germany), (2000).

[38] M. Feuerstack-Raible, *Overview of Microstrip Readout Chips*, Nucl. Instr. and Meth. **A447**, 35 (2000).

[39] U. Koetz et al., *Nucl. Instrum. and Methods*, **A235**, 481 (1985).

[40] M. Milite, *The Internal Structure of Charmed Jets in Photoproduction at HERA and Tests of the ZEUS Microvertex Silicon Sensors* , PhD thesis, University of Hamburg (2001).

[41] I. Redondo, *Charm Electroproduction at HERA*, PhD thesis, University of Madrid (2001).

[42] D. Dannheim, *The Silicon Strip Detectors of the ZEUS Microvertex Detector*, DESY-THESIS-1999-027, Diplomarbeit, University of Hamburg (1999).

[43] J. Martens, *Simulationen und Qualitätssicherung der Siliziumstreifendetektoren des ZEUS-Mikrovertexdetektors*, DESY-THESIS-1999-044, Diplomarbeit, University of Hamburg (1999).

[44] C. Colledani et al., *Nucl. Instr. and Meth.*, **A372**, 379 (1996).

[45] C. Burgard, *TESA - A Test-stand Analysis Framework*, not published, Hamburg (Germany), (1999).

[46] E. Belau et al., *Nucl. Instr. and Meth.*, **214**, 253 (1983);
R.Turchetta, *Nucl. Instr. and Meth.*, **A335**, 44 (1993).

[47] D.E. Groom *The European Physical Journal C- review of Particle Physics* Number 1-4, 144 (1998).

[48] M. Goosens et al. *GEANT 3.21*, CERN, Geneva (Switzerland), (1994).

[49] R. Turchetta, *Nucl. Instr. and Meth.*, **A335**, 44 (1993);
T. Kawasaki et al., *Measurement of the Spatial Resolution of Wide-pitch Silicon Strip Detectors with Large Incident Angle*, KEK Preprint 96-172 (1996).

[50] G. Bashindzhagyan and N. Korotkova, *Simulation of Silicon Microstrip Detector Resolution for ZEUS Vertex Upgrade*, internal ZEUS note, 99-023, Hamburg (Germany), (1999).

[51] H. Spiesberger, *Web page (http://www.desy.de/~hspiesb/djangoh.html)*, accessed July 2001.

[52] H. Spiesberger, *HERACLES. An Event Generator for ep Interactions at HERA Including Radiative Processes, Version 4.6*, DESY, Hamburg (Germany), (1996).

[53] G. Ingelman, A. Edin and J. Rathsman, *Comp. Phys. Commun.*, **101**, 108 (1997).

[54] L. Lönnblad, *Comp. Phys. Commun.*, **71**, 15 (1992).

[55] T. Sjöstrand, *Comp. Phys. Commun.* 82 (1994) 74.

[56] CTEQ Collaboration, H.L.Lai et al., *Eur.Phys.J.*, **C12**, 375 (2000).

[57] H1 Collaboration: S. Aid et al., *Nucl. Phys.*, **B470**, 3 (1996); C. Adloff et al., *Nucl. Phys.*, **B497**, 3 (1997).

[58] ZEUS Collaboration: M. Derrick et al., *Zeit. Phys.*, **C69**, 607 (1996); J. Breitweg et al., *Eur.Phys.J.*, **C7**, 609 (1999).

[59] ZEUS Collaboration: M. Derrick et al., *Phys. Lett.*, **B315**, 481 (1993).

[60] H1 Collaboration: T. Ahmed et al., *Nucl. Phys.*, **B429**, 477 (1994).

[61] H. Jung, *Web page (http://www-h1.desy.de/~jung/rapgap)*, accessed July 2001.

[62] G. Marchesini et al., *Comp. Phys. Commun.*, **67**, 465 (1992);
G. Marchesini et al., *Herwig 6.3 release note*, hep-ph/0107071, (2001).

[63] M. Wodarczyk, *Measurement of the F_2 Structure Function of the Proton at HERA from 1996 and 1997 ZEUS Data*, PhD thesis, University of Wisconsin, (1999).

[64] H. Schnurbusch, *PhD thesis in preparation*, University of Bonn, (2002).

[65] ZEUS Luminosity Group; L. Adamczyk et al., *Luminosity Measurement in the ZEUS Experiment*, internal ZEUS note, 01-004 Hamburg (Germany), (2001).

[66] H. Abramowicz et al., *Nucl. Instr. and Meth.*, **A365** 508 (1995); R. Sinkus, *Nucl. Instr. and Meth.*, **A391**, 360 (1997).

[67] A. López-Durán Viani and S. Schlenstedt, *Electron Finder Efficiencies and Impurities. A comparison between SINISTRA95, EM and EMNET*, internal ZEUS note, 99-077 Hamburg (Germany), (2000)

[68] N. Tuning, *Proton Structure Funtions at HERA* , PhD thesis, University of Amsterdam, (2001).

[69] A. Caldwell, W. Liu and B. Straub *BCAL Electron Studies Part 1: MC and Test Beam Energy Studies*, internal ZEUS Note, 98-002 Hamburg (Germany), (1998).

[70] T. Doeker, A. Frey and M. Nakao, *Electron Position Reconstruction - Update of the ELECPO routines*, internal ZEUS-Note, 94-123 Hamburg (Germany), (1994).

[71] Ch. Amelung, *Electron Position Reconstruction in ZEUS: Further Update on the ELECPO Package (Based on 1995 Data)*, internal ZEUS-Note, 96-093 Hamburg (Germany), (1996).

[72] A. Kappes, *Measurement of $e^-p \rightarrow e^-X$ Differential Cross Sections at High Q^2 and of the Structure Function xF_3 with ZEUS at HERA*, University of Bonn, (2001).

[73] M. Martinez, *Calorimeter Noisy Cell Study for 1998-2000 ZEUS Data*, internal ZEUS-Note, 00-016 Hamburg (Germany), (2000).

[74] G.M. Briskin, *Diffractive Dissociation in ep Deep Inelastic Scattering*, PhD. thesis, Tel Aviv University, (1998).

[75] J. Grosse-Knetter,*Energy Correction for Islands*, internal ZEUS note, 97-039 Hamburg (Germany), (1997),
J. Grosse-Knetter, *Corrections for the Hadronic Final State*, internal ZEUS note, 98-031 Hamburg (Germany), (1998)

[76] F. Jacquet and A. Blondel, *Proc. of the study of an ep facility for Europe*, DESY 79-48, edited by U. Amaldi, Hamburg (Germany), 391 (1979).

[77] S. Bentvelsen, J. Engelen and P. Koijman, *Reconstruction of (x, Q^2) and Extraction of Structure Functions in Neutral Current Scattering at HERA*, in Proc. Workshop Physics at HERA, eds. W. Buchmüller and G. Ingelmann, Vol. 1, 23, Hamburg (Germany), (1991).

[78] D.E. Groom et al. (Particle Data Group), *Eur. Phys. Jour.*, **C15**, 1 (2000).

[79] M. Moritz, *Web page (http://giroz.desy.de/~moritz/thesis/tables/tables.html)*, accessed November 2001.

[80] ZEUS Collaboration, M. Derrick et al., *Zeit. Phys.*, **C72**, 399 (1996).

[81] C. Cormack, *Determination of the ZEUS UCAL Energy Scales using Diffractive DIS Events and High E_T Jets*, internal ZEUS note in preparation, R. Goncalo, *Neutral Current 98/99 e^-p and 99/00 e^+p*, Talk at ZEUS Collaboration Meeting, October 2001.

[82] ZEUS Collaboration, S. Chekanov et al., *The ZEUS NLOQCD Fit to Determine Parton Distribution Functions and α_s.*, Inter. Eur. Conf. on High Energy Physics, Budapest (Hungary), **628**, (2001).

[83] A. López-Durán Viani, *Measurement of the Proton Structure Function xF_3 in High Q2 DIS Events Using ZEUS Data*, PhD thesis, Humbold University Berlin (Germany), (2001).

[84] ZEUS Collaboration, S. Chekanov et al., *Search for Large Extra Dimensions, Finite Quark Radius and Contact Interactions in ep Collisions at HERA*, Inter. Eur. Conf. on High Energy Physics, Budapest (Hungary), **602**, (2001).

[85] D0 Collaboration, D. Abbott et al., *Phys. Rev. Lett.*, **86**, 1156 (2001).

[86] L3 Collaboration, M. Acciarri et al., *Phys. Lett.*, **B470**, 281 (1999).

[87] H1 Collaboration, C. Adloff et al., *Phys. Lett.*, **B479**, 358 (2000).

[88] ALEPH Collaboration, R.Barate et al., *Eur. Phys. J.*, **C12**, 183 (2000); DELPHI Collaboration, P. Abreu et al., *Eur. Phys. J.*, **C11**, 383 (1999); L3 Collaboration, M. Acciarri et al., *Phys. Lett.*, **B433**, 163 (1998); OPAL Collaboration, G. Abbiendi et al., *Eur. Phys. J.*, **C6**, 1 (1999).

[89] CDF Collaboration, F. Abe et al., *Phys. Rev. Lett.*, **79**, 2192 (1997); D0 Collaboration, D. Abbott et al., *Phys. Rev. Lett.*, **82**, 4769 (1999).

[90] L3 Collaboration, M. Acciarri et al., *Phys. Lett.*, **B489**, 81 (2000).

[91] W. Buchmüller, R. Rückl and D. Wyler, *Phys. Lett.*, **B191**, 442 (1987). Erratum in *Phys. Lett.*, **B448**, 320 (1998).

Acknowledgments

Many people contributed to the work presented here and supported me during my time as a Ph.D. student. Here I would like to take the opportunity to thank all of them.

In particular I would like to thank Prof. Robert Klanner who gave me the opportunity to work on my Ph.D. within the ZEUS collaboration at DESY. I am thankful for all his support during my work. I would also like to thank Tancredi Carli for many long and fruitful discussions and patient explanations and for reading and discussing my thesis draft.

Moreover, I would like to thank Alberto Garfagnini, Christoph Burgard and Uli Kötz for their guidance and help during my work for the ZEUS MVD project. Very special thanks to Margherita Milite who enlightened with her positive attitude some dark periods in the beginning of my work.

The work in the ZEUS high Q^2 NC group I enjoyed very much. I would like to thank Ken Long and Chris Cormack for their coordinating efforts and for answering numerous questions concerning the analysis. The achievement of the results was possible due to the very good collaboration with my colleagues Henning Schnurbusch, Ricardo Goncalo and in particular with Amaya López-Durán Viani.

I am very grateful for the friendly atmosphere within the ZEUS collaboration. Many thanks in particular to Dominik Dannheim, Ulrich Fricke, Florian Goebel, Oscar Gonzalez, Oliver Gutsche, Dorian Kcira, Ignacio Redondo, Stefan Stonjek, Mónica Vázquez, the already mentioned and all other students of the ZEUS Hamburg group for many discussions and for the activities we shared outside physics.

Last but not least I would like to thank my family for their continuous support and all friends outside DESY for their care and friendship, in particular the ones who managed that charm and beauty also exist for me outside physics.